University of Alberta

Solid-State Nuclear Magnetic Resonance and Computational Investigation of Half

-integer Quadrupolar Nuclei

Roshanak Teymoori

A thesis submitted to the Faculty of Graduate Studies and Research
in partial fulfillment of the requirements for the degree of

Doctor of Philosophy

Department of Chemistry

Spring 2014
Edmonton, Alberta

To Mom and Dad

"Everything in the universe is within you.

Ask all from yourself."

Rumi

Abstract

This thesis is concerned with applications of modern solid-state NMR spectroscopy. Investigations of three quadrupolar nuclei (^{51}V, ^{17}O, and ^{23}Na) are undertaken to demonstrate the practicality of solid-state nuclear magnetic resonance, SSNMR in studies of compounds containing these nuclei. The goal of each project is to gain insight into the effect of the local environment on the NMR observables.

Vanadium-51 solid-state NMR has been used to study oxo- and peroxo-vanadium compounds. The ^{51}V nucleus is examined to determine the vanadium magnetic shielding, MS and electric field gradient, EFG tensors. Density functional theory, DFT, has been utilized to calculate MS and EFG tensors to corroborate experimental data and to provide insight into the relationship between molecular and electronic structure. In addition the hyperbolic secant, HS pulse sequence has been used to provide spectra from which information about the shielding anisotropy of $[V(O)(ONMe_2)_2]_2O$ could be gained.

An investigation of oxygen-17 solid-state NMR studies of ligand, $^{17}OP(p\text{-Anis})_3$ and complex of $InI_3[^{17}OP(p\text{-Anis})_3]_2$ powder samples has also been carried out. Coordination of oxygen to indium causes a change in the ^{17}O chemical shift tensor. DFT calculations are also utilized and the theoretical results are compared with the corresponding experimental values.

Finally, solid-state sodium-23 NMR investigations of series of sodium salts, (sodium nitroprusside dihydrate, sodium bromate, sodium chlorate, sodium nitrate, sodium nitrite, sodium selenite and anhydrous disodium hydrogen phosphate) were carried out to determine ^{23}Na MS and EFG tensor parameters. The CASTEP and BAND codes were employed to calculate the EFG and MS tensors. In addition, in the case of sodium nitroprusside solid-state ^{17}O and ^{15}N NMR studies, as well as computational investigations of the corresponding EFG and MS tensors, were undertaken.

This *Thesis* reported the first experimental demonstration of sodium CS tensors determined from solid-state NMR spectroscopy of powder samples of these sodium salts. It also demonstrated the use of first-principles calculations, based on DFT theory in the CASTEP and BAND codes, to investigate the ^{23}Na EFG and MS tensors for these sodium salts.

Acknowledgements

First, I would like to thank my supervisor, Rod Wasylishen, for providing guidance and direction over the years. I thank him for giving me the opportunity to work in his very well-equipped laboratory, for proof reading my manuscripts and financial support.

Second, I thank the current group members: Alex, Jennifer, Michelle, Tom and Guy. Specifically I thank Guy for proof reading my manuscript, and for readily answering many naive questions, and always treating me with respect. Alex, thanks for some great food, wine, and company during the stresses of thesis preparation, and hopefully we will never repeat that IKEA fish experience ever again!! (Also, if your food was on fire, you should probably have already known there was alcohol in it!)

Also thanks to Kris Harris for computational help. Thanks to Dr. Gubin Ma for synthesis of several compounds, and Dr. Stanislav Stoyko for X-ray data.

I thank the former members of the solid-state NMR group, Kris Ooms, Kirk, Matt and Fu for hands-on training on the spectrometers and sharing with me their knowledge of NMR and computational chemistry.

I thank Profs. Elliott Burnell, Yunjie Xu, Alex Brown, Arthur Mar, for serving on my Ph.D. exam and for reading through this thesis.

I thank Dr. Victor Terskikh for CASTEP calculations and for acquiring NMR spectra at the 900 MHz spectrometer in Ottawa.

Within the chemistry department, I would like to thank many staff who did lots of supporting work for my Ph.D. program, especially Anita Weiler. Bob

McDonald for the help of understanding space groups, etc. I thank Prof. Arthur Mar for allowing me to use his X-ray laboratory, also, thanks, ladies, Diane and Lynne for the visits and talks.

For generous financial support over the years, I thank the University of Alberta.

The life of a graduate student is full of ups and downs and you get by with a little help from your friends. Without the support of my wonderful family and friends, during the difficult last two years, I'm not sure I would have survived. Thanks to my friends in Alberta Cross Cancer Institute for your never ending support and prayers. Thanks for your much-appreciated advice and encouragement. To my far-away sister, Hedyeh, thanks for always believing in me! I would like to thank Dr**.** Renee Polziehn, Renee you are wonderful boss, friend and mentor. I have learned a lot from you.

Finally, I thank my Mom and Dad for their unconditional love and support during my studies. I would like to thank my friends, Jacquelyn, Behnaz, Mohadesseh, and Zahra for providing private counseling sessions over the years.

TABLE OF CONTENTS

Chapter 3: Experimental Techniques, Data Processing

Chapter 4: Solid-State ^{51}V NMR Study of Vanadium Complexes

Chapter 8. Concluding Remarks and Suggestions for Future Work

Appendices

List of Tables

List of Figures

List of Symbols, Nomenclature and Abbreviations

ADF	Amsterdam Density Functional
CP	Cross-polarization
CT	Central transition
CW	Continuous wave
DAS	Dynamic-angle spinning
DFT	Density functional theory
DOR	Double rotation
DZ	Double-zeta
EF	Electric field
EFG	Electric field gradient
FC	Fermi contact mechanism
FID	Free-induction decay
FT	Fourier transforms
GGA	Generalized gradient approximation
HOMO	Highest occupied molecular orbital
HS	Hyperbolic secant pulse
LCAO	Linear combination of atomic orbitals
LUMO	Lowest unoccupied molecular orbital
MAS	Magic-angle spinning; $\theta = \arccos\left(1/\sqrt{3}\right) \approx 54.7356^{\circ}$

MO	Molecular orbital
MS	Magnetic shielding
MQMAS	Multiple quantum MAS
MRI	Magnetic resonance imaging
NMR	Nuclear magnetic resonance
NQR	Nuclear quadrupole resonance
PAS	Principal axis system
PSO	Paramagnetic spin-orbit mechanism
QZ4P	Quadruple-zeta quadruply-polarized
SD	Spin dipolar
SIMPSON	Simulation of solid-state NMR spectra (simulation program)
ST	Satellite transition
TPPM	Two-pulse phase‑modulated
TZ2P	Triple-zeta doubly-polarized
VWN	Vosko-Wilk-Nusair
XRD	X-ray diffraction
ZORA	Zeroth-order regular approximation
α, β, γ	Euler angles defining the relative orientation of two tensors
δ	Chemical shift tensor
ΔE	Energy difference, $E_n - E_0$

δ_{ii}	Principal components of $\boldsymbol{\delta}$, where i = 1, 2, 3, iso
ΔJ	Anisotropy in **J**
$\Delta\sigma$	Shielding anisotropy
γ_N	Gyromagnetic ratio
η_Q	Nuclear quadrupole asymmetry parameter
κ	Skew of magnetic shielding tensor
μ_0	Vacuum permeability
μ_N	nuclear magnetic moment
ν_L	Larmor frequency
ν_Q	Quadrupolar frequency
ν_{rot}	Sample spinning rate
θ and ϕ	Polar angles describing the orientation of **V** with respect to B_0
$(\pi/2)_x$	90º *rf* pulse with phase "*x*"
$\boldsymbol{\sigma}$	Nuclear magnetic shielding tensor
σ(free atom)	Nuclear magnetic shielding for a free atom
σ^{dia}	Diamagnetic component of $\boldsymbol{\sigma}$
σ^{para}	Paramagnetic component of $\boldsymbol{\sigma}$
σ_{ii}	Principal components of $\boldsymbol{\sigma}$, where i = 1, 2, 3, iso
τ_c	Rotational correlation time

Ω	Span of $\boldsymbol{\sigma}$ or shielding anisotropy
ε_0	Vacuum permittivity
Ξ	Absolute frequency (%)
Φ	Electric potential
Ψ_0	Wavefunction of ground state
Ψ_n	Wavefunction of nth excited state
B_0	External applied magnetic field
B_1	External magnetic field of *rf* pulse
BW	Bandwidth of the *rf* pulse
C_I	Nuclear spin-rotation constant
C_n	Principal rotation axis of *n*-fold symmetry
C_Q	Nuclear quadrupolar coupling constant
$\mathbf{D}$	Direct spin-spin coupling tensor
e	Charge of an electron
E_0	Electronic energy of the ground state
E_n	Electronic energy of the n^{th} excited state
$\hbar$	Reduced Plank's constant, $h/2\pi$
$\hat{\mathcal{H}}(t)$	Time-dependent Hamiltonian describing the relevant interactions
$\hat{\mathcal{H}}_{\mathbf{D}}$	Direct spin-spin coupling Hamiltonian

$\widehat{\mathcal{H}}_{\mathbf{J}}$	Indirect spin-spin coupling Hamiltonian
$\widehat{\mathcal{H}}_{\mathrm{Q}}$	Quadrupolar Hamiltonian
$\widehat{\mathcal{H}}_{\mathrm{S}}$	Nuclear magnetic shielding Hamiltonian
$\widehat{\mathcal{H}}_{\mathrm{total}}$	Total NMR Hamiltonian
$\widehat{\mathcal{H}}_{\mathrm{Z}}$	Zeeman Hamiltonian
I	Nuclear spin quantum number
I_z	z-component of the nuclear spin angular momentum operator
J	Indirect spin-spin coupling tensor
k	Boltzmann constant
l_k	Electron angular momentum operator with respect to the gauge origin
l_{kn}	Electron angular momentum operator with respect to the observe nucleus
L_i	Nuclear spin orbital angular momentum operator ($i = x, y, z$)
m_e	Mass of an electron
m_p	Mass of a proton
$\mathbf{M}_z$	Equilibrium magnetization aligned along the z-axis
N.A.	Isotopic natural abundance
ν_c	Transmitter or carrier frequency
Q	Nuclear quadrupole moment

R_{DD}	Direct dipolar coupling constant
R_{eff}	Effective dipolar coupling constant
rf	*R*adiofrequency
r_k	Position vector of electron, *k*, to the chosen origin
r_{kn}	Position vector of electron, *k*, to the observe nucleus, n
S/N	Signal-to-noise
sinc*x*	(sin*x*)/*x*
SO	Spin-orbit
ssb	Spinning sideband
S	Electron spin quantum number
T	Temperature
T	General second-rank tensor
T_1	Spin-lattice relaxation time
T_2	Spin-spin relaxation time
T_p	Duration of the *rf* pulse
V	Electric field gradient tensor
V_{ii}	Principal components of **V**, where *i* = X, Y, Z; also written as eq_{ii}
V_{ZZ}	Largest component of the EFG tensor, **V**
x, *y*, *z*	Cartesian coordinates
Z	Atomic number

Chapter 1. Objectives and Thesis Outline

1.1. Introduction

Nuclear magnetic resonance, NMR, is a valuable tool for the investigation of both solutions and solids. Recent improvements in hardware and the development of a wide range of pulse sequences have considerably increased the applications of solid-state NMR. Most high-resolution solid-state NMR studies have focused on spin-1/2 nuclei such as ^{13}C, ^{29}Si, and ^{31}P. Much less routine are NMR studies of solids containing quadrupolar nuclei (*i.e.*, those with spin-quantum numbers, *I*, greater than ½). One such example is ^{17}O, which is a quadrupolar nucleus (S = 5/2) with a low natural abundance, N.A = 0.038%, moderate magnetic and quadrupole moments resulting in low receptivity and NMR spectra with a low signal-to-noise ratio. Therefore, even with current technical improvements ^{17}O NMR remains challenging, even when samples are enriched in ^{17}O.

Recent hardware and software developments have also enabled the widespread use of density functional theory (DFT) based calculations to accurately predict NMR parameters for isolated molecule and periodic crystal structures. When used in conjunction with solid-state NMR, DFT calculations are an indispensable tool for the analysis and interpretation of NMR spectra.

1.2. Historical Overview of NMR Spectroscopy

NMR,[1,2] is a phenomenon which occurs when the nuclei of certain atoms are immersed in a static magnetic field and exposed to a second oscillating magnetic field that induces transitions between energy levels of a nucleus arising from its spin angular momentum. Nuclear magnetic resonance was first described and measured in molecular beams by Isidor Rabi[3] who won the Nobel Prize in Physics in 1944 for his discovery. In 1945, Felix Bloch and Edward Mills Purcell expanded the technique for use on liquids and solids, for which they shared the

Nobel Prize in Physics in 1952. The use of solid-state NMR by chemists did not spread rapidly, remaining in the realm of physics until the mid-to late 1950's.[4]

Early applications of NMR spectroscopy in studying solids were summarized by Abragam[5] and Andrew.[6] Many techniques have been developed to improve the resolution and sensitivity of NMR spectra of solid materials, such as magic angle spinning (MAS),[7] which was first reported in 1959.[8,9] In 1973, Pines *et al.*[10] described a cross-polarization, (CP) technique which typically transfers polarization from abundant spins (*e.g.*, ^{1}H) to dilute or rare spins (*e.g.*, ^{13}C) in solids.[11] With the combined use of MAS and CP,[12] many new applications of solid-state NMR spectroscopy became possible and interest in the field expanded rapidly.

An important development of NMR was magnetic resonance imaging (MRI) which was first introduced during the 1970's. In 1971, Damadian measured the T_1 and T_2 relaxation time of water in various tumors in comparison with related tissues. This finding, published in *Science,*[13] excited the magnetic resonance community because it suggested that there could be an important medical application for NMR in testing tissues for the presence of cancer. But it was really Lauterbur who had the transforming idea and demonstrated that nuclear magnetic resonance can be used as a viable imaging method.[14] In 1979, Mansfield developed techniques to speed-up imaging. He showed how the signals could be mathematically analyzed, which made it possible to develop a useful imaging technique.[15]

Since the early days of NMR an enormous number of NMR experiments have been conducted on diverse solid materials, such as glasses, ceramics, plastics, proteins, catalysts, fossil fuels, plants, polymers, etc., providing chemical and structural information which is in some cases unobtainable using other techniques.[16] Application of NMR spectroscopy to such diversified fields proves its versatility and power.

In summary, the success of NMR spectroscopy is evidenced by the five

Nobel prizes awarded to renowned and respected pioneers in the field: Isaac I. Rabi (Physics, 1944); Felix Bloch and Edward M. Purcell (Physics, 1952); Richard R. Ernst (Chemistry, 1991); Kurt Wuthrich (Chemistry, 2002), Paul C. Lauterbur and Sir Peter Mansfield (Medicine, 2003). The field is still expanding and new methodologies and techniques are being introduced to open up new areas of study.

1.3. Application of NMR Spectroscopy

NMR spectroscopy can conveniently be separated into liquid-state (solution) and solid-state NMR. In general, in liquids, the molecules usually tumble randomly at rates fast enough (~ GHz in frequency) to average anisotropic magnetic interactions. The advantage of this inherent isotropy (*i.e.*, same in all directions) is that the NMR spectrum usually appears as a set of narrow, well- defined sharp peaks. The disadvantage of this is that orientation-dependent (anisotropic) information is lost. On the other hand, in solids all of the anisotropic features are usually present in their full measure resulting in broad peaks. These broad NMR lineshapes provide much information on structure and dynamics in the solid state, but the complex pattern may be difficult to analyze.

There are several other benefits of employing solid-state NMR over solution NMR. For example, some samples are insoluble (*e.g.*, glasses, coal) or moisture-sensitive and thus dealing with them in the solid state is more straightforward. Another example, many compounds are not stable when dissolved in solution; therefore, obtaining the desired structural information is not possible in such cases Therefore, as outlined below, by employing solid-state NMR both molecular and electronic structural information may be obtained through the characterization of the full NMR interactions.

1.4. Thesis Outline

This *Thesis* describes the use of both solid-state NMR and DFT calculations to study quadrupolar nuclei, vanadium-51 (S = 7/2), oxygen-17 (S = 5/2), and sodium-23 (S = 3/2) and characterise their local electronic environment in a few selected inorganic compounds. Specifically, this *Thesis* involves the experimental determination and theoretical interpretations of the nuclear magnetic shielding, MS, and electric field gradient, EFG, tensors for the above nuclei.

This *Thesis* is partitioned as follows: *Chapter* 2 introduces and explains the basic principles behind solid-state NMR and describes the range of interactions present and their effects upon the NMR spectra. *Chapter 3* deals with the experimental and computational methods utilized in this work. The solid-state NMR techniques employed in this work are discussed. A summary of data processing is provided, as well as a general discussion of quantum computations of NMR parameters.

Solid-state ^{51}V NMR studies of a series of oxo-, and peroxo-vanadium compounds are the focus of *Chapter 4*. The ^{51}V nucleus is examined to measure the vanadium MS and EFG tensors. In this chapter experimental and theoretical characterization of the vanadium shielding and EFG tensors are discussed. These results provide insight about the local vanadium environment in these series of the compounds. In oxo and peroxo compounds, the vanadium likely plays an important role as insulin mimetic.[17]

In *Chapter 5*, solid-state ^{17}O NMR studies of $InI_3(^{17}OP(p\text{-Anis})_3)_2$ are discussed. In the first part of this chapter the experimental determination of the EFG and MS tensors for ^{17}O of this indium complex are discussed. DFT calculations were also employed and the theoretical results are compared with the corresponding experimental values in the latter part of this chapter. The goal of this study was to determine how the oxygen NMR parameters change from the phosphine oxide to phosphine oxide metal complexes.

Chapter 6 discusses solid-state ^{23}Na, ^{17}O and ^{15}N NMR studies of sodium nitroprusside, SNP, as well as computational investigations of the corresponding EFG and MS tensors. In this Chapter the computational results obtained by the BAND code are compared with those obtained with the CASTEP code. Initially we were interested in studying photo-induced linkage isomerism in this complex, but, such studies proved to be beyond the scope of this *Thesis*.

Chapter 7 addresses the possibility of obtaining sodium magnetic shielding tensor parameters from solid-state ^{23}Na NMR measurements. As well, shielding and EFG results obtained using the BAND and CASTEP methods are compared with those determined from experiments.

Finally, the highlights of the research presented in this *Thesis* are summarized in the concluding *Chapter 8* along with some suggestions for future investigations.

1.5. References

[1] E. M. Purcell, H. C. Torrey, R. V. Pound. *Phys. Rev*. **69**, 37, (1946).

[2] F. Bloch, W. W. Hansen, M. Packard. *Phys. Rev*. **69**, 127, (1946).

[3] I. I. Rabi, J. R. Zacharias, S. Millman, P. Kusch. *Phys. Rev*. **53**, 318, (1938).

[4] J. A. Pople, W. G. Schneider, H. J. Bernstein. *High Resolution Nuclear Magnetic Resonance*; McGraw-Hill Book Company: New York, US, 1959.

[5] A. Abragam. *Principles of Nuclear Magnetism*; Oxford University Press: Oxford, 1961.

[6] E. R. Andrew. *Nuclear Magnetic Resonance*; Cambridge University Press: 1955.

[7] M. Mehring. *Principles of High Resolution NMR Spectroscopy in Solids*; Springer-Verlag: New York, 1983.

[8] E. R. Andrew, A. Bradbury, R. G. Eades. *Nature*. **183**, 1802, (1959).

[9] I. J. Lowe. *Phys. Rev. Lett*. **2**, 285, (1959).

[10] A. Pines, M. G. Gibby, J. S. Waugh. *J. Chem. Phys*. **59**, 569, (1973).

[11] S. R. Hartmann, E. L. Hahn. *Phys. Rev*. **128**, 2046, (1962).

[12] J. Schaefer, E. O. Stejskal. *J. Am. Chem. Soc*. **98**, 1031, (1976).

[13] R. V. Damadian. *Science*. **171**, 1151, (1971).

[14] P. C. Lauterbur. *Nature*. **242**, 190, (1973).

[15] P. Mansfield, A. A. Maudsley, P. G. Morris, I. L. Pykett. *J. Magn. Reson.* **33**, 261, (1979).

[16] E. R. Andrew, E. Szczesniak. *Prog. Nucl. Magn. Reson. Spectrosc*. **28**, 11, (1995).

[17] K. H. Thompson, C. Orvig. *Dalton Trans*. 761, (2006).

Chapter 2. An Introduction to Solid-State NMR, Background and Techniques

2.1. Interactions in NMR

2.1.1. Spin Angular Momentum, Magnetic Moments, and Net Magnetization

In classical physics, when a particle rotates about a point, it possesses angular momentum, with the direction of the vector given by the right-hand rule (*i.e.* Let the fingers of your right hand curl in the direction of rotation and then your thumb points in the direction of the rotation vector). one can treat rotation and other angular motion quantities as vectors by using the right-hand rule: if the fingers of your right hand follow the rotation direction, then your thumb points along the rotation axis in the vector direction of the angular velocity ω. The spin angular momentum of a nucleus, denoted by **P**, is directly related to quantum mechanical quantity known as spin, **I**. The magnitude of the spin angular momentum vector is given by $P = \hbar\sqrt{I(I+1)}$, where I is the *nuclear spin quantum number*, and $\hbar$ is Planck's constant (h, divided by 2π).

Fundamental particles (*e.g.*, neutrons, protons and electrons) have spin ½ and all nuclei with $I > 0$ have magnetic moments, **μ**, in addition to spin angular momentum. Nuclear magnetic resonance may be defined as an interaction of a nuclear magnetic moment with an external magnetic field. The nuclear spin angular momentum is related to the magnetic moment by the *magnetogyric ratio*, γ, $\boldsymbol{\mu} = \gamma\mathbf{P} = \gamma\hbar\mathbf{I}$. Each NMR-active isotope possesses a specific magnetogyric ratio.[1] For a nucleus, the nuclear spin quantum number is determined by the relative numbers of neutrons and protons of the particular nuclear isotope. Isotopes with even numbers of neutrons and protons such as ^{12}C, ^{16}O, and ^{32}S have $I = 0$, and hence no magnetic moment.[2] Magnetically active nuclei such as ^{1}H, ^{13}C, ^{15}N, ^{29}Si and ^{31}P contain an odd number of either protons or neutrons and have $I = 1/2$. Quadrupolar nuclei, which comprise approximately 70% of stable NMR-active nuclei in the periodic table as shown in Figure 2.1, are those

with nuclear spin quantum numbers greater than ½.[3] For the remainder of this *Thesis*, *I* will be used to denote the spin-1/2 nucleus and *S* will denote the quadrupolar nucleus.

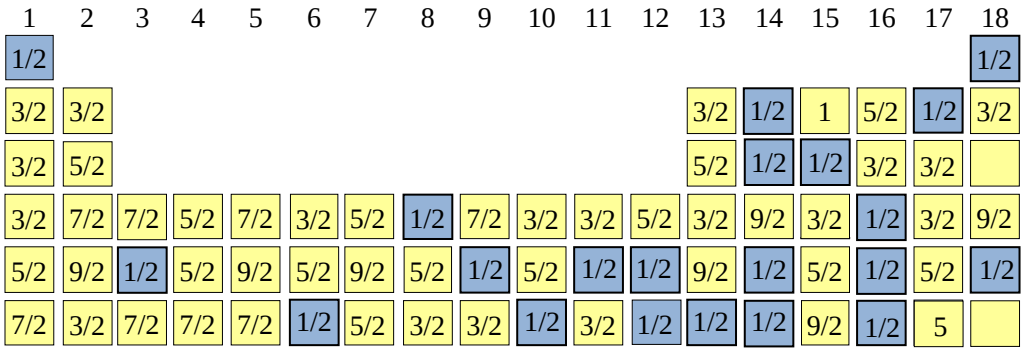

Figure 2.1. NMR periodic table indicating the magnetically active isotope with the highest naturally abundance, the blank square refers to $I = 0$.

Bulk samples, usually several milligrams, are used in solid-state NMR experiments. Thus, numerous nuclei are present in a sample resulting in an ensemble of nuclear spins. For a nucleus with $I = 1/2$ in an applied magnetic field there are two possible Zeeman energy levels. For a nucleus with a positive magnetogyric ratio the lower energy state belongs to $m_I = 1/2$ and the higher energy state to $m_I = -1/2$, where m_I is the *magnetic quantum number*. For an ensemble of spins, at equilibrium the energy levels will be populated as determined by the Boltzmann distribution:

$$\frac{N_{m_I=1/2}}{N_{m_I=-1/2}} = \exp\left(\frac{\Delta E}{k_B T}\right) = \exp\left(\frac{\nu_0}{k_B T} h\right) = \exp\left(\frac{\gamma B_0 \hbar}{k_B T}\right) \qquad (2.1)$$

where k_B is the Boltzmann constant, T is the absolute temperature, and ν_0 is the *Larmor frequency*, $\nu_0 = |\gamma/2\pi|B_0$. At typical temperatures, $k_B T$ is very large compared to $h\nu_0$, thus $N_{m_I=1/2} \cong N_{m_I=-1/2}$. Under the so-called *high-temperature approximation* ($kT >> \gamma\hbar B_0$), the population difference, ΔN, between the lower and upper energy levels is given by

$$\Delta N = \frac{N\Delta E}{(2k_B T)} = \frac{N\gamma\hbar B_0}{(2k_B T)} \qquad (2.2)$$

where N is the total number of spins in the sample. From equation 2.22, one can see that the population difference of the Zeeman states depends directly on the energy difference between these states, magnetic field B_0, and inversely proportional to temperature. In NMR, this difference is very small compared to those observed for other spectroscopic techniques. As a result, for ^{1}H, the ratio between the Zeeman states is 1.000081, where $\gamma_H = 26.752 \times 10^7$ rad $s^{-1}T^{-1}$, at $\mathbf{B_0}$ = 11.75 T and T = 298 K, while for ^{13}C, in the same magnetic field at the same temperature, the ratio is 1.000020, where $\gamma_C = 6.728284 \times 10^7$ rad $s^{-1}T^{-1}$. This implies that for 1 million protons, the population difference between the two energy levels is only 40, while for a million ^{13}C spins, the population difference is only about 10 spins. The low fractional polarization, ~ 10^{-5}, and weak magnetic moments per spin result in the need for samples that have a minimum of ~ 10^{18} nuclear spins for adequate sensitivity.

2.1.2. The NMR Hamiltonian

A theoretical description of a spin system begins with the spin *Hamiltonians*.[4] The total Hamiltonian for a spin system is a summation of all the individual Hamiltonians that describe particular interactions, $\mathcal{H}_i$

$$\mathcal{H} = \sum_i \mathcal{H}_i \tag{2.3}$$

The Hamiltonian $\mathcal{H}$ which describes the total nuclear spin interaction may be written as the sum of the individual interactions:

$$\mathcal{H} = \mathcal{H}_Z + \mathcal{H}_{MS} + \mathcal{H}_D + \mathcal{H}_J + \mathcal{H}_Q \tag{2.4}$$

where,

a) $\mathcal{H}_Z$ is the Zeeman interaction of the nucleus with the applied magnetic field.

b) $\mathcal{H}_{MS}$ describes the magnetic shielding interaction caused by magnetic shielding from the surrounding electrons.

c) $\mathcal{H}_D$ describes the direct dipolar interaction with other nuclei.

d) $\mathcal{H}_J$ describes the indirect spin-spin coupling interaction with other nuclei.

e) $\mathcal{H}_Q$ describes the nuclear quadrupolar interaction, (only important for nuclei with $I > ½$).

For most cases, including all cases considered in this *Thesis*, we can assume the high-field approximation; that is, the Zeeman interaction is much greater than all other internal NMR interactions. Correspondingly, these internal interactions can be treated as perturbations on the Zeeman Hamiltonian, $\mathcal{H}_Z$. In general, the interactions in the solid-state are proportional to the product of the appropriate vectors (*e.g.*, **I**, **S**, $\mathbf{B_0}$) and a second-rank tensor describes the three-dimensional nature of the interaction (*e.g.*, the magnetic shielding tensor, **σ**). In the solid state, each of these interactions can make contributions causing spin-state energies to shift, resulting in a direct manifestation of these interactions in the NMR spectra.

Mathematically, a tensor is a set of quantities that transforms in a prescribed way.[5] Scalar quantities are tensors of rank zero, and vectors are of rank one. The magnetic shielding, quadrupolar, direct dipolar and indirect nuclear spin-spin coupling interactions are each described by a second-rank tensor composed of 3^2 quantities and can be represented as 3×3 matrix which characterizes the three-dimensional nature (*i.e.*, the magnitudes and directions) of the interaction.

In the general case, a given interaction T can be described by a second-order tensor:

$$\begin{pmatrix} T_{xx} & T_{xy} & T_{xz} \\ T_{yx} & T_{yy} & T_{yz} \\ T_{zx} & T_{zy} & T_{zz} \end{pmatrix} \tag{2.5}$$

where *x*, *y* and *z* refer to the axes. By diagonalising this matrix, the interaction can be described in its own axis system called the "Principal Axis System" (PAS) of the interaction. In the PAS the new matrix is diagonal, *i.e.*,

$$\begin{pmatrix} T_{11} & 0 & 0 \\ 0 & T_{22} & 0 \\ 0 & 0 & T_{33} \end{pmatrix} \tag{2.6}$$

This axis system is shown in Figure 2.2

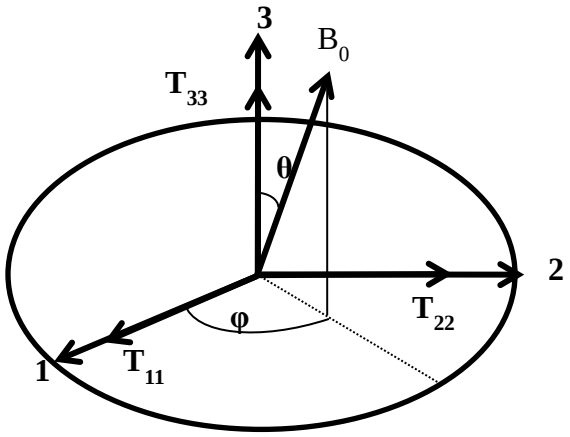

Figure 2.2. Tensorial representation of an interaction.

Some of the useful quantities used in NMR analysis can be extracted from this tensor amongst which, the isotropic contribution T_{iso} which is invariant to axis system, is given by:

$$T_{iso} = \frac{1}{3}TrT = \frac{1}{3}(T_{11} + T_{22} + T_{33}) \qquad (2.7)$$

The anisotropy of the interaction δ_T is described (*Haeberlen* notation):[6]

$$\delta_T = T_{iso} - T_{33} \quad \text{where} \quad |T_{33} - T_{iso}| \geq |T_{11} - T_{iso}| \geq |T_{22} - T_{iso}| \qquad (2.8)$$

For a spherical tensor ($T_{11} = T_{22} = T_{33} = T_{iso}$) the tensor is therefore isotropic and $\delta_T = 0$. The deviation from axial symmetry ($T_{11} = T_{22}$) is referred to as the asymmetry of the interaction and given by:

$$\eta_T = \frac{T_{22} - T_{11}}{\delta_T} \qquad (2.9)$$

All the NMR interactions can be described as a sum of an isotropic and an anisotropic contribution. For interactions that are relatively small compared to the Zeeman interaction, this sum is expressed as follows:

$$T_{iso} + T_{aniso} = T_{iso} + \delta_T \left[P_2(\cos\theta) - \frac{\eta_T}{2}\sin^2\theta \cos 2\varphi \right] \qquad (2.10)$$

Where $P_2(\cos\theta) = \frac{(3\cos^2\theta - 1)}{2}$ is the second-order Legendre polynomial and θ and φ are the angles describing the orientation of the tensor axes as shown in Figure 2.2. In the following, we use this tensorial model to describe the different magnetic interactions encountered in NMR.

2.1.3. Zeeman Interaction

The fundamental interaction responsible for the nuclear magnetic resonance phenomenon is the Zeeman interaction, $\mathcal{H}_Z$, which involves the interaction of $\boldsymbol{\mu}$ with $\mathbf{B_0}$, and occurs for all magnetically active nuclei. This interaction causes the normally degenerate magnetic spin energy levels to become non-degenerate, yielding $2I + 1$ energy levels with separation $h\nu_0 = \gamma\hbar B_0$. Induced transitions between these energy levels produce magnetic resonance. The Zeeman interaction $\mathcal{H}_Z$ may be written as

$$\mathcal{H}_Z = -\boldsymbol{\mu} \cdot \boldsymbol{B_0} = -\gamma_N \hbar I_Z \cdot B_0 = -g_N \mu_N B_0 I_Z \qquad (2.11)$$

where γ_N is the magnetogyric ratio for a particular given nucleus, $\boldsymbol{\mu} = \gamma \mathbf{I}\hbar$, g_N is the nuclear g factor, $\mu_N = \frac{e\hbar}{2m_p}$ is the nuclear Bohr magneton, and I_Z is the spin operator corresponding to the z-component of the spin-angular momentum. The energy difference between the quantized energy levels is proportional to $\mathbf{B_0}$ which can be expressed by

$$\Delta E = \gamma_N \hbar B_0 \qquad (2.12)$$

Since a larger energy difference leads to a greater population difference between the levels, which corresponds to an increase in the sensitivity of the NMR experiment, it might seem that working at the highest possible magnetic field would be most desirable. This is generally true, but the magnetic shielding interaction (see below) becomes larger at higher fields, and is more difficult to average in solid-state NMR experiments.

In Figure 2.3, the Zeeman interaction is illustrated, which is linear in the applied magnetic field $\mathbf{B_0}$. This splitting of the energy levels when a magnetic field is applied is called the *Zeeman effect*.

Figure 2.4 shows a schematic of a typical apparatus used in NMR experiments. A large, homogenous field $\mathbf{B_0}$ at the sample is provided by a superconducting magnet. The sample is placed in a coil of conducting wire which provides the rf irradiation used to induce NMR transitions. An ac voltage is applied across the coil circuit at a frequency ν which provides a linearly polarized time-dependent magnetic field with amplitude $2\mathbf{B_1}$ orthogonal to $\mathbf{B_0}$.

It is possible to induce a transition based on the selection rule $\Delta m_I = \pm 1$ by applying electromagnetic radiation of the appropriate frequency. For an isolated nucleus, NMR transition energies are given by

$$\nu_0 = \left(\frac{\gamma_N B_0}{2\pi}\right) \tag{2.13}$$

where ν_0 is the *Larmor* frequency. The *Larmor* frequency may also be written in terms of rad s^{-1}, as $\omega_0 = \gamma B_0$, which can be used to simplify the appearance of certain equations.

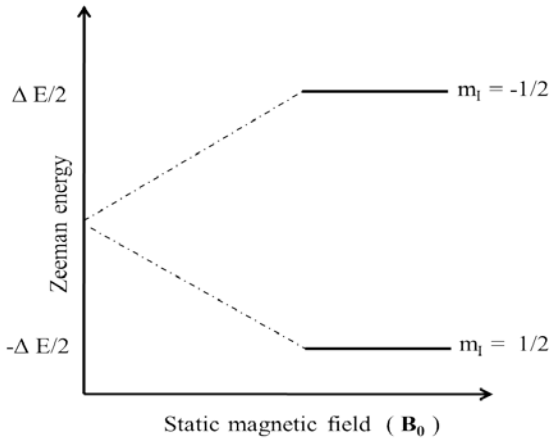

Figure 2.3. Zeeman energy splitting of nuclear spin states for I = ½ nuclei, labelled according to the allowed values of m_I, the projection of the dimensionless nuclear spin angular momentum I along $\mathbf{B_0}$, for the case where $m_I = \pm ½$.

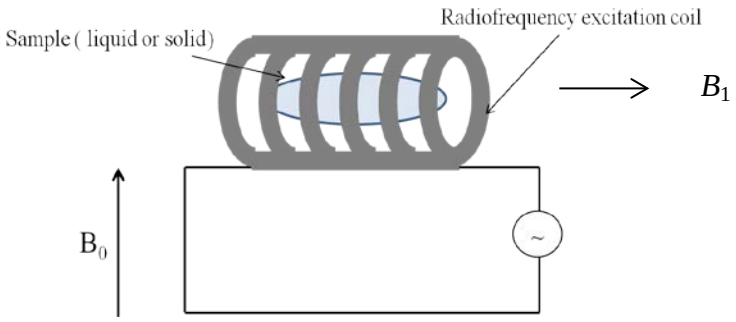

Figure 2.4. Basic NMR experimental apparatus. The static magnetic field $\mathbf{B_0}$ may be provided by superconducting magnets, electromagnets, permanent magnets or the earth's field.

The introduction of Fourier transform methods in the early 1970s allowed experiments to be performed in the time-domain where pulses of broadband irradiation excite transitions that yield subsequent time evolution of the total nuclear magnetization, M_0:

$$M_0 = \frac{1}{3} N \gamma_N^2 \frac{\hbar^2 I(I+1)}{k_B T} B_0 \qquad (2.14)$$

where N is the number of spins in the ensemble and I is the dimensionless nuclear spin angular momentum. A short resonant rf pulse tips M_0 away from $\mathbf{B_0}$ and if the pulse duration, $t_{P,}$ is such that $\gamma_N B_1 t_P = \pi/2$, then the tip angle is $\pi/2$ rad and the magnetization is placed in the transverse plane. This is shown in Figure 2.5.

As the magnetization evolves in the transverse plane, a voltage is induced in the rf coil via Faraday's law of induction and is proportional to $(d/dt)M_0$. The signal voltage is given by[7]

$$S(\mathrm{t}) = S_0 \exp(\mathrm{i}(\omega_0 - \omega_\mathrm{t}))\exp(\frac{-t}{T_2}) \qquad (2.15)$$

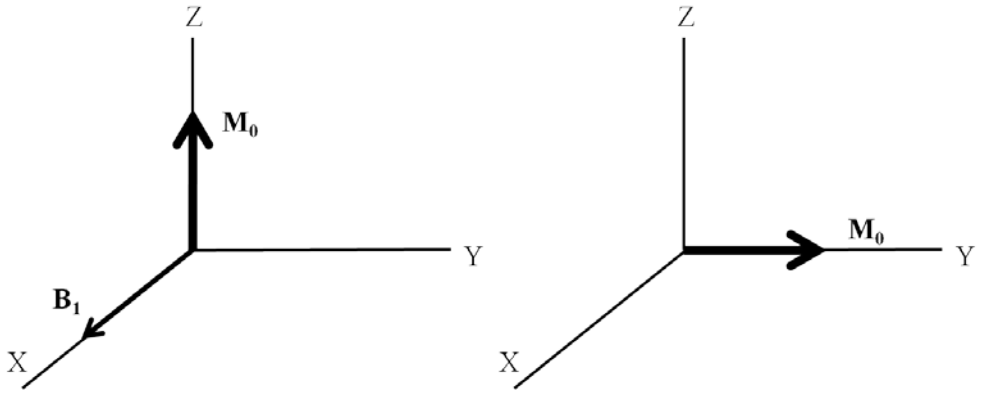

Figure 2.5. The magnitude of the nuclear magnetic moment is shown before (left) and after (right) application of resonant $\pi/2$ pulse in the rotating frame.

where S_0 is a scaling factor proportional to M_0, T_2 is the transverse nuclear relaxation time, ω_0 and ω_t are *Larmor* and transmitter frequencies, respectively. The time domain signal, $S(t)$ is known as the free induction decay, and by Fourier transforming this time domain signal, the frequency domain spectrum is usually obtained as a single Lorentzian peak as shown in Figure 2.6. Fourier transform methods have also allowed sophisticated pulse sequences to be employed to selectively edit the spin Hamiltonian to provide specific chemical or spatial information. [8]

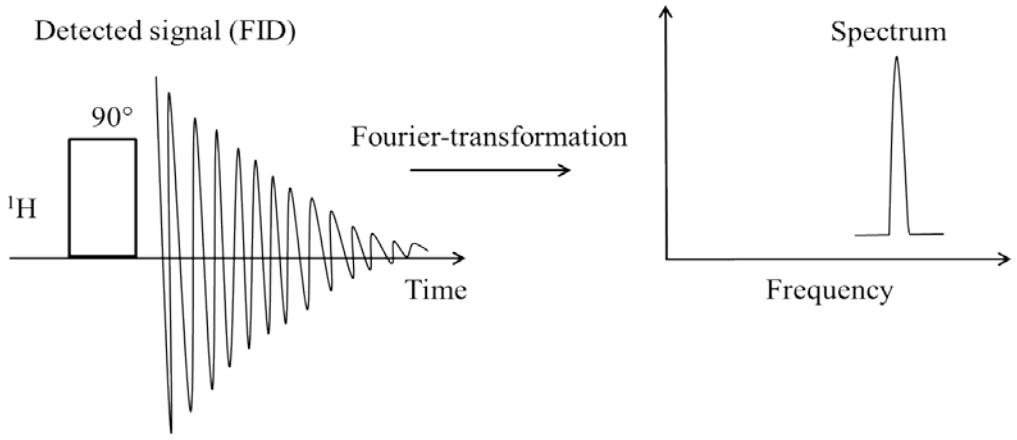

Figure 2.6. A time domain NMR signal is converted to the frequency domain by Fourier transformation.

2.1.4. Magnetic Shielding and the Chemical Shift

Magnetic shielding is usually expressed in dimensionless units, ppm, which is independent of $\mathbf{B}_0$. The magnetic shielding Hamiltonian can be written as

$$\mathcal{H}_{\mathrm{MS}} = \gamma\hbar\mathbf{I}\cdot\boldsymbol{\sigma}\cdot\mathbf{B_0} \tag{2.16}$$

which describes magnetic shielding as the coupling of the spin I and $\mathbf{B_0}$ with the magnetic shielding tensor, $\boldsymbol{\sigma}$.

If we consider an atom within a sample, the magnetic field experienced by the nucleus will vary slightly, depending on its electronic environment. In the presence of the external magnetic field $\mathbf{B}_0$, the circulation of the electrons around a given nucleus in an atom creates a small local magnetic field, $\mathbf{B}'$, in the opposite direction to $\mathbf{B}_0$ and the field effectively interacting with a nucleus i, ($\mathbf{B}_{eff}$) can therefore be written:

$$B' = \sigma B_0 \qquad B_{eff} = B_0 - B' \qquad B_{\mathrm{eff}} = (1-\sigma)B_0 \tag{2.17}$$

where σ is the magnetic shielding constant and depends on the local electronic structure around the nucleus i. Note, for a nucleus in a molecule σ maybe positive or negative (vide infra). The chemical shift, δ, is related to the magnetic shielding by

$$\delta_{\mathrm{sample}} = \frac{\upsilon_{\mathrm{sample}}-\upsilon_{\mathrm{reference}}}{\upsilon_{\mathrm{reference}}} = \frac{\frac{\gamma B_0}{2\pi}(1-\sigma_{\mathrm{sample}})-\frac{\gamma B_0}{2\pi}(1-\sigma_{\mathrm{reference}})}{\frac{\gamma B_0}{2\pi}(1-\sigma_{\mathrm{reference}})} = \tag{2.18}$$

$$\frac{\sigma_{\mathrm{reference}}-\sigma_{\mathrm{sample}}}{1-\sigma_{\mathrm{reference}}}$$

where $\sigma_{\mathrm{reference}}$ is the magnetic shielding for a chosen reference sample. Both σ and δ are measured in ppm. For most nuclei, and in particular for low-mass nuclei, $\sigma_{\mathrm{reference}} \ll 1$, so equation 2.18 can be approximated by

$$\delta \cong \sigma_{reference} - \sigma_{sample} \quad (2.19)$$

In practice, one measures the resonance frequency of the sample of interest with respect to that of a primary or secondary reference. The principal components of the chemical shift (CS) tensor, δ_{ii}, correspond to those of the shielding tensor according to equation 2.18, *i.e.*, δ_{11} corresponds to σ_{11} etc. It is convenient to define two related quantities, the span Ω and the skew κ which help in describing the shape of the NMR powder pattern resulting from a particular magnetic shielding tensor,[9]

$$\delta_{iso} = \frac{1}{3}(\delta_{11} + \delta_{22} + \delta_{33}) \quad (2.20)$$

$$\Omega = \delta_{11} - \delta_{33} = \sigma_{33} - \sigma_{11} \quad (2.21)$$

$$\kappa = \frac{3(\sigma_{iso} - \sigma_{22})}{\Omega} \approx \frac{3(\delta_{22} - \delta_{iso})}{\Omega} \quad (2.22)$$

The skews are unitless and can take on values between -1 and +1. The span is always positive since $\delta_{11} \geq \delta_{22} \geq \delta_{33}$ and $\sigma_{11} \leq \sigma_{22} \leq \sigma_{33}$.

In isotropic liquid, because of rapid molecular tumbling, the three-dimensional nature of the shielding is typically averaged to an isotropic value. The observed chemical shift represents this isotropic average. For rapidly tumbling molecules in solution, $\mathbf{B}'$ is related to the external field by the magnetic shielding, σ, see equation (2.17).

In a solid, however, there are usually few or no rapid molecular motions. For a rigid solid, the chemical shift depends on the orientation of each crystallite with respect to $\mathbf{B_0}$. Therefore, in a polycrystalline or powder sample where all crystallite orientations are present, a broad resonance pattern or chemical shift powder pattern is observed. Magnetic shielding can be described by a second-rank Cartesian tensor, $\boldsymbol{\sigma}$, which has nine independent values that specify the magnitude and orientation of the magnetic shielding tensor (MS) with respect to

the laboratory frame. The MS tensor can be written as the sum of symmetric and antisymmetric second-rank tensors.[10] However, to a reasonable approximation, only the symmetric portion of the MS tensor, σ_{sym}, makes a contribution to observed magnetic shielding;[10] therefore, the antisymmetric components are not considered here. In its PAS, σ_{sym} is diagonal, the off-diagonal components are zero and the diagonal entries are the principal components: σ_{11}, σ_{22}, and σ_{33}, $\sigma_{33} > \sigma_{22} > \sigma_{11}$.

$$\sigma^{\text{molecule}} = \begin{bmatrix} \sigma_{xx} & \sigma_{xy} & \sigma_{xz} \\ \sigma_{yx} & \sigma_{yy} & \sigma_{yz} \\ \sigma_{zx} & \sigma_{zy} & \sigma_{zz} \end{bmatrix} \qquad \sigma^{PAS} = \begin{bmatrix} \sigma_{11} & 0 & 0 \\ 0 & \sigma_{22} & 0 \\ 0 & 0 & \sigma_{33} \end{bmatrix} \tag{2.23}$$

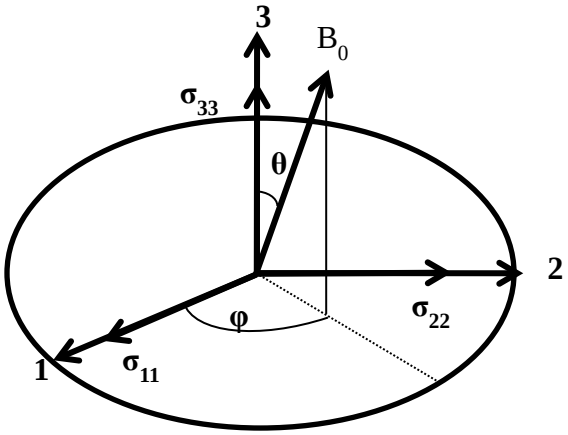

Figure 2.7. Simplified diagram illustrating the orientation of the magnetic shielding tensor with respect to the magnetic field, as defined by the polar angles, θ, φ.

The orientation of the MS tensor with respect to $\mathbf{B_0}$ is defined by the polar angles θ and φ, shown in Figure. 2.7. The resonance frequency of spin *I* can then be expressed as[10]

$$\nu_I(\theta, \varphi) = \nu_0 - \nu_{CS} \tag{2.24}$$

$$\nu_{CS} = \nu_0 \left(\sigma_{11} \sin^2\theta \cos^2\varphi + \sigma_{22} \sin^2\theta \sin^2\varphi + \sigma_{33} \cos^2\theta\right) \tag{2.25}$$

The orientation of the MS tensor in the molecular frame can be determined from

single-crystal NMR studies, with the relative orientation of the two frames given by three Euler angles.[11] However, in most instances single crystals suitable for such NMR studies are not available, and experiments are time consuming. Therefore, experiments are generally conducted on powder samples, in which the molecules assume random distributions with respect to the applied magnetic field, $\mathbf{B}_0$. The presence of the magnetic shielding interaction gives rise to characteristic solid-state NMR powder patterns as shown in Figure 2.8.

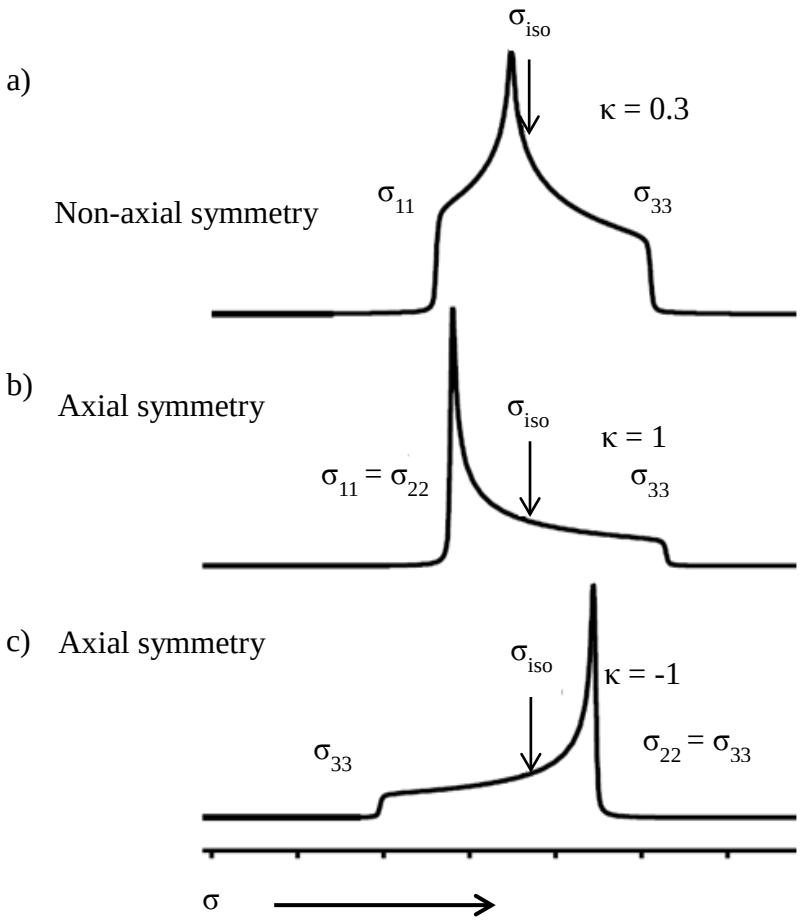

Figure 2.8. Solid-state NMR spectra exhibiting magnetic shielding anisotropy, CSA (a) Non-axial, (b) axial, $\kappa = 1$, (c) axial, $\kappa = -1$.

As illustrated above, NMR spectra of stationary powder samples contain information on the orientation dependence of the magnetic shielding interaction. Analysis of such spectra yield the principal components of the MS tensor, but

usually no information is obtained regarding the orientation of the MS tensor with respect to the molecular frame, unless it is required by molecular symmetry.

The chemical shift phenomenon was first observed in 1950.[12,13,14] Several years later, Norman Ramsey formalized the theory of nuclear magnetic shielding. According to Ramsey's theory,[15] magnetic shielding can be divided into diamagnetic, σ^{d} and paramagnetic, σ^{p}, terms, which depend on the ground and excited electronic states, respectively, of the molecule,[16] such that $\sigma = \sigma^{d} + \sigma^{p}$. The diamagnetic shielding contribution is positive and yields an increase in shielding which can be expressed as follow:

$$\sigma_{ij}^{d} = \frac{e^2\mu_0}{8\pi m_e}\left\langle\psi_0\left|\sum_k \frac{r_{k\cdot}r_{kN}\delta_{ij}^{k} - r_{kNi}r_{kNj}}{r_{kN}^{3}}\right|\psi_0\right\rangle \qquad (2.26)$$

where σ_{ij}^{d} is element *ij* of a diamagnetic shielding tensor, ψ_0 is a ground-state wave function, δ_{ij}^{k} is the Kröneker delta function, and r_k, r_{kN} are position vectors for electron *k* relative to the chosen origin. Qualitatively, diamagnetic shielding is dominated by the core electrons of an atom. Consequently, it generally exhibits small variations for a given nucleus, and it is relatively insensitive to the nature of the molecular system under investigation.

On the other hand, the paramagnetic term is usually negative and governs the shielding for any multi-electron molecular system. The paramagnetic term can be expressed as

$$\sigma_{ij}^{p} = -\frac{e^2\mu_0}{8\pi m_e^2}\sum_{n>0}\frac{1}{E_n - E_0} \times$$

$$\left[\begin{array}{c}\left\langle\psi_0\left|\sum_k \frac{l_{ki}}{r_k^3}\right|\psi_n\right\rangle\langle\psi_n|\sum_k l_{ki}\,|\psi_0\rangle + \\ \langle\psi_0|\sum_k l_{ki}\,|\psi_n\rangle\left\langle\psi_n\left|\sum_r \frac{l_{ki}}{r_k^3}\right|\psi_0\right\rangle\end{array}\right] \qquad (2.27)$$

where l_{ki} is the electron angular momentum operator with respect to the gauge origin. As evident from the equation, the paramagnetic term is governed by

symmetry-allowed mixing of occupied and virtual orbitals that are centred at the nucleus of interest and by the inverse of the energy difference between these states, $(E_n - E_0)^{-1}$. Thus, smaller ΔE values and greater overlap of molecular orbitals lead to a larger deshielding with respect to the bare nucleus. Consequently, the paramagnetic shielding contribution to the total magnetic shielding tensor is intricately related to both the local symmetry and structure of the electronic framework of a molecule in the vicinity of the nucleus.

2.1.5. The Direct and Indirect Nuclear Spin-Spin Coupling Interactions

2.1.5.1. Dipolar Interaction

The dipolar interaction arises from the direct through-space dipole-dipole interaction between two nuclei and can be either heteronuclear (*e.g.*, ^{1}H-^{13}C) or homonuclear (*e.g.*, ^{1}H -^{1}H) in nature. Figure 2.9 shows the direct dipolar interaction for two spins, I_A, and I_B, in the absence of a magnetic field. Since each spin has a magnetic moment, a given spin generates a magnetic field which interacts with the other spin of the spin pair. The dipolar interaction between spins I_A and I_B can be described by the *Hamiltonian*, $\mathcal{H}_D$:

$$\mathcal{H}_D = \mathbf{I_A} \cdot \mathbf{D} \cdot \mathbf{I_B} \tag{2.28}$$

Here, I_A and I_B are the nuclear spin operators of the two nuclei involved. In its PAS, the direct dipolar coupling tensor, **D**, is given in Cartesian coordinates as follows:

$$\boldsymbol{D} = R_{DD}\begin{bmatrix} 1 & 0 & 0 \\ 0 & 1 & 0 \\ 0 & 0 & -2 \end{bmatrix} \tag{2.29}$$

This tensor is axially symmetric about the internuclear vector joining the dipolar-coupled nuclei. The direct dipolar coupling constant, R_{DD}, depends directly on the distance separating the two coupled spins:

$$R_{DD} = \frac{\mu_0}{4\pi}\frac{\gamma_{\mathrm{I_A}}\gamma_{\mathrm{I_B}}\hbar}{2\pi}\langle r_{AB}^{-3}\rangle \tag{2.30}$$

Here, $\langle r_{AB}^{-3}\rangle$ is the motionally averaged inverse cube of the internuclear distance. In a completely general coordinate system, this interaction is written as[17]

$$\mathcal{H}_{\mathrm{D}} = \hbar R_{DD}\left[\mathbf{I}_{\mathrm{A}}\cdot\ \mathbf{I}_{\mathrm{B}} - \frac{3(\mathbf{I}_{\mathrm{A}}\cdot\boldsymbol{r}_{\mathrm{AB}})(\mathbf{I}_{\mathrm{B}}\cdot\boldsymbol{r}_{\mathrm{AB}})}{r_{\mathrm{AB}}^2}\right] \tag{2.31}$$

The expansion of the Hamiltonian for a spin-pair known as the dipolar alphabet A to F[18] as opposed to Cartesian cooridnates is generally performed in spherical coordinates. The first term, A, which is important for a heteronuclear spin system is given by

$$A = R_{DD}\ (1 - 3\cos^2\theta)\hat{I}_{\mathrm{Z,A}}\cdot\hat{I}_{Z,B} \tag{2.32}$$

where θ is the angle between the dipolar vector r_{AB} and $\mathbf{B_0}$.

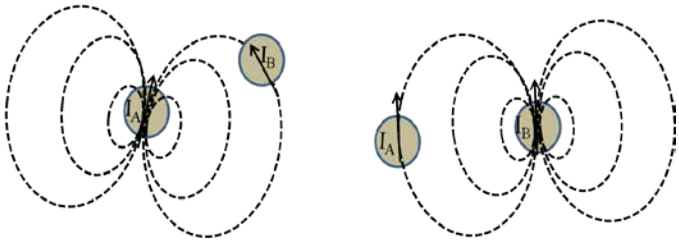

Figure 2.9. Schematic diagram of the direct dipolar interaction between two nuclear spins, I_{A}, and I_{B}.

The dipolar interaction is directly proportional to the magnetogyric ratios of the two nuclei and inversely proportional to their internuclear separation cubed; therefore, dipolar interactions will be more important for nuclei with large magnetic moments (*e.g.*, ^{1}H) that are close to each other. This dependence can be utilized to determine distances between pairs of nuclei. While the indirect spin-spin coupling interaction is a through-bond interaction, the dipolar interaction is an entirely through-space interaction. This means that atoms need not be bonded to each other to experience a dipolar interaction. However, the observed value for

the dipolar interaction may be affected if there is significant anisotropy in the indirect coupling (see section 2.1.5.2).

In isotropic liquid NMR, rapid molecular tumbling causes the dipolar interaction to be averaged to zero. In the solid-state, however, where molecules are much more rigid, the dipolar interaction usually does not undergo such averaging, although vibrational motion generally reduces the observed values slightly. For an isolated spin-pair, in the absence of magnetic shielding anisotropy, the orientation dependence is precisely mapped in a well-defined powder pattern, known as the Pake pattern, after its discovery by G.E. Pake.[19]

2.1.5.2. Indirect Nuclear Spin-Spin Coupling Interaction, J- Coupling

The indirect nuclear spin-spin coupling interaction, often referred to as *J*-coupling, arises from the interaction between two spins transmitted via their electronic surroundings. The coupling occurs when the spin of a nucleus correlates with the spin of a bonding electron, which in turn influences other neighbouring nuclear spins. The mechanism of the indirect nuclear spin-spin coupling interaction is more complicated and does not depend on distance in an obvious way. First, nuclear spin I_A perturbs the electron in its vicinity, L_A, and this perturbation is carried via the electronic framework to a second nuclear spin, I_B, where a small magnetic field is produced. This two-stage process is illustrated in Figure 2.10.

Figure 2.10. Schematic diagram illustrating the origin of the indirect spin-spin coupling interaction, *J*, between two nuclear spins, I_A and I_B.

The indirect nuclear spin-spin coupling interaction appears as a splitting in an NMR spectrum, and is used extensively in solution NMR for structural and conformational analysis. Like the dipolar interaction, the indirect spin-pair interaction can be either heteronuclear or homonuclear in nature. The indirect nuclear spin-spin coupling interaction $\mathcal{H}_{\mathrm{J}}$ between spins *I* and S can be written as

$$\mathcal{H}_{\mathrm{J}} = \mathbf{I}_{\mathrm{A}} \cdot \mathbf{J} \cdot \mathbf{S}_{\mathrm{B}} \tag{2.33}$$

where **J** is the J-coupling tensor.

The **J** tensor is a general second-rank tensor; however, for this discussion it will be assumed that the **J** tensor is axially symmetric with the unique component coincident with r_{AB}.[17] The isotropic J-coupling, J_{iso} is given by $\frac{1}{3}(J_{11} + J_{22} + J_{33})$. In principle, solid-state NMR is capable of eliciting information on the magnitude of $\Delta J = J_{33} - \frac{J_{11} + J_{22}}{2}$,[17,20] experimentally one measures an effective dipolar coupling containing contributions from R_{DD} and the anisotropy in the **J** tensor:[21]

$$R_{eff} = R_{DD} - \frac{\Delta J}{3} \tag{2.34}$$

2.1.6 . Quadrupolar Interaction

2.1.6.1 . Quadrupolar Nuclei and the Quadrupolar Interaction

Quadrupolar nuclei have a spin $I > 1/2$, and an asymmetric distribution of nucleons giving rise to a non-spherical electric charge distribution; this is in contrast to spin-1/2 nuclei, which have a spherical distribution of electric charge.[22] The asymmetric charge distribution of the nucleus is described by the nuclear quadrupole moment, *Q*, which is measured in m^2. *Q* is an intrinsic property of the nucleus, and is the same regardless of the environment. The quadrupole moment is often expressed as *eQ*, in which case the units are Cm^2, given by

$$eQ = \int \rho_n(r)(3z^2 - r^2)dr \tag{2.35}$$

where $\rho_n(\mathbf{r})$ is the nuclear charge density and the *z*-directon is parallel to the nuclear spin axis. Three different distributions of nuclear charge are depicted in Figure 2.11. For spin-1/2 nuclei, $\rho_n(\mathbf{r})$ is spherically symmetric, or isotropic, hence, $eQ = 0$ (Figure 2.11(b)); however, $\rho_n(\mathbf{r})$ may be distorted from the shape of a sphere to that of a cigar-shape (ρ_n (**r**) elongated along the spin-axis); these nuclei are termed *prolate* and, by convention, have $eQ > 0$ (Figure 2.11(a)). Nuclei with charge distribution in a disc shape (ρ_n (**r**) contracted along the spin-axis) are termed *oblate* and have $eQ < 0$ (Figure 2.11(c)).

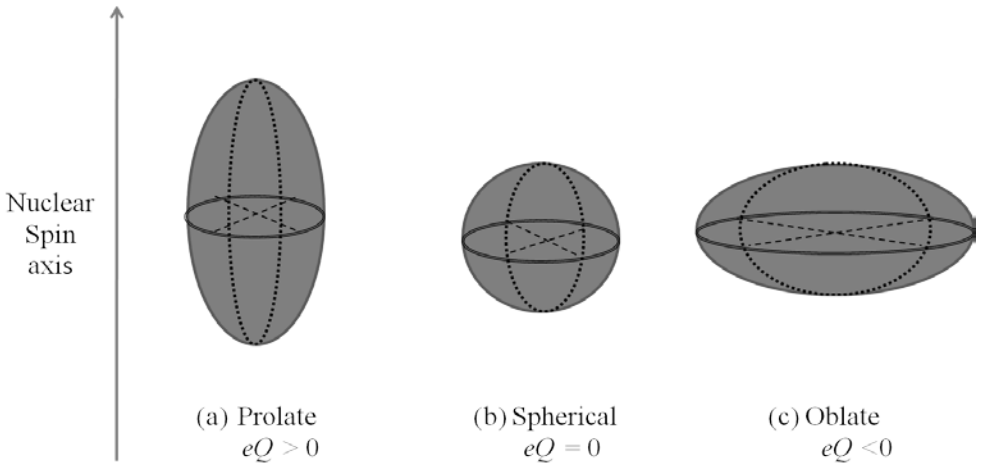

Figure 2.11. Depiction of nuclear charge distribution with respect to the nuclear spin-axis for (a) prolate and (c) oblate quadrupolar nuclei and (b) a spin-1/2 nucleus.

The quadrupolar interaction arises from the interaction of the nuclear quadrupole moment, *eQ* with the non-spherically symmetric electric field gradient (EFG) about the nucleus. The interaction may be written as[23,24,25]

$$\mathcal{H}_Q = \mathbf{S} \cdot \mathbf{Q} \cdot \mathbf{S} \tag{2.36}$$

$$\mathbf{Q} = \frac{eQ}{6S(2S-1)}\mathbf{V} \tag{2.37}$$

In Eqs. (2.36) and (2.37), $\boldsymbol{Q}$ is the quadrupolar coupling tensor which describes the three dimensional nature of the interaction, and **V** is the EFG tensor at the nuclear site. The components of **V** completely describe the orientation and magnitude of the EFG. The **V** tensor at the quadrupolar nucleus is described by a symmetric traceless tensor.

$$\mathbf{V} = \begin{pmatrix} V_{11} & V_{12} & V_{13} \\ V_{21} & V_{22} & V_{23} \\ V_{31} & V_{32} & V_{33} \end{pmatrix} \tag{2.38}$$

In a suitable coordinate system (the principal axis system), **V** is converted to a diagonal form where the principal elements V_{xx}, V_{yy} and V_{zz} describe the size and shape of the EFG.

$$\mathrm{V}^{\mathrm{PAS}} = \begin{pmatrix} V_{\mathrm{xx}} & 0 & 0 \\ 0 & V_{\mathrm{yy}} & 0 \\ 0 & 0 & V_{\mathrm{zz}} \end{pmatrix} \tag{2.39}$$

The principal components of the EFG tensor are defined such that $|V_{xx}| \leq |V_{yy}| \leq |V_{zz}|$. Since the EFG tensor is traceless, isotropic tumbling in solution averages it to zero (unlike **J** and **σ**). The sign and magnitude of the quadrupolar interaction is given by the nuclear quadrupole coupling constant:

$$C_{\mathrm{Q}} = \frac{eQ \cdot V_{\mathrm{zz}}}{\mathrm{h}} \tag{2.40}$$

As one can see from the above equation, the magnitude of the nuclear quadrupolar coupling constant directly depends on the magnitude of both the largest component of the EFG and the quadrupole moment, and in some cases C_{Q} can exceed 1.0 GHz.

The asymmetry of the quadrupolar interaction is defined by the asymmetry parameter,

$$\eta_Q = \frac{V_{XX} - V_{YY}}{V_{ZZ}} \tag{2.41}$$

where $0 \leq \eta_Q \leq 1$ and $V_{ZZ} = eq_{ZZ}$, where, q_{ZZ} is the largest component of the EFG tensor. If the quadrupolar nucleus is in a symmetry site with 3-fold or greater symmetry, V_{zz} is unique, $V_{xx} = V_{yy}$, $\eta_Q = 0$, and the EFG is "axially symmetric".

The quadrupolar frequency ν_Q in units of Hz or ω_Q in units of rad s^{-1}, is given by

$$\nu_Q = \frac{\omega_Q}{2\pi} = \frac{3C_Q}{2S(2S-1)} \tag{2.42}$$

Hence for $S = 3/2$, $\nu_Q = (1/2)\ C_Q$, for $S = 5/2$, $\nu_Q = (3/20)\ C_Q$ and for $S = 7/2$, $\nu_Q = (1/14)\ C_Q$.

2.1.6.2. Quadrupolar Nuclei in a Magnetic Field

The quadrupolar interaction at a nuclear site results in a modification of the Zeeman energy levels, and its magnitude can be larger, the same, or smaller than the Zeeman energy. For results presented in this *Thesis*, the Zeeman interaction is much larger than the quadrupolar interaction and therefore, the latter is treated as a perturbation of the Zeeman Hamiltonian. The magnitude of $\mathcal{H}_Q$, besides being larger than all other anisotropic NMR Hamiltonians for the work presented here, is often stronger than the radio frequency (rf) fields used in NMR. Hence for an analysis of most quadrupolar spectra, the first two terms in the expansion of $\mathcal{H}_Q$ are considered: the first-order, $\mathcal{H}_Q^{(1)}$, and second-order, $\mathcal{H}_Q^{(2)}$ terms, following standard perturbation theory. The quadrupolar Hamiltonian is rearranged into a form with components that commute with the Zeeman spin operators

$$\mathcal{H}_Q = \mathcal{H}_Q^{(1)} + \mathcal{H}_Q^{(2)} \tag{2.43}$$

The effect of the first-order quadrupolar interaction on an NMR spectrum can be written as,[26]

$$\nu^{(1)}_{m_s,m_{s-1}} = \nu_0 + (\frac{\nu_Q}{4})(1-2m_S)(3\cos^2\theta - 1 + \eta_Q \sin^2\theta \cos 2\varphi) \qquad (2.44)$$

where θ and φ are polar angles describing the orientation of the EFG tensor with respect to the applied magnetic field, as shown in Figure 2.12.

From equation (2.44) it is obvious that the *central transition* (+1/2 ↔ -1/2) is not affected by the first-order quadrupolar interaction; $\mathcal{H}_Q^{(1)}$ affects only the *satellite transitions*, often causing large shifts (on the order of MHz) in the energy levels. As a result, the observable satellite transitions are broadened extensively, often making their observation difficult. Since there is a geometrical term of ($3\cos^2\theta$ - 1) present, this interaction can, in principle, be averaged by rapid magic-angle spinning. Figure 2.13 shows the energy level diagram of spin-3/2 system in the presence of the Zeeman, first and second-order quadrupolar interactions.

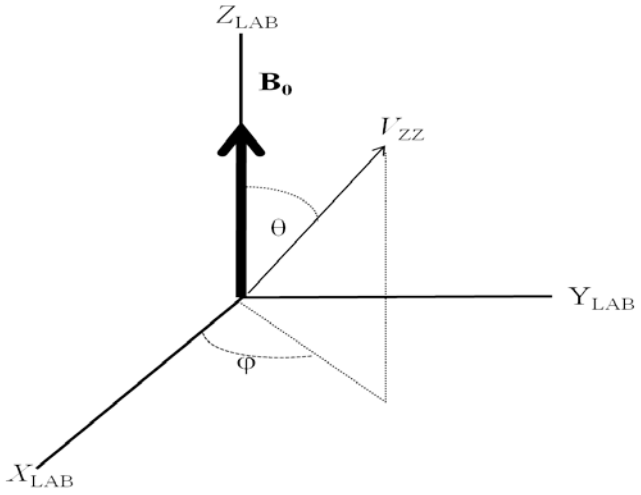

Figure 2.12. Projection of V_{ZZ} in the laboratory frame, indicating polar angles, θ and φ.

As the quadrupolar interaction becomes larger, the central transition is largely affected by the so-called second-order quadrupolar interaction. The effect

of the second-order quadrupolar interaction on the different energy levels is given by[4]

$$\nu^{(2)}_{m,m-1} = -\left(\frac{\nu_Q^2}{12\nu_L}\right) m_I \left[\left(\frac{3}{2}\mu^2(1-\mu^2)(8m^2-4b+1) + \frac{3}{8}(1-\mu^2)^2(-2m^2+2b-1)\right]\right. \quad (2.45)$$

where $b = I\ (I + 1)$ and $\mu = \cos\theta$. The second-order quadrupolar interaction cannot be completely averaged by MAS, so the acquisition of isotropic, solution-like spectra of quadrupolar nuclei in the solid-state is difficult. It can be seen here that the first-order quadrupolar interaction scales as ν_Q whereas the second-order quadrupolar interaction scales as $\frac{\nu_Q^2}{\nu_L}$, when the ν_Q and ν_L are quadrupole and Larmor frequency, respectively. Consequently, in the absence of CSA, the higher the static magnetic field the greater the resolution of NMR spectra.

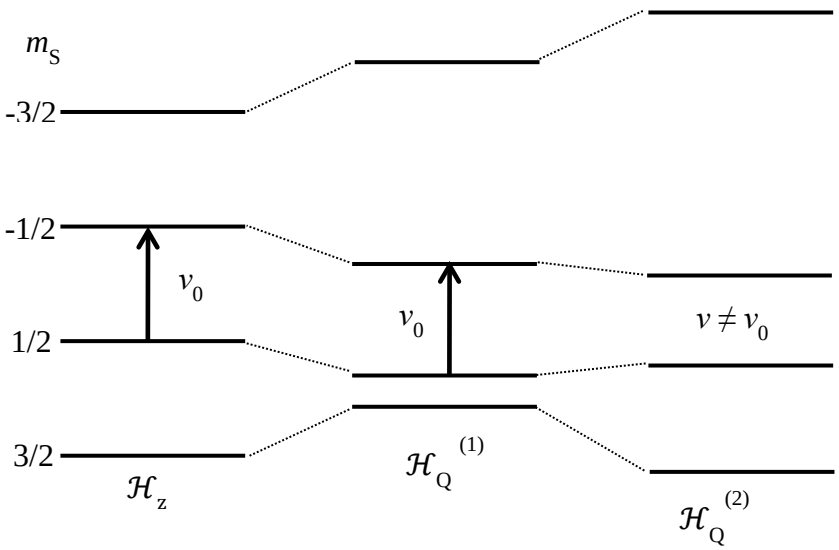

Figure 2.13. Effects of the first- and second-order quadrupolar interactions on a nucleus with $S = 3/2$

As mentioned earlier, NMR powder patterns arise from the random distribution of crystallites with respect to the magnetic field. For each crystallite, the EFG at a particular nucleus is fixed, but the orientation of the EFG varies with the varying crystallite orientations within the magnetic field, thus, the powder patterns results from the superposition of frequency and intensity contributions for all combinations of the angles θ and φ. Figure 2.14 shows the NMR powder pattern

for a spin-3/2 nucleus which depicts the effect of the first-order quadrupolar interaction, where all of the transitions are visible, and of the second-order quadrupolar interaction, where only the central transition is shown. In Figure 2.14(a), the central transition is truncated, and is much more intense than the broadened satellite transitions. The appearance of the spectrum in Figure 2.14(b) arises only from the effect of the second-order quadrupolar interaction on the central transition.

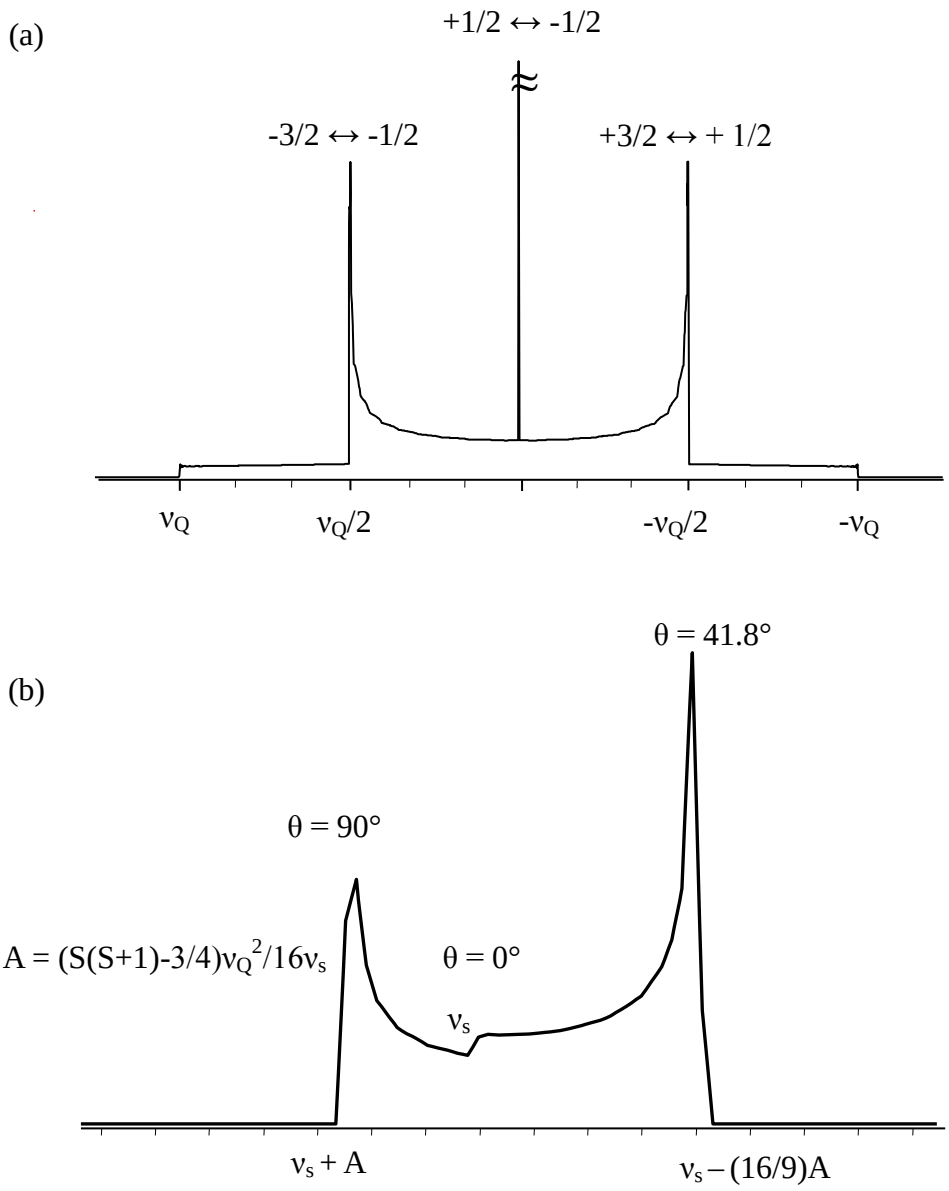

Figure 2.14. Simulated NMR spectra of a quadrupolar nucleus, *S* = 3/2, for a stationary sample, full spectrum (a), and central transition (b). Spectrum (a) results from the

superposition of three powder patterns corresponding to transitions between the Zeeman states of the quadrupolar nucleus. Here, $\eta_Q = 0$ and no CSA assumed for the simulations.

2.2. Euler Angles

This section will explain the fundamentals of rotations as pertaining to NMR. More detailed explanations can be found in literature.[27-29] In the general case, if two or more NMR interactions contribute to a given NMR spectrum, it is desirable to determine their respective magnitudes and orientations. Unless required by symmetry, the relative orientations of these tensors are not necessarily coincident. First, we will define the Euler angles, α, β, and γ, which describe the relationship of one reference frame to another. In other words, the Euler angles define what rotations are needed to transform from the first frame to the second.

The definition of Euler angles is not universal, and several conventions exist. That which will be used here is the convention of Rose,[27] referred to as *passive rotations* by Duer,[22] whereby a right-handed, mathematically positive sense of rotations, occurring in a counter-clockwise fashion, is employed. Figure 2.15, shows the progression of Euler angles, where the original coordinate system is defined by (x_1, y_1, z_1). The first rotation, $R_{z_1}(\alpha)$, about the original z_1 by the angle α gives a new coordinate system (x_2, y_2, z_2). The second rotation $R_{y_2}(\beta)$, about the new y_2 axis, gives a coordinate system (x_3, y_3, z_3) and finally, the third rotation $R_{z_3}(\gamma)$, about z_3 yields the final coordinate system (x_4, y_4, z_4).

The relative orientations of various NMR tensors may strongly affect solid-state NMR lineshapes and are generally determined using computer simulations. The ranges for the Euler angles are $0 \leq \alpha \leq 360$, $0 \leq \beta \leq 180°$ and $\leq \gamma \leq 360°$; however, restrictions are often placed on the Euler angles, depending on the site symmetry of the nucleus in the crystal lattice. Symmetry plays an important role and is very helpful in the determination of Euler angles by reducing the number of possible values for α, β, and γ. When symmetry does not dictate the relative orientation of two tensors, the Euler angles are determined by manual iteration and visual inspection of the calculated (simulated) spectrum compared to

that obtained by experiment. In these circumstances, the accuracy of the solution is increased by performing experiments at two or more applied magnetic fields.

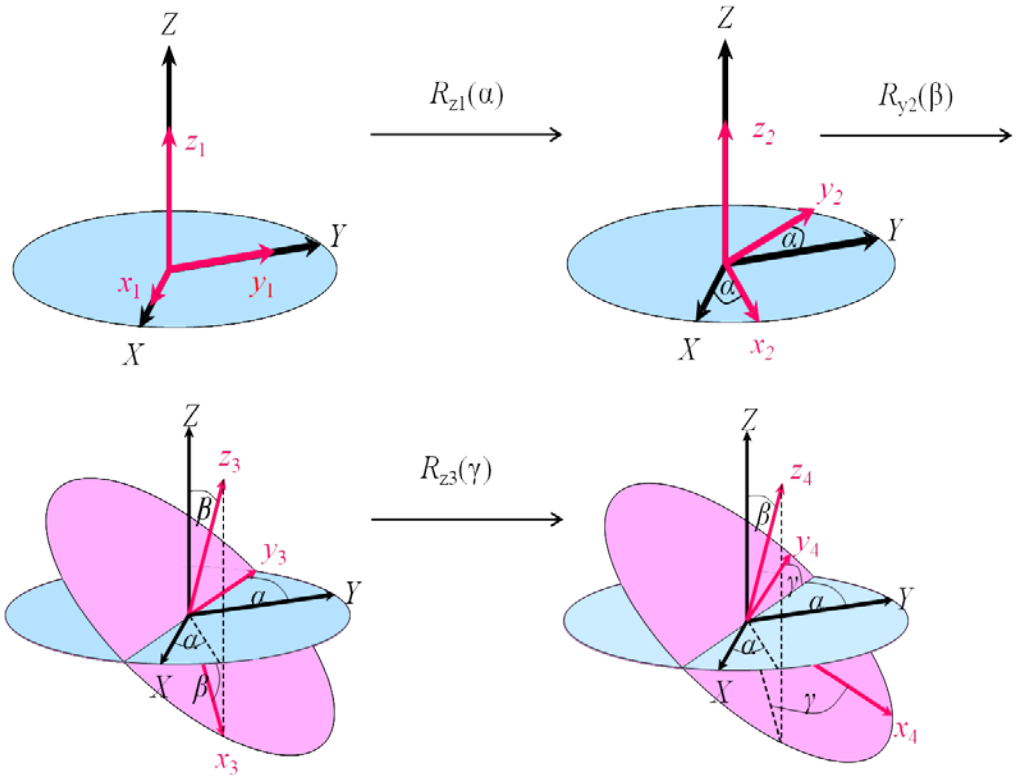

Figure 2.15. Schematic representation of the Euler angles (α, β, γ) which describe the relative orientation of coordinate systems (x_1, y_1, z_1) and (x_4, y_4, z_4).

Mathematically, we can express the rotation of a tensor T of rank l, T_l, by the Euler angles α, β, and γ as

$$T_{lm} = \sum_{m'=-l}^{l} D^{(l)}_{m'm}(\alpha,\beta,\gamma) T_{lm'} \tag{2.46}$$

where $D^{(l)}_{nm}(\alpha,\beta,\gamma)$ is a Wigner rotation matrix element of rank l which is defined as

$$D^{(l)}_{mn}(\alpha,\beta,\gamma) = e^{-im\alpha} d^{(l)}_{mn}(\beta) e^{-in\gamma} \tag{2.47}$$

The term $d_{mn}^{(l)}(\beta)$ is known as a reduced Wigner rotation matrix element of rank l. The methods of calculating reduced matrix elements can be found in the texts on angular momentum. One important property of the Wigner rotation matrices is

$$D_{00}^{(l)}(\alpha,\beta,\gamma) = d_{00}^{(l)}(\beta) = P_l(\cos\theta) \tag{2.48}$$

where $P_l(\cos\theta)$ is the l^{th} order Legendre polynomial of $(\cos\theta)$. Of particular interest are the Legendre polynomials of rank $l = 2$ and $l = 4$ which are given by,

$$P_2(\cos\theta) = \frac{1}{2}(3\cos^2\theta - 1) \tag{2.49}$$

and

$$P_4(\cos\theta) = \frac{1}{8}(35\ \cos^4\theta - 30\ \cos^2\theta + 3) \tag{2.50}$$

These polynomials will prove important in the explanation of magic-angle spinning in the following section.

2.3. References

[1] R. K. Harris. *Nuclear Magnetic Resonance Spectroscopy*: *A Physicochemical View*; Pearson Education Limited: Essex, UK, 1987.

[2] R. K. Harris, E. D. Becker, S. M. C. de Menezes, R. Goodfellow, P. Granger. *Solid State. Nucl. Magn. Reson.* **22**, 458, (2002).

[3] J. P. Amoureux, C. Fernandez, P. Granger. *Multinuclear Magnetic Resonance in Liquids and Solids Chemical Applications*, NATO ASI Series C, P. Granger, R. K. Harris, Eds. Kluwer Academic Publications, Dordrecht, 322, Chapter XXII, 1990.

[4] A. Abragam. *Principles of Nuclear Magnetism*; Oxford University Press: Oxford, 1961.

[5] N. Jeevanjee, *An Introduction to Tensors and Group Theory for Physicists*; Birkhauser Boston: US, 2011.

[6] R. K. Harris, E. D. Becker, S. M. C. de Menezes, P. Granger, R. E. Hoffman, K. W. Zilm. *Pure Appl. Chem*, **80**, 59, (2008).

[7] J. Keeler. *Understaning NMR Spectroscopy*; John Wiley & Sons: Chichester, West Sussex, UK, 2005.

[8] R. R. Ernst. *Principles of Nuclear Magnetic Resonance in One and Two Dimensions*; Clarendon Press: Lincoln, UK, 1987.

[9] J. Mason. *Solid State Nucl. Magn. Reson*. **2**, 285, (1993).

[10] F. A. L. Anet, D. J. O'Leary. *Concepts Magn. Reson*. **3**, 193, (1991).

[11] M. A. Kennedy, P. D. Ellis. *Concepts Magn. Reson.* **1**, 35, (1989).

[12] W. G. Proctor, F. C. Yu. *Phys. Rev*. **77**, 717, (1950).

[13] W. C. Dickinson. *Phys. Rev*. **77**, 736, (1950).

[14] J. T. Arnold, S. S. Dharmatti, M .E. Packard. *J. Chem. Phys*. **19**, 507, (1951).

[15] N. F. Ramsey. *Phys. Rev*. **78**, 699, (1950).

[16] A. D. Buckingham, S. M. Malm. *Mol. Phys*. **22**, 1127, (1971).

[17] R. E. Wasylishen. *Encyclopedia of Nuclear Magnetic Resonance*, Vol. 9; D. M. Grant, R. K. Harris; John Wiley & Sons: Chichester, UK, 274, 2002.

[18] E. R. Andrew, E. Szczesniak. *Prog. Nucl. Magn. Reson. Spectrosc*. **28**, 11, (1995).

[19] G. E. Pake. *J. Chem. Phys*. **16**, 327, (1948).

[20] P. Tutunjian, J. S, Waugh. *J. Magn. Reson*. **49**, 155, (1982).

[21] F. Chen, G. Ma, G. M. Bernard, R. G. Cavell, R. McDonald, M. J. Ferguson, R. E. Wasylishen. *J. Am. Chem. Soc*, **132**, 5479, (2010).

[22] M. J. Duer. *Introduction to Solid-State NMR Spectroscopy*; Blackwell Science Ltd: Oxford, UK, 2004.

[23] M. H. Cohen, F. Reif. *Solid State Phys*. **5**, 321, (1957).

[24] E. A. C. Lucken. *Nuclear Quadrupole Coupling Constants*; Academic Press, Inc: London, UK, 1969.

[25] P. P. Man, *Encyclopedia of Nuclear Magnetic Resonance*, Vol. 6; D.M. Grant, P. K. Harris, Eds.; John Wiley & sons: Chichester, U.K, 1996.

[26] F. Taulelle. *Multinuclear Magnetic Resonance in Liquid and Solids, Chemical Applications. NATO ASI Series*, Vol. 322; P. Granger; R.K. Harris., Eds. Kluwer Academic Publishers: Dordrecht, 1990.

[27] M. E. Rose. *Elementary Theory of Angular Momentum;* John Wiley & Sons: New York, US, 1957.

[28] A. R. Edmonds. *Angular Momentum in Quantum Mechanics;* Princeton University Press: Princeton, US, 1960.

[29] R. N. Zare. *Angular Momentum: Understanding Spatial Aspects in Chemistry and Physics;* John Wiley & Sons: New York, US, 1988.

Chapter 3. Experimental Techniques and Data Processing

3.1. Standard Techniques Used in Solid-State NMR Spectroscopy

3.1.1. Magic Angle Spinning (MAS)

Line broadening in solid-state NMR spectra is primarily due to the dipolar, magnetic shielding anisotropy, and quadrupolar interactions. All of these interactions have, to first order, an orientation dependence containing the factor $(3\cos^2\theta\text{-}1)$ where θ is the angle between a specific molecule-fixed vector (*e.g.*, the internuclear vector for the dipolar interaction) and the applied magnetic field $\mathbf{B}_0$, see Figure 3.1. In solution, rapid molecular tumbling averages $<\cos^2\theta>=\frac{1}{3}$ so the value of $(3\cos^2\theta\text{-}1)$ is zero, generally yielding narrow peaks.[1] In the solid state, even when the molecules are rigid, motion of the nuclei can be introduced if the sample is rotated with an angular velocity ω_r about an axis **R** which is inclined at an angle α to $\mathbf{B}_0$, as shown in Figure 3.1. The specific molecule-fixed vector **r** makes an angle β with respect to the spinning axis **R**. The angle θ between **r** and $\mathbf{B}_0$ will thus vary between (β - α) and (β + α). The value of each interaction depends on the average value of $(3\cos^2\theta - 1)$ about the conical path, which can be expanded as[2]

$$(3\cos^2\theta - 1) = \tfrac{1}{2}(3\cos^2\alpha - 1)(3\cos^2\beta - 1) + \frac{3}{2}\sin 2\alpha \sin 2\beta \cos(\omega_r t) + \frac{3}{2}\sin^2\alpha \sin^2\beta \cos(2\omega_r t) \quad (3.1)$$

At a sufficiently high value of ω_r (*i.e.*, "fast spinning" compared to the interaction in frequency units) the time-dependent parts of equation 3.1 average to zero (*i.e.*, the average values of both $\cos(\omega_r t)$ and $\cos(2\omega_r t)$ become zero). The term $\frac{1}{2}(3\cos^2\beta - 1)$ therefore, acts as a scaling factor for $\frac{1}{2}(3\cos^2\theta - 1)$. If β

= 0° (rotation about $\mathbf{B}_0$), then $\frac{1}{2}(3\cos^2\beta - 1) = 1$, and there is no scaling of the interactions. Therefore, measuring a spectrum while spinning at 0° is equivalent to measuring a spectrum of a stationary sample. At an angle of β = 54.736°, however, $\frac{1}{2}(3\cos^2\beta - 1) = 0$. Thus, the average value of $(3\cos^2\theta - 1)$ is zero for all orientations, and the effects of all first-order interactions in the spectrum are entirely removed (provided the spinning frequency is fast enough), resulting in sharp NMR peaks. The angle 54.736° is therefore called the "magic angle", and spinning about this angle is known as "magic angle spinning" (MAS). The discovery of MAS was made independently in 1958-59 by Andrew *et al.*[3] and Lowe.[4]

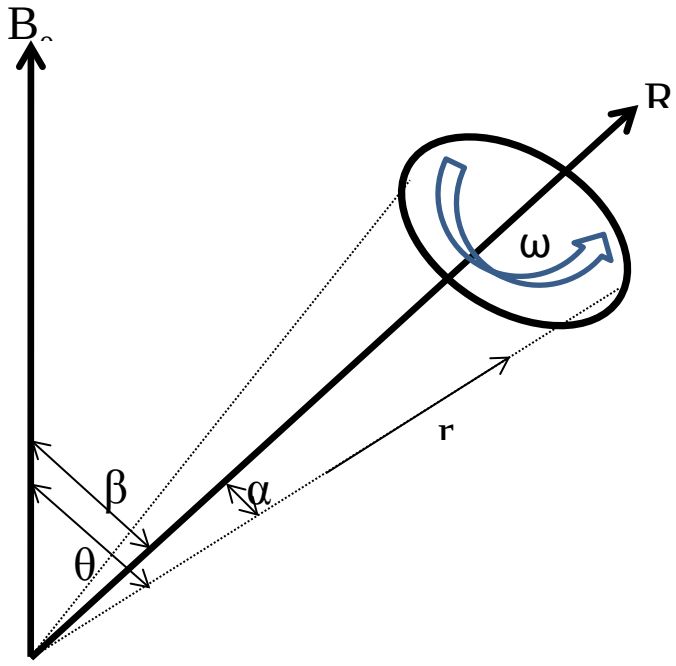

Figure 3.1. Schematic representation of the geometric arrangement for mechanical sample spinning. The solid sample is rotated with an angular velocity ω_r about an axis **R**, which is inclined to the magnetic field $\mathbf{B}_0$ by an angle α. This specific molecule-fixed verctor **r** makes an angle β with the rotation axis and is inclined to the magnetic field by an angle θ which varies periodically as the sample rotates.

MAS thus simulate isotropic molecular tumbling, resulting in high-resolution NMR spectra of solids. There are, however, limitations to the MAS technique. Dipolar interactions can only be completely averaged by spinning faster than the static coupling strength,[5] which can be up to several tens of kHz. This has led to the development of fast[6] and ultra-fast spinning devices which are, at present, capable of reaching frequencies greater than 100 kHz.[7] The problem of homonuclear dipolar coupling is greatly reduced if the nucleus being studied is of low natural abundance (*e.g.*, ^{13}C, 1.1% abundance), since the NMR-active nuclei are diluted in the sample. In cases where the natural abundance is high, there may be physical dilution if few such nuclei are present (often the case for ^{31}P), or the nucleus may be artificially diluted in a different isotope (*e.g.*, ^{1}H diluted in ^{2}H in highly deuterated materials). For a dilute nucleus where homonuclear interactions are negligible, spinning at frequencies lower than the frequency width of the chemical shift anisotropy powder pattern does not completely average the time-dependent parts of equation 3.1. This produces a series of spinning sidebands, ssb, spaced at multiples of the rotation frequency and centred about the isotropic chemical shift.[8] Since the width of the chemical shift anisotropy pattern is proportional to the applied magnetic field strength, there will be a larger sideband pattern at higher field strengths for the same spinning rate.

As an example, consider the effect of anisotropic magnetic shielding on the NMR spectrum of a spin-1/2 nucleus. As well known, [2,5] spinning sidebands result under conditions of magic angle spinning. The ssb are separated at intervals equal to the spinning frequency and flank the isotropic peak. The isotropic peak then is usually easily determined when more than one spinning frequency is employed because the frequency corresponding to δ_{iso} is independent of spinning frequency.[9]

3.1.2. MAS of Quadrupolar Nuclei

For quadrupolar nuclei in a solid sample, often only the central ($m_I = +1/2 \rightarrow m_I = -1/2$) transition is excited and detected in the spectrum. This transition does not depend on the quadrupolar interaction to first-order, but is broadened and shifted from its isotropic chemical shift by the second-order interaction. The second-order quadrupolar interaction, which becomes larger as the quadrupolar interaction becomes larger ($\nu_Q^2 \propto \frac{C_Q^2}{\nu_L}$), is reduced but not completely eliminated by MAS.[10] Therefore, a distinct lineshape persists, even at higher MAS frequencies, and peak shifts caused by the second-order quadrupolar interaction are still present under MAS conditions, although they are smaller at higher magnetic field strengths (*i.e.*, proportional to $1/\mathbf{B}_0$). Therefore, for quadrupolar nuclei, it is often desirable to use the highest magnetic field strength possible.

For the *S* spins in solution under extreme narrowing conditions, however, the energy levels are effectively degenerate and all of the transitions are usually observed. However, for a solid with a significant C_Q, the 90° pulse length for the *S* nuclei is scaled by a factor of $1/(S+1/2)$ as compared to that for the *S* nuclei in isotropic solution.[11,12] For ^{27}Al ($S = 5/2$) nuclei, for example, the 90° pulse length measured on a solid sample is 1/3 of the 90° pulse length for ^{27}Al spins in solution. Therefore, to obtain quantitative spectra, small pulse angles should be used, this will be discussed in more detail in section 3.1.3.

Although the resonances in the MAS spectra of quadrupolar nuclei are broadened due to the second-order quadrupolar interaction, in many cases there is still enough resolution to clearly distinguish signals from distinct environments. In other cases, however, the second-order quadrupolar interaction can broaden the peaks to the extent that MAS can no longer resolve the resonances from different environments.

In the late 1980's Samoson *et al*.[13] and Llor and Virlet[14] developed two different techniques known as double rotation**,** DOR and dynamic angle spinning, DAS,[15] to suppress this second-order quadrupole broadening. Similar to MAS, both DOR and DAS involve mechanical rotation of the sample. However, instead of spinning the sample at one angle as in the MAS experiment, DOR requires sample spinning at two different angles simultaneously in order to average both of the Legendre polynomials in equation 2.43. In the case of DAS, it requires to flip the sample's spinning axis rapidly from one angle to another sequentially. These techniques are not easy to implement and require sophisticated probes.

In 1995, Frydman and Harwood[16] developed a new technique called multiple quantum magic angle spinning, MQMAS, which is much easier to apply than DOR and DAS, and can also achieve high-resolution NMR spectra for quadrupolar nuclei. MQMAS, which is a two dimensional technique, allows extraction of NMR parameters from overlapping peak features and also has the advantage that it avoids the instrumentation demand and bandwidth limitations involved in composite sample rotation methods. It should be noted that ever since this technique was developed in 1995, solid-state NMR studies of quadrupolar nuclei have been accelerated dramatically. However, these techniques become impractical if the second-order quadrupolar broadening is greater than 100 kHz.

3.1.3. Radiofrequency Pulses

In NMR spectrometers, radiofrequency, rf, electromagnetic radiation is utilized to induce transitions between the nuclear-spin energy levels in an applied magnetic field. A typical rf pulse used in an NMR experiment and its corresponding excitation profile in the frequency domain are shown in Figure 3.2.

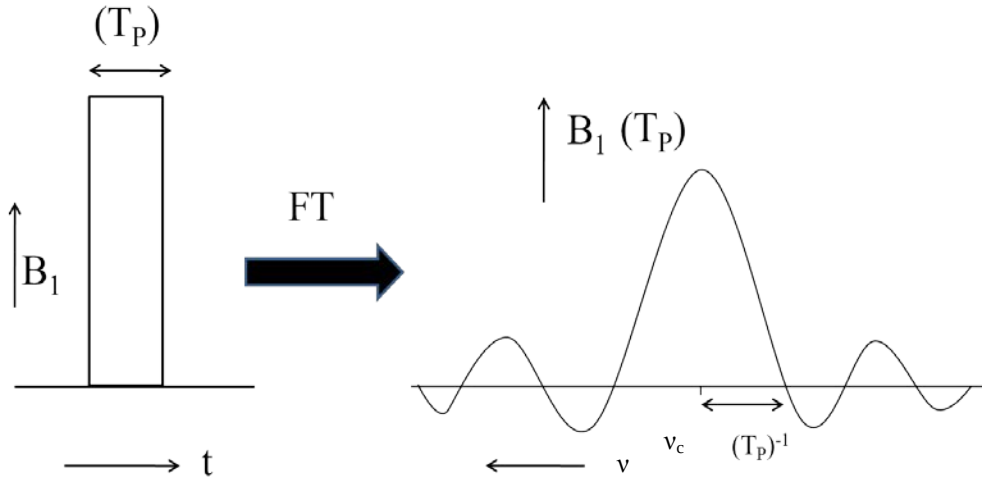

Figure 3.2. Relationship between the rectangular pulses applied for duration T_p in the time domain and its frequency counterpart, the $\mathrm{sinc}[\pi(\nu-\nu_c)T_P]$ function after FT. The nutation behaviour of this function illustrates the non-uniform excitation profile of the square pulse.

The rf pulse is applied for duration T_p (on the order of μs) at a specific location in the frequency domain, which is often referred to as the carrier frequency, ν_c. During the time T_p the oscillating magnetic field component of the rf pulse, B_1, is turned on. The excitation profile in the frequency domain can be calculated from the FT of the pulse in the time domain, and is given by a sinx/x or sincx function of the form

$$\frac{\sin[\pi(\nu-\nu_c)T_P]}{\pi(\nu-\nu_c)T_P} = \mathrm{sinc}[\pi(\nu-\nu_c)T_P] \qquad (3.2)$$

The B_1 amplitude in the frequency domain is not uniform as shown in Figure 3.2; in fact, only approximately 10% of the region centred about ν_c is relatively flat. Hence, to obtain uniform excitation, $(T_P)^{-1}$ should be appreciably greater than the region to be excited. Typical T_p values for selective 90° rf pulses range from 2.0 to 5.0 μs, resulting in effective excitation ranges on the order of 125 kHz to 50 kHz.

As mentioned earlier in Section 3.1.2, either non-selective or selective rf pulses may be used when studying quadrupolar nuclei.[17,18] The non-selective 90° pulse is optimized using a solution sample or a solid sample with cubic symmetry. The signal intensity of the central transition, $S(T_p)$, for a non-selective pulse displays oscillatory behaviour described by

$$S(T_P) = S_0 \sin \omega_1 T_p \tag{3.3}$$

while $S(T_p)$ for a selective pulse is described by[19]

$$S(T_P) = \frac{S_0}{\left(I+\frac{1}{2}\right)} \sin[(I+\frac{1}{2})\omega_1 T_P] \tag{3.4}$$

For quadrupolar nuclei with sizable quadrupole moments, it is common for the second-order quadrupolar lineshape to significantly exceed the pulse excitation profile, making it impossible to uniformly excite the entire NMR spectrum in a single experiment; the result is acquisition of an incomplete spectrum or a distorted lineshape. An alternative way for exciting broad frequency ranges is using the “chirped pulses” which applies the conventional rectangular pulses of fixed frequency and phases. In particular, the wide-band, uniform-rate, and smooth truncation (WURST) pulses of Kupče and Freeman,[20] which are utilized for uniform excitation of broad frequency regions.

3.1.4. High-Power Decoupling

For most dilute spin-1/2 systems, the major source of line broadening in solid state NMR spectra is the heteronuclear dipolar coupling between the dilute spins and abundant spins (*e.g.*, ^{1}H), which causes a modulation of the effective local field about the dilute nucleus. It is possible to eliminate this interaction by applying a strong radiofrequency field to the abundant spins at their Larmor frequency. Therefore, the abundant spins are generally "decoupled" from the dilute spins, greatly improving the resolution of the dilute spin spectrum.[21]

Decoupling is a concept familiar from solution-state NMR, in which ^{1}H decoupling is employed to remove indirect spin-spin couplings. Since the indirect spin-spin couplings are very small (usually < 200 Hz), only low-power decoupling (~5 W) is required. In solid-state NMR, decoupling techniques are usually applied to suppress large direct dipolar interactions between dilute nuclei and abundant nuclei. Since, in the solid state, dipolar coupling interactions are generally sizable (> 10^3 Hz), the power level of the *I* decoupling *rf* field, B_{1I}, is also on the order of 100 kHz; compared to typical solution NMR decoupling powers, solid-state methods require much higher power. The effect of indirect spin-spin coupling interactions between nuclei is also removed by decoupling.

For proton decoupling, two commonly used techniques are a strong, continuous wave, rf field or two-pulse phase-modulated (TPPM)[22] decoupling is usually applied at or near Larmor frequency of the abundant spin, *e.g.*, ^{1}H. TPPM decoupling is easy to implement and provides results comparable or superior to those obtained with CW decoupling.

3.1.5. Cross-Polarization

The techniques of magic angle spinning (MAS) and high-power decoupling (if ^{1}H nuclei are present) usually provide the resolution necessary to obtain chemical information about individual dilute spins in solids. However, for most dilute spin-1/2 nuclei (*e.g.*, ^{13}C), the pulse NMR experiment suffers from the disadvantages of low sensitivity and the requirement of long recycle delays due to the relatively long spin-lattice relaxation times, T_1 of many dilute spins. The technique of cross-polarization (CP), introduced by Pines, Gibby and Waugh,[23,24] in which spin polarization and thus net magnetization is transferred from the abundant spins (usually ^{1}H) to dilute spins via the dipolar interaction, usually eliminates these disadvantages. The CP experiment provides a maximum signal enhancement of γ_I/γ_s where *I* and *S* represent the abundant and dilute spins, respectively. For example, in the case of $^1\text{H} \rightarrow {}^{13}\text{C}$ CP, the maximum enhancement

is $\gamma_H/\gamma_C \approx 4$. CP also allows for much shorter recycle delays, since the repeat time of the experiment is determined by the T_1 value of the source ^{1}H nuclei, which is usually much shorter than those of the dilute nuclei.

The cross-polarization experiment is a double-resonance experiment with polarization transfer from *I* spins to *S* spins, where the *I* and *S* spins are normally both spin-1/2 (*e.g.*,^{1}H and ^{13}C). Figure 3.3 shows the pulse sequence for the CP experiment.

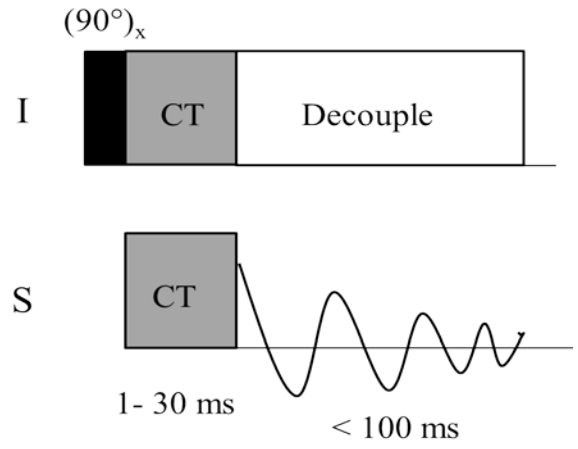

Figure 3.3. Basis pulse sequence for the cross-polarization experiment from *I* spins to *S* spins.

Initially, both *I* and *S* spins are at their equilibrium magnetization distributions. The first step in the CP experiment is to apply a 90° rf pulse (along the *x* axis in the rotating frame) to the *I* spin, which rotates the *I* spin magnetization the *y* axis. The *I* spin magnetization is then spin-locked by applying a spin-locking rf field of strength $\mathbf{B}_1$ along *y*. Note that the phase of the spin-lock pulse is shifted by 90° from that of the initial pulse. This spin-locking field causes the individual magnetization vectors to rotate about the *y* axis, resulting in a net magnetization along *y*. During this $\mathbf{B}_{1,I}$ spin lock pulse, a field $\mathbf{B}_{1,S}$ pulse is applied to the *S* spins. The time period during which both spin-locking fields are

applied is known as the *contact time*. The amplitudes of the two rf fields are adjusted so that the Hartmann-Hahn matching condition is satisfied during the contact time.

The Hartmann-Hahn matching condition[25] requires that, in their respective rotating frames, the *I* and *S* nuclei both precess at equal frequencies around their spin locking fields. Therefore, the energy required for spin flips is identical for both spins, allowing an efficient transfer of magnetization via the dipolar interaction. For cross-polarization involving only spin-1/2 nuclei (*e.g.*, ^{1}H $\rightarrow$ ^{13}C CP), the matching condition for stationary sample is set such that the two rf field strengths, $\gamma_{\mathrm{X}}\mathbf{B}_{1\mathrm{x}}$, are equal:

$$\gamma_{\mathrm{I}}\mathbf{B}_{1,\mathrm{I}} = \gamma_{\mathrm{S}}\,\mathbf{B}_{1,\mathrm{S}} \tag{3.5}$$

with γ_{X} the magnetogyric ratio, and $\mathbf{B}_{1,\mathrm{X}}$ the strength of the *X* nucleus rf field. Since the rf field strength (in frequency units) is equal to the reciprocal of the 360° pulse time, t_{360}^{X}.

$$\gamma_{\mathrm{X}}B_{1,\mathrm{X}} = \frac{2\pi}{t_{360}^{\mathrm{X}}} = \frac{\pi}{2}\,\frac{1}{t_{90}^{\mathrm{X}}} \tag{3.6}$$

The matching condition corresponds experimentally to setting the 90° pulse times, t_{90}^{X}, to be equal on both channels. After the contact time, the *S* spin free induction decay signal is recorded in the presence of the $\mathbf{B}_{1,I}$ field for decoupling of the *I* (^{1}H) spins.

CP experiments involving quadrupolar nuclei are not popular compared to that for spin-1/2 nuclei such as ^{15}N. The main issue which complicates this experiment is the orientation dependence of the quadrupolar interaction.[26] Due to this dependency, only some of the spins in a powder sample can satisfy the Hartmann-Hahn condition for the applied radio frequency field strength, which leads to distorted line shapes.[27,28] In recent decade, with the development of the

two-dimensional multiple quantum MAS experiment,[16,29] CP experiments involving quadrupolar nuclei, have been reported by several groups.[30,31,32,33]

3.1.6. Spin Echo

Erwin Hahn[34] introduced the echo experiment in NMR for the purpose of measuring the spin-spin relaxation time, T_2, in solution. The primary echo experiment involves applications of two 90° pulses, followed by detection of the FID, and later it was named *solid echo* or *quadrupolar sequence*

$$\left[\left(\frac{\pi}{2}\right)_x - \tau - \left(\frac{\pi}{2}\right)_y - \tau - acq\right]$$

which resembles Hahn's original experiment. This experiment was later modified by Carr and Purcell[35] by replacing the second 90° pulse with a 180° pulse. A schematic diagram of the Hahn-echo pulse sequence is illustrated in Figure. 3.4. The first applied $(90°)_x$ pulse (*i*) transfers the equilibrium magnetization initially along the *z*-axis, M_0, onto the *y*-axis, M_y. Since the chemical shift interaction is orientation dependent and because of inhomogeneities in $\mathbf{B}_0$, spins in the sample experience different chemical shifts, and therefore they precess at slightly different Larmor frequencies; hence, during the period τ (*ii*), anisotropic dispersion occurs in the *xy* plane. Applying a $(180°)_y$ pulse (*iii*) reverses the dephasing effect by refocusing the magnetization back along the *y*-axis after time *τ*, (*iv*). The FID is then detected (ν) and, upon Fourier transformation, the NMR spectrum is obtained.

There are numerous variations of the original spin echo, depending on the nature of the spin system under study. A very useful recent paper by Bodart *et al.*[36] provides a theoretical analysis and experimental investigation of quadrupolar echoes for half-integer quadrupolar nuclei in stationary samples.

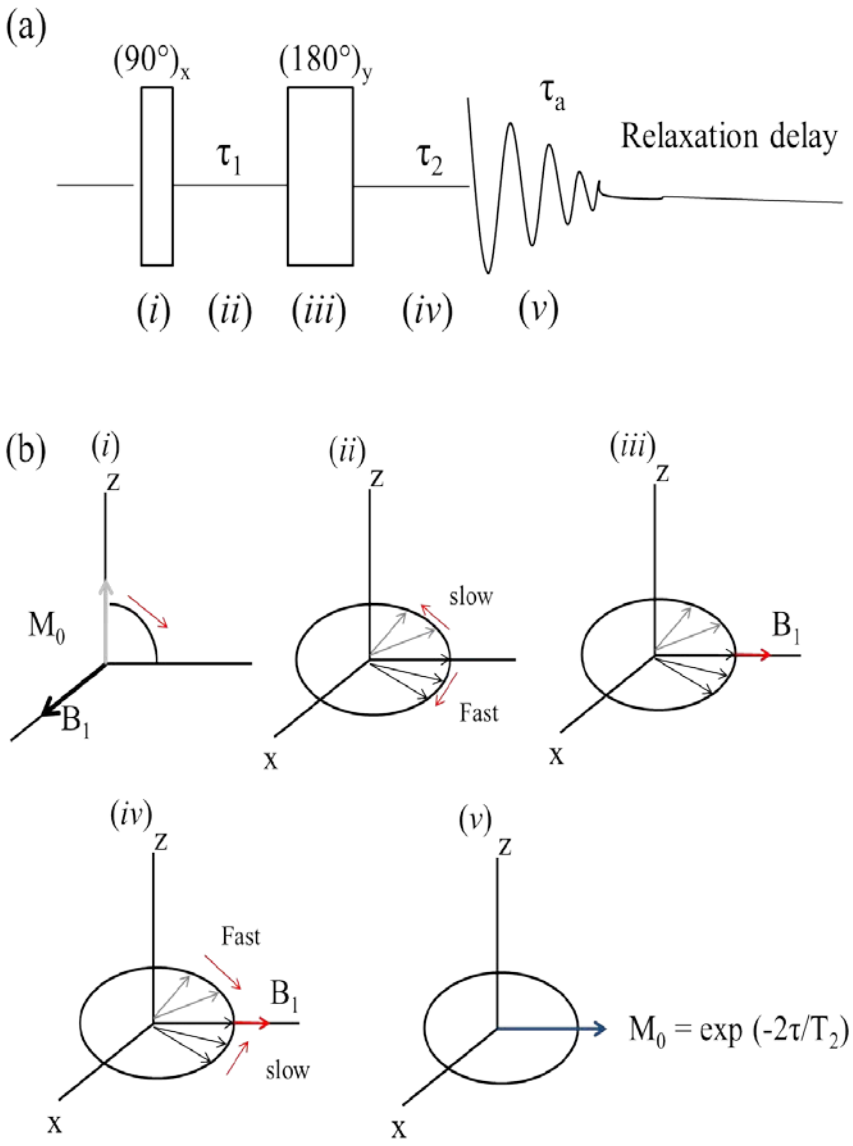

Figure 3.4 (a) Pulse sequence for the spin-echo experiment. (b) Depiction of spin dynamics in various stages of the spin-echo experiment: (*i*) application of the $(90°)_x$ pulse forces magnetization along y-axis; (*ii*) during time period τ, the individual spin vectors dephase in the xy-plane; (*iii*) application of $(180°)_y$ pulse effectively reflects the spin vectors into the x*y*-plane; (*iv*) spin vectors refocus after the second τ period, (*v*) magnetization is aligned along *y*-axis and described by $\boldsymbol{M}_0 \exp(-(2\tau)/T_2)$.

The spin-echo experiment is often preferred over a standard one-pulse experiment when acquiring NMR spectra of stationary samples or systems that give rise to broad NMR spectra. Since broad NMR lineshapes necessarily have short FIDs, interference from instrument dead time and probe ringing (on the order of μs) at the beginning of the FID will introduce artifacts, which result in spectral distortion and a loss of pertinent information. The echo experiments can remove the effects of probe ringing by refocusing the desired NMR signal at a later time. In practice, two delays (τ_1, τ_2) are set independently to give more control over experiment. A proper setting of τ (on the order of μs) is crucial to obtain accurate NMR lineshapes. If τ_2 is too small, unnecessary data will be acquired and the points prior to the top of echo must be deleted, *i.e.*, the data must be left shifted to give the proper NMR spectrum. On the other hand, if τ_2 is too long, important NMR information is lost and an incorrect NMR lineshape is obtained. When employing MAS with the spin-echo experiment, rotor-synchronization must be used which must satisfy the condition $\tau \approx n\ \upsilon_{rot}^{-1}$. In 1958, Meiboom and Gill[37] extended Carr and Purcell's echo experiment by introducing a train of 180° pulses; following the echo pulse, this experiment was named Carr-Purcell, Meiboom-Gill, CPMG. Several years later, Larsen and coworkers[38] discovered that the CPMG experiment could be used as a means of signal enhancement of half-integer spin quadrupolar nuclei and termed the experiment "Q"CPMG, because of its application to quadrupolar nuclei.

The benefits of employing the QCPMG experiment are numerous. The QCPMG technique offers the flexibility to study a range of systems of stationary and MAS samples, and provides NMR spectra that are of comparable or superior quality to those obtained using the conventional spin echo experiment; hence, the quadrupolar and CS tensors, may be characterized in the usual way. Most important is that there is a substantial gain in signal-to-noise, allowing NMR spectra to be acquired in considerably less time; further, this provides an opportunity to study some traditionally challenging nuclei.

3.1.7. Hyperbolic Secant Pulses

In a strong applied magnetic field, the equilibrium thermal populations of the nuclear Zeeman energy states can be altered by applying saturation or inversion pulses to one or more NMR transitions. From an energy level diagram applicable to an ensemble of spin-3/2 nuclei,[39,40] it is clear that a substantial enhancement in the intensity of the central transition, CT can be achieved if the Boltzmann populations are modified.

For example, it has been shown that inverting the populations of the m_I = 3/2 to m_I = 1/2 energy levels prior to selectively exciting the m_I = 1/2 to m_I = -1/2 transition results in a CT enhancement of up to 2.0. If both the $m_I = 3/2 \rightarrow m_I =$ 1/2 and the $m_I = -1/2 \rightarrow m_I = -3/2$ transitions are inverted prior to excitation of the CT, the maximum enhancement due to population transfer is 3.0. It is straightforward to show that an enhancement of 5.0 is possible for an ensemble of spin-5/2 nuclei[41] and, in general, for an ensemble of nuclei of spin *I*, an enhancement of 2*I* is possible. On the other hand, simultaneous saturation of the STs prior to selective excitation of the CT yields an enhancement (I + 1/2)."

For powder samples, the maximum enhancements are reduced because the, STs are more difficult to manipulate since they are typically spread over frequencies of many MHz due to the orientation dependence of the nuclear quadrupolar interaction.

HS pulses, first used in laser spectroscopy in 1969 by McCall and Hahn,[42] were used by Silver *et al.*,[43] to provide highly selective, low-power π-pulses for MRI applications.[43,44] The HS pulse is created using both amplitude, x_1(t), and phase variation, u(t), given by:[43-45]

$$\omega_1(t) = \omega_{1,max}\,\mathrm{sech}\left(\beta\left(\frac{2t}{T_P} - 1\right)\right) \qquad (3.7)$$

$$\varphi(t) = \left(\frac{\lambda}{\beta}\right)\left(\frac{T_P}{2}\right) ln\left[cosh\left(\beta\left(\frac{2t}{T_P} - 1\right)\right)\right] + \Delta\omega_0 t \qquad (3.8)$$

where $\omega_{1,max}$ is the maximum amplitude of the pulse, T_p is the pulse length, β (= 5.3) is a truncation factor which limits the *sech* function at an amplitude of 1%, λ is equal to one-half of the inversion bandwidth, and $\Delta\omega_0$ is the offset of the HS pulse from the carrier frequency. The pulse variation, $\varphi(t)$, generates an effective frequency sweep (*i.e.*, the derivative of the phase), $\Delta\omega(t)$, over the bandwidth centred at a particular offset, $\Delta\omega_0$, given by

$$\Delta\omega(t) = \lambda tanh\left(\beta\left(\frac{2t}{T_P} - 1\right)\right) + \Delta\omega_0 \qquad (3.9)$$

Population inversion can only occur if the frequency sweep is adiabatic, that is, if the sweep rate is sufficiently slow that the magnetization vector, $\boldsymbol{M}$, is continuously aligned with $\boldsymbol{B}_{\text{eff}}$. On the other hand, the sweep must be fast enough that longitudinal spin relaxation during the sweep is negligible. Before discussing the requirements for an adiabatic sweep in systems of quadrupolar nuclei,[46,47] it is instructive to first discuss a spin-1/2 system. Consider an ensemble of spin-1/2 nuclei described by the following time-dependent Hamiltonian

$$\mathcal{H}(t) = \Delta\omega(t) I_Z + \omega_1(t) I_x \qquad (3.10)$$

where $\Delta\omega(t)$ is the offset of the rf from the exact resonance and $\omega_1(t)$ is the amplitude of the rf field. The adiabaticity of the pulse is given by[48]

$$A = \frac{\omega_{eff}(t)}{\frac{d}{dt}\alpha(t)} = \frac{[\omega_1^2(t) + \Delta\omega^2(t)]^{\frac{3}{2}}}{\omega_1(t)\frac{d}{dt}\Delta\omega(t) - \Delta\omega(t)\frac{d}{dt}\omega_1(t)} \qquad (3.11)$$

where α is the angle between $\boldsymbol{B}_{\text{eff}}$ and $\boldsymbol{B}_0$. For the HS pulse the adiabaticity factor is given by

$$A = \frac{1}{2\beta}\boldsymbol{\lambda}\mathrm{T_P}\ \frac{\left[\cosh^2\left(\beta\left(\frac{2t}{\mathrm{T_P}}-1\right)\right)+\left(\frac{\omega_{1,\max}}{\lambda}\right)^2-1\right]^{\frac{3}{2}}}{\left(\frac{\omega_{1,\max}}{\lambda}\right)\cosh^2\left(\beta\left(\frac{2t}{\mathrm{T_P}}-1\right)\right)} \tag{3.12}$$

Small values of *A* correspond to rapid changes in the angle α and lead to a sudden passage, *i.e.*, the Hamiltonian varies too rapidly for the magnetization to respond and the states of the system remain unchanged. Under these conditions, the sweep has no effect on the population transfer of the energy levels. On the other hand, large values of *A* lead to an adiabatic passage, and inversion of the populations of the energy level occurs. For spin-1/2 nuclei, a passage is generally considered adiabatic when $A \geq 1$. For a spinning powder sample containing quadrupolar nuclei, the expression for the adiabaticity factor is more complicated because the quadrupole frequency, as indicated above, is orientation dependent and, due to sample spinning, becomes time dependent. Experimentally, the adiabaticity of the HS pulse can be modified by either changing the rf field or the sweep rate, *i.e.*, the bandwidth or the duration of the HS pulse.

Several methods of enhancing the CT and ST in NMR spectra of half-integer spin quadrupolar nuclei have been discussed in literature,[49] and are beyond the scope of this *Thesis*. Application of these techniques will almost always result in significant enhancements of the CT, which is discussed in more details in *Chapter 4*, of this *Thesis.*

3.2. Spectral Simulation

Once the NMR data have been acquired and processed, the next step is to analyze the spectrum (*i.e.*, extract C_Q, η_Q, information on the shielding tensor, etc). If several nuclear spin interactions contribute to the NMR spectrum, the lineshape may be very complex; thus, it may not be possible to deduce the

magnitude of the relevant parameters upon visual inspection.[50,51] By carrying out spectral simulations, the NMR lineshape may be separated into the various nuclear spin interactions that contribute to the overall spectrum. If the contribution of both quadrupolar interactions and magnetic shielding for a system are significant, eight parameters, δ_{iso}, Ω, κ, C_Q, η_Q, α, β, and γ must be determined to fit the spectra. In this case, acquiring an NMR spectrum of an MAS sample would be beneficial, because in favourable cases, it would average the magnetic shielding interaction, allowing δ_{iso}, C_Q, and η_Q to be determined. Afterwards, when simulating an NMR spectrum of a stationary sample, these parameters are held constant and the remaining five parameters can be determined.

A best fit calculated spectrum is determined by systematic and manual iteration of the NMR interaction variables and a careful visual comparison with the experimental spectrum. NMR experiments are usually carried out at more than one magnetic field strength to rule out any ambiguities in the calculated spectrum, *i.e.*, to ensure that spectral features are not assigned incorrectly and to ensure that the best fit for spectra acquired at multiple fields is the unique solution.

For a coupled spin pair, it is beneficial to acquire NMR spectra for both nuclei; some parameters determined from the NMR spectra for one nucleus can be used to simulate the NMR spectra for the other nucleus, *e.g.*, J and C_Q. Spectra discussed in this *Thesis* were calculated using either the WSOLIDS[52] or SIMPSON[53] programs, however, each has its advantage and limitations, as discussed below.

3.2.1 SIMPSON

SIMPSON (simulation program for solid-state NMR spectroscopy), allows the user to explicitly specify the nuclear spin-system, internal Hamiltonian, and pulse sequence; in addition, experimental parameters (rf irradiation, time delays, transmitter offsets and phase cycling) and processing parameters (line

broadening, phasing and zero-filling) may be specified, thus emulating an NMR spectrometer.

The simulation of an NMR experiment using SIMPSON involves the numerical evaluation of the Liouville-von Neumann time dependent equation of motion.[53] Once the calculation is complete, the results are visualized and further processed using SIMPLOT, a program included in the SIMPSON package, or other external programs, such as WINNMR or WSOLIDS.

Another factor affecting the length and quality of a SIMPSON simulation is the choice of crystal file. To replicate a powder sample, SIMPSON implements a powder averaging file, which specifies the number of crystallites distributed over a sphere. Some calculations require the largest available crystal files for reasonable results and may take hours to complete a single iteration, thus, iterative fitting may be impractical.

3.2.2. WSOLIDS

WSOLIDS[52]is a user-friendly Windows–based program for the calculation of solid-state NMR spectra. Simulation using WSOLIDS are based on an analytical method which implements the efficient space-tiling algorithm of Aldermann and coworkers[54] allowing calculations to be executed in a matter of seconds. When carrying out a simulation using WSOLIDS, the first step involves choosing an appropriate calculation mode from a pre-composed list. Several essential experimental parameters can be specified, namely, the spectral frequency, number of data points, and sweep width, while data processing features are limited to Gaussian and Lorentzian line broadening. A typical aspect of WSOLIDS is its ability to sequentially calculate spectra at more than one magnetic field. Similar to SIMPSON, iterations of the calculated spectra are carried out manually, however, in WSOLIDS, the results are displayed almost instantaneously and do not have to be imported into a separate program for

viewing. An important difference between SIMPSON and WSOLIDS is their choice of convention for defining the chemical shift interaction and the Euler angles.

3.3. Theoretical Approach: Computation of NMR Parameters

Although NMR parameters can be determined from an analysis of the NMR spectra, some information about NMR parameters still cannot be determined from NMR spectroscopy, such as the sign of C_Q, the sign of J, etc. In addition, the magnitude and the orientation of MS, EFG and J tensors are obtainable by calculation. Thus, several theoretical methods have been developed to calculate these NMR parameters.[55,56]

NMR parameters depend on the electronic structure at the nucleus of study, thus in order to obtain accurate and reliable calculations results, a highly accurate description of the nuclear core region is required. This can be obtained by using large basis sets and a high level of theory, but this increases the computational time. In recent years, the use of first-principles calculations to determine molecular or nuclear properties has become increasingly popular with the increasing performance of computers. The significant advances that have been made in development and improvement of accurate computational methods, namely, the *ab initio* approach and those based on density functional theory (DFT).[57]

DFT methods have many benefits, such as their flexibility and reliability. In addition, DFT calculations may be carried out on large molecular systems with heavy atoms, while producing reliable results at a relatively low computational cost.

A significant component of this *Thesis* is dedicated to the computation of NMR parameters. The computational packages used in this *Thesis* to calculate

NMR parameters are: a) ADF[58,59] using the zeroth-order regular approximation,[60] ZORA-DFT, b) Gaussian03,[61] c) CASTEP code using the gauge-including projector augmented-wave (GIPAW)[62] approach and d) BAND[63,64,65] which is the periodic density functional theory extension of the ADF method.

The NMR modules of the Amsterdam Density Functional (ADF) package are made up of three main components which allow the calculation of MS,[55] **J** [56]and EFG[66] tensors. All ADF calculations presented herein utilized the Vosko-Wilk-Nusair (VWN) local density approximation[67] with the Becke-Perdew[68,69] generalized gradient approximation (GGA) for the exchange-correlation functional. ZORA-type basis sets, composed of Slater-type orbitals (STOs), are used in this work since STOs describe the nucleus very well. When calculating NMR parameters, higher basis sets are generally required to obtain accurate results; hence, the double-zeta (DZ), triple-zeta polarized (TZP), triple-zeta doubly-polarized (TZ2P) or quadruple-zeta quadruply-polarized (QZ4P) basis sets have been employed herein. The ZORA[70] allows inclusion of both scalar and spin-orbital relativistic effects.

The DFT calculations of electric field gradient and nuclear magnetic shielding tensors were performed with Gaussian03,[61] employing Becke's[71] three-parameter hybrid functional for exchange along with the Lee-Yang-Parr[72] correlation functional, B3LYP. For all compounds extensive calculations with different types of basis sets such as Ahlrichs basis set (TZV and TZVP),[73,74] Pople's double-ζ and triple-ζ basis sets (6-31G and 6-311G)[75,76] with optional polarization functions of *d*-type or *p*-type and diffuse functions (+) were used.[77] The magnetic shielding tensor was calculated with the gauge-including atomic orbitals (GIAO) method[78] implemented in Gaussian03**.**

The CASTEP code[62] uses planewave pseudopotentials[79] to reconstruct the electron density throughout a material. Crystalline materials are particularly

suited to CASTEP calculations, as they exploit the periodicity in the crystal lattice. Gauge included projector augmented waves, GIPAW[62,80,81,82] calculations with the CASTEP code were employed to yield MS and EFG parameters.

In the BAND code, the Bloch basis set is constructed from Slater-type orbitals (STOs) or numeric atomic orbitals (NAOs). The electronic density matrix near the nuclei is very important for NMR shielding and both STOs and NAOs afford a potentially accurate description of the Kohn-Sham (KS)[83] orbitals in this region. Atomic centred basis functions allow for further use of gauge-included atomic orbitals (GIAOs) to ensure gauge invariant results. The BAND code will be discussed in more detail in *Chapter 7*.

When the reliability of a method has been determined, significant information can be gained from the computed results. For experimental NMR spectroscopy, the main goal is to understand the relationship between NMR observables and the molecular and electronic structure of a molecule. In summary, computation helps to achieve this goal in a number of ways. First, geometry modifications can be carried out such as bond-length or bond-angle variation can be carried out to examine the sensitivity of NMR parameters to a geometrical variable. Second, experimental results can be rationalized and explained and the importance of relativistic effects investigated with the use of computations. In these cases, computations can help solve chemical problems or complement experimental data.

3.4. References

[1] A. J. Vega. *NMR of Quadrupolar Nuclei in Solid Material*; R. E. Wasylishen, S. E. Ashbrook, S. Wimperis, Eds.; John Wiley & Sons: Chichester, 2012.

[2] E. R. Andrew. *Encyclopedia of Nuclear Magnetic Resonance;* D. M. Grant, R. K. Harris, Eds.; John Wiley & Sons: Chichester, 2891, 1996.

[3] E. R. Andrew, A. Bradbury, R. G. Eades. *Nature* (*London*). **182**, 1659, (1958).

[4] I. J. Lowe. *Phys. Rev. Lett.* **2**, 285, (1959).

[5] M. M. Maricq, J. S. Waugh. *J. Chem. Phys*. **70**, 3300, (1979).

[6] S. F. Dec, C. E. Bronnimann, R. A. Wind, G. E. Maciel. *J. Magn. Reson*. **82**, 454, (1989).

[7] A. Samoson, T. Tuherm, J. Past, A. Reinhold, I. Heinmaa, T. Anupold. *Encyclopedia of Nuclear Magnetic Resonance*; Vol.**10,** R. K. Harris, R. E. Wasylishen, Eds.; John Wiley & Sons: Chichester, 2012.

[8] J. Schaefer, E. O. Stejskal. *J. Am. Chem. Soc*. **98**, 1031, (1976).

[9] J. Herzfeld, A. E. Berger. *J. Chem. Phys*. **73**, 6021, (1980).

[10] P. P. Man. *NMR of Quadrupolar Nuclei in Solid Material*; Vol 3, R. E. Wasylishen, S. E. Ashbrook, S. Wimperis, Eds.; John Wiley & Sons: Chichester, 2012.

[11] V. H. Schmidt. *Pulsed Magn. Opt. Reson. Proc. Ampere Int. Summer Sch. II*, 1971.

[12] P. P. Man, J. Klinowski, A. Trokiner, H. Zanni, P. Papon. *Chem. Phys. Lett*. **151**, 143, (1988).

[13] A. Samoson, E. Lippmaa, A. Pines. *Mol. Phys*. **65**, 1013, (1988).

[14] A. Llor, J. Virlet. *Chem. Phys. Lett*. **152**, 248, (1988).

[15] K. T. Mueller, B. Q. Sun, G. C. Chingas, J. W. Zwanziger, T. Terao, A. Pines. *J. Magn. Reson.* **86**, 470, (1990).

[16] L. Frydman, J. S. Harwood. *J. Am. Chem. Soc*. **117,** 5367, (1995).

[17] A. Abragam. *Principles of Nuclear Magnetism*; Oxford University Press: Oxford, 1961.

[18] D. Freude, J. Haase, *NMR-Basic Princ. Prog*. **29**, 1, (1993).

[19] A. Samoson, E. Lippmaa. *Phys. Rev.* **B 28**, 6567, (1983).

[20] E. Kupče, R. Freeman. *J. Magn. Reson*. **A 115**, 273, (1995).

[21] J. Keeler. *Understanding NMR Spectroscopy*; Eds.; John Wiley & Sons: Chichester, UK, 2005.

[22] A. E. Bennett, C. M. Rienstra, M. Auger, K. V. Lakshmi, R. G. Griffin. *J. Chem. Phys*. **103**, 6951, (1995).

[23] A. Pines, M. G. Gibby, J. S. Waugh. *J. Chem. Phys*. **56**, 1776, (1972).

[24] A. Pines, M. G. Gibby, J. S. Waugh, *J. Chem. Phys*. **59**, 569, (1973).

[25] S. R. Hartmann, E. L. Hahn. *Phys. Rev*. **128**, 2042, (1962).

[26] D. L. Bryce, G. M. Bernard, M. Gee, M. D. Lumsden, K. Eichele, R. E. Wasylishen. *Can. J. Anal. Sci. Spectrosc*. **46**, 46, (2001).

[27] P. J. Barrie. *Chem. Phys. Lett*. **208**, 486, (1993).

[28] S. Ding, C. A. McDowell. *J. Magn. Reson.* **A 114**, 80, (1995).

[29] A. Medek, J. S. Harwood, L. Frydman. *J. Am. Chem. Soc*. **117**, 12779, (1995).

[30] S. E. Ashbrook, S. Wimperis. *Mol. Phys*. **98**, 1, (2000).

[31] K. H. Lim, C. P. Grey. *Chem. Phys. Lett*. **312**, 45, (1999).

[32] K. H. Lim, C. P. Grey. *J. Chem. Phys*. **112**, 7490, (2000).

[33] D. Rovnyak, M. Baldus, R. G. Griffin, *J. Magn. Reson*. **142**, 145, (2000).

[34] E. L. Hahn. *Phys. Rev*. **77**, 297, (1950).

[35] H. Y. Carr, E. M. Purcell. *Phys. Rev*. **94**, 630, (1954).

[36] P. R. Bodart, J-P. Amoureux, Y. Dumazy, R. Lefort. *Mol. Phys*. **98**, 1545, (2000).

[37] S. Meiboom, D. Gill. *Rev. Sci. Instrum*. **29**, 688, (1958).

[38] F. H. Larsen, H. J. Jakobsen, P. D. Ellis, N. C. Nielsen. *J. Phys. Chem*. **A 101**, 8597, (1997).

[39] R. Siegel, T. T. Nakashima, R. E. Wasylishen. *Conceps Magn. Reson*. **A 26**, 47, (2005).

[40] R. Siegel, T. T. Nakashima, R. E. Wasylishen. *Chem. Phys. Lett*. **388**, 441, (2004).

[41] R. Siegel, T. T. Nakashima, R. E. Wasylishen. *Chem. Phys. Lett*. **421**, 529, (2006).

[42] S. L. McCall, E. L. Hahn. *Phys. Rev*. **183**, 457, (1969).

[43] M. S. Silver, R. I. Joseph, D. I. Hoult. *J. Magn. Reson*. **59**, 347, (1984).

[44] M. S. Silver, R. I. Joseph, D. I. Hoult. *Magn. Reson. Med*. **1**, 294, (1984).

[45] M. R. Bendall. *J. Magn. Reson*. **A 116**, 46, (1995).

[46] A. P. M. Kentgens, *J. Magn. Reson*. **95**, 619, (1991).

[47] E. Van Veenendaal, B. H. Meier, A. P. M. Kentgens. *Mol. Phys*. **93**, 195, (1998).

[48] J. Baum, R. Tycko, A. Pines. *Phys. Rev*. **A 32**, 3435, (1985).

[49] T. T. Nakashima, R. E. Wasylishen. *NMR of Quadrupolar Nuclei in Solid Material*; R. E. Wasylishen, S. E. Ashbrook, S. Wimperis, Eds.; John Wiley & Sons: Chichester, UK, 2012.

[50] J. F. Baugher, P. C. Taylor, T. Oja, P. J. Bray. *J. Chem. Phys*. **50**, 4914, (1969).

[51] P. Granger. *Magn. Reson. Chem*. **28**, 156, (1990).

[52] K. Eichele, R. E. Wasylishen, *WSOLIDS NMR Simulation Package*; version1. 17.26.

[53] M. Bak, J. T. Rasmussen, N. C. Nielsen. *J. Magn, Reson*. **147**, 296, (2000).

[54] D. W. Alderman, M. S. Solum, D. M. Grant. *J. Chem. Phys*. **84**, 3717, (1986).

[55] G. Schreckenbach, T. Ziegler. *Int. J. Quantum Chem*. **61**, 899, (1997); (b) S. K. Wolff, T. Ziegler. *Chem. Phys*. **109**, 895, (1998).

[56] (a) R. M. Dickson, T. J. Ziegler. *J. Phys. Chem*. **100**, 5286 (1996); (b) J. Autschbach, T. Ziegler. *J. Chem. Phys*. **113**, 936, (2000); (d) J. Khandogin, T. Ziegler. *Spectrochim. Acta, Part A*, **55**, 607, (1999).

[57] P. Hohenberg, W. Kohn. *Phys. Rev*. **B 136**, 864, (1964).

[58] ADF 2006.01, Theoretical Chemistry, Vrije Universiteit, Amsterdam, http://www.Scm.com.

[59] (a) E. J. Baerends, D. E. Ellis, P. Ros. *Chem. Phys*. **2**, 41, (1973); (b) L. Versluis, T. Ziegler. *J. Chem. Phys*. **88**, 322, (1988).

[60] (a) C. Chang, M. Pelissier, P. Durand. *Phys. Scr*. **34**, 394, (1986), (b) E. Van Lenthe, E. J. Baerends, J. G. Snijders. *J. Chem. Phys*. **99**, 4597, (1993).

[61] Gaussian 03, Revision C.02, M. J. Frisch, G. W. Trucks, H. B. Schlegel, G. E. Scuseria, M. A. Robb, J. R. Cheeseman, J. A. Montgomery, Jr., T. Vreven, K. N. Kudin, J. C. Burant, J. M. Millam, S. S. Iyengar, J. Tomasi, V. Barone, B. Mennucci, M. Cossi, G. Scalmani, N. Rega, G. A. Petersson, H. Nakatsuji, M. Hada, M. Ehara, K. Toyota, R. Fukuda, J. Hasegawa, M. Ishida, T. Nakajima, Y. Honda, O. Kitao, H. Nakai, M. Klene, X. Li, J. E. Knox, H. P. Hratchian, J. B. Cross, V. Bakken, C. Adamo, J. Jaramillo, R. Gomperts, R. E. Stratmann, O. Yazyev, A. J. Austin, R. Cammi, C. Pomelli, J. W. Ochterski, P. Y. Ayala, K. Morokuma, G. A. Voth, P. Salvador, J. J. Dannenberg, V. G. Zakrzewski, S. Dapprich, A. D. Daniels, M. C. Strain, O. Farkas, D. K. Malick, A. D. Rabuck, K. Raghavachari, J. B. Foresman, J. V. Ortiz, Q. Cui, A. G. Baboul, S. Clifford, J. Cioslowski, B. B. Stefanov, G. Liu, A. Liashenko, P. Piskorz, I. Komaromi, R. L. Martin, D. J. Fox, T. Keith, M. A. Al-Laham, C. Y. Peng, A. Nanayakkara, M. Challacombe, P. M. W. Gill, B. Johnson, W. Chen, M. W. Wong, C. Gonzalez, and J. A. Pople, Gaussian, Inc., Wallingford CT, 2004.

[62] C. J. Pickard. F. Mauri, *Phys. Rev*. **B 63**, 245101, (2001).

[63] G. te Velde, E. J. Baerends. *Condens. Matt. Phys*. **44**, 7888, (1991).

[64] G. Wiesenekker, G. te Velde, E. J. Baerends, E. *J. Phys. C:Solid State Phys*, **21**, 4263, (1988).

[65] G. Wiesenekker, E. J. Baerends. *J. Phys. Condens. Matter*, **3**, 6721, (1991).

[66] E. van Lenthe, E. J. Baerends. *J. Chem. Phys*. **112**, 8279, (2000).

[67] S. H. Vosko, L. Wilk, M. Nusair. *Can. J. Phys*. **58**, 1200, (1980).

[68] A. D. Becke. *Phys. Rev.* **A 38**, 3098, (1988).

[69] (a) J. P. Perdew. *Phys. Rev*. **B 33**, 8822, (1986); (b) J. P. Perdew. *Phys. Rev* **B 34**, 7406, (1986).

[70] (a) E. van Lenthe, E. J. Baerends, J. G. Snijders. *J. Chem. Ph*ys. **101**, 9783, (1994); (b) E. van Lenthe, A. E. Ehlers, E. J. Baerends. *J. Chem. Phys*. **110**, 8943, (1999); (e) E. van Lenthe, R. van Leeuwen, E. J. Baerends, J. G. Snijders. *Int. J. Quantum Chem*. **57**, 281, (1996).

[71] A. D. Becke. *J. Chem. Phys*. **98,** 5648, (1993).

[72] C. T. Lee, W. T. Yang, R. G. Parr. *Phys. Rev*. **B 37** (2), 785, (1988).

[73] A. Schafer, H. Horn, R. Ahlrichs. *J. Chem. Phys*. **97** (4), 2571, (1992).

[74] A. Schafer, C. Huber, R. Ahlrichs. *J. Chem. Phys*. **100** (8), 5829, (1994).

[75] W. J. Hehre, R. Ditchfield, J. A. Pople. *J. Chem. Phys*. **56** (5), 2257, (1972).

[76] P. C. Harihara, J. A. Pople. *Theor. Chim. Acta*, **28** (3), 213, (1973).

[77] T. Clark, J. Chandrasekhar, G. W. Spitznagel, P. v. R. Schleyer. *J. Comput. Chem*. **4**, 294, (1983).

[78] K. Wolinski, J. F. Hinton, P. Pulay. *J. Am. Chem. Soc*. **112** (23), 8251, (1990).

[79] D. Vanderbilt. *Phys. Rev*. **B 41**,7892, (1990).

[80] J. R. Yates, C. J. Pickard, F. Mauri. *Phys. Rev*. **B 76**, 024401, (2007).

[81] R. K. Harris, P. Hodgkinson, C. J. Pickard, J. R. Yates, V. Zorin. *Magn. Reson. Chem*. **45**, 174, (2007).

[82] C. Bonhomme, C. Gervais, F. Babonneau, C. Coelho, F. Pourpoint, T. Azaïs, S. E. Ashbrook, J. M. Griffin, J. R. Yates, F. Mauri, C. J. Pickard. *Chem. Rev*. **112**, 5733, (2012).

[83] W. Kohn, L. Sham. *J. Phys. Rev*. **A 140**, 1133, (1965).

Chapter 4: A Solid-State ^{51}V NMR Study of Vanadium Complexes

4.1. Introduction and History

In the past few years, solid-state ^{51}V NMR spectroscopy has developed to be an important technique for investigating the structural properties of vanadium-containing systems.[1-13] Vanadium-51 is a half-integer spin quadrupolar nucleus (S = 7/2) with a high natural abundance (99.8%), a relatively large magnetogyric ratio, and a small nuclear quadrupole moment (Q = -5.2 × 10^{-30} m^2).[14,15] Due to these favourable nuclear magnetic properties, relatively small amounts of vanadium can be readily detected by SSNMR. Recent research has shown that solid-state ^{51}V NMR provides useful information on the electronic structure of vanadium compounds.[3,4,6,7,8,10]

Vanadium does not occur naturally as the free metal, but is found in a number of geologic materials, including iron ores, rock phosphates, coals and crude oil. An early use of vanadium was its incorporation into armor plates.[16] Due to its superior alloy properties, small quantities of vanadium (< 0.2%) impart considerable shock and wear resistance to steel and hence are commonly employed in the manufacturing of aircraft, automobiles and trains.

Vanadium in living systems is normally present at very low concentrations in virtually all cells in plants and animals and is an essential element for many living organisms.[17]Although the formal oxidation states of vanadium can range between –3 to +5, in biological systems the naturally occurring states are +3, +4 and +5, but only one of these oxidation states is diamagnetic (+5).Vanadium(IV) and (V) are the most common oxidation states found in nature. Vanadium(IV) has been determined to be essential in the functioning of vanadium nitrogenase, whilst vanadium(V) is fundamental for vanadium haloperoxidases.[18,19] Vanadium(V)-dependent enzymes are found in haloperoxidases in marine algae, as well as in lichens and fungi;[6,20] vanadium(V)-containing compounds also have shown

excellent potential in the treatment of diabetes, particularly as insulin enhancing or insulin mimetic compounds.[21]

The study of vanadium compounds as an insulin mimetic has a 20-year history.[22-26] Among vanadium compounds that were synthesized, oxovanadium and peroxovanadium compounds have been of great interest because of their insulin-mimetic character. These complexes are typically prepared by reacting vanadium(IV) or vanadium(V) complexes with hydrogen peroxide. Ligands derived from oxo-vanadium complexes usually favour the five-coordinate coordination geometry,[27,28] with geometries similar to the transition states of several enzymes involved in phosphorylation reactions.[29]

Vanadium-51 NMR spectroscopy of solid samples has a long tradition and there is a large volume of experimental data available for a wide variety of systems and materials.[1-9,13] In 1949, Knight and Cohen[30] recorded the first solid-state ^{51}V NMR spectra of polycrystalline $Pb(VO_3)_2$ and V_2O_5 samples in order to determine the gyromagnetic ratio for the ^{51}V nucleus. In 1961, Ragle[31] used NMR spectroscopy to investigate the ^{51}V magnetic shielding anisotropy in a polycrystalline V_2O_5 sample. With the development of pulsed FT-NMR instruments it became more practical to determine magnetic shielding parameters of ^{51}V nuclei.[2,18,19,32,33] One of the first ^{51}V NMR spectra of MAS vanadium compounds were recorded by Oldfield and coworkers.[34,35] In this study, the authors successfully minimized the effects of dipolar interactions, magnetic shielding anisotropy and first-order quadrupolar interactions by using magic angle spinning. A major problem at that time with the low spinning frequencies, below 4 kHz, was overlapping spinning sidebands from the satellite transitions with central transitions sidebands, which complicated the interpretation of the spectra. However, the final choice of the MAS spinning rate depends on the system under investigation. Skibsted and coworkers.[3,7] showed that enhanced information about the local environments of ^{51}V nuclei can be obtained from ^{51}V NMR spectra of MAS samples by determination of the combined effect of the ^{51}V quadruple coupling and anisotropic magnetic shielding interactions from the complete

manifold of spinning sidebands (ssbs) observed for the central and satellite transitions. In addition to the magnitudes of the two interactions, the quadrupolar coupling (C_Q and η_Q) and CSA parameters, the ssb intensities of the NMR spectra of MAS samples also reflect the relative orientations of the EFG and shielding tensors.

A major early review on solid-state ^{51}V NMR was done by Lapina and coworkers on a wide range of vanadia-based catalysts.[36] In more recent years Ooms *et al*.[8] investigated geometric and electronic environments in vanadium haloperoxidases and in oxovanadium(V) complexes by using ^{51}V MAS NMR spectroscopy. In their more recent work,[6,8] the chemical shift and quadrupolar coupling parameters of a series of eight hydroxylamido vanadium(V) dipicolinate complexes of the general formula VO(dipic)(ONR_1R_2)(H_2O), where R_1 and R_2 can be H, CH_3, or CH_2CH_3, have been characterized using ^{51}V magic angle spinning SSNMR spectroscopy and quantum chemical DFT calculations. These studies have shown that both the quadrupolar coupling and the chemical shift anisotropy, which can be determined from an analysis of the ^{51}V SSNMR spectra, are sensitive to the local vanadium environment and can be used to understand changes in the local molecular structure and ground state charge distribution at the vanadium sites.[3–12] Generally solid-state ^{51}V NMR investigations aim to extract information about the vanadium environments from the isotropic ^{51}V chemical shifts (δ_{iso}) and the principal components of the EFG and CSA tensors. These parameters have been determined from either stationary-powder or MAS ^{51}V NMR spectra of the central (m = 1/2 ↔ -1/2) transition, utilizing the fact that spectra for this transition are usually dominated by the CSA interaction at high magnetic fields.[5-8,10,11]

For a long time, computational chemistry of transition metal complexes was less well developed than that of common organic molecules, because the former requires highly sophisticated, expensive, quantum chemical methods. This situation has changed with the development of DFT in its modern implementation, which turned out to be extremely useful for the study of

geometries, energies, and properties of transition metal complexes.[37−40] Recall here that in general the key quantity that can affect spectroscopic observation of quadrupolar nuclei is the electric field gradient (EFG) at the nucleus. This effect is described by two independent parameters, the nuclear quadrupole coupling constant (C_Q) and the asymmetry parameter (η_Q). C_Q is proportional to the product of the nuclear quadrupole moment, Q, and the largest component of the EFG, V_{ZZ}. DFT calculations provide values for C_Q and η_Q that can be compared to experimental data. Several examples of DFT NMR calculations for vanadium are available in the literature,[6,8,41,42,43] indicating good agreement between experimental and calculated parameters. To obtain accurate calculated DFT NMR results, it is important to select the appropriate type of calculation method to be performed. There are several variables that influence the quality of calculated parameters such as the structural model, the size of the model, the type of functional and basis sets used, and the size of the basis sets.

As has been mentioned earlier, an important application of oxo- and peroxo-vanadium complexes is in the treatment of diabetes, as a tool to aid patients to better control of glycemic levels. To understand the biological activity of this class of compounds, studies of their geometry must be investigated further. An aim of this study is therefore the determination of the magnitudes and relative orientations of ^{51}V EFG and shielding tensors. For this purpose, ^{51}V solid-state NMR spectroscopy has been performed on series of oxo- and peroxo-vanadium complexes at several different fields. The spectroscopic NMR observables then have been extracted by simulations. The highly frequency-selective, HS pulses have also been applied to separate the CT peaks from STs on the vanadium site for $[V(O)(ONMe_2)_2]_2O$ compound.

4.2. Experimental and Computational Details

4.2.1. Sample Preparation

I) Cyclopentadienyl Vanadium Tetracarbonyl, $(C_5H_5)V(CO)_4$ was purchased from Strem Chemicals and used with no further purification.

II) $[V(O)(ONMe_2)_2]_2O$ was prepared by a previously described method;[44] 0.10 g of solid V_2O_5 was added to a solution of 2 mL of tetraethylammonium hydroxide and heated to 60 °C with continuous stirring; at this stage the pH of the solution was 10. A solution of 0.213 g of *N, N*-dimethylhydroxylamine hydroxide dissolved in 2 mL of water with a pH of 6 was added to the primary solution with continuous stirring, yielding a yellow solution with a pH of 8. After crystallization was completed, the final yellow solid was filtered and dried in a vacuum. The vanadium chemical shift of $[V(O)(ONMe_2)_2]_2O$ dissolved in chloroform, -728 ppm, is in agreement with that reported by Paul *et al*.

III) Ammonium oxodiperoxoamminevanadate $[NH_4][VO(O_2)_2(NH_3)]$ was synthesized following literature methods.[45] Divanadium pentoxide, V_2O_5 (1.82 g), was dissolved in 30% H_2O_2. To the deep red solution obtained, ammonium nitrate (1.60 g) was added, followed immediately by concentrated ammonium hydroxide, which was added dropwise until a bright yellow solution was obtained; this solution was allowed to stand for 12 h, after which bright yellow crystals were obtained (calculated for $VO_5N_2H_7$: N, 16.9%, H, 4.3% . Found: N, 16.6%, H, 4.2%).

IV) Tripotassium Oxalato-oxodiperoxovanadate Monohydate

$K_3[VO(O_2)_2(C_2O_4)]\cdot 1H_2O$ was prepared by the following synthesis.[46] 0.91g of divanadium pentoxide and 1.95 g of potassium hydroxide were dissolved in 20 mL of water, followed by the addition of a solution of 1.26 g of oxalic acid dissolved in 10 mL of water, and finally 20 mL of hydrogen peroxide (30%) was added to the solution. Ethanol was then added gradually until a precipitate started

to appear. The precipitate redissolved, and the reaction mixture was set aside to crystallize at room temperature. The final product, which was orange crystals, was then filtered and dried on filter paper. (Calculated for $K_3VO_{10}C_2H_2$: C, 6.4%, H, 0.59%. Found: C, 6.5%, H, 0.57%).

V) Tripotassium bis(Oxalato)dioxovanadate Trihydrate

$K_3[V(O)_2(C_2O_4)_2]\cdot 3H_2O$ was prepared by the procedure described by Drew *et al.*,[47] 1.26 g of oxalic acid, 1.84 g of potassium oxalate, 0.56 g of potassium hydroxide, and 0.90 g of divanadium pentoxide were dissolved in 40 mL of hydrogen peroxide, H_2O_2, (15%). The final product, which was a deep red solution, was allowed to stand in air until chunky orange crystals formed. (Calculated for $K_3VO_{13}C_4H_6$: C, 11.1%, H, 1.39%. Found: C, 11.2%, H, 1.36%).

4.2.2. NMR Experimental Details

All vanadium samples were packed in 4 mm ZrO_2 rotors under air except for cyclopentadienyl vanadium tetracarbonyl, $(C_5H_5)V(CO)_4$, which is air sensitive and was packed in a glove box under nitrogen. Solid-state NMR experiments were performed on MAS and stationary samples using a 4.0 mm MAS probe and applying a variety of different spinning rates. All spectra were acquired by applying either a standard single-pulse or a Hahn-echo pulse sequence using a CMX spectrometer operating at 52.62 MHz for ^{51}V as well as Bruker Avance 300 and 500 spectrometers operating at 78.89 and 131.47 MHz, respectively, and a Bruker Avance 900 spectrometer operating at 236.74 MHz for ^{51}V. Proton TPPM decoupling[48] was used for all spectra. The recycle delay and acquisition time were 1 s and 32 ms, respectively. Proton 90° pulse widths of 2.5 or 4.0 μs were used to acquire most of the ^{51}V NMR spectra. Each vanadium spectrum is the sum of 4000 to 77000 scans. All spectra were acquired with a spinning frequency of 7.0 to 15.0 kHz at ambient temperature. A KBr powder sample was used to adjust the magic angle.

The primary ^{51}V NMR chemical shift reference is neat liquid $VOCl_3$ (Ξ = 26.302948 %) at 0.00 ppm and a secondary reference is 0.16 M $NaVO_3$ (aq) at -574.38 ppm;[49] the latter has been used for this study.

4.2.3. Practical Considerations for ^{51}V Solid-State NMR Spectroscopy of Vanadium Coordination Complexes

In the NMR spectra of many solids, both quadrupolar and chemical shift effects are present. When present together these two contributions can considerably complicate NMR spectra and their analyses. When a single crystal of suitable size and quality is available, it is usually a straightforward process to separate the two effects.[50-53] However, if only a powdered sample is available it can be a rather difficult process to extract the relevant quadrupolar and chemical shift parameters from the resulting NMR spectra. Quadrupole coupling interactions usually cause the powder spectra to extend over a large frequency range. For small or intermediate quadrupole coupling constants, the spectrum resulting from all single-quantum transitions will normally be observable with the first-order quadrupolar interaction dominating the satellite transitions. It is common for ^{51}V to exhibit quadrupolar coupling constants ranging from 2 to 8 MHz, but rarely exceeding 10 MHz.[2,36] At the same time the magnetic shielding anisotropy is normally below 1000 ppm, and is often found within the 100-500 ppm range,[2,36] depending on the coordination environment. In order to gets an idea of the magnitude of anisotropic shielding interaction, consider a system with Ω = 1000 ppm at 21.14 T ($\nu(^{51}V)$ = 236.748 MHz). In frequency unit this anisotropic interaction is 236.75 kHz.

The general trend for ^{51}V chemical shifts is shown in Figure 4.1, which is the result of the compilation of about 6 reports approximately since 1992.[5-8,12,36] In addition, this figure summarizes values for quadrupolar coupling constants that have been measured for vanadium in different chemical environment for inorganic molecules.

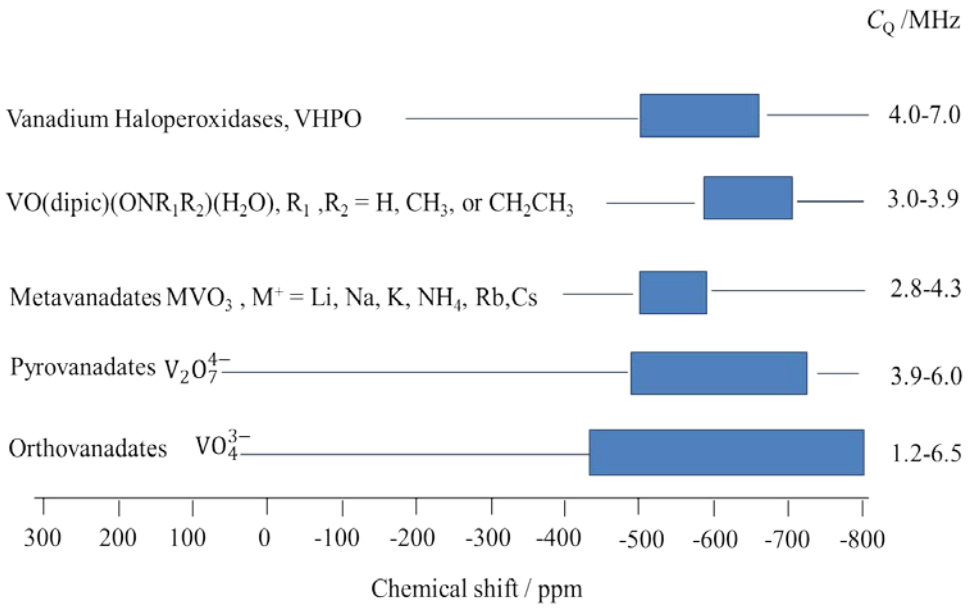

Figure 4.1. ^{51}V isotropic chemical shift and quadrupole coupling constant range for inorganic molecules in the solid-state.

The spectra which are dominated by the first-order quadrupole interaction are described by the quadrupolar coupling constant C_Q and the asymmetry parameter, η_Q.[54] In the presence of quadrupolar coupling, several factors affect the lineshape, the intensity, and the observed frequency of the NMR signals, resulting in an asymmetric lineshape for individual spinning sidebands. The magnitude of C_Q is reflected in the spectral width, whereas the shape of the spectral envelope is determined by η_Q, as shown in Figure 4.2.

As mentioned earlier, the combined effects of the quadrupolar coupling and CSA interactions gives rise to asymmetrical features in the spinning sideband envelope. The quadrupolar and shielding tensors and their relative orientations can be determined by numerical simulations of the complete spinning sideband manifold encompassing the central and satellite transitions.[12,13]

In analyzing the NMR spectra of solid stationary samples, the effect of CSA on the line shape must be considered, if the CSA is significant. There are many examples in the literature where the CSA and EFG tensor parameters have

been extracted through analysis of powder NMR spectra of stationary samples.[55] Simulation of the central transition is quite facile if the EFG and CSA tensors are coincident; however, this is most often not the case, and knowledge of the relative orientations of the EFG and CSA tensors is necessary when simulating the NMR spectra. The convention used in this *Thesis* is to describe the CSA interaction with respect to PAS of the EFG.

Considering that the second-order quadrupole coupling interaction, in frequency units, is inversely proportional to $\mathbf{B}_0$, a simplification of the spectra may be achieved by increasing the field strength. At the same time, since the CSA interaction is proportional to the magnetic field strength the use of a very high magnetic field strength increases the effect of the CSA interaction. Analysis of powder spectra in terms of the combined effect of quadrupole coupling and CSA was introduced by Baugher and co-workers,[56,57] on the assumption of coincident principal axis systems for the two interactions. Non-coincidence of the EFG and magnetic shielding tensors was first treated by Power *et al*.,[58] and by Chu and Gerstein.[59]

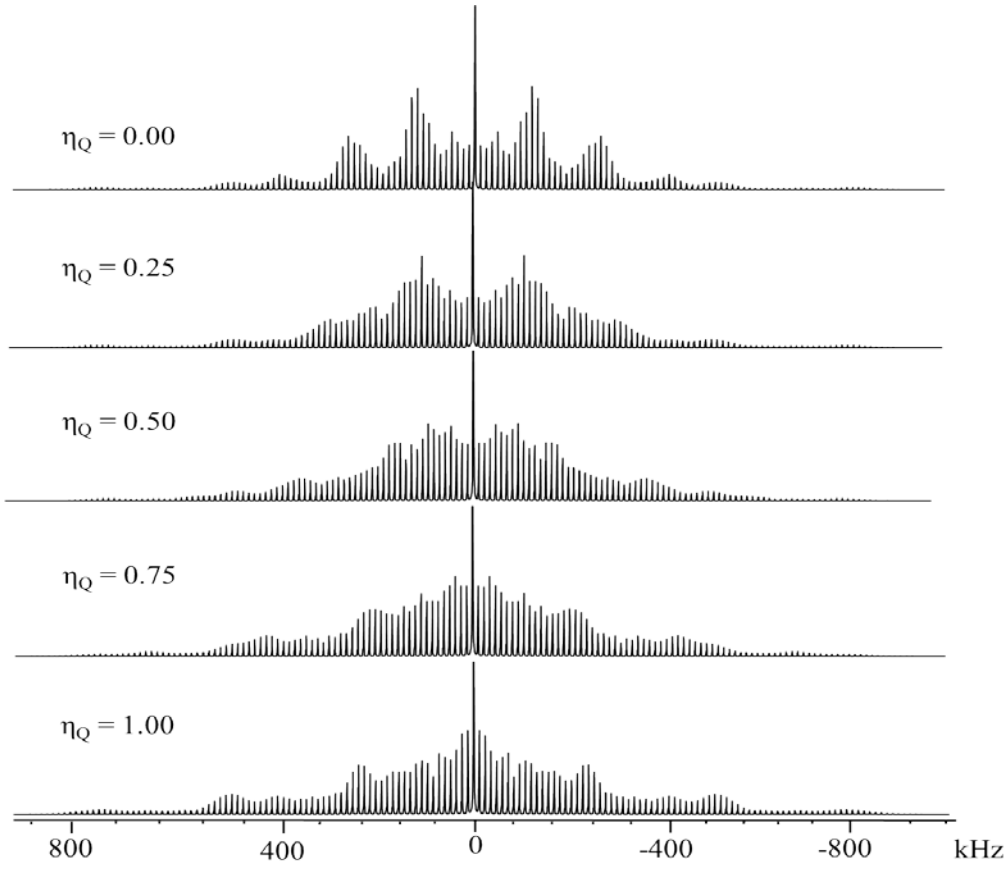

Figure 4.2. Simulated MAS NMR spectra for the satellite transitions of a spin S = 7/2 nucleus, assuming C_Q = 4.0 MHz and that no CSA is present. The intensity of the central transition has been reduced to 20% to illustrate the satellite transitions (up to 1.6 MHz is shown).

4.2.4. Simulation of the NMR Spectra

Simulations of the experimental ^{51}V solid-state NMR spectra were performed using the WSOLIDS[60] and SIMPSON[61] software packages. The combined effects of the quadrupolar interaction and chemical shift anisotropy were taken into account in the simulations. The quadrupolar and CSA tensor elements were defined according to the standard notation. All NMR parameters, C_Q, η_Q, δ_{iso}, Ω, κ and the Euler angles, α, β, γ, defining the relative orientations of the ^{51}V EFG and CS tensors, were determined by simulation of the NMR spectra. The results of quantum chemical calculations were used as starting parameters in determining experimental Euler angles.

To test the accuracy of our conversions of determined parameters to the SIMPSON conventions, first we examined this procedure with a widely studied compound, ammonium metavanadate,[62] NH_4VO_3. Figure 4.3(a) shows the 7.05 T experimental ^{51}V MAS spectrum of NH_4VO_3 and Figure 4.3(b) shows the good agreement of the simulated ^{51}V MAS spectrum of NH_4VO_3 calculated using the SIMPSON simulation program with the experimental one.

The following conventions are used:

$$\delta_{iso} = 1/3\ (\delta_{11} + \delta_{22} + \delta_{33})\ ,\ \delta_{\sigma} = \delta_{iso} - \delta_{33}\ ,\ \eta_{\sigma} = (\delta_{22} - \delta_{11})/\delta_{33}$$

$$|\delta_{zz} - \delta_{iso}| \geq |\delta_{xx} - \delta_{iso}| \geq |\delta_{yy} - \delta_{iso}|$$

where η_{σ} is the asymmetry parameter of the CSA tensor.

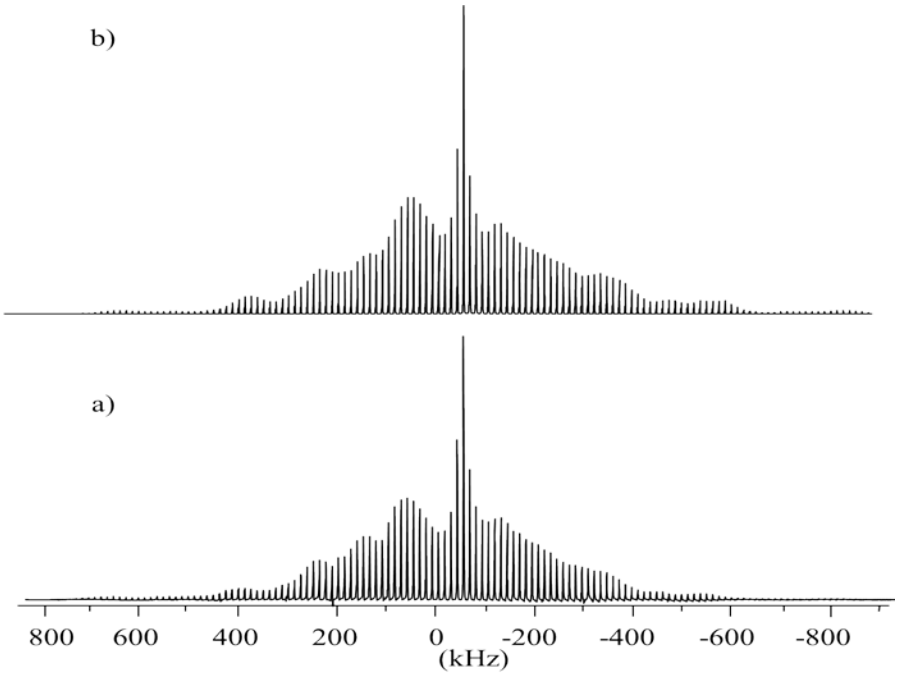

Figure 4.3. ^{51}V MAS NMR spectra of the central and satellite transitions for NH_4VO_3, a) Experimental spectrum acquired at 7.05 T; the spectrum was acquired at a spinning frequency of 7 kHz, b) Simulated spectrum.

4.2.5. Quantum Chemical Calculations

Computation of vanadium EFG and CS tensors via the zeroth-order regular approximation DFT (ZORA DFT) method were undertaken with the Amsterdam Density Functional (ADF) package.[63] Calculations presented here utilized the Vosko-Wilk–Nusair (VWN)[64] local density approximation with the Becke,[65] Perdew[66] generalized gradient approximation (GGA) for the exchange correlation functional. The basis sets available with the ADF program are Slater-type functions. The QZ4P basis set is of quadruple-ζ quality with four sets of polarization functions while TZ2P basis set is of triple-ζ quality with two set of polarization functions. Electric field gradient and nuclear magnetic shielding calculations were performed using the QZ4P and TZ2P basis sets, optimized for ZORA calculations. The calculations provide both the principal components of the two tensors and their orientations in the molecular framework. Generally, solid-state NMR experiments on powder samples provide only the relative orientation of the MS and EFG tensors.

DFT calculations of electric field gradient and nuclear magnetic shielding tensors were also performed with Gaussian03,[67] employing Becke's[68] three-parameter hybrid functional for exchange along with the Lee-Yang-Parr[69] correlation functional, B3LYP. For all compounds extensive calculations with different types of basis sets such as Ahlrichs basis set (TZV and TZVP),[70,71] Pople's double-ζ and triple-ζ basis sets[72,73] with optional polarization function of *d*-type or *p*-type and diffuse function (+)[74] were done. The magnetic shielding tensor was calculated with the gauge-including atomic orbitals (GIAO) method[75] implemented in Gaussian03**.**

DFT calculations for vanadium compounds were also kindly performed by Dr. Victor Terskikh using the CASTEP NMR program.[76,77] The Perdew, Burke, and Ernzerhof (PBE) functionals were used in the generalized gradient approximation (GGA) for the exchange-correlation energy.[78,79] Finally, the magnetic shielding tensors for ^{51}V were calculated with an ultrafine accuracy

basis set using the gauge-included projector-augmented wave method (GIPAW) implemented in the CASTEP code.[80,81]

The calculated isotropic chemical shifts are reported with respect to $VOCl_3$ optimized at the same level of theory. The calculated principal components of the magnetic shielding tensor, σ_{ii} (i = 1, 2, or 3) are converted to the principal components of the chemical shift tensor, δ_{ii}, using the relation $\delta_{ii} = \sigma_{iso}(ref) - \sigma_{ii}$, where $\sigma_{iso}(ref)$ is the calculated isotropic magnetic shielding of $VOCl_3$.

4.2.6. Computational Results for the Vanadium NMR Parameters of $VOCl_3$

In this and in almost any other ^{51}V NMR study, isotropic chemical shifts are reported with respect to neat $VOCl_3$, whose ^{51}V NMR spectrum was recorded and used as an external reference standard. To compare calculated and experimental vanadium CS tensors, absolute isotropic vanadium shielding values for $VOCl_3$ are computed using different methods. For the calculations of the NMR parameters we worked with two different reported structures for $VOCl_3$: that by Galy *et al*. (shown in appendix 4.1) from 1983,[82] and that by Troyanov from 2005.[83] The latter has a slightly larger volume of the unit cell. The single-point energy computations also find the Troyanov structure to be slightly lower in energy than that by Galy *et al*. In this study, the calculated isotropic vanadium shielding values of the Troyanov structure were used to determine $\sigma_{iso}(ref)$ used to convert calculated magnetic shielding to calculate chemical shift for the compounds of interest. These NMR calculations were performed using ADF, Gaussian03, and the CASTEP code for different basis sets as summarized in Table 4.1, which are in good agreement with the literature.[84,85,86] Calculated values of C_Q = 5.6 to 5.9 MHz for high basis sets (6-311++G(d,p), 6-31+G(df,2pd), QZ4P, and CASTEP) also are in good agreement with the experimental value of C_Q = 5.7 MHz reported by Basler *et al*.[87]

Table 4.1. Calculated NMR Parameters for $VOCl_3$ with Different Basis Sets.[1]

Program/Method	Basis sets	σ_{iso} (ppm)	Ω(ppm)	C_Q(MHz)
Gaussian/B3LYP	6-31G	-2018	491	7.3
Gaussian/B3LYP	6-31G(d)	-1944	491	7.3
Gaussian/B3LYP	6-31G(d, p)	-1944	527	6.2
Gaussian/B3LYP	6-31++G(d, p)	-1952	527	6.2
Gaussian/B3LYP	6-311G	-2340	696	7.5
Gaussian/B3LYP	6-311G(d)	-2240	594	6.7
Gaussian/B3LYP	6-311+G	-2288	699	6.6
Gaussian/B3LYP	6-311+G(d)	-2203	639	5.8
Gaussian/B3LYP	6-311++G(d, p)	-2203	639	5.8
Gaussian/B3LYP	6-31+G(df, 2pd)	-1968	530	5.9
Gaussian/B3LYP	TZV	-2498	620	5.4
Gaussian/B3LYP	TZVP	-2223	613	5.2
ADF/ZORA DFT	QZ4P	-1990	550	5.6
CASTEP	GIPAW	-2019	520	5.7

[1] Geometry of $VOCl_3$ from ref. 83.

4.3. Results and Discussion

The section is organized as follows: in Section 4.3.1 experimental and simulation results for compounds:

I) $(C_5H_5)V(CO)_4$

II) $[V(O)(ONMe_2)_2]_2O$

III) $[NH_4][V(O)(O_2)_2(NH_3)]$

IV) $K_3[VO(O_2)_2(C_2O_4)]\cdot 1H_2O$

V) $K_3[V(O)_2(C_2O_4)_2]\cdot 3H_2O$

are presented. Section 4.3.2 deals with theoretical results for compounds **I) - V)**. In this section some details of computational techniques and basis sets for each compound are presented. A comparison of calculated NMR parameters with experimental results for each vanadium compound is also discussed in this section. Experimental data for each vanadium compound including the three chemical shift principal components are tabulated. Computational results are also tabulated for compounds **I)-V)**. To have comparison between computational and experimental results, these Tables are presented in Section 4.3.2.2.

4.3.1. Experimental Spectra and Simulation

I) Cyclopentadienyl Vanadium Tetracarbonyl, $(C_5H_5)V(CO)_4$

Cyclopentadienyl vanadium tetracarbonyl, has been used as a precursor for the synthesis of many other vanadium organometallic compounds. It is an orange-coloured, crystalline, air sensitive solid, melting at 139 °C and subliming at 90 °C (0.5 mm Hg). It was first prepared by Fischer and Hafner in 1954.[88] The crystal structure of this compound was first reported to be orthorhombic with the P*nma* space group by Wilford *et al*., in 1967,[89] meaning that the molecule has mirror symmetry. The structure of the compound is described as a vanadium atom that is in a special position in a mirror plane, and the cylopentadienyl ring is disordered over two equally preferred, orientations one of which is shown Figure

4.4. The molecular structure of this compound has also been determined by gas-phase electron diffraction assuming local C_{4v} symmetry for the V-$(CO)_4$ moiety and C_{5v} symmetry for the C_5H_5-V group, however the relative positions of these two groups could not be determined unequivocally.[90]

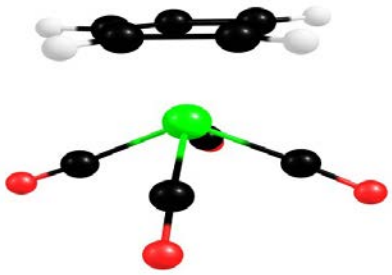

Figure 4.4. Molecular structure of $(C_5H_5)V(CO)_4$ (projection of a molecule with respect to the plane of the cylopentadienyl ring).

Figures 4.5-4.6 show the spectra of $(C_5H_5)V(CO)_4$ acquired at 11.75 and 7.05 T. The overall breaths of the spectra are approximately 1.5 MHz. The shape of the spinning sideband envelopes with horns near -124 and -260 kHz indicate that η_Q is nearly zero; therefore, the EFG tensor at the ^{51}V nucleus is close to axially symmetric. The central transition (dominated by magnetic shielding anisotropy) has a breadth of ≈ 270 ppm. The shape of the central transition also indicates an axially or close to axially symmetric CSA tensor with a skew = 1, and that δ_{33} is the unique component of the tensor; thus, V_{zz} is coincident with δ_{33}. By fitting calculated spectra to the experimental spectra, Figures 4.7 and 4.8, the ^{51}V NMR parameters were obtained and are summarized in Table 4.2. A microwave study of this compound has been reported by the McKay *et al*,[91] and coworkers. In 1995; in this study a value of -4.77 (6) MHz for C_Q was determined in the gas phase.

Table. 4.2. Experimental Solid-State NMR Parameters for $(C_5H_5)V(CO)_4$.

C_Q (MHz)	3.0 ± 0.05	δ_{iso} (ppm)	-1562 ± 2	α (°)	0.0
η_Q	0.0	Ω (ppm)	240 ± 40	β (°)	0.0
		κ	1.0	γ (°)	0.0

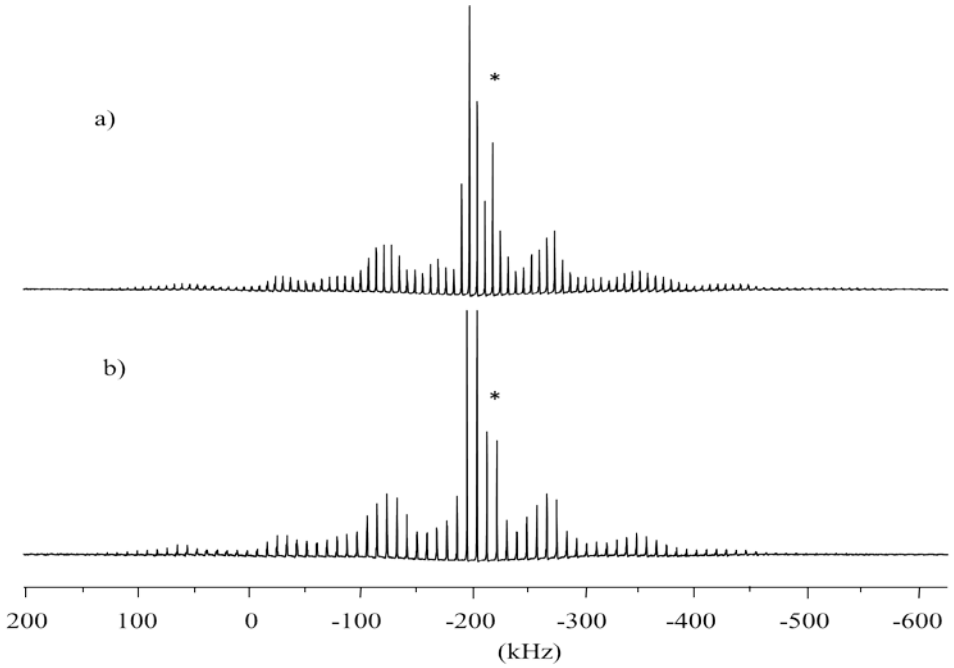

Figure 4.5. ^{51}V NMR spectra of $(C_5H_5)V(CO)_4$ acquired at 11.75 T with MAS rates of a) 7 kHz and b) 9 kHz. Each spectrum is the sum of 12000 scans. The isotropic chemical shifts are indicated with asterisks.

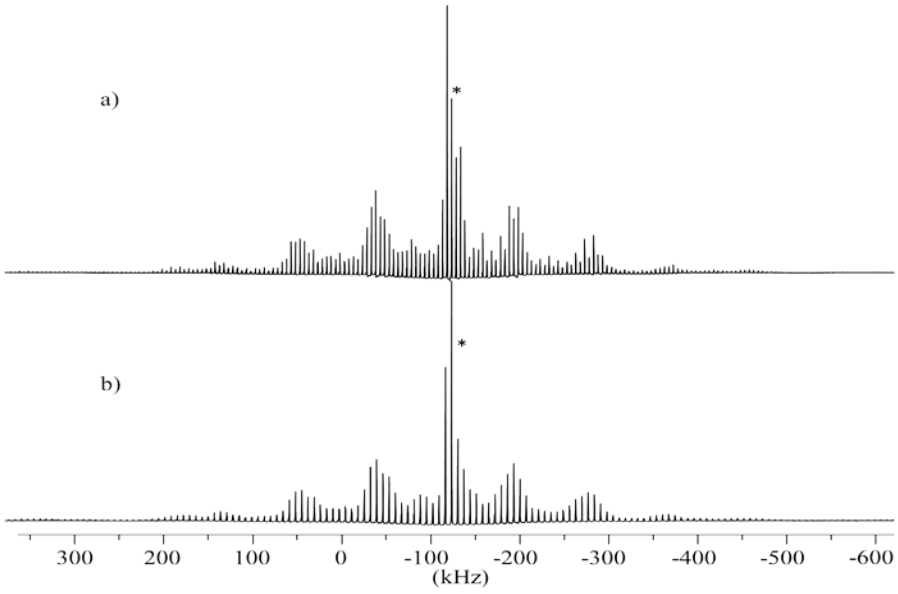

Figure 4.6. Vanadium-51 NMR spectra of $(C_5H_5)V(CO)_4$ acquired at 7.05 T with MAS rates of a) 5 kHz and b) 7 kHz. Each spectrum is the sum of 10000 scans. The isotropic chemical shifts are indicated with asterisks.

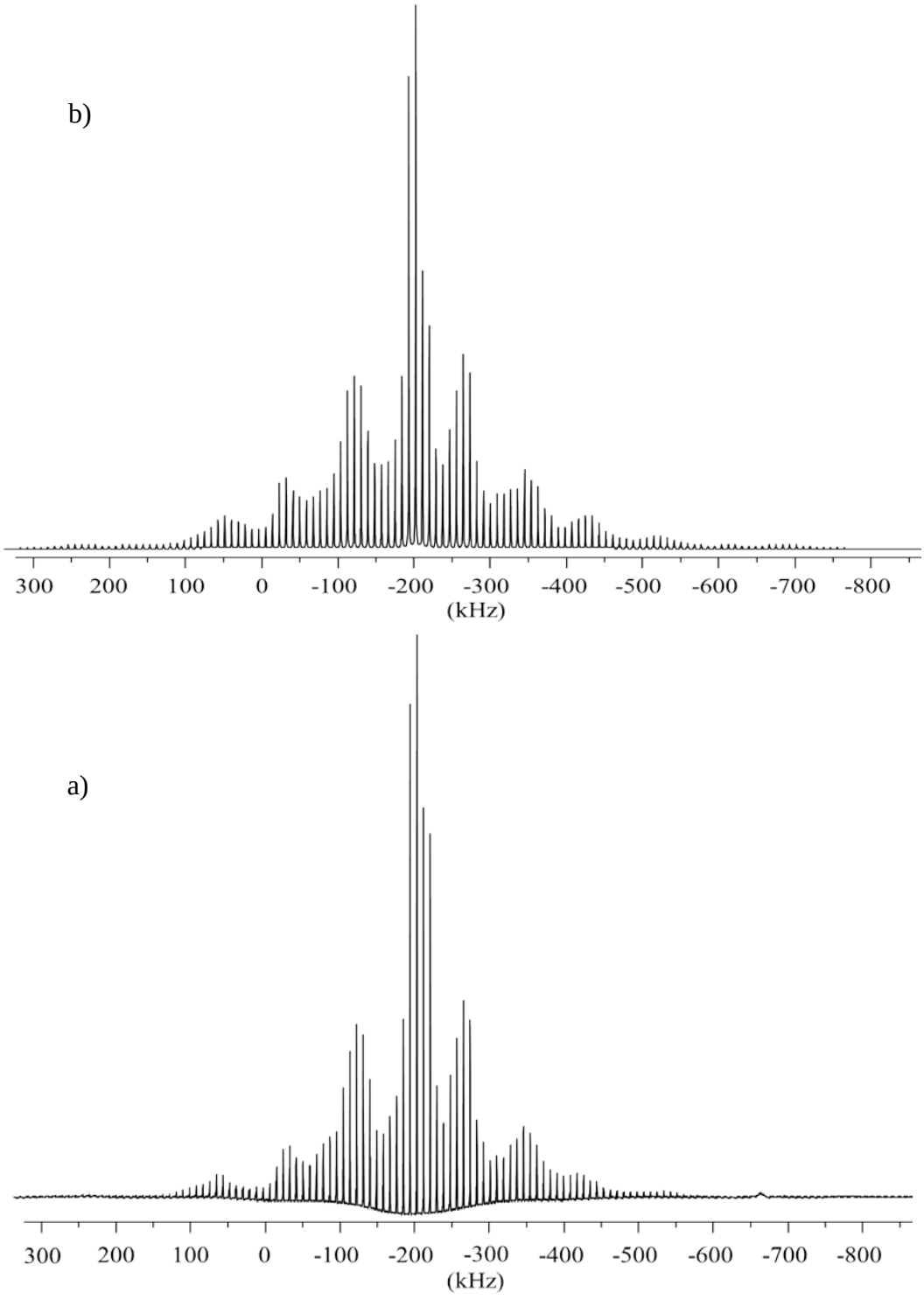

Figure 4.7. Vanadium-51 NMR spectra of $(C_5H_5)V(CO)_4$ acquired at 11.75 T with an MAS rate of 9 kHz a). The calculated spectrum (b) was obtained using the parameters presented in Table 4.2.

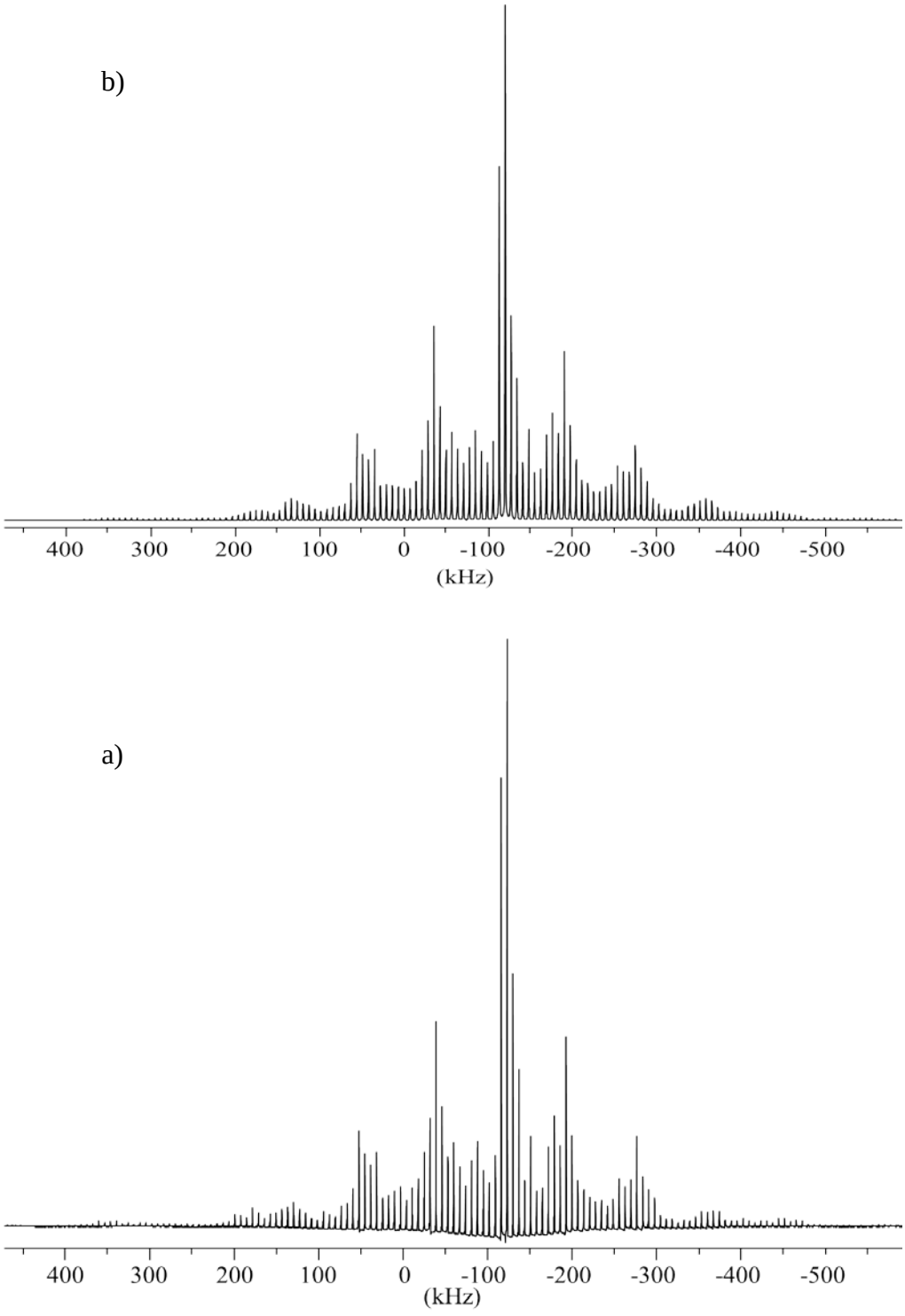

Figure 4.8. Vanadium-51 NMR spectra of $(C_5H_5)V(CO)_4$ acquired at 7.05 T with an MAS rate of 7 kHz a). The calculated spectrum (b) was obtained using the parameters presented in Table 4.2.

II) $[V(O)(ONMe_2)_2]_2O$

The X-ray crystallography structure of $[V(O)(ONMe_2)_2]_2O$ has been determined by Paul *et al*.[44] (Figure 4.9). The molecule has crystallographic two-fold symmetry, with the two-fold axis passing through the bridging oxygen. The vanadium atoms are six-coordinate, but the arrangement about the vanadium might be described as approximately tetrahedral, considering the centre of the N-O bond in each dimethylhydroxamide ligand as one vertex.

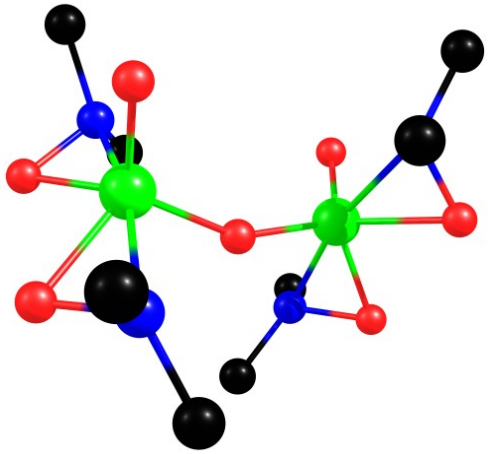

Figure 4.9. Molecular structure of $[V(O)(ONMe_2)_2]_2O$

However, the vanadium atom is slightly displaced toward the terminal oxygen, so the geometry may also be described as a pentagonal pyramid, as is often found for oxoperoxovanadate complexes. In this compound, the bond from V to bridging oxygen is much shorter (1.806Å) than typical V-O bonds in similar oxoperoxovanadate complexes (1.994-2.013 Å).[92] The other V-O bond lengths are similar to those for other oxobisperoxovanadate(V) complexes.[92-94]

Figure 4.10 shows the experimental NMR spectra of an MAS sample of solid $[V(O)(ONMe_2)_2]_2O$ acquired at several spinning frequencies. Comparison of these spectra permits determination of the isotropic chemical shift, δ_{iso} = -714 ± 3 ppm. Vanadium-51 NMR spectra of MAS samples of $[V(O)(ONMe_2)_2]_2O$

display the complete manifold of spinning sidebands (ssbs) from the satellite transitions.

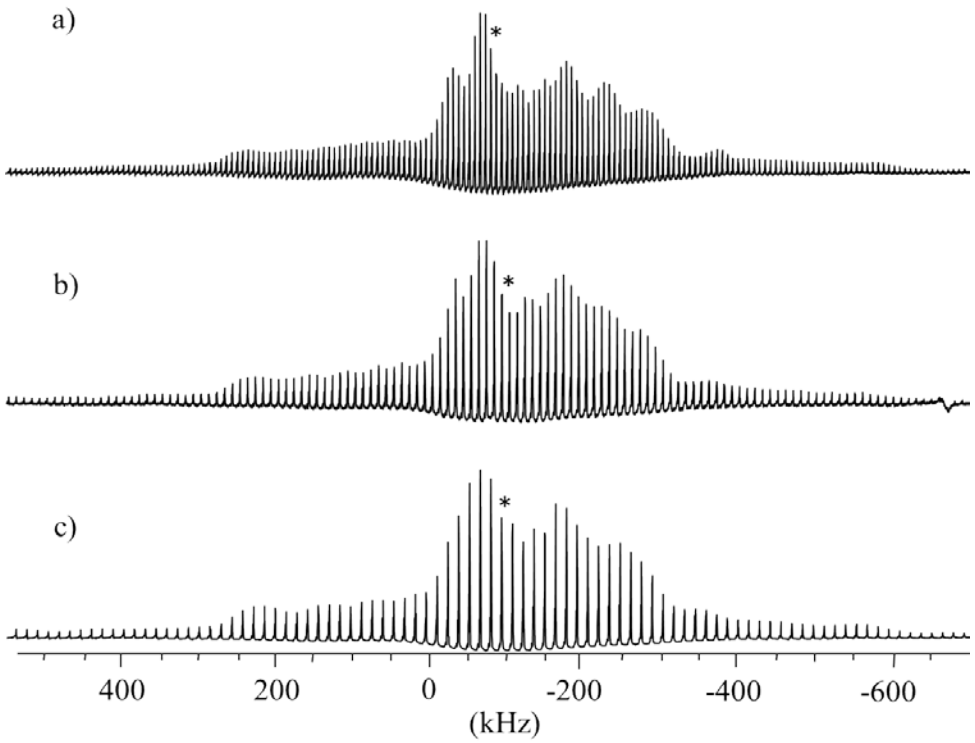

Figure 4.10. ^{51}V MAS NMR spectra of $[V(O)(ONMe_2)_2]_2O$ acquired at B_0 = 11.75 T with MAS frequencies of (a) 7 kHz, (b) 10 kHz, and (c) 12 kHz.

The satellite (±7/2 ↔ ±5/2, ±5/2 ↔ ±3/2, and ±3/2 ↔ ±1/2) and central (+1/2 ↔ -1/2) transitions resulted in spectral breadths that span several hundred kHz. Both the ^{51}V quadrupolar interaction and the CSA make significant contributions to the breadth and shape of the ^{51}V NMR spectra at all fields employed here. Therefore, ^{51}V solid-state NMR spectra are dominated by eight independent parameters corresponding to C_Q and η_Q for the quadrupolar tensor, δ_{iso}, Ω, κ for the CS tensor and the Euler angles α, β, γ defining their relative orientations.

The second-order quadrupolar interaction is generally relatively small for ^{51}V, so typically one does not observe a lineshape for the CT that would allow straightforward extraction of C_Q and η_Q values from NMR spectra acquired with MAS. The overall breadths of the spectra are in excess of 1 MHz. In most cases,

an estimate of C_Q may be obtained from $6\nu_Q = 18C_Q / [2I(2I+1)]$ of the spinning sidebands manifold, (where $6\nu_Q$ is the total breadth of the MAS spectrum). However in this example C_Q is estimated from $4\nu_Q = 12C_Q / [2I(2I+1)]$ since peaks from ± 5/2 ↔ ± 3/2 transitions are more readily observed than are those from the ± 7/2 ↔ ± 5/2 transitions. By careful analysis of vanadium MAS spectra of $[V(O)(ONMe_2)_2]_2O$ at different spinning frequencies and fields, shown in Figures 4.10 and 4.11, respectively, the isotropic chemical shift, δ_{iso}, quadrupolar coupling constant, C_Q, and asymmetry parameter, η_Q were obtained. These three parameters were kept constant while simulating the NMR spectrum of the stationary sample (Figure 4.12), aiding in the determination of the remaining parameters.

There are some factors which made the extraction of the CSA parameters and Euler angles more difficult. First, the experimentally measured span of the shielding tensor for this compound, 1437 ± 15 ppm, is the largest measured for a vanadium compound. Second, because of overlap of the CT peaks with those of the STs, the determination of the CSA parameters from the manifold of ssbs is complicated. In another study,[95] we demonstrated the application of the highly frequency-selective inversion properties of HS pulses to separate the CT peaks form STs; this will be discussed in the next section. And finally because of lack of symmetry in this compound, there is no obvious hint about the value of the Euler angles.

SIMPSON numerical simulations of the $[V(O)(ONMe_2)_2]_2O$ NMR spectra were performed, and the ^{51}V chemical shift, quadrupolar coupling parameters, as well as the Euler angles were extracted. The experimental and best-fit simulated spectra are in excellent agreement, as illustrated in Figure 4.13 (a-d). Experimental results are summarized in Table 4.3.

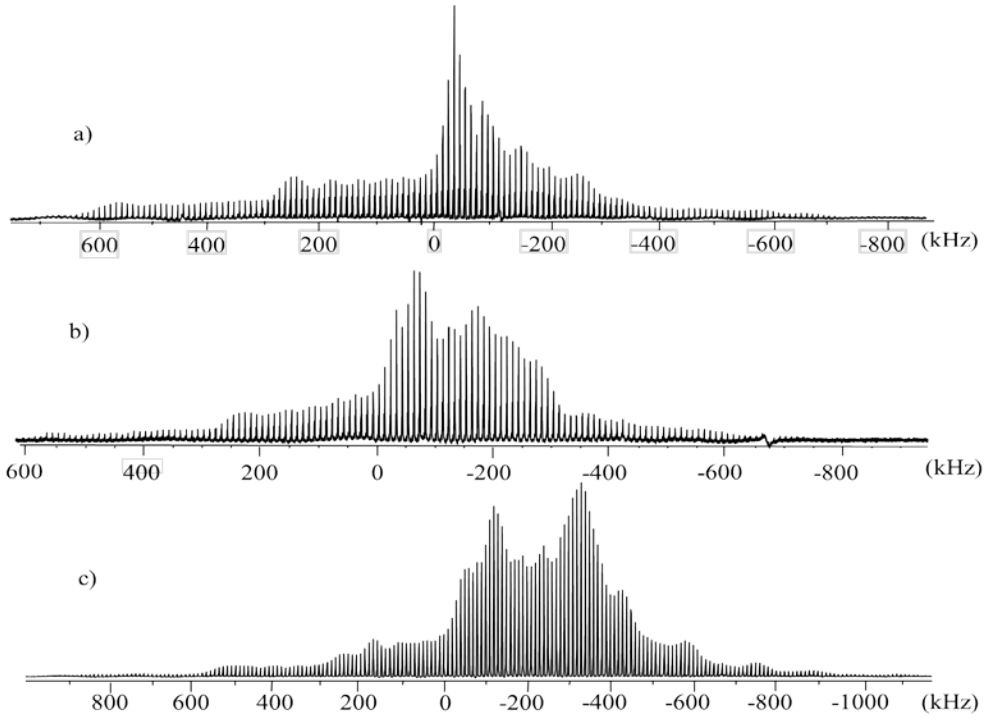

Figure 4.11. Experimental ^{51}V MAS NMR spectra of $[V(O)(ONMe_2)_2]_2O$ a) 7.05 T, b) 11.75 T, and c) 21.14 T. The spectra were acquired at a spinning frequency of 10 kHz.

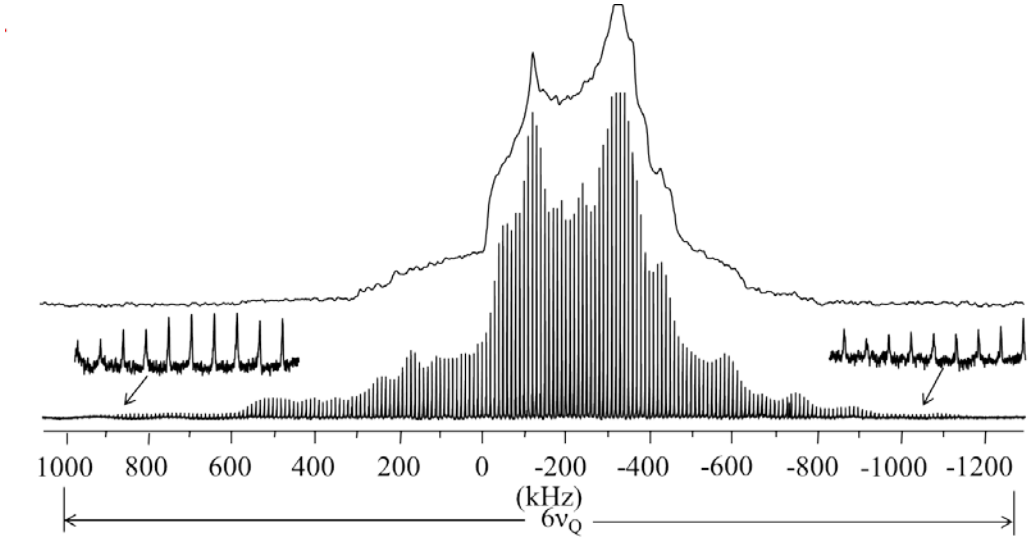

Figure 4.12. Experimental ^{51}V stationary (upper trace) and MAS NMR (lower trace) spectra of $[V(O)(ONMe_2)_2]_2O$ acquired at 21.14 T. The MAS spectrum was acquired at a spinning frequency of 10 kHz.

Table 4.3. Experimental Solid-State NMR Parameters for $[V(O)(ONMe_2)_2]_2O$.

C_Q (MHz)	4.8 ± 0.1	δ_{iso} (ppm)	-714 ± 3	α (°)	10 ± 10
η_Q	0.68 ± 0.05	Ω (ppm)	1437 ± 15	β (°)	76 ± 10
		κ	0.33 ± 0.05	γ (°)	0

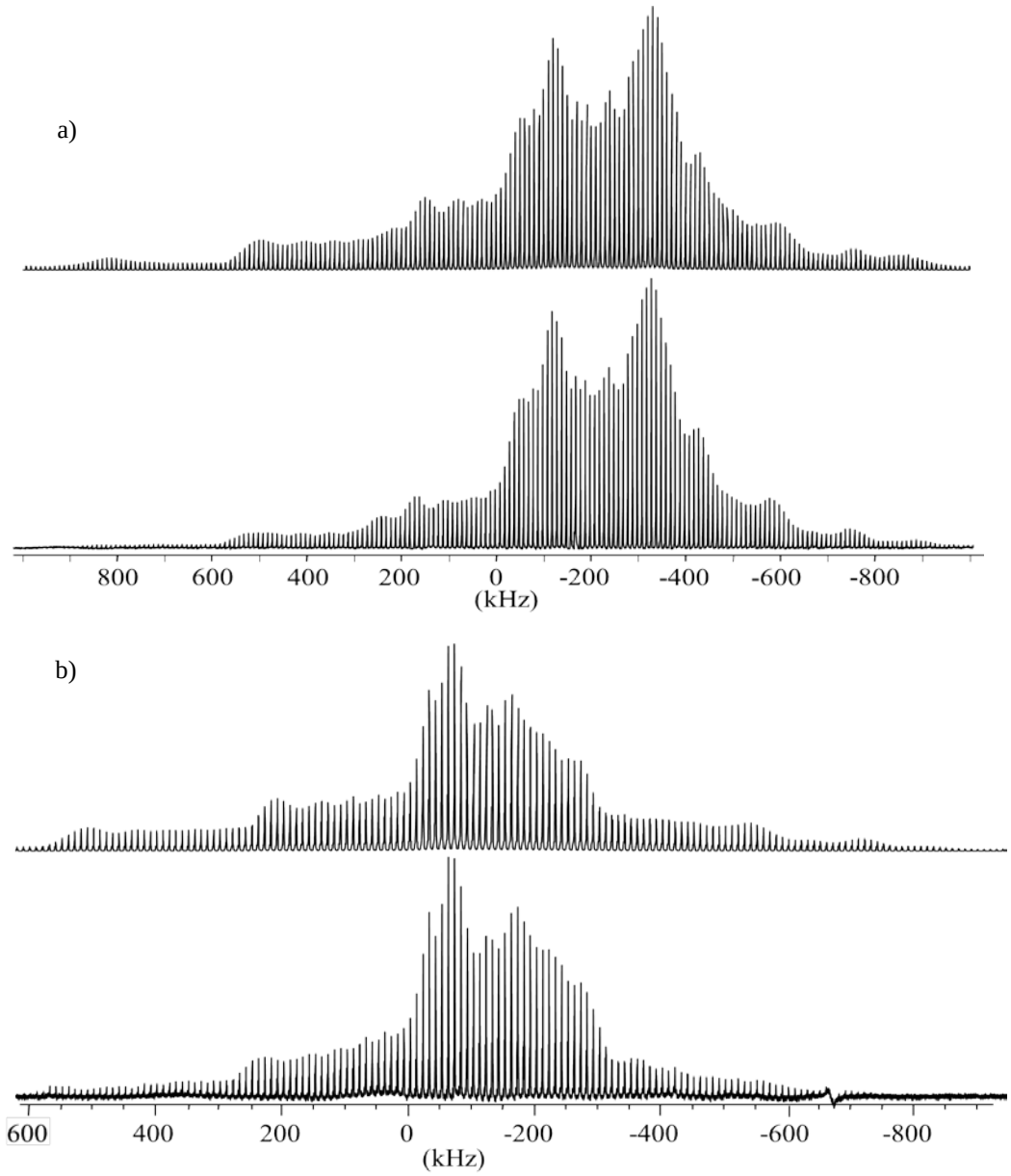

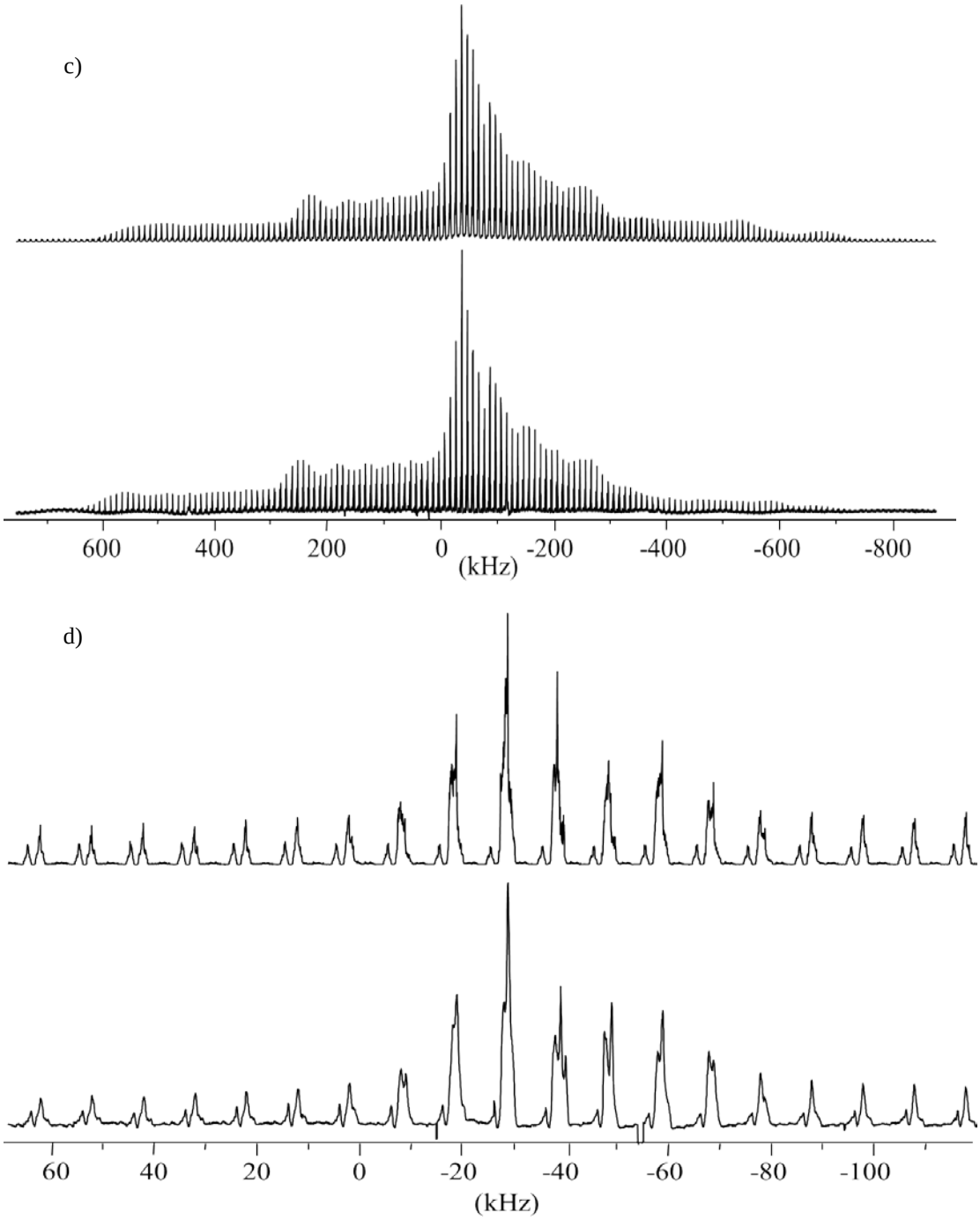

Figure 4.13. Experimental and simulated ^{51}V NMR spectra of $[V(O)(ONMe_2)_2]_2O$ at a) 21.14 T, b) 11.75 , c) 7.05, and d) 4.70 T. The spectra were acquied at a spinning frequency of 10 kHz. The NMR parameters obtained from the simulation are summarized in Table 4.3.

In general the principal components of the CS tensor may be determined from an analysis of NMR spectra obtained from a stationary powder sample, but in our case the resulting spectrum had a poor signal-to-noise ratio at some fields. Another issue is the overlap of the CT peaks with those of the STs, which makes the determination of the CSA parameters complicated. In an earlier report,[95] we demonstrated the application of the highly frequency-selective inversion properties of HS pulses to separate the CT peaks from those of the STs, thereby simplifying the determination of the CSA parameters from the complex manifold of ssbs generated from all single-quantum transitions obtained for spin-7/2 quadrupolar nuclei having moderate C_Q values (of the order of 4 MHz) and relatively large CSA values (up to approximately 1500 ppm). To test our HS techniques, we used samples whose CSAs had been well characterized previously by other NMR methods. The theory and application of this technique have been widely discussed in the literature.[96- 100] The technique we used here is called the CT method (see ref 94 for details), which means "application of an HS pulse centred on a central transition spinning sideband". With this technique one can generate a difference spectrum containing only CT intensity. The CT method is a three-step process: 1) a spectrum of the sample is obtained without applying HS pulse; 2) a spectrum is acquired by applying a very low power, selective HS pulse with a bandwidth of 2.0 kHz to a single CT spinning sideband and 3) by subtracting the spectrum from a spectrum acquired originally without applying an HS pulse, a spectrum of only the CT is obtained. We applied this technique to obtain a spectrum from which the vanadium CSA parameters for an MAS powder sample of $[V(O)(ONMe_2)_2]_2O$ could be determined. The ^{51}V NMR spectrum of $[V(O)(ONMe_2)_2]_2O$ acquired without an HS pulse is shown in Figure 4.14 (a) while the spectrum acquired with a selective HS pulse applied to a first-order spinning side band for the central transition is shown in Figure 4.14 (b). The difference spectrum shown in Figure 4.14 (c) was then analyzed and the results are tabulated in Table 4.8. These results are in good agreement with those obtained previously using the WSOLIDS and SIMPSON simulation packages.

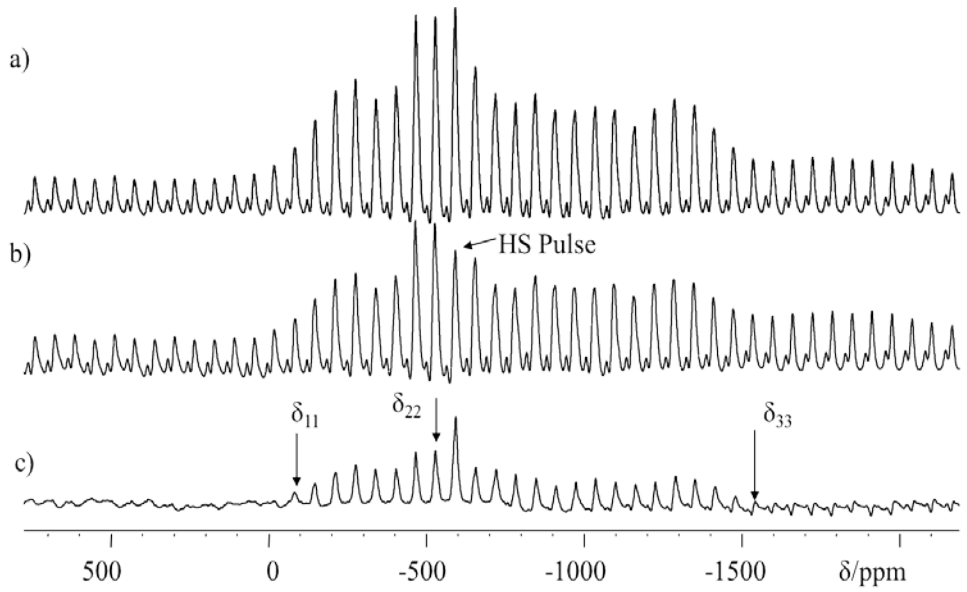

Figure 4.14. Central transition region of the ^{51}V NMR spectra of $[V(O)(ONMe_2)_2]_2O$ with MAS (5.0 kHz) (a) with no HS pulse (b) with a 2.0 kHz bandwidth HS pulse applied at the indicated position and (c) the difference spectrum a-b.

III) Ammonium Oxodiperoxoamminevanadate, $[NH_4][V(O)(O_2)_2(NH_3)]$

The structure of $[NH_4][V(O)(O_2)_2(NH_3)]$ was determined by Drew and Einstein[101] using X-ray crystallography, Figure 4.15. This compound crystallizes in the orthorhombic space group *Pnma*. The vanadium atom is bonded to five oxygen atoms and one nitrogen atom in what can best be described as a pentagonal pyramid, the four oxygens of the two peroxo groups and the ammonia nitrogen atoms forming the base of the distorted pyramid and the vanadyl oxygen occupying the apical positions.

Because peroxo-type coordination compounds are usually soluble in water, they are of great interest as molecular precursors for the preparation of oxide materials, more specifically, multimetallic oxide involving some transition metals for which the availability of well-defined water-soluble complexes is very limited.[102] These oxide materials are often prepared by solid-state reactions of the oxides. Another method of preparing these materials is thermal decomposition of

precursors; a suitable precursor coordination compound with molecular or anionic ligands which is easily released or decomposed in heating (*e.g.*, H_2O, NH_3) can be used. The peroxo complexes of transition metals are often used for such purposes. This compound thermally decomposes to ammonium metavanadate, which then decomposes to vanadium pentoxide. The first decomposition step occurs between 74 and 102 ˚C. For this reason the samples were heated first at 70 and then at 110 ºC for 10 hours. XRD experiments were performed on these samples to detect any structural changes. There were no changes observed for the sample which was heated at 70 ºC as shown in Figure 4.16, but the structure changed dramatically for the sample heated at 110 ˚C, shown in Figure 4.17.

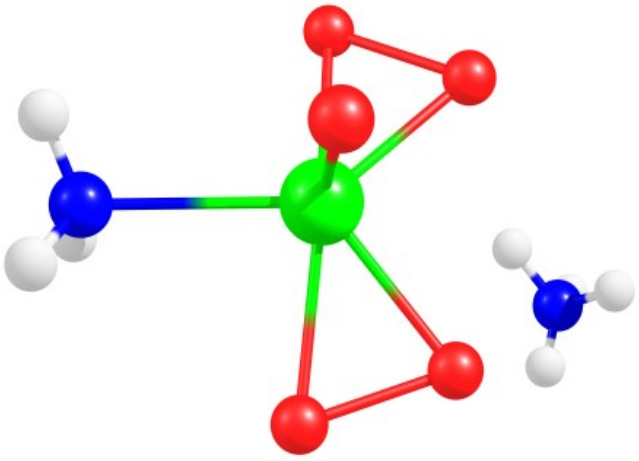

Figure 4.15. Molecular structure of $[NH_4][V(O)(O_2)_2(NH_3)]$.

The ^{51}V MAS NMR spectra of $[NH_4][V(O)(O_2)_2(NH_3)]$ recorded at 11.75 T at three different spinning frequencies, shown in Figure 4.18, demonstrated that spinning sidebands extend over a spectral width of about 3.0 MHz (up to 1 MHz shown in Figure 4.18). As mentioned earlier an estimate of C_Q may be obtained from $4\nu_Q = 12C_Q / [2I(2I+1)]$ from an analysis of the sidebands from $\pm 5/2 \leftrightarrow \pm 3/2$ transitions. [103] From the span of the spinning sideband pattern, value for C_Q, 7.0 ± 0.4 MHz and for η, 0.75 ± 0.05 were estimated.

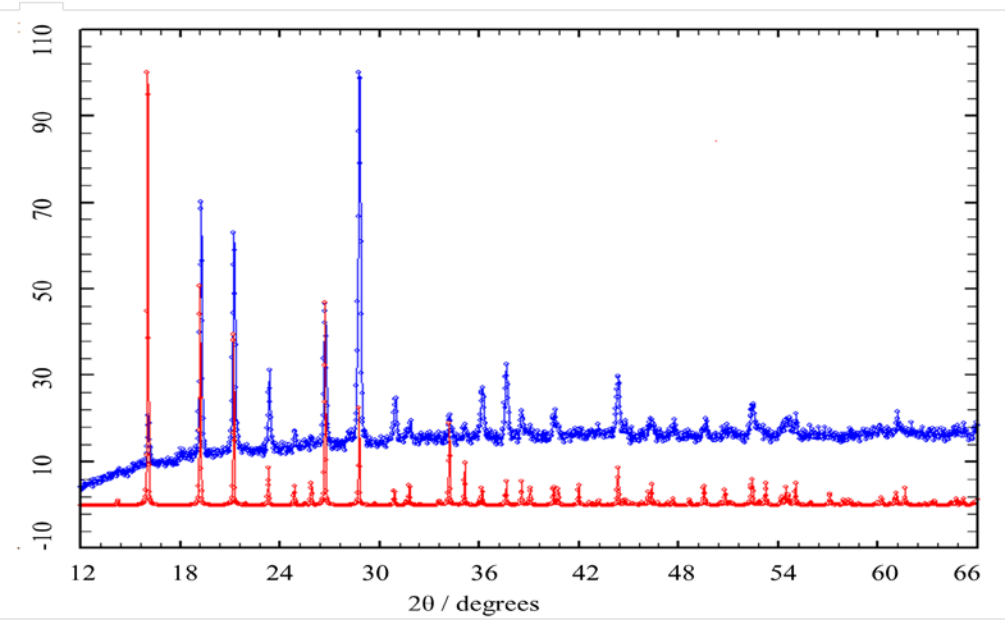

Figure 4.16. XRD powder pattern for a powder sample of $[NH_4][V(O)(O_2)_2(NH_3)]$ heated at 70 ºC, (predicted = lower trace, experimental = upper trace).

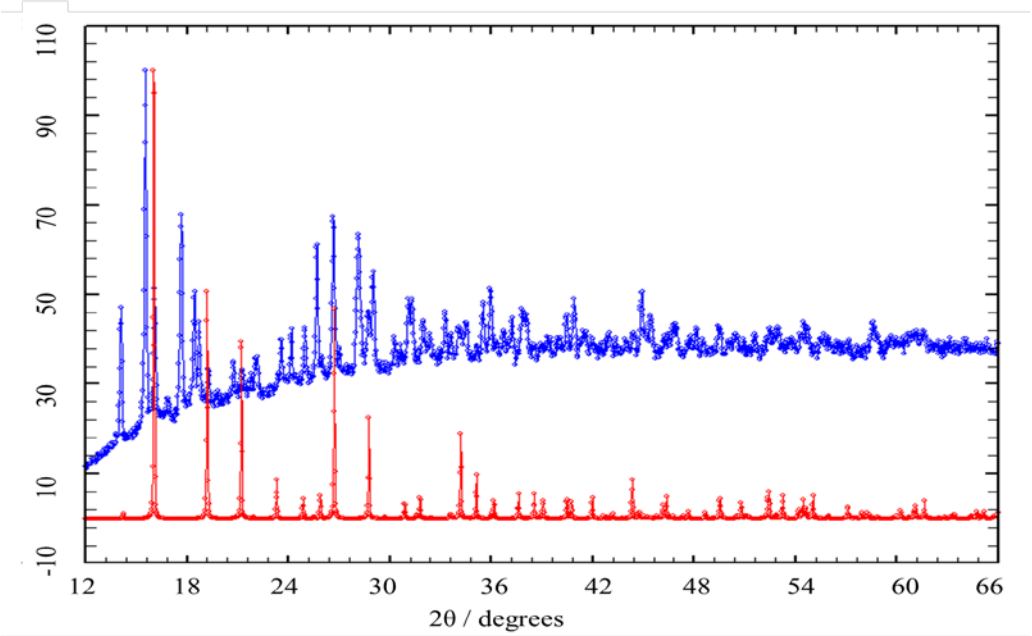

Figure 4.17. XRD powder pattern for a powder sample of $[NH_4][V(O)(O_2)_2(NH_3)]$ heated at 110 ºC, (predicted = lower trace, experimental = upper trace).

Spectra of a stationary sample were acquired at 7.05 and 11.75 T, shown in Figure 4.19 and 4.20; the data obtained from analyses of these spectra are summarized in Table. 4.4. Employing WSOLIDS with DFT calculation results as starting parameters led to the final parameters listed in Table 4.4. In a final step, SIMPSON calculations were conducted using these NMR parameters; the best-fit simulated and experimental spectra are in good agreement as shown in Figures 4.21 and 4.22.

Table 4.4. Experimental Solid-State NMR Parameters for $[NH_4][V(O)(O_2)_2(NH_3)]$.

C_Q (MHz)	7.0 ± 0.4	δ_{iso} (ppm)	-768 ± 5	α (°)	0.0
η_Q	0.75 ± 0.05	Ω (ppm)	1350 ± 20	β (°)	10 ± 5
		κ	0.52 ± 0.05	γ (°)	0.0

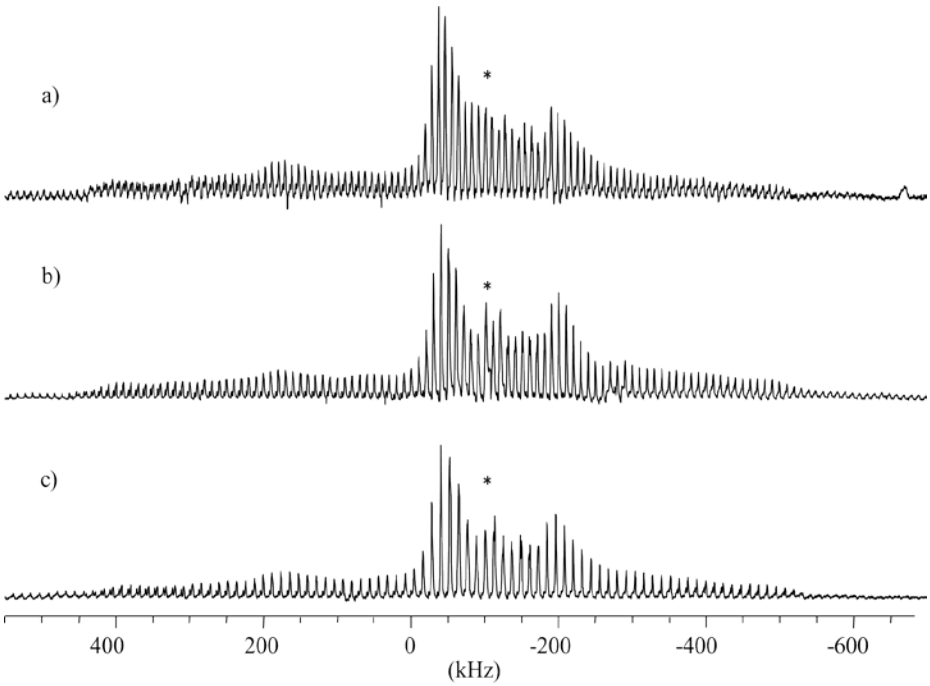

Figure 4.18. ^{51}V NMR spectra of $[NH_4]$ $[V(O)(O_2)_2(NH_3)]$ acquired at 11.75 T with MAS rates of a) 9 kHz, b) 10 kHz and c) 12 kHz. Each spectrum is the sum of 4000 scans. The isotropic chemical shifts are indicated with asterisks.

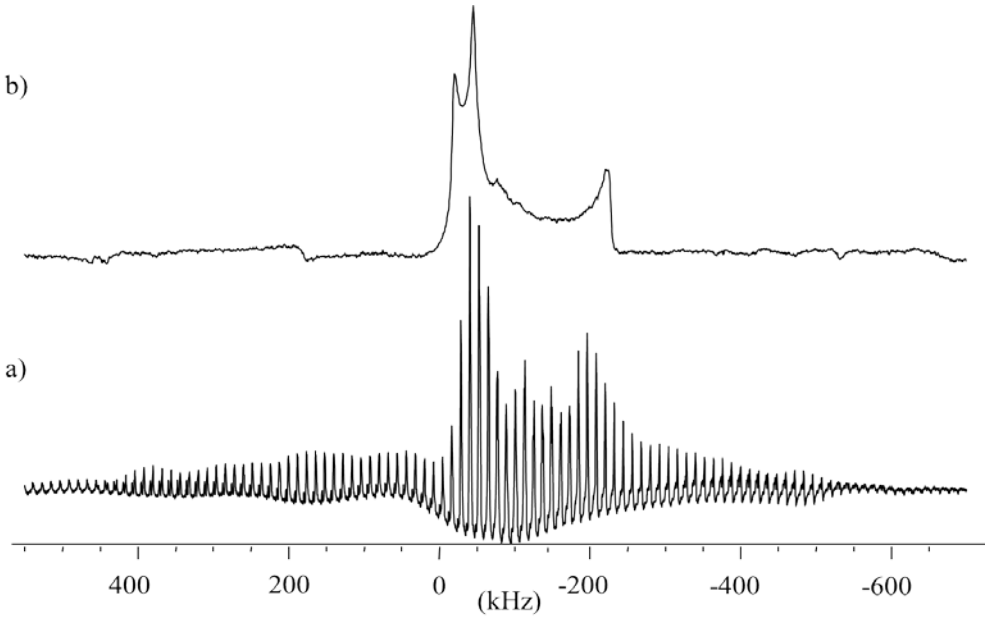

Figure 4.19. ^{51}V NMR spectra of $[NH_4][V(O)(O_2)_2(NH_3)]$ acquired at 11.75 T a) with an MAS rate of 9 kHz b) static. Each spectrum is the sum of approximately 3000 scans.

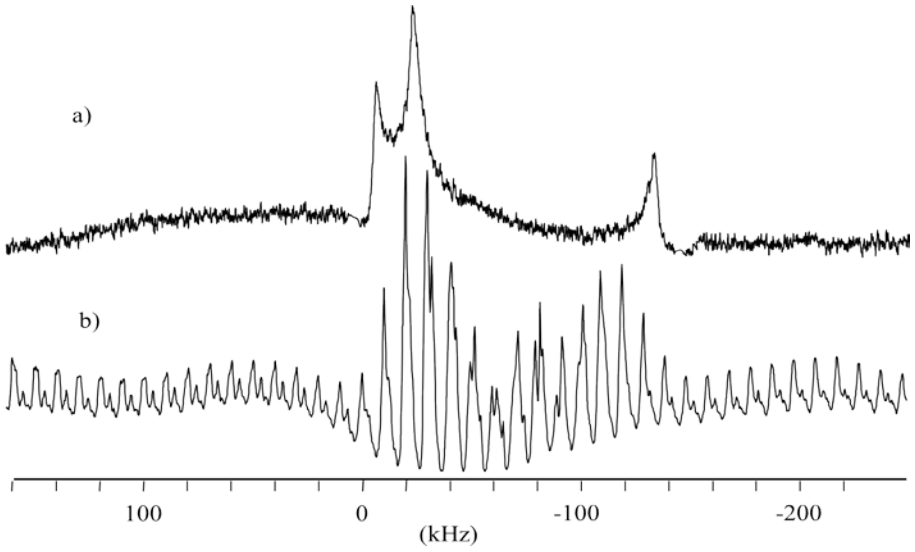

Figure 4.20. ^{51}V NMR spectra of $[NH_4][V(O)(O_2)_2(NH_3)]$ acquired at 7.05 T a) static and b) with an MAS rate of 7 kHz. Each spectrum is the sum of approximately 3000 scans.

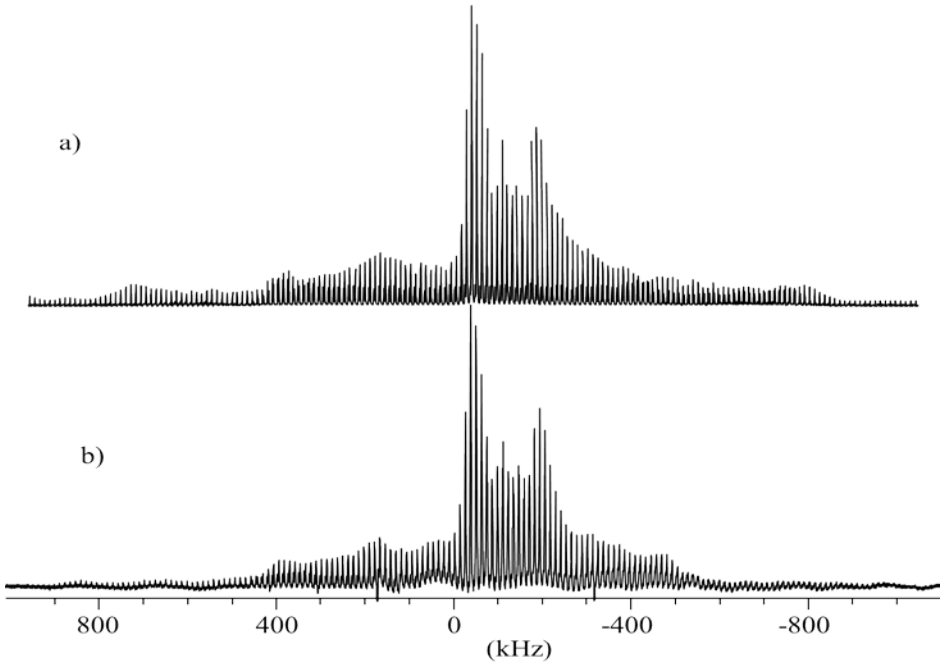

Figure 4.21. ^{51}V NMR spectra of $[NH_4][V(O)(O_2)_2(NH_3)]$ acquired at 11.75 T. a) Simulated and b) experimental with an MAS rate of 12 kHz. The NMR parameters used for the simulation are summarized in Table 4.4.

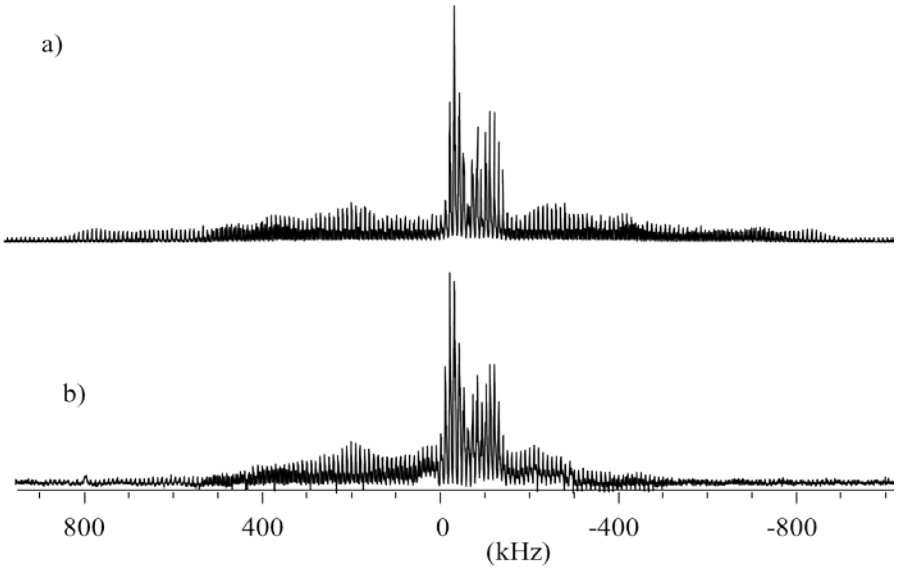

Figure 4.22. Vanadium-51 NMR spectra of $[NH_4][V(O)(O_2)_2(NH_3)]$ acquired at 7.05 T. a) Simulated and b) experimental with an MAS rate of 10 kHz. The NMR parameters used for the simulation are summarized in Table 4.4.

IV) Tripotassium Oxalato-oxodiperoxovanadate, $K_3[VO(O_2)_2(C_2O_4)]\cdot 1H_2O$

Crystals of $K_3[VO(O_2)_2(C_2O_4)]\cdot 1H_2O$ are monoclinic;[46,104] the molecular structure is shown in Figure 4.23. The anion, $[VO(O_2)_2(C_2O_4)]^{-3}$, is pentagonal bipyramidal in shape. Crystals of $K_3[VO(O_2)_2(C_2O_4)]\cdot 1H_2O$ contain four formula units in the primitive monoclinic unit cell with the potassium ions, oxodiperoxooxalatovanadate(V) anions, and water molecules held together by electrostatic forces and hydrogen bonding. The vanadium atom is seven-coordinate; the two peroxo groups and one oxygen atom from the oxalate ligand make up the pentagonal girdle, while the oxo ligands and an oxygen atom of the oxalato group occupy the apical positions. The crystal structure of this compound suggests no local symmetry for the vanadium site.

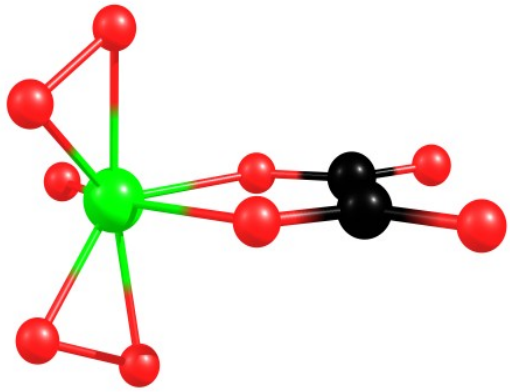

Figure 4.23. Molecular structure of $[VO(O_2)_2(C_2O_4)]^{-3}$

The experimental MAS NMR spectra of $K_3[VO(O_2)_2(C_2O_4)]\cdot 1H_2O$, acquired at several spinning frequencies are shown in Figures 4.24 and 4.25. By comparing spectra obtained at different spinning rates, the isotropic chemical shift, δ_{iso}= -708 ± 4 ppm, was determined. The asymmetry of the lineshapes in the NMR spectra shows the combined effect of the anisotropic quadrupolar and CSA interactions. The relative orientation of the two tensors also play an important role in determining the line shape of the spinning sideband envelope, especially the angle β, which defines the angle between the largest components of the shielding and EFG tensors. We acquired and simulated MAS spectra of the compound at two different field strengths and at different spinning rates, in order to extract with

greater accuracy the quadrupolar and CSA tensor elements. This was particularly important because there is no local symmetry for the vanadium site. From the spectral width of the spinning sideband pattern, a value of C_Q = 4.8 ± 0.2 MHz was determined. The remaining parameters describing the quadrupolar and the CSA interaction parameters as well as the Euler angles were determined from numerical simulations of the static solid-state NMR spectra, Figures 4.26 and 4.27.

Finally, SIMPSON calculations were conducted using the NMR parameters. The best-fit simulated and experimental spectra are in good agreement as is shown in Figure 4.28-4.29; data from these fits are summarized in Table 4.5. These results are in good agreement with the experimental values of C_Q = 4.8 ± 0.5 MHz, η = 0.9 ± 0.1, δ_{iso} = -704 ppm, Ω = 1449 ± 30 ppm and κ = 0.75, which reported by Zeng *et al*[105](summarized in Table 4.8).

Table 4.5. Experimental Solid-State NMR Parameters for $K_3[VO(O_2)_2(C_2O_4)]\cdot H_2O$

C_Q (MHz)	4.8 ± 0.2	δ_{iso} (ppm)	-708 ± 4	α (°)	20 ± 10
η_Q	0.9 ± 0.05	Ω (ppm)	1400 ± 15	β (°)	75 ± 5
		κ	0.6 ± 0.05	γ (°)	0.0

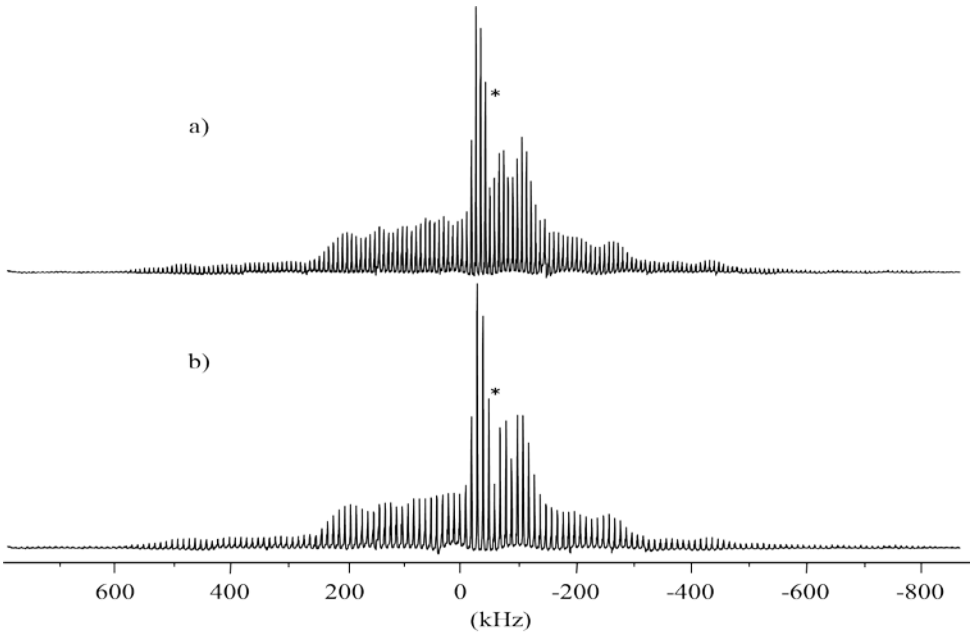

Figure 4.24. ^{51}V NMR spectra of $K_3[VO(O_2)_2(C_2O_4)]\cdot 1H_2O$ acquired at 7.05 T with MAS rates of a) 8 kHz and b) 10 kHz. Each spectrum is the sum of 4000 scans. The asterisk indicates the isotropic peak.

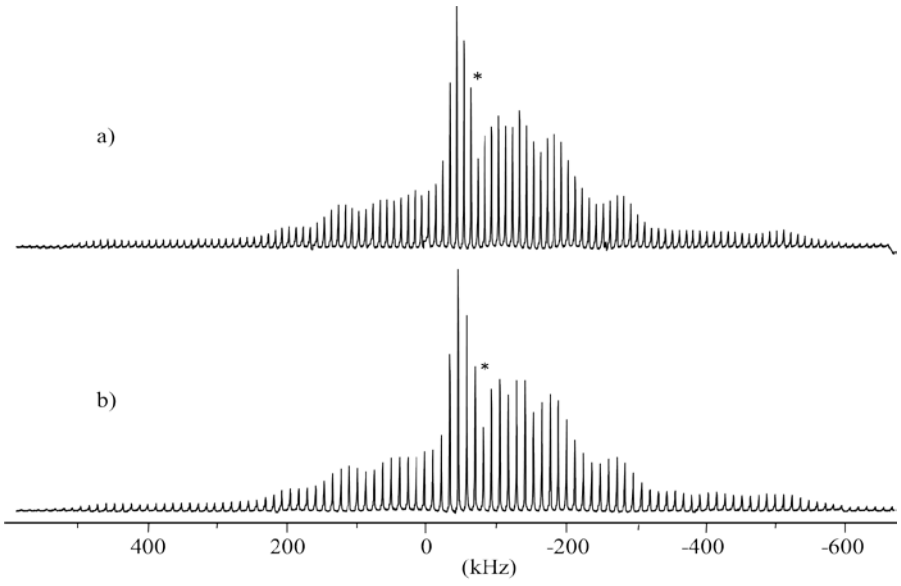

Figure 4.25. ^{51}V NMR spectra of $K_3[VO(O_2)_2(C_2O_4)]\cdot 1H_2O$ acquired at 11.75 T with MAS rates of a) 10 kHz and b) 12 kHz. Each spectrum is the sum of 5000 scans. The asterisk indicates the isotropic peak.

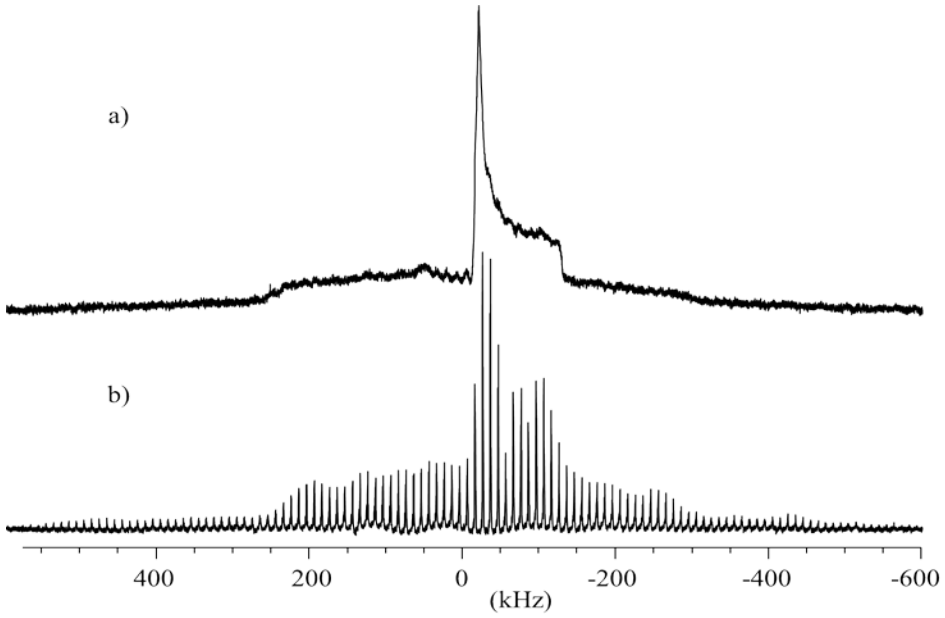

Figure 4.26. ^{51}V NMR spectra of $K_3[VO(O_2)_2(C_2O_4)]\cdot 1H_2O$ acquired at 7.05 T. a) Static and b) with an MAS rate of 10 kHz. Each spectrum is the sum of approximately 20000 scans.

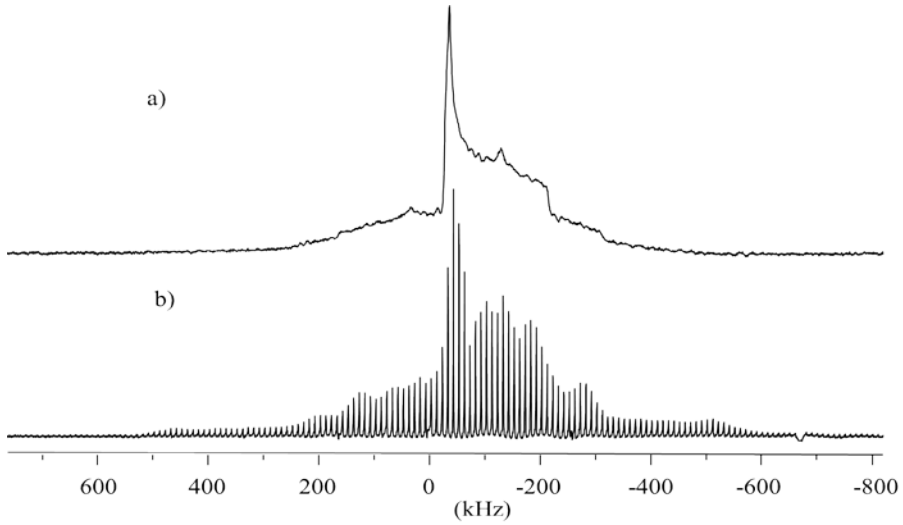

Figure 4.27. ^{51}V NMR spectra of $K_3[VO(O_2)_2(C_2O_4)]\cdot 1H_2O$ acquired at 11.75 T. a) Static and b) with an MAS rate of 10 kHz. Each spectrum is the sum of approximately 20000 scans.

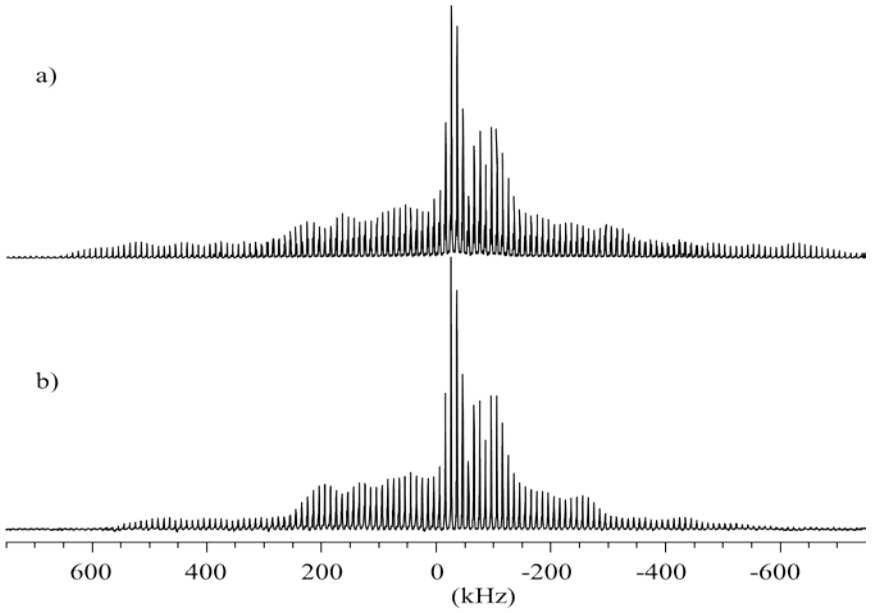

Figure 4.28. ^{51}V NMR spectra of $K_3[VO(O_2)_2(C_2O_4)]\cdot 1H_2O$ acquired at 7.05 T. a) Simulated and b) experimental with an MAS rate of 10 kHz. The NMR parameters obtained from the simulation are summarized in Table 4.5.

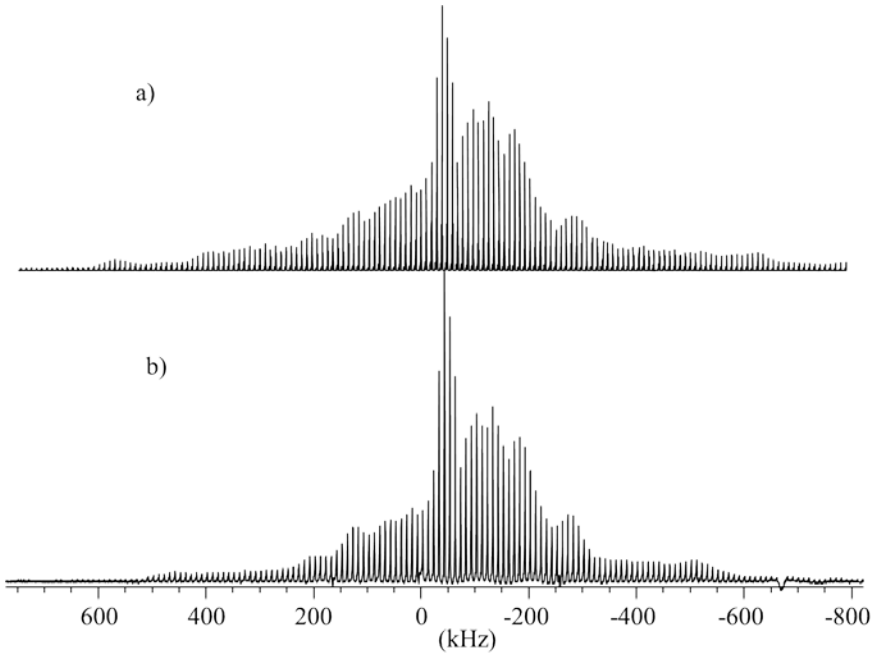

Figure 4.29. ^{51}V NMR spectra of $K_3[VO(O_2)_2(C_2O_4)]\cdot 1H_2O$ acquired at 11.75 T. a) Simulated and b) experimental with an MAS rate of 10 kHz. The NMR parameters obtained from the simulation are summarized in Table 4.5.

V) Tripotassium bis(oxalato) dioxovanadate(V) Trihydrate, $K_3[V(O_2)(C_2O_4)_2]\cdot 3H_2O$

The potassium salt $K_3[V(O_2)(C_2O_4)_2]\cdot 3H_2O$ crystallizes in a triclinic lattice with space group P*I*. The $[V(O_2)(C_2O_4)_2]^{3-}$ anion as shown in Figure 4.30 shows a slightly irregular octahedral geometry in which the two OXO ligands are cis to each other. The two OXO oxygen atoms have short V-O bonds (1.628 and 1.639 Å) compared to the other four metal-oxygen bonds. The oxalate groups all contain planar CO_2 fragments which are twisted about the C-C bond so that the ligand as a whole is not planar. There is no local symmetry at the vanadium site.

Figures 4.31, and 4.32 show the experimental NMR spectra for $K_3[V(O_2)(C_2O_4)_2]\cdot 3H_2O$ acquired at several MAS spinning frequencies, from which the isotropic chemical shift, δ_{iso} = -622 ± 3 ppm, value is obtained. A value for C_Q of 4.2 ± 0.3 MHz was determined from the overall breadth of the spectra, which exceed 1.0 MHz. The parameters were obtained from simulations using WSOLIDS. These values were confirmed by simulating the full spinning side band envelope including the satellite transitions. To verify that the NMR parameters are reasonable SIMPSON calculations were undertaken. The experimental and the best-fit simulated spectra are in good agreement, as illustrated in Figures 4.33 and 4.34. The results are summarized in Table 4.6.

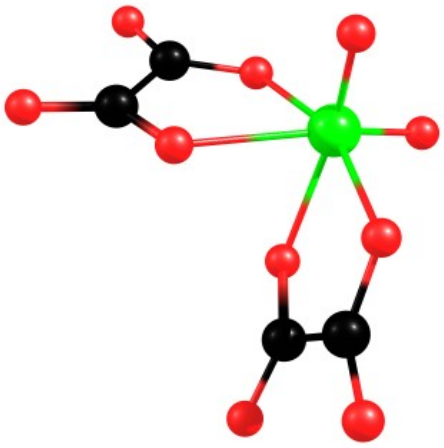

Figure 4.30. Molecular structure of, $[V(O_2)(C_2O_4)_2]^{-3}$.

Table 4.6. Experimental Solid-State NMR Parameters for $K_3[V(O_2)(C_2O_4)_2]\cdot 3H_2O$.

C_Q (MHz)	4.2 ± 0.3	δ_{iso} (ppm)	-622 ± 3	α (°)	10 ± 5
η_Q	0.35 ± 0.05	Ω (ppm)	1110 ± 20	β (°)	80 ± 5
		κ	0.52 ± 0.05	γ (°)	0.0

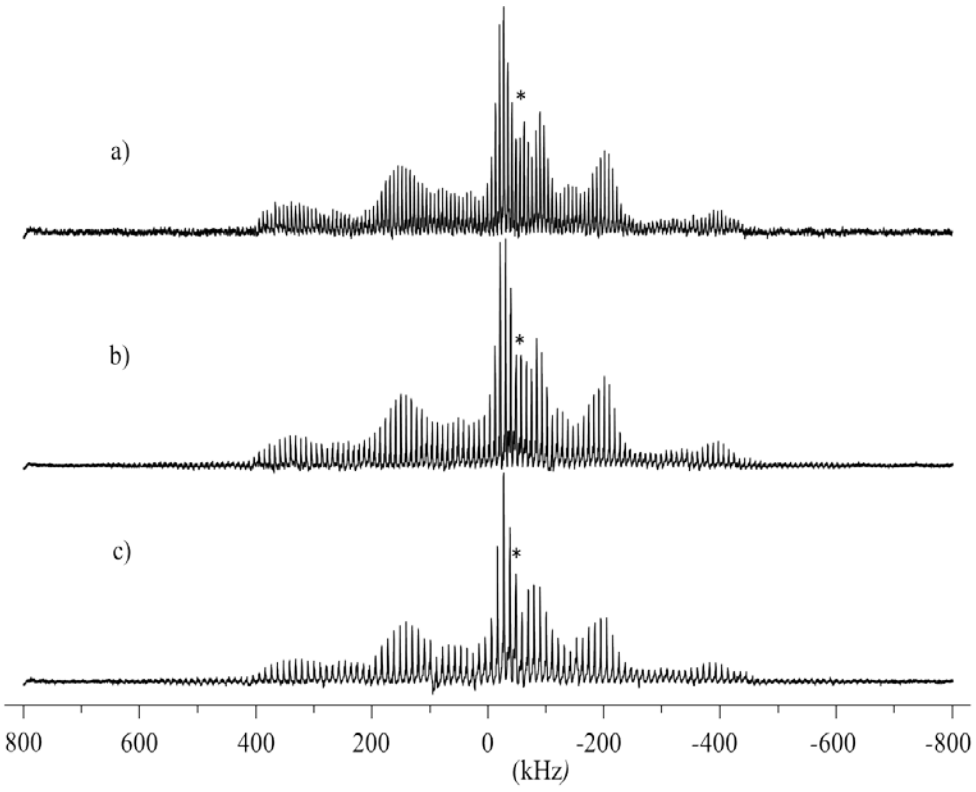

Figure 4.31. ^{51}V NMR spectra of $K_3[V(O)_2(C_2O_4)_2]\cdot 3H_2O$ acquired at 7.05 T with MAS rates of a) 7 kHz, b) 9 kHz and c) 10 kHz. Each spectrum is the sum of 4000 scans.

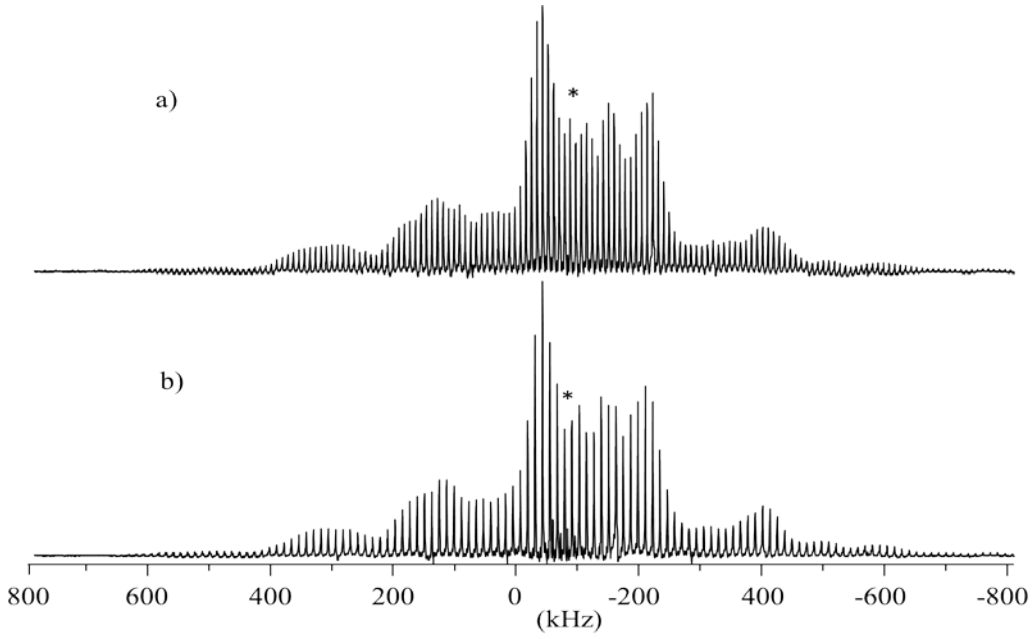

Figure 4.32. ^{51}V NMR spectra of $K_3[V(O)_2(C_2O_4)_2]\cdot 3H_2O$ acquired at 11.75 T with MAS rates of a) 9 kHz and b) 12 kHz. Each spectrum is the sum of 4000 scans.

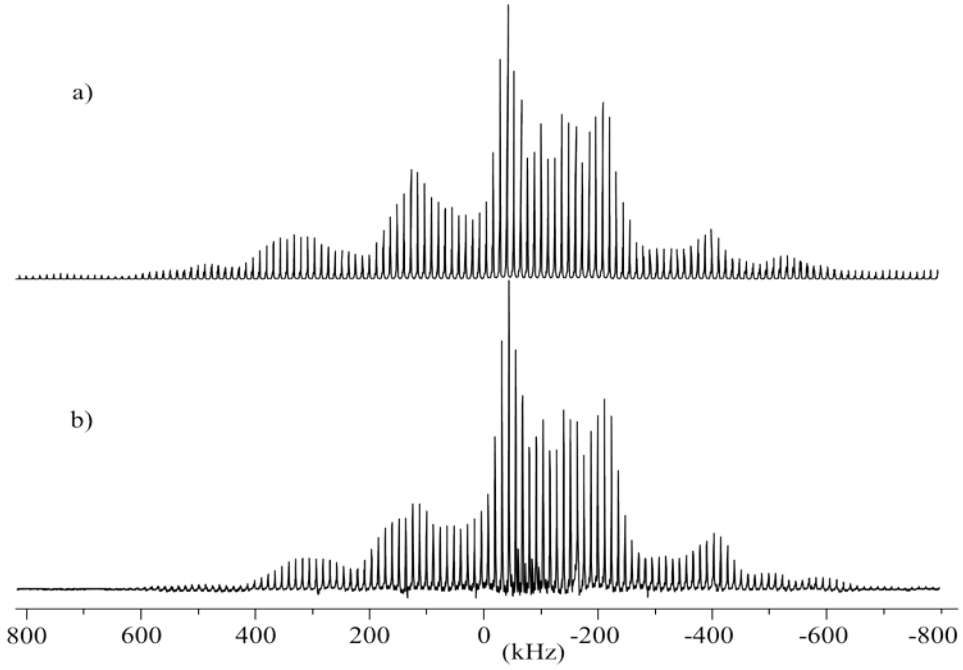

Figure 4.33. Vanadium-51 NMR spectra of $K_3[V(O)_2(C_2O_4)_2]\cdot 3H_2O$ acquired at 11.75 T. a) Simulated and b) experimental with MAS rates 10 kHz. The NMR parameters obtained from the simulation are summarized in Table 4.6.

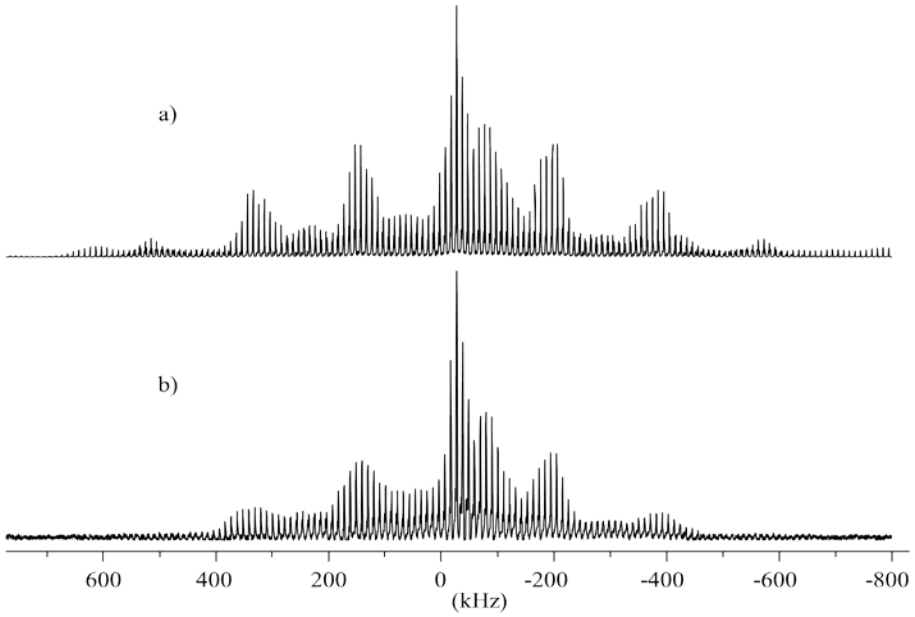

Figure 4.34. Vanadium-51 NMR spectra of $K_3[V(O)_2(C_2O_4)_2]\cdot 3H_2O$ acquired at 7.05 T. a) Simulated and b) experimental with MAS rates 10 kHz. The NMR parameters obtained from the simulation are summarized in Table 4.6.

4.3.2. Theoretical Results

4.3.2.1. Comparison of Calculated NMR Parameters with Experimental Values for $(C_5H_5)V(CO)_4$

$(C_5H_5)V(CO)_4$ does not belong to oxo- and peroxo-vanadium compounds. Analysis shows the $\eta_Q = 0$ and $\kappa = 1$ which indicates that the EFG and CS tensors are axially symmetric and that δ_{33} is the unique component of the CS tensor and thus is coincident with V_{zz}.

The crystal structure obtained by Wilford *et al.*, was used to calculate the magnetic shielding and the EFG tensors at the vanadium nucleus. The results are presented in Table 4.9. Our results for the DFT calculations using the B3LYP functional employing various basis sets and experimental values for δ_{iso}, Ω, κ, C_Q

, and η_Q, shown in Figure 4.35, demonstrate that the best overall agreement for the B3LYP functional with experimental data was found for the basis sets 6-31+G(df,2pd) and 6-311++G(d,p). The calculated shielding tensors exhibit spans ranging from 298 ppm (B3YLP/6-31+G(df,2pd)) to 344 ppm (CASTEP) and complement the experimental observation. All calculations predict a skew in range of 0.8-1.0 for the vanadium shielding tensor, compare d to the experimental value of 1.00. The calculated quadrupolar coupling constant reported here (Table 4.9) ranges from -3.5MHz (ADF/QZ4P) to -3.91 MHz (B3YLP/6-31+G(df,2pd)) and are all in reasonable accord with the experimental value of 3.0 ± 0.05 MHz. The calculated asymmetry parameter at the B3LYP level of theory is 0.18 while the ADF/QZ4P and CASTEP predict a value of zero in agreement with experiment. In all cases, the calculated η_Q values indicate an EFG tensor of axial or near axial symmetry. For δ_{iso}, and Ω, the results obtained with B3LYP/6-311++G(d,p) and ADF/QZ4P yielded the better agreement with experimental values.

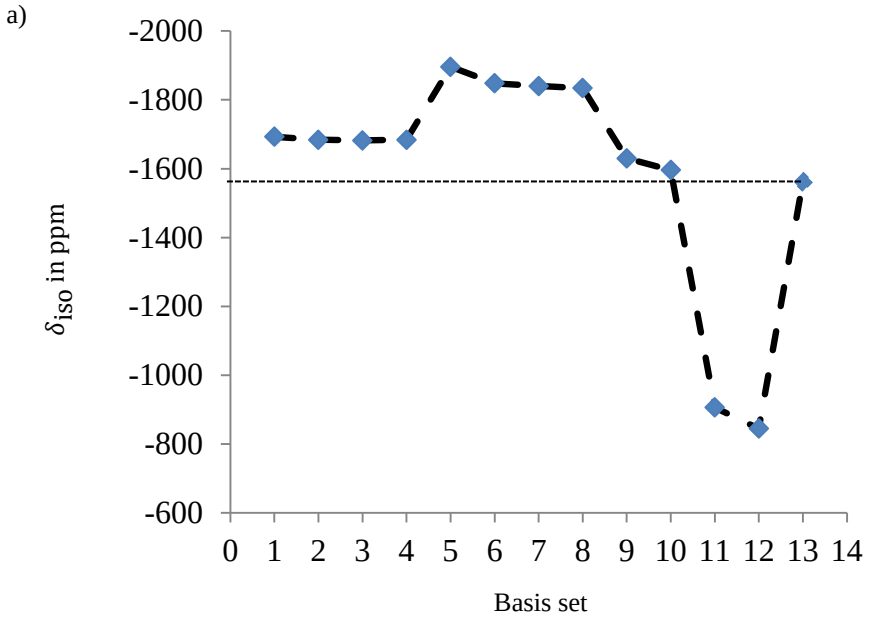

b)

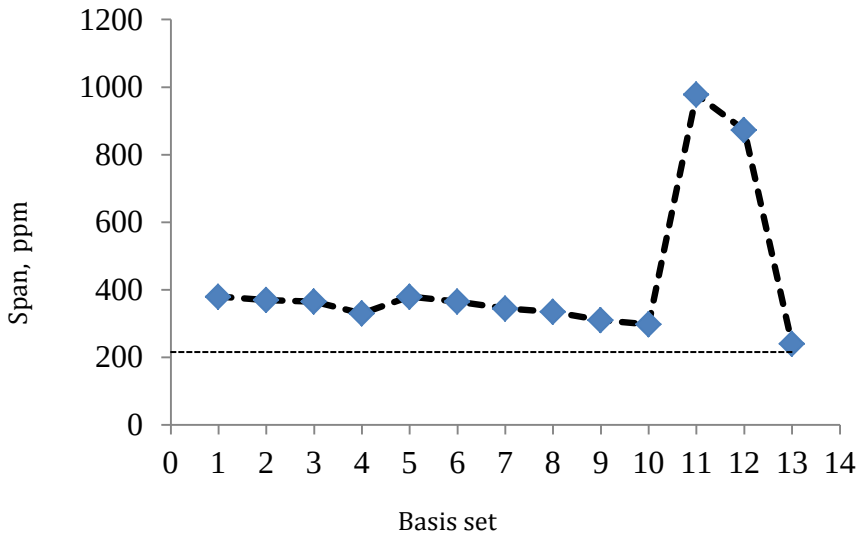
1200
1000
800
600
400
200
0
Span, ppm
0 1 2 3 4 5 6 7 8 9 10 11 12 13 14
Basis set

c)

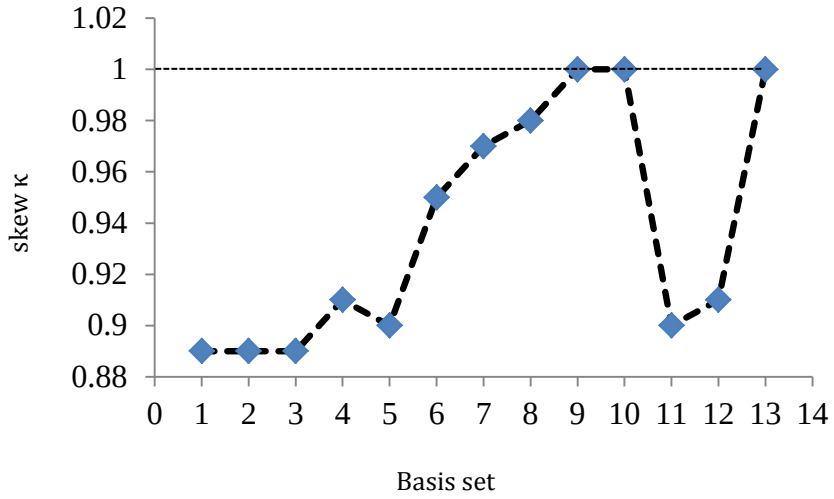
1.02
1
0.98
0.96
0.94
0.92
0.9
0.88
skew κ
0 1 2 3 4 5 6 7 8 9 10 11 12 13 14
Basis set

d)

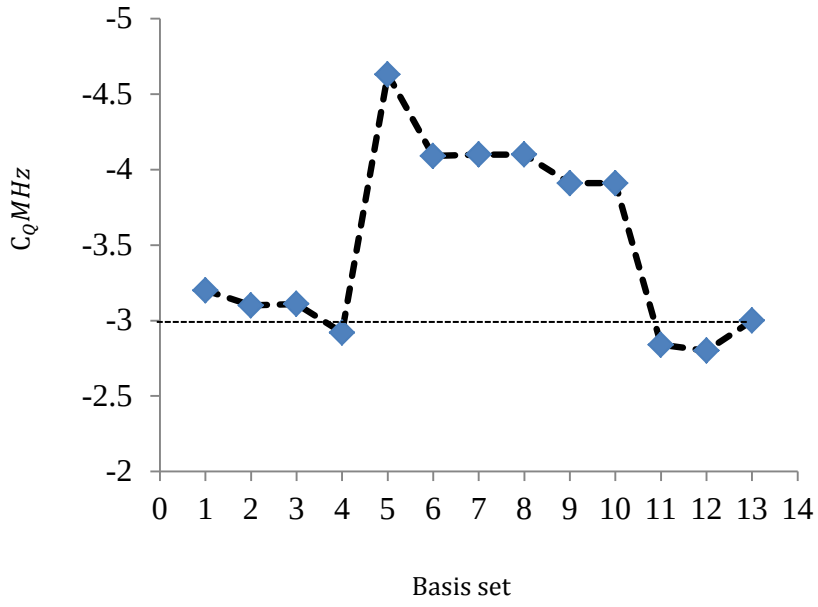
-5
-4.5
-4
-3.5
-3
-2.5
-2
$C_Q MHz$
0 1 2 3 4 5 6 7 8 9 10 11 12 13 14
Basis set

e)

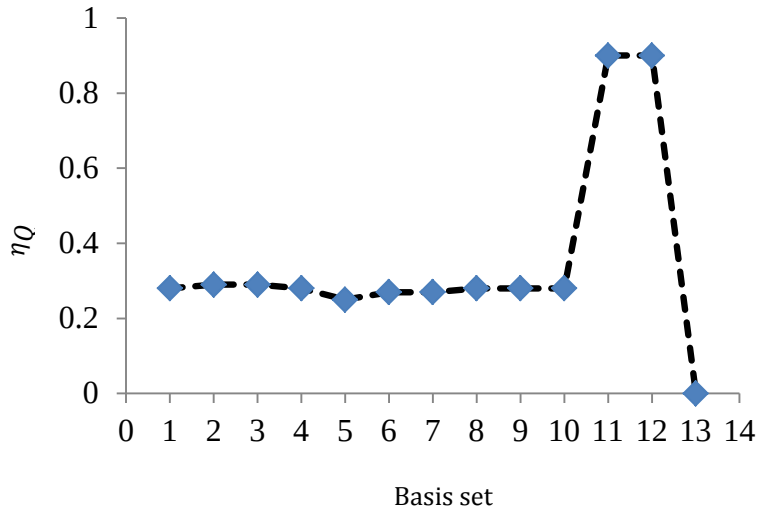

Figure 4.35. a) Isotropic chemical shift, b) span, c) skew, d) quadrupolar coupling constant and e) asymmetry of the EFG tensor for $(C_5H_5)V(CO)_4$, calculated with different basis sets; see Table 4.7 for a definition of the basis sets.

Table 4.7. Basis sets

1	6-31G	8	6-311+G(d)
2	6-31G(d)	9	6-311++G(d,p)
3	6-31G (d,p)	10	6-31+G(df,2pd)
4	6-31++G(d,p)	11	TZV
5	6-311G	12	TZVP
6	6-311G(d)	13	experimental value
7	6-311+G		

Overall results show that asymmetry parameter of the EFG and magnetic shielding tensors are close to the experimental values; however, for some basis sets, the calculated C_Q is much larger than the experimental value. In particular, best agreement with experimental quadrupolar parameters is seen for the CASTEP/DFT and ADF/DFT calculations employing the QZ4P basis sets. There are several factors which may account for the discrepancy between experimental and theoretical EFG tensor parameters, including the model used for the calculation and the basis set. Perhaps most significant is that calculations were performed on an isolated $(C_5H_5)V(CO)_4$ molecule, and thus do not take into account long-range electrostatic effects in the EFG tensor. In addition,

calculations are conducted upon a static molecule, thereby eliminating the possibility that the experimental values of C_Q and η_Q are average EFG tensor parameters. The orientation of the tensors in the molecular frame has also been obtained from the calculations. However; given the errors in the EFG parameter the reliability of the EFG orientation obtained from the calculations might appear questionable. On the other hand, for this particular example the axial symmetry of the magnetic shielding is required from the known structure, so the orientation of the tensor is also qualitatively correct.

4.3.2.2. Calculated NMR Parameters for Compounds II)-V) Using Different Models and Basis Sets.

In this study, the Gaussian03, ADF and CASTEP program packages were used to perform DFT calculations of EFG and nuclear magnetic shielding tensors on compounds

II) $[V(O)(ONMe_2)_2]_2O$

III) $[NH_4]\,[V(O)(O_2)_2(NH_3)]$

IV) $K_3[VO(O_2)_2(C_2O_4)]\cdot 1H_2O$

V) $K_3[V(O_2)\,(C_2O_4)_2]\cdot 3H_2O$

whose crystal structures have been previously determined.[44,47,101,104] The bond lengths and bond angles obtained in these studies (experimental geometries) were used in all quantum mechanical calculations.

Gaussian03 Calculations: DFT calculations were carried out on **II) - V)** to compare the performance of a common functional (B3LYP), employing Pople's and Ahlrichs basis sets, with polarization and diffuse functions. The complete compilation of the computed NMR parameters for each compound at each level of theory is given in Tables 4.10-4.13. Figure 4.36 compares the calculated and experimental δ_{iso}, Ω, and κ values for compounds **II) - V)** employing B3LYP, with various basis sets. Experimental results are added for comparison (Table 4.8).

Table 4.8. Experimental Solid-State NMR Parameters for Vanadium Complexes.

Compound	C_Q/ MHz	η_Q	δ_{iso}/ppm	δ_{11}/ ppm	δ_{22}/ ppm	δ_{33}/ ppm	α/ deg	β/ deg	γ/ deg	Ω/ppm	κ
$[V(O)(ONMe_2)_2]_2O$	4.8 ± 0.1	0.68 ± 0.05	-714 ± 3	-75	-555	-1512	10 ± 10	76 ± 10	0	1437 ± 15	0.33 ± 0.05
$[V(O)(ONMe_2)_2]_2O$			-713	-91	-528	-1522				1431	0.38 ± 0.5
$[NH_4][VO(O_2)_2(NH_3)]$	7.0 ± 0.4	0.75 ± 0.05	-768 ± 5	-210	-534	-1560	0	10 ± 5	0	1350 ± 20	0.52 ± 0.05
$K_3[VO(O_2)_2(C_2O_4)]\cdot 1H_2O$	4.8 ± 0.2	0.9 ± 0.05	-708 ± 4	-148	-428	-1548	20 ± 10	75 ± 5	0	1400 ± 15	0.60 ± 0.05
Ref	4.8 ± 0.5	0.9 ± 0.1	-704 ± 5	-175	-313	-1624				1449 ± 30	0.75 ± 0.10
$K_3[VO(O_2)(C_2O_4)_2]\cdot 3H_2O$	4.2 ± 0.3	0.35 ± 0.05	-622 ± 3	-178	-398	-1288	10 ± 5	80 ± 5	0	1110 ± 20	0.52 ± 0.05
$(C_5H_5)V(CO)_4$	3.0 ± 0.05	0.0	-1562 ±2	-1482	-1482	-1722	0	0	0	240 ± 40	+1.00

Table 4.9. Calculated ^{51}V NMR Parameters for **$(C_5H_5)V(CO)_4$**.

Program/Method	Basis set	C_Q/MHz	η_Q	δ_{iso}/ppm	δ_{11}/ppm	δ_{22}/ppm	δ_{33}/ppm	Ω/ppm	κ	α/deg	β/deg	γ/deg
Gaussian/B3LYP	6-31G	-3.20	0.28	-1693	-1562	-1583	-1932	380	0.89	4	0	1
Gaussian/B3LYP	6-31G(d)	-3.10	0.29	-1684	-1553	-1574	-1923	370	0.89	4	0	1
Gaussian/B3LYP	6-31G(d,p)	-3.11	0.29	-1682	-1553	-1573	-1918	365	0.89	4	0	1
Gaussian/B3LYP	6-31++G(d,p)	-2.92	0.28	-1684	-1569	-1583	-1899	330	0.91	4	0	1
Gaussian/B3LYP	6-311G	-4.63	0.25	-1896	-1762	-1762	-2142	380	0.90	4	0	1
Gaussian/B3LYP	6-311G(d)	-4.09	0.27	-1848	-1720	-1738	-2085	365	0.95	4	0	1
Gaussian/B3LYP	6-311+G	-4.20	0.27	-1840	-1727	-1744	-2072	345	0.97	4	0	1
Gaussian/B3LYP	6-311+G(d)	-4.20	0.28	-1834	-1716	-1733	-2051	335	0.98	4	0	1
Gaussian/B3LYP	6311++G(d,p)	-3.91	0.28	-1630	-1532	-1533	-1833	310	0.99	4	0	1
Gaussian/B3LYP	631+G(df,2pd)	-3.91	0.28	-1596	-1494	-1495	-1792	298	0.99	4	0	1
Gaussian/B3LYP	TZV	-2.84	0.90	-906	-563	-612	-1541	978	0.90	4	0	1
Gaussian/B3LYP	TZVP	-2.80	0.90	-845	-540	-580	-1413	873	0.91	4	0	1
ADF/ZORA	QZ4P	-3.51	0.05	-1568	-1468	-1468	-1768	300	1.00	4	0	1
CASTEP		-3.65	0.04	-1944	-1829	-1829	-2173	344	1.00	4	0	0

Table 4.10. Calculated ^{51}V NMR Parameters for **$[V(O)(ONMe_2)_2]_2O$**.

Program/Method	Basis set	C_Q/MHz	η_Q	δ_{iso}/ppm	δ_{11}/ppm	δ_{22}/ppm	δ_{33}/ppm	Ω/ppm	κ	α/deg	β/deg	γ/deg
Gaussian/B3LYP	6-31G	-4.90	0.51	-802	-137	-631	-1636	1499	0.34	8	88	1
Gaussian/B3LYP	6-31G(d)	-4.27	0.55	-766	-93	-611	-1592	1499	0.31	12	87	1
Gaussian/B3LYP	6-31G(d,p)	-4.27	0.55	-766	-94	-611	-1591	1498	0.31	12	87	1
Gaussian/B3LYP	6-31++G(d,p)	-4.56	0.58	-788	-134	-637	-1591	1457	0.31	10	88	1
Gaussian/B3LYP	6-311G	-5.90	0.67	-910	-181	-742	-1806	1625	0.31	11	88	1
Gaussian/B3LYP	6-311G(d)	-5.73	0.74	-861	-132	-705	-1745	1613	0.29	8	88	1
Gaussian/B3LYP	6-311+G	-5.61	0.74	-873	-163	-723	-1763	1600	0.30	12	88	1
Gaussian/B3LYP	6-311+G(d)	-5.48	0.78	-823	-129	-685	-1720	1591	0.27	9	88	1
Gaussian/B3LYP	6311++G(d,p)	-5.27	0.77	-712	-75	-550	-1510	1435	0.33	9	88	0
Gaussian/B3LYP	631+G(df,2pd)	-5.25	0.66	-711	-73	-550	-1512	1439	0.33	9	88	0
Gaussian/B3LYP	TZV	-5.50	0.69	-1093	-385	-929	-1963	1578	0.31	12	89	1
Gaussian/B3LYP	TZVP	-6.00	0.57	-877	-166	-713	-1751	1585	0.31	10	88	1
ADF/ZORA	QZ4P	-5.10	0.78	-780	-160	-681	-1498	1338	0.22	5	88	1
CASTEP		-5.01	0.71	-583	-70	-464	-1354	1425	0.25	10	87	0

Table 4.11. Calculated ^{51}V NMR Parameters for **$[NH_4][VO(O_2)_2(NH_3)]$**.

Program/Method	Basis set	C_Q/MHz	η_Q	δ_{iso}/ppm	δ_{11}/ppm	δ_{22}/ppm	δ_{33}/ppm	Ω/ppm	κ	α/deg	β/deg	γ/deg
Gaussian/B3LYP	6-31G	-6.90	0.56	-630	74	-248	-1715	1790	0.64	0	11	0
Gaussian/B3LYP	6-31G(d)	-7.44	0.60	-607	83	-232	-1671	1755	0.64	0	9	0
Gaussian/B3LYP	6-31G(d,p)	-7.44	0.62	-607	-100	-390	-1792	1675	0.64	0	9	0
Gaussian/B3LYP	6-31++G(d,p)	-7.49	0.78	-766	-105	-400	-1792	1678	0.65	0	12	0
Gaussian/B3LYP	6-311G	-8.5	0.4	-714	-100	-390	-1178	1678	0.60	0	5.5	0
Gaussian/B3LYP	6-311G(d)	-8.34	0.41	-719	-79	-82	-1637	1558	0.61	0	6	0
Gaussian/B3LYP	6-311+G	-8.15	0.44	-750	-130	-440	-1680	1550	0.60	0	6	0
Gaussian/B3LYP	6-311+G(d)	-7.90	0.61	-673	-205	-489	-1555	1350	0.58	0	7	0
Gaussian/B3LYP	6311++G(d,p)	-7.87	0.69	-760	-204	-525	-1549	1345	0.52	0	10	0
Gaussian/B3LYP	631+G(df,2pd)	-7.63	0.75	-768	-210	-534	1350	1350	0.52	0	11	0
Gaussian/B3LYP	TZV	-8.70	0.49	-892	-126	-493	-2055	1929	0.60	0	4	0
Gaussian/B3LYP	TZVP	-8.31	0.71	-675	87	-285	-1826	1914	0.61	0	6	0
ADF/ZORA	QZ4P	-7.60	0.84	-760	-202	-526	-1552	1350	0.50	0	4	0
CASTEP		-8.60	0.63	-664	-100	-260	-1632	`1532	0.69	0	8	0

Table 4.12. Calculated ^{51}V NMR Parameters for **$K_3[VO(O_2)_2(C_2O_4)]\cdot 1H_2O$**.

Program/Method	Basis set	C_Q/MHz	η_Q	δ_{iso}/ppm	δ_{11}/ppm	δ_{22}/ppm	δ_{33}/ppm	Ω/ppm	κ	α/deg	β/deg	γ/deg
Gaussian/B3LYP	6-31G	-5.30	0.67	-760	-182	-370	-1727	1545	0.756	18	85	1
Gaussian/B3LYP	6-31G(d)	-5.25	0.68	-686	-109	-297	-1651	1542	0.75	19	85	1
Gaussian/B3LYP	6-31G(d,p)	-5.25	0.68	-688	-111	-299	-1652	1541	0.75	19	85	1
Gaussian/B3LYP	6-31++G(d,p)	-5.00	0.76	-717	-182	-348	-1619	1437	0.77	18	85	1
Gaussian/B3LYP	6-311G	-5.60	0.77	-874	-264	-481	-1876	1611	0.73	19	85	1
Gaussian/B3LYP	6-311G(d)	-5.40	0.76	-834	-197	-559	-1745	1548	0.532	19	85	1
Gaussian/B3LYP	6-311+G	-5.00	0.82	-792	-183	-529	-1663	1480	0.532	20	85	1
Gaussian/B3LYP	6-311+G(d)	-5.00	0.86	-718	-146	-465	-1540	1400	0.55	20	85	1
Gaussian/B3LYP	6311++G(d,p)	-4.90	0.88	-718	-146	-461	-1546	1400	0.55	20	70	2
Gaussian/B3LYP	631+G(df,2pd)	-4.90	0.88	-718	-149	-457	-1547	1398	0.56	20	70	2
Gaussian/B3LYP	TZV	-5.16	0.37	-962	-109	-766	-2010	1901	0.309	35	85	1
Gaussian/B3LYP	TZVP	-5.06	0.44	-784	-218	-351	-1782	1564	0.83	25	90	1
ADF/ZORA	QZ4P	-4.8	0.90	-710	-223	-491	-1415	1192	0.55	10	75	1
CASTEP		-4.63	0.76	-678	-114	-335	-1583	1469	0.70	13	88	2

Table 4.13. Calculated ^{51}V NMR Parameters for **$K_3[V(O_2)(C_2O_4)_2]\cdot 3H_2O$**.

Program/Method	Basis set	C_Q/MHz	η_Q	δ_{iso}/ppm	δ_{11}/ppm	δ_{22}/ppm	δ_{33}/ppm	Ω/ppm	κ	α/deg	β/deg	γ/deg
Gaussian/B3LYP	6-31G	5.71	0.25	-710	-191	-517	-1421	1230	0.47	9	76	0
Gaussian/B3LYP	6-31G(d)	5.42	0.20	-680	-177	-474	-1387	1210	0.51	9	77	0
Gaussian/B3LYP	6-31G(d,p)	5.42	0.20	-680	-176	-475	-1387	1210	0.51	9	77	0
Gaussian/B3LYP	6-31++G(d,p)	5.01	0.28	-660	-162	-456	-1362	1200	0.51	9	77	0
Gaussian/B3LYP	6-311G	5.90	0.39	-720	-172	-495	-1492	1320	0.51	9	77	0
Gaussian/B3LYP	6-311G(d)	5.72	0.35	-700	-195	-478	-1425	1230	0.54	9	78	0
Gaussian/B3LYP	6-311+G	5.65	0.41	-636	-94	-419	-1394	1300	0.50	9	78	0
Gaussian/B3LYP	6-311+G(d)	5.32	0.34	-615	-118	-397	-1328	1210	0.54	9	78	0
Gaussian/B3LYP	6311++G(d,p)	5.33	0.34	-703	-206	-485	-1416	1210	0.54	9	78	0
Gaussian/B3LYP	631+G(df,2pd)	5.22	0.34	-620	-119	-410	-1329	1200	0.52	10	78	0
Gaussian/B3LYP	TZV	6.15	0.34	-832	-231	-603	-1661	1430	0.48	10	80	0
Gaussian/B3LYP	TZVP	6.70	0.26	-612	-74	-386	-1374	1300	0.52	10	80	0
ADF/ZORA	QZ4P	5.20	0.35	-640	-216	-437	-1266	1050	0.58	9	79	0
CASTEP												

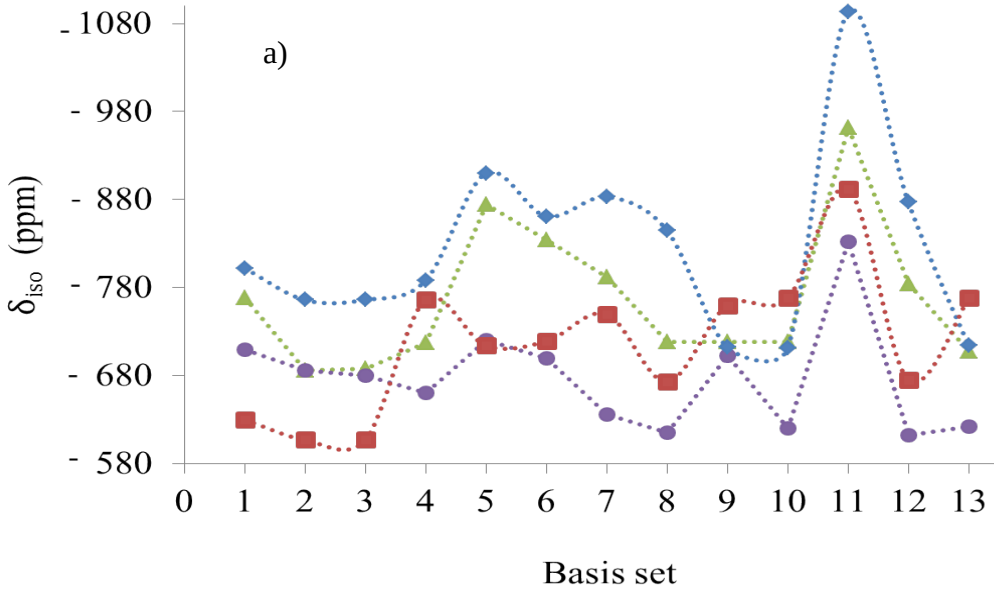
a)
- 1080
- 980
- 880
- 780
- 680
- 580
δiso (ppm)
0 1 2 3 4 5 6 7 8 9 10 11 12 13
Basis set

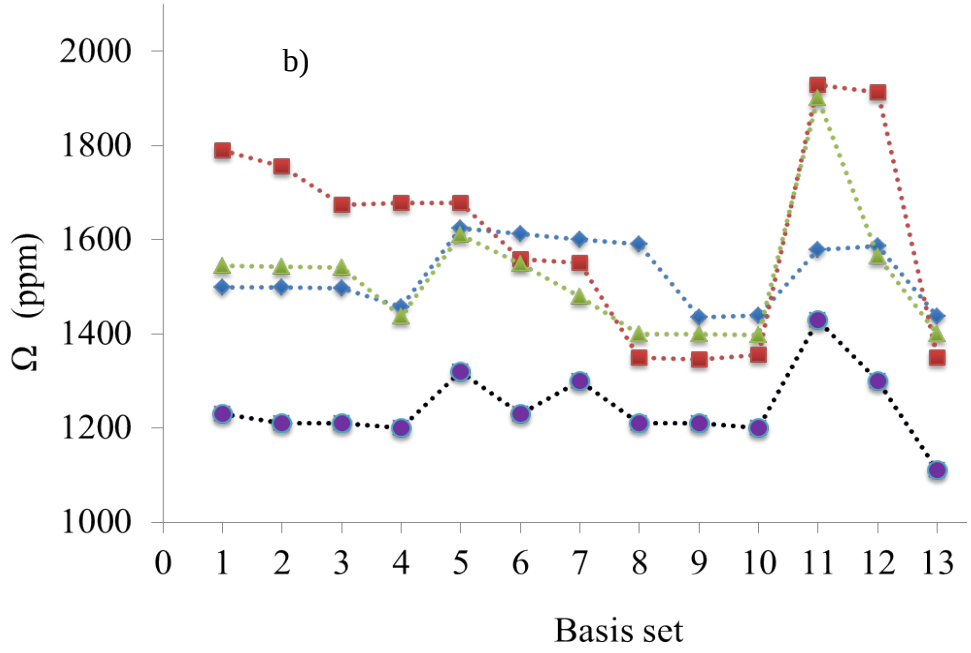
b)
2000
1800
1600
1400
1200
1000
Ω (ppm)
0 1 2 3 4 5 6 7 8 9 10 11 12 13
Basis set

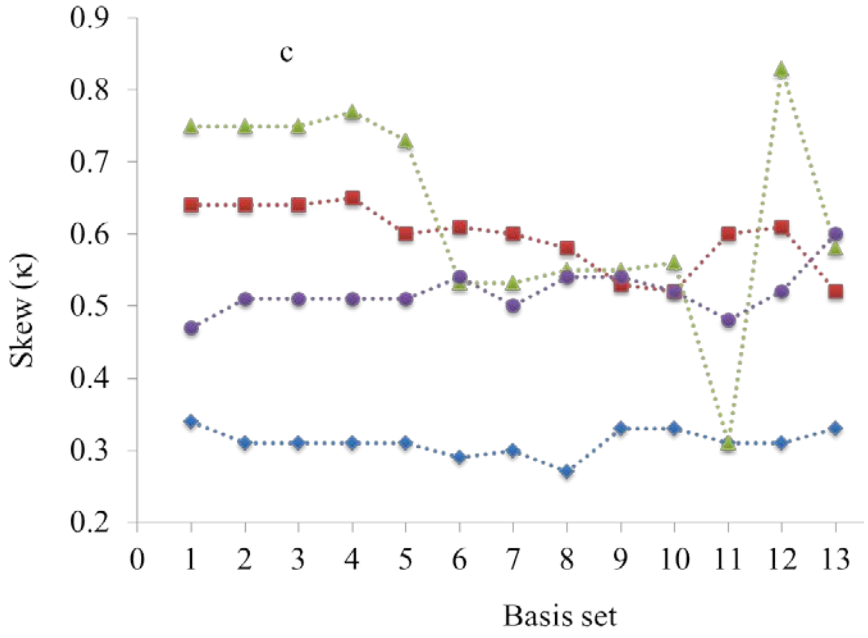

Figure 4.36. a) Isotropic chemical shift, b) span, and c) skew of II) ♦, III) ■, IV) ▲, V) ● referenced to $VOCl_3$ calculated with the same basis sets as applied here. (X-axis scale defined in Table 4.7).

In all these complexes the formal oxidation state of vanadium is +5, therefore the vanadium has no *d*-valence electrons. Furthermore the addition of *d*-polarization functions and diffuse functions (+) leads to better results for δ_{iso}. For a better description of calculated parameters, *f*-polarization functions were used which shows a small improvement to the results. Similar results were obtained for the Ω and κ, (Figure 4.36(b) and (c)).

Figure 4.37 compares the calculated and experimental C_Q and η_Q values for compounds **II)-V)** employing the B3LYPhybrid function with various basis sets. In most cases the triple-ζ basis sets of Pople leads to overestimated C_Q values, while the double-ζ basis sets with polarization and diffuse functions lead to good agreement with the experimental data.

The orientation of the CS and EFG tensors, in the molecular reference were also determined from the DFT calculations and visualized using the EFGShield[106] program. The results are summarized in Tables 4.10 - 4.13. It

should be noted that the computed Euler angles for all compounds here are nearly independent of the basis sets employed for the computation, with angles varying only in the range of 5 to 15° between basis sets. The largest deviation of the β angles belongs to compounds III and IV.

Summarizing calculations using B3LYP function indicates that the best overall agreement between theoretical and experimental data was found for the basis sets 6-31+G(df,2pd) and 6-311++G(d,p). This conclusion is consistent with the best overall basis sets reported in literature[8,10] for similar vanadium compounds.

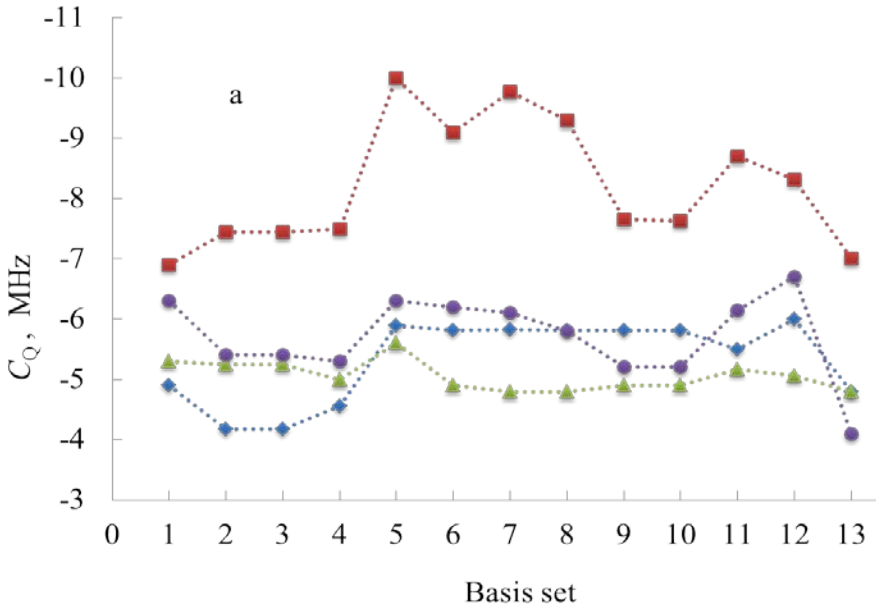

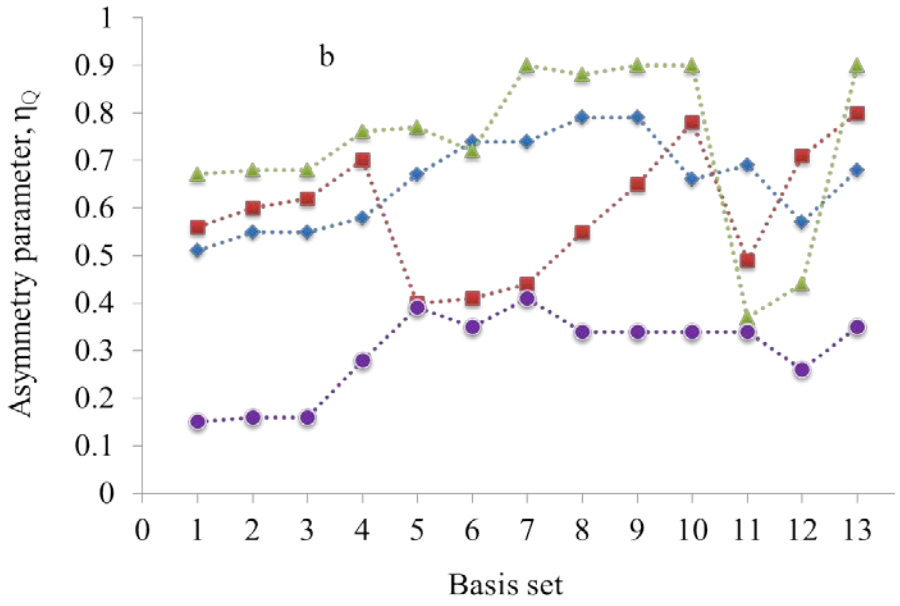

Figure 4.37. a) Calculated C_Q (MHz) and b) asymmetry of the EFG tensor for II) ♦, III) ■, IV) ▲, V) ● referenced to $VOCl_3$ calculated with the same basis sets as applied here, (X-axis scale defined in Table 4.7).

ADF: Electric field gradient and nuclear magnetic shielding calculations were performed on vanadium compounds **II) - V)**, using the QZ4P basis set, optimized for ZORA calculations for the vanadium atoms, triple-zeta doubly polarized (TZ2P) basis sets for O, N, and double-zeta singly polarized (DZP) basis sets for C and H. The calculations provide both the principal components of the two tensors and their orientations in the molecular frame. A program called Trafo, part of the WSOLIDS package,was used to determine the Euler angles from the ADF output. The computational results, summarized in Tables 4.10-4.13, show an excellent agreement with the experimental solid-state NMR data.

CASTEP: DFT calculations of the ^{51}V EFG and CS tensors on vanadium compounds **II) -IV)** were also carried out using CASTEP. The results of these calculations are presented in Tables 4.10-4.12. For compounds **II)** and **III)** the

full geometry optimization was performed. For compound **IV)** hydrogen positions were "normalized" but the full geometry optimization was not performed due to the large unit cell. The CASTEP results in two cases reveal a slightly improved agreement with experimental values compared to ADF and Gaussian03 calculation results.

4.3.2.3. Comparison of Calculated NMR Parameters with Experimental Values for Vanadium Compounds II)-V)

As discussed above, Gaussian03 calculations of NMR parameters using 6-31+G(df,2pd) and 6-311++G(d,p) basis sets show the best agreement with experimental values. Figure 4.38 illustrates the correlations between the experimental and calculated C_Q and η_Q values for the DFT calculations of vanadium coordination complexes using ZORA/QZ4P, Gaussian 6-31+G (df,2pd) and 6-311++G(d,p), and CASTEP. The ideal $y = x$ line is illustrated in Figure 4.38 as well as the best fit lines. This figure illustrates the good agreement between the calculated and experimental C_Q and η_Q (see Tables 4.14 and 4.15).

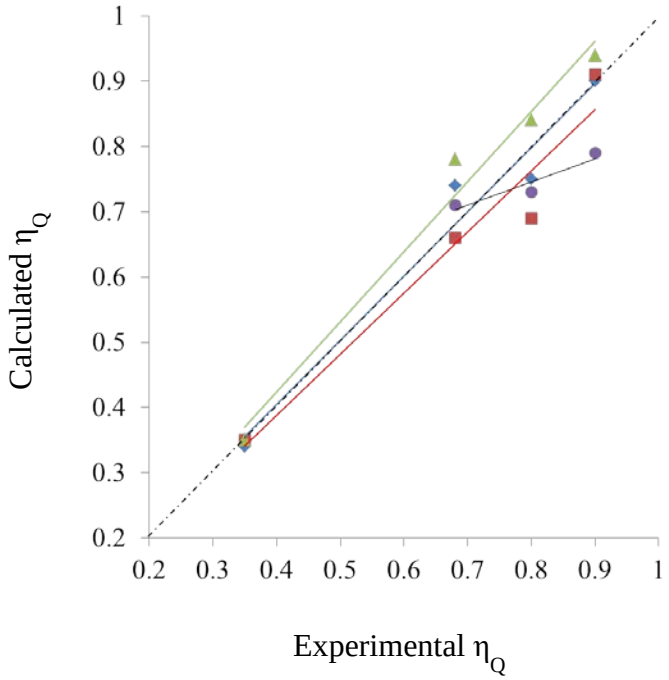

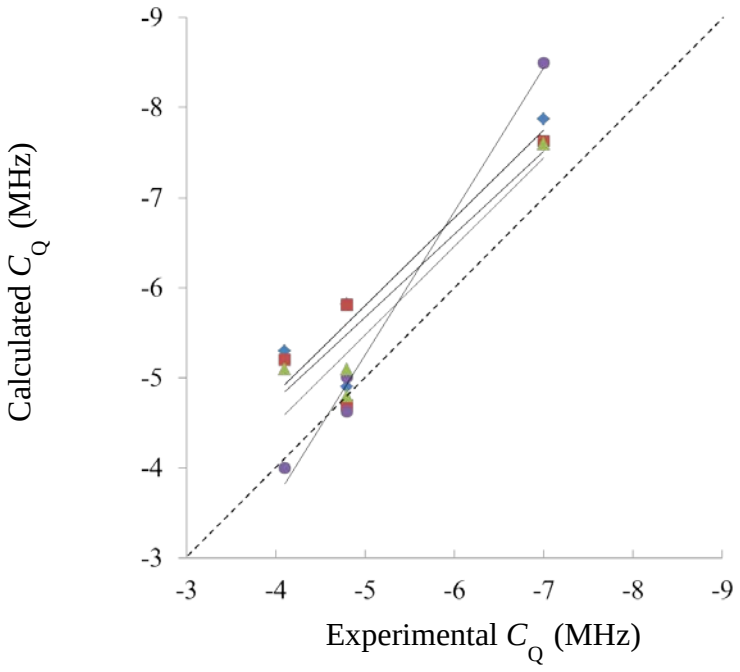

Figure 4.38. Comparison of experimental and calculated C_Q and η_Q values for the vanadium(V) complexes under investigation computed using different computation packages. The dotted line represents ideal agreement between calculated and experimental values, the solid line is the best fit. Different symbols represent different DFT methods used: ♦ represents B3LYP/631+G(df,2pd), ■ represents B3LYP/6-311++G(d,p), ▲represents BP-GGA ZORA/QZ4P, and ● represents PBE/CASTEP results.

Table 4.14. Comparison of Calculated and Experimental Results, for C_Q.

Function/Basis set	slope	intercept	R^2
BP-GGA/QZ4P	0.98	0.57	0.89
B3LYP/6-31+G(df,2pd)	0.97	0.93	0.86
B3LYP/6-311++G(d,p)	0.92	1.06	0.82
PBE/CASTEP	1.67	3.20	0.99

Table 4.15. Comparison of Calculated and Experimental Results, for η_Q.

Basis set	slope	intercept	R^2
ZORA/QZ4P	1.07	0.0	0.97
Gaussian/6-31+G(df,2pd)	0.97	0.01	0.96
Gaussian/6-311++G(d,p)	0.93	0.01	0.94
CASTEP	0.35	4.6	0.89

The graph shown in Figure 4.39 illustrates the correlation between the experimental and the calculated principal components of the chemical shift tensors.

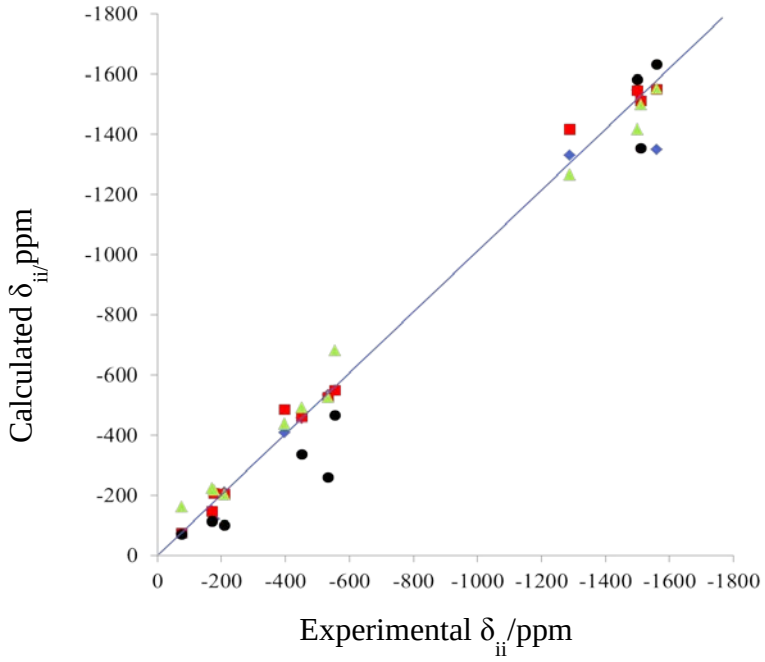

Figure 4.39. Comparison of experimental and calculated principal components of the chemical shift tensors for the vanadium(V) complexes under investigation computed using different computation packages. The dotted line represents ideal agreement between calculated and experimental values, the solid line is the best fit. Different symbols represent different DFT methods used: ♦ represents B3LYP/6-31+G(df,2pd), ■ represents B3LYP/6-311++G(d,p), ▲ represents BP-GGA ZORA/QZ4P, and ● represent PBE/CASTEP results.

Table 4.16. Comparison of Calculated and Experimental Results for Chemical Shift Components.

Basis set	slope	intercept	R^2
ZORA/QZ4P	0.93	0.63	0.99
Gaussian/6-31+G(df, 2pd)	0.97	1.08	0.98
Gaussian/6-311++G(d, p)	1.02	6.20	0.99
CASTEP	1.06	1.19	0.97

These results show a strong correlation between the experimental and computed chemical shift tensors for all computational models/basis sets employed here (see Table 4.16).

According to experimental results, the magnitude of C_Q, varies from 4.2 to 7.0 MHz and η_Q ranges from 0.35 to 0.9 for the oxo- and peroxo-vanadium complexes under investigation. These variations are caused both by the nature of the coordination environment and by the differences in geometry. The results of the simulations also indicate that varying the substituent on the ligand has a significant effect on the CS; δ_{iso} varies from -622 to -768 ppm, Ω ranges from 1110 to 1437 ppm and finally κ ranges from 0.3 to 0.6. This difference can be explained by the different three-dimensional geometry of the complexes, together with the anisotropy introduced by the electronic structure of the V=O groups. While oxo-diperoxo complexes have distorted pentagonal pyramid coordination about the vanadium atoms, the di-oxo complex shows distorted octahedral coordination geometry. Therefore the charge distribution at the vanadium in the di-oxo complex is closer to spherical symmetry than for the oxo-diperoxo complexes. The value for the chemical shift anisotropy is a measure of the distortion of the CS tensor from perfect spherical symmetry. That may explain why the di-oxo complex has a smaller chemical shift anisotropy than the oxo-diperoxo complexes.

The Euler angles have also been determined by simulations (Table 4.8). For these four vanadium complexes, β is quite well defined due to its influence on

the line shapes. According to the calculations, the relative orientations of δ_{33} and *V*zz range from 5 to 88˚ in the oxo-peroxo complexes. Thus, the CS and EFG tensors are noncoincident, confirming the experimental solid-state NMR conclusions (except for compound III). The α values range from 0 to 20˚ and have a smaller influence on the line shapes. There are some similarities between $[NH_4][V(O)(O_2)_2(NH_3)]$ and $K_3[VO(O_2)_2(C_2O_4)]\cdot 1H_2O$ probably because they both contain the $V(O)(O_2)_2$ group; results also confirm some similarities on the nature of the CS tensor.

Overall, the SSNMR data indicate that ligand substitution of the vanadium(V) coordinate complexes under current studies primarily affects the EFG and CS tensor at the vanadium site. The variations in the EFG tensors across the series are affected by combinations of factors. An important factor is the subtle structural changes caused by ligand substitution. The current results indicate that the EFG tensor is strongly influenced by the vanadium environment.

4.3.2.4. Calculated Contributions to the Magnetic Shielding

To properly understand the chemical shift tensor, one must examine the contributions of the individual molecular orbitals, MOs, to the magnetic shielding. According to Ramsey's[107] formalism, σ may be partitioned into diamagnetic and paramagnetic components (see section 2.1.4).

However, Ramsey's equations, as expressed in equation 2.26 and 2.27, are not employed by computational software for calculating CS parameters. For example the ADF software, which has been used extensively in the current study to calculate the magnetic shielding parameters, uses MOs that are generated from linear combinations of fragment orbitals (FOs)[108] to parameterize the electron density, according to Kohn and Sham,[109] which is then used to calculate the total electronic energy. Using the calculated energy, the total paramagnetic shielding contribution, σ^p, is decomposed into occupied-occupied and occupied-virtual MOs, and detailed contributions to paramagnetic shielding may be analysed

according to pair-wise MO mixing. A more detailed account of how the ADF software implements shielding calculations is provided in the literature.[110,111]

In the work reported by Widdifield and Schurko,[112] the ADF software was used to study the relationship between molecular symmetry and CS tensors. In this study, a number of specific examples are discussed, involving CS tensors of different nuclei in molecules of different symmetries. To verify that the computational strategy was properly implemented and thus to extend that strategy to the present work, the results of Widdifield and Schurko for ethylene, trifluorophosphine, and formaldehyde are reproduced as described in Appendix 4.2. These produced results in good agreement with those presented in the related literature.

4.3.2.4.1. Vanadium Shielding

In the next step, the magnitude and orientation of the principal components of the vanadium magnetic shielding tensor for the series VOX_3 (X = F, Cl, Br) were calculated using the same method and procedures which have been explained earlier in this section. VOF_3 has C_{3V} symmetry, therefore the CS tensor is axially symmetric and calculations show that σ_{33} is the unique component, along the V = O bond. In the following discussion σ_{11} is along the y axis and σ_{22} is along the x axis as shown for VOF_3 in Figure 4.40 (magnitude of CS tensor components are shown in Table 4.17). Note these are computational results; due to symmetry the perpendicular directions are all equal.

Table 4.17. Calculated Contributions to the Vanadium Magnetic Shielding[a] for VOF_3

Contribution	σ_{11} (ppm)	σ_{22} (ppm)	σ_{33} (ppm)	σ_{iso} (ppm)
σ^d(total)	1686	1686	1691	1687
σ^p(total)	-3104	-3104	-2523	-2910
σ (total)	-1418	-1418	-832	-1223

[a] QZ4P basis sets on all atoms.

As expected, the major contributions to diamagnetic vanadium shielding (Table 4.18) arise from MOs with *s* and *p* character of the three MOs (1, 5, 9).

Table 4.18. Significant Diamagnetic Contributions to Vanadium Magnetic Shielding for VOF_3

MO	σ_{11} (ppm)	σ_{22} (ppm)	σ_{33} (ppm)	σ_{iso} (ppm)
1	799	799	799	799
5	168	168	168	168
9	198	198	99	165

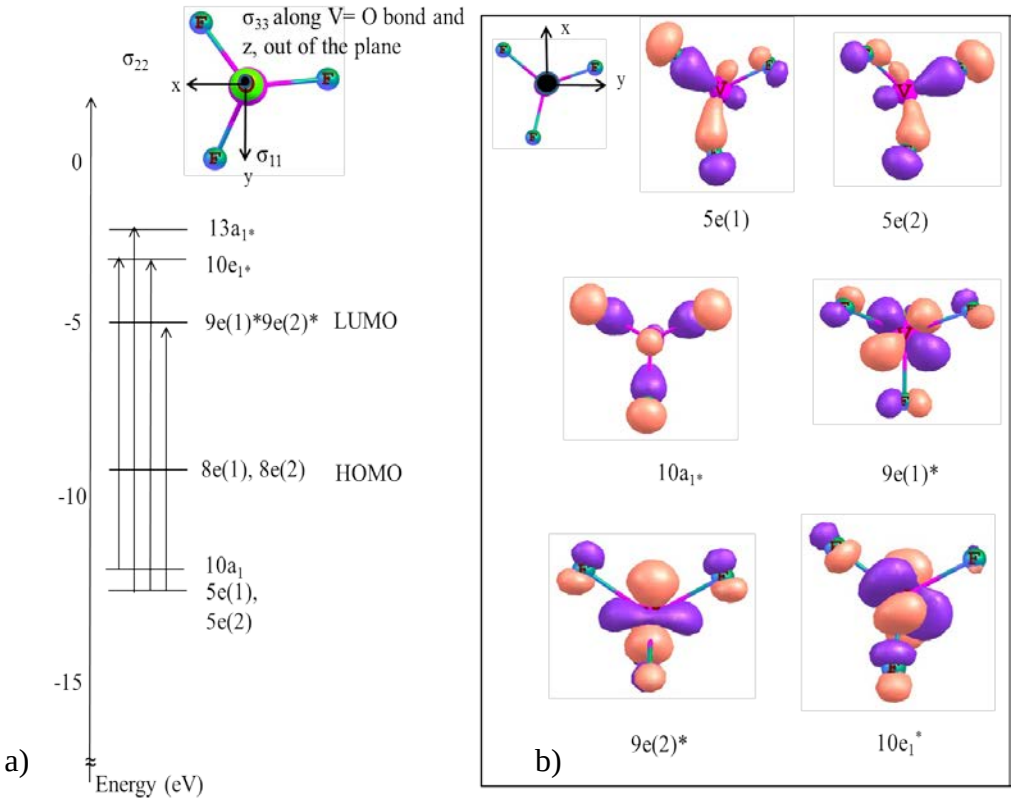

Figure 4.40. a) MO energy-level diagram and vanadium magnetic shielding tensor orientation for VOF_3. b) Visual representation of the MOs which contribute substantially to the paramagnetic shielding tensor.

In VOF_3, the occ-vir contributions to σ^p dominate the occ-occ contributions. As can be seen from the calculation results in Table 4.19, paramagnetic shielding contributions from 16 pairs of MOs account for 70% of all occ-vir contributions to the isotropic paramagnetic shielding values.

Table 4.19. Significant Paramagnetic Contributions to Vanadium Magnetic Shielding for VOF_3

MO-Occ	MO-Vir	σ_{11}(ppm)	σ_{22} (ppm)	σ_{33} (ppm)	σ_{iso} (ppm)	$\langle\phi_b\|R_n\|\phi_a\rangle$
18	30	0	0	-820	-271	$\langle 5e_1\|R_z\|9e_1^*\rangle$
18	31	0	-178	0	-59	$\langle 5e_1\|R_x,R_y\|9e_1^*\rangle$
18	32	-140	0	0	-47	$\langle 5e_1\|R_x,R_y\|10e_1^*\rangle$
18	34	0	-213	0	-71	$\langle 5e_1\|R_x,R_y\|13a_1^*\rangle$
19	30	-178	0	0	-59	$\langle 5e_1\|R_x,R_y\|9e_1^*\rangle$
19	31	0	0	-820	-272	$\langle 5e_1\|R_z\|9e_1^*\rangle$
19	33	0	-140	0	-47	$\langle 5e_1\|R_x,R_y\|11e_1^*\rangle$
19	34	-213	0	0	-71	$\langle 5e_1\|R_x,R_y\|13a_1^*\rangle$
20	32	-322	0	0	-107	$\langle 10a_1\|R_x,R_y\|10e_1^*\rangle$
20	33	0	-322	0	-107	$\langle 10a_1\|R_x,R_y\|11e_1^*\rangle$
21	33	-245	0	0	-82	$\langle 11a_1\|R_x,R_y\|11e_1^*\rangle$
21	34	-265	0	0	-88	$\langle 11a_1\|R_x,R_y\|13e_1^*\rangle$
22	32	0	-245	0	-82	$\langle 6e_1\|R_x,R_y\|10e_1^*\rangle$
22	34	0	-265	0	-88	$\langle 6e_1\|R_x,R_y\|13a_1^*\rangle$
27	32	-596	0	0	-198	$\langle 12a_1\|R_x,R_y\|10e_1^*\rangle$
27	33	0	-596	0	-198	$\langle 12a_1\|R_x,R_y\|11e_1^*\rangle$

For example, it is clear that mixing of 18($5e_1$) with 30($9e_1^*$) and 19($5e_1$) with 31($9e_1^*$), contribute significantly to deshielding along the σ_{33} direction. These

MOs are relatively close in energy, (ΔE = 7.4 eV). By evaluating the selection rule for this point group,

$$\phi_b \times R_n \times \phi_a = E \times \begin{bmatrix} R_x \\ R_y \\ R_z \end{bmatrix} \times E = E \times \begin{bmatrix} E \\ A_2 \end{bmatrix} \times E = \begin{bmatrix} 3E + A_2 + A_1 \\ E + A_2 + A_1 \end{bmatrix}$$

it is clear that the contributions to magnetic shielding are nonzero along any three coordinates (Tables 4.20, 4.21).

Table 4.20. Character Table for the C_{3v} Point Group[113]

	E	**$2C_3(Z)$**	**$3\sigma_v$**	Linear rotation	quadratic
A_1	1	1	1	z	x^2, y^2, z^2
A_2	1	1	-1	R_z	
E	2	-1	0	x, (R_y, R_x)	(xz,yz) (x^2-y^2,xy)

Table 4.21. Product Table for the C_{3v} Point Group

	A_1	**A_2**	**E**
A_1	A_1	A_2	E
A_2	A_2	A_1	E
E	E	E	A_1+A_2+E

Similar calculations were performed on $VOCl_3$ and $VOBr_3$ and are tabulated in Tables 4.22(a-b), and 4.23(a-b), respectively. These calculations indicate that the unique components of the vanadium shielding tensors for $VOCl_3$ and $VOBr_3$ are along the V= O bond as expected from the symmetry of the molecule (shown in Figures 4.41and 4.42, respectively).

Table 4.22a. Contributions to Vanadium Magnetic Shielding for $VOCl_3$.

Contribution	σ_{11} (ppm)	σ_{22} (ppm)	σ_{33} (ppm)	σ_{iso} (ppm)
σ^d(total)	1701	1694	1694	1696
σ^p(total)	-4053	-3462	-3462	-3659
σ (total)	-2351	-1767	-1767	-1962

Table 4.22b. Significant Paramagnetic Contributions to Vanadium Magnetic Shielding for $VOCl_3$.

MO-Occ	MO-Vir	σ_{11} (ppm)	σ_{22} (ppm)	σ_{33} (ppm)	σ_{iso} (ppm)	$\langle\phi_b\|R_n\|\phi_a\rangle$
30	44	0	-866	0	-288	$\langle 13a_1 \| R_x, R_y \| 14e_1^* \rangle$
30	45	0	0	-866	-288	$\langle 13a_1 \| R_x, R_y \| 14e_1^* \rangle$
31	42	0	-346	0	-115	$\langle 9e_1 \| R_x, R_y \| 13e_1^* \rangle$
31	43	0	-344	0	-114	$\langle 9e_1 \| R_x, R_y \| 13a_1^* \rangle$
31	46	0	-638	0	-212	$\langle 9e_1 \| R_x, R_y \| 16a_1^* \rangle$
32	42	0	0	-344	-114	$\langle 14e_1 \| R_x, R_y \| 13e_1^* \rangle$
32	43	0	0	-346	-115	$\langle 14e_1 \| R_x, R_y \| 13e_1^* \rangle$
32	46	0	0	-638	-212	$\langle 14e_1 \| R_x, R_y \| 16a_1^* \rangle$
34	42	-1308	0	0	-436	$\langle 10e_1 \| R_z \| 13e_1^* \rangle$
35	43	-1308	0	0	-436	$\langle 10e_1 \| R_z \| 13e_1^* \rangle$
34	44	0	0	-345	-115	$\langle 10e_1 \| R_x, R_y \| 14e_1^* \rangle$
34	45	0	-345	0	-115	$\langle 10e_1 \| R_x, R_y \| 14e_1^* \rangle$

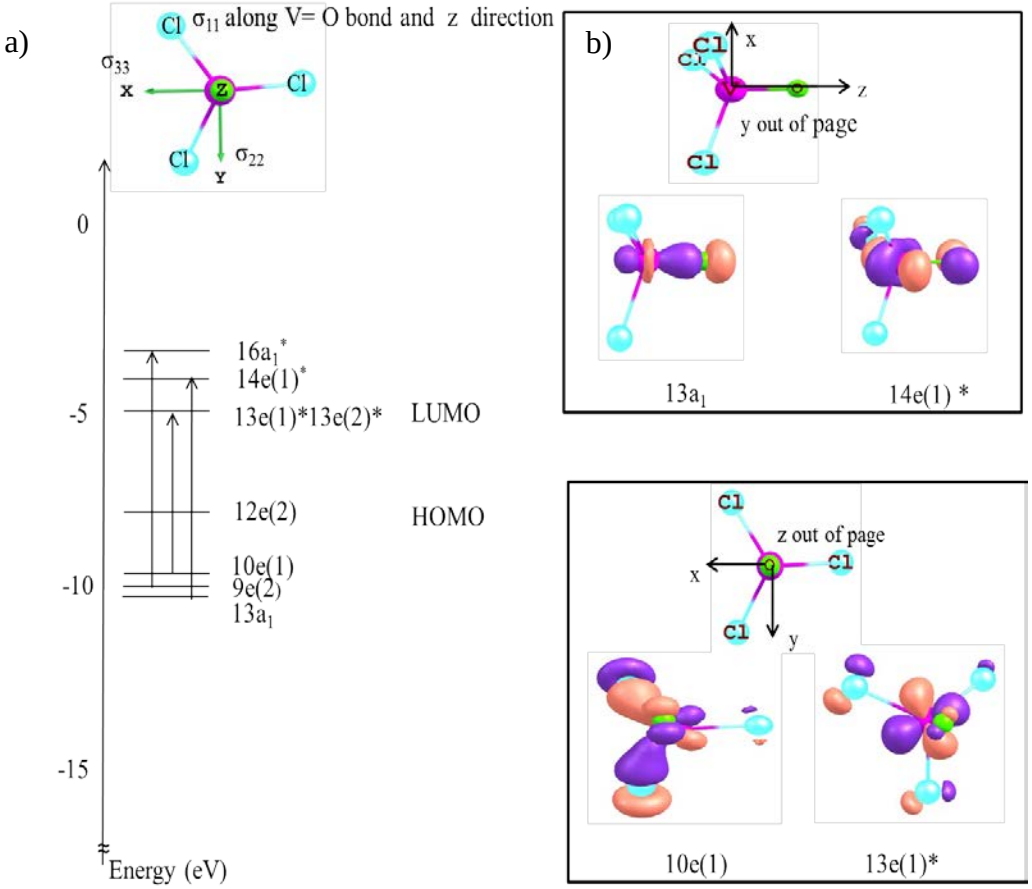

Figure 4.41. a) MO energy-level diagram and vanadium magnetic shielding tensor orientation for $VOCl_3$. b) Visual representation of the MOs which contribute substantially to the paramagnetic shielding tensor.

Table 4.23a. Contributions to the Vanadium Magnetic Shielding for $VOBr_3$.

Contribution	σ_{11} (ppm)	σ_{22} (ppm)	σ_{33} (ppm)	σ_{iso} (ppm)
σ^d(total)	1708	1701	1701	1703
σ^p(total)	-4642	-3649	-3649	-3980
σ (total)	-2935	-1948	-1948	-2276

Table 4.23b. Significant Paramagnetic Contributions to Vanadium Magnetic Shielding for $VOBr_3$.

MO-Occ	MO-Vir	σ_{11} (ppm)	σ_{22} (ppm)	σ_{33} (ppm)	σ_{iso} (ppm)	$\langle \phi_b \vert R_n \vert \phi_a \rangle$
57	71	0	0	-1141	-380	$\langle 19\mathrm{a}_1 \vert R_x, R_y \vert 23e_1^* \rangle$
57	72	0	-1141	0	-380	$\langle 19\mathrm{a}_1 \vert R_x, R_y \vert 23e_1^* \rangle$
58	70	0	-425	0	-142	$\langle 18\mathrm{e}_1 \vert R_x, R_y \vert 22e_1^* \rangle$
58	73	0	0	-571	-190	$\langle 18\mathrm{e}_1 \vert R_x, R_y \vert 22a_1^* \rangle$
59	69	0	0	-425	-142	$\langle 18\mathrm{e}_1 \vert R_x, R_y \vert 22e_1^* \rangle$
59	73	0	0	-571	-190	$\langle 18\mathrm{e}_1 \vert R_x, R_y \vert 22a_1^* \rangle$
61	69	-1879	0	0	-626	$\langle 19\mathrm{e}_1 \vert R_z \vert 22e_1^* \rangle$
61	71	0	-317	0	-106	$\langle 19\mathrm{e}_1 \vert R_x, R_y \vert 23e_1^* \rangle$
62	70	-1879	0	0	-626	$\langle 19\mathrm{e}_1 \vert R_z \vert 22e_1^* \rangle$
62	72	0	0	-317	-106	$\langle 19\mathrm{e}_1 \vert R_x, R_y \vert 23e_1^* \rangle$

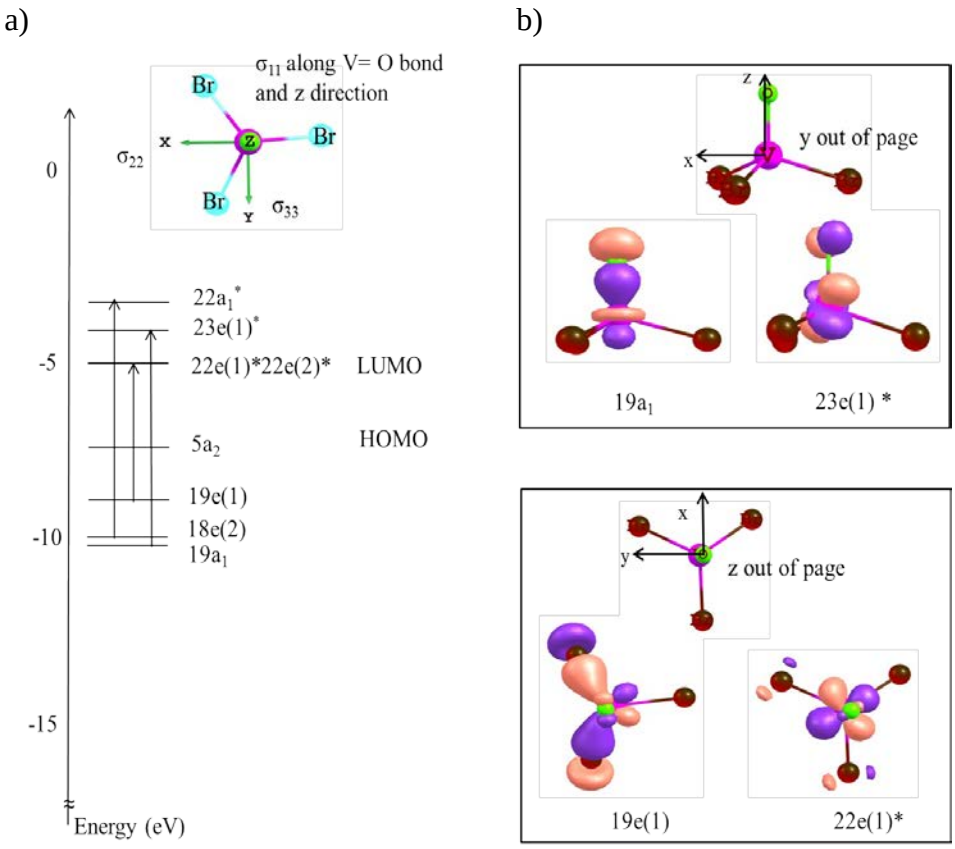

Figure 4.42. a) MO energy-level diagram and vanadium magnetic shielding tensor orientation for $VOBr_3$. b) Visual representation of the MOs which contribute substantially to the paramagnetic shielding tensor.

As can be noted from Tables 4.22 and 4.23, the unique components of the vanadium shielding tensor are the least shielding components which are in direction of VO bond. For $VOCl_3$, according to the calculation results, mixing of $10e_1$ with $13e_1$* (MOs 34 and 42*, respectively) leads to paramagnetic deshielding along z-axis parallel to σ_{11} (ΔE = 4.7 eV). This can be compared to $VOBr_3$, the $19e_1 \leftrightarrow 22e_1$* (MOs 61 and 69 respectively) mixing leads to paramagnetic deshielding along z-axis parallel to σ_{11} (ΔE = 3.9 eV).

An interesting distinction about VOF_3 is that σ_{33} is its unique component, in contrast to $VOCl_3$ and $VOBr_3$, for which σ_{11} is the unique component. In Figure 4.43, and Table 4.24, an energy-level diagram for the HOMO-LUMO regions and vanadium magnetic shielding components for VOX_3, (X= F, Cl and Br) are shown, respectively. For $VOBr_3$ and $VOCl_3$, contributing HOMOs are σ(VX), π(VX) and π(V=O) bonding orbitals but only π(V=O) for VOF_3. It can be seen from Figure 4.44 that with increasing electronegativity, ΔE increases, since the LUMOs are the same for all three (nonbonding V(3*d*) orbitals located around -5.0 eV) but the HOMO is significantly lower for VOF_3. This results in a decrease of σ^p for VOF_3, which is well documented as an "inverse electronegativity" dependence of metal shielding in (d^0) complexes.[114,115] This trend can be seen from results in Tables 4.18, 4.22, and 4.23; σ^p along V=O increases from -2523 to -4642 ppm for VOF_3 and $VOBr_3$ respectively, in contrast σ^p is perpendicular to VO only increases from -3104 to 3650 ppm, thus this explains why the direction of greatest shielding is along V=O bond for VOF_3 but perpendicular to V=O bond for $VOBr_3$ and $VOCl_3$. In conclusion, these calculations highlight the fact that the gap between π (V=O) orbitals of V(3*d*) character and nonbonding V(3*d*) orbitals is the major factor responsible for the shielding variations at the vanadium nucleus.

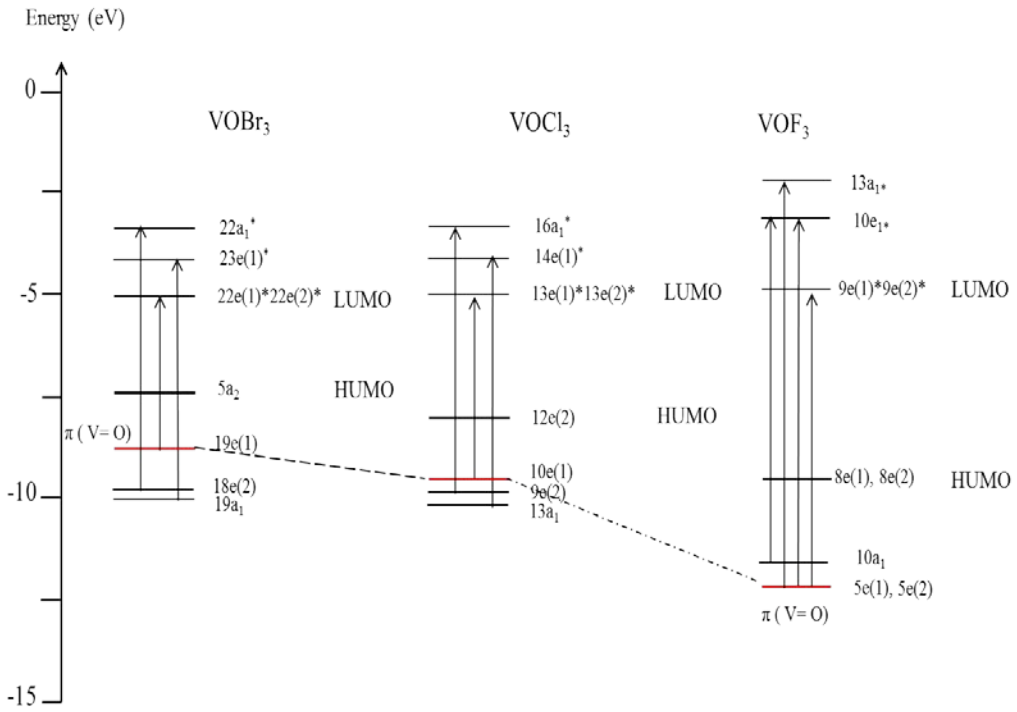

Figure 4.43. Selected MO energy-level diagram for VOX_3 (X= Br, Cl, F) , with energy data taken from calculation results.

Table 4.24. Vanadium Magnetic Shielding (ppm) for VOX_3, (X= F, Cl and Br).

Compound	σ_{11} (ppm)	σ_{22} (ppm)	σ_{33} (ppm)	σ_{iso} (ppm)
VOF_3	-1418	-1418	-832	-1223
$VOCl_3$	-2351	-3462	-3462	-3659
$VOBr_3$	-2935	-1948	-1948	-2276

Figure 4.44 shows the orientation of the σ_{33} component of the vanadium magnetic shielding tensor for vanadium compounds **II) –V)** investigated in the current research. Recall here that all these vanadium compounds have a V=O bond, with bond lengths of 1.5997, 1.5989, 1.6211 and 1.6363 Å for **II)-V)**, respectively. Calculations indicate that σ_{33} for these compounds is almost along the V=O bond. To understand the origins of the magnetic shielding, contributions to the paramagnetic shielding from MOs have been investigated for the vanadium compound II) which has the largest span among the compounds in this study (similar to the VOX_3).

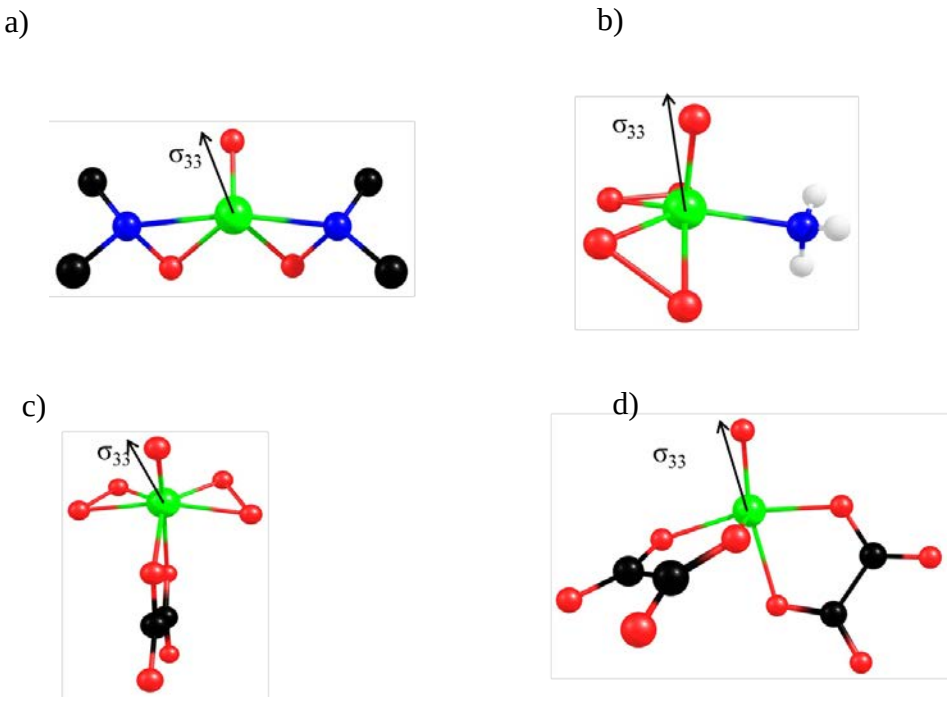

Figure 4.44. Orientation of σ_{33} for a) $V(O)(ONMe_2)_2$, b) $[VO(O_2)_2(NH_3)]^{-1}$, c) $[VO(O_2)_2(C_2O_4)]^{-3}$ and d) $[V(O_2)(C_2O_4)_2]^{-3}$ obtained from computational results.

Recall here that the paramagnetic contribution to the shielding is related to the magnetic-dipole allowed mixing between symmetry-appropriate occupied and unoccupied MOs. Efficient mixing requires that the symmetries of the occupied MOs after a rotation about the axis of the applied magnetic field be the same as those of the unoccupied MOs. The nature (suitability for mixing) of the MOs and percent vanadium *d*-orbital character obtained from DFT magnetic shielding

calculations were studied to understand which MOs contribute to the magnetic shielding. However, analyzing MOs for this vanadium compound is very challenging compared to the analyses of the previous examples, due to the lack of symmetry about the vanadium centre (*i.e.*, no group symmetry). Generally for transition metal complexes, the MOs that contribute most to magnetic deshielding are often those with significant *d* character. The role of the *d* orbitals in determining transition metal nuclear magnetic shielding tensors has been discussed more generally for d^6 and d^8 metals.[116,117]

Figure 4.45 shows the four occupied MOs that contain the majority of the vanadium *d*-orbital character. They also contribute the most to the magnetic shielding of the vanadium; the percent contributions to the isotropic magnetic shielding are indicated in Figure 4.45. For example, the HOMO (a) in Figure 4.45 has a 20 % contribution from the d_{xy} orbital, and when it mixes with unoccupied MOs of the appropriate symmetry accounts for 17% contribution to the total isotropic paramagnetic shielding. There are a number of low-lying virtual MOs which have significant contributions from *d* orbitals. The MOs illustrated in the Figure 4.45 can be said to have a symmetry closely related to the vanadium *d* orbitals. The CS anisotropy and orientations, as well as the MO analysis also suggest that the vanadium magnetic shielding is dictated primarily by the V=O bond. In fact most of the occupied and unoccupied MOs that have significant vanadium *d*-orbital character are primarily centred on the V=O bond, Figure 4.46. Analysis of the effects of structural changes on the metal magnetic shielding, by Justino *et al.*,[118] concluded that in peroxo V(V) species, the ^{51}V chemical shifts are extremely sensitive to the V=O bond lengths.

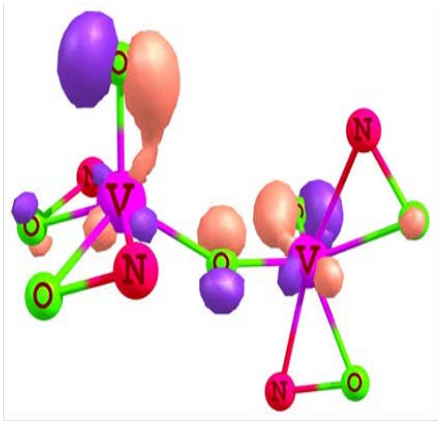

d_{xy}

-7.939 eV, 17 %

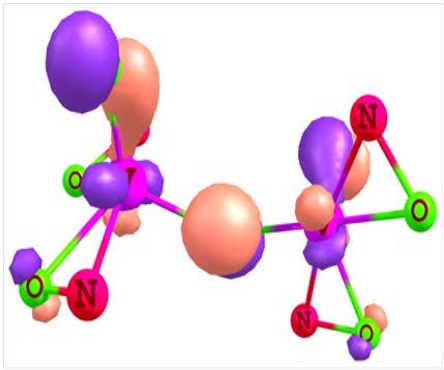

d_{xz}

-7.862 eV, 15 %

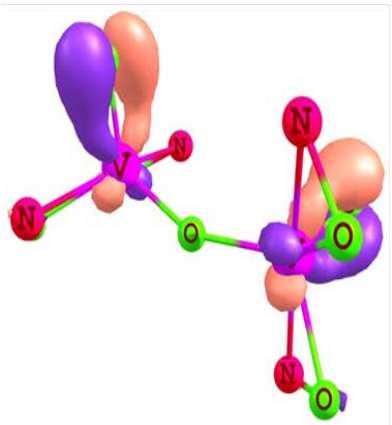

d_z^2

-7.806 eV, 8 %

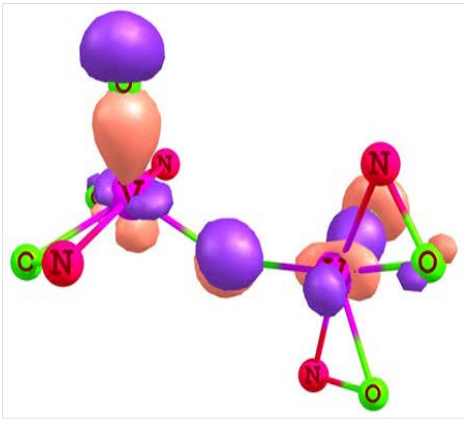

d_{xy}

-8.335 eV, 8 %

Figure 4.45. Four of the MOs for $V(O)(ONMe_2)_2$, obtained from B3LYP calculations, which contribute significantly to the calculated paramagnetic shielding and contain significant vanadium *d*-orbital character; contributions are given as a % of the total paramagnetic shielding. The B3LYP functional and the 6-311+G(p,d) basis set were employed for all atoms, as available in the Gaussian package; molecular orbitals electro- were displayed using ChemCraft 1.7.

4.4. Conclusions

In the first part of this study, vanadium chemical shift and EFG tensors for cyclopentadienyl vanadium tetracarbonyl were investigated. Solid-state ^{51}V NMR spectra of spinning and stationary samples provide detailed information on the nature of the chemical shift and electric field gradient tensors. DFT calculations were carried out with varying basis sets. DFT results for the EFG and chemical shift tensors and their orientations were calculated approximately equally well by all methods.

In the second part of this study, an investigation of a series of oxo-peroxo vanadium(V) complexes was successfully accomplished by ^{51}V solid-state NMR spectroscopy, which was used to directly probe the vanadium site. Analysis of the ^{51}V solid-state NMR spectra allowed the determination of the vanadium quadrupolar and CS tensors. The ^{51}V NMR results demonstrated that the CS interaction plays a dominant role in defining the solid-state NMR spectra of this quadrupolar nucleus. The spectroscopic parameters, corresponding to the quadrupolar and chemical shift tensors, yielded valuable information about the environment at the vanadium site. To complement the experimental results, density functional theory (DFT) calculations have also been performed using three different functionals and a wide range of basis sets. Theoretical calculations qualitatively reproduce the available experimental ^{51}V EFG and CS tensors, including their relative orientations. Overall, the DFT calculations yield reasonable agreement with the experimental solid-state NMR data employing the proper basis sets. Both the electric field gradient and magnetic shielding tensors were reproduced by the DFT calculations. Interestingly, all calculations for the oxo-peroxo vanadium compounds studied here except compound (IV) using different basis sets yield a negative sign for C_Q. The signs of the quadrupolar coupling constant cannot be obtained from the solid-state NMR data available in this study, and theoretical calculations thus complement the experimental results. The orientations of the CSA and EFG tensors in the molecular reference frame, which is difficult to obtain from the NMR experiments, have also been obtained

from the DFT calculations. Overall, the agreement between theory and experiment is reasonable, and all basis sets utilized in the calculations yield very similar orientations for the EFG and CSA tensors. These experimental parameters were subsequently correlated with the geometry of the oxo and peroxo vanadium(V) complexes via density functional theory calculations. A combination of experimental solid-state NMR spectroscopy and theoretical DFT calculations can provide a fairly accurate description of the molecular and electronic structure in the vanadium-containing systems, as has been shown for the four crystallographically characterized complexes addressed in this work.

In conclusion, the combination of ^{51}V solid-state NMR spectroscopy with quantum chemical calculations employing proper basis sets provides a promising tool for the study of this class of oxo, peroxo vanadium compounds.

4.5. References

[1] O. B. Lapina, D. F. Khabibulin, A. A. Shubin, V. V. Terskikh. *Prog. Nucl. Magn. Reson. Spectrosc*. **53**, 128, (2008).

[2] D. Rehder, T. Polenova, M. Buhl. *Ann. Rep. NMR Spectrosc*. **62**, 49, (2007).

[3] U. G. Nielsen, A. Boisen, M. Brorson, C. J. H. Jacobsen, H. J. Jakobsen, J. Skibsted. *Inorg*. *Chem*. **41**, 6432, (2002).

[4] U. G. Nielsen, J. Skibsted, H. J. Jakobsen. *Chem. Phys. Lett*. **356**, 73, (2002).

[5] A. A. Shubin, O. B. Lapina, D. Courcot. *Catal. Today*. **56**, 379, (2000).

[6] S. E. Bolte, K. J. Ooms, T. Polenova, B. Baruah, D. C. Crans, J. J. Smee. *J. Chem. Phys*. **128**, 052317, (2008).

[7] J. Skibsted, C. J. H. Jacobsen, H. J. Jakobesn. *Inorg*. *Chem*. **37**, 3083, (1998).

[8] K. J. Ooms, S. E. Bolte, J. J. Smee, B. Baruah, D. C. Crans, T. Polenova. *Inorg. Chem*. **46**, 9285, (2007).

[9] P. B. Chatterjee, O. Goncharov-Zapata, L. L. Quinn, G. Hou, H. Hamaed, R.W. Schurko, T. Polenova, D. C. Crans. *Inorg. Chem*. **50**, 9794, (2011).

[10] M. Wächtler, A. Schweitzer, T. Gutmann, H. Breitzke, G. Buntkowsky. *Solid State Nucl. Magn. Reson.* **35**, 37, (2009).

[11] A. Fenn, M. Wächtler, H. Breitzke, A. Buchholz, I. Lippold, W. Plass, G. Buntkowsky. *Solid State Nucl. Magn. Reson.* **40**, 60, (2011).

[12] N. Pooransingh, E. Pomerantseva, M. Ebel, S. Jamtzen, D. Rehder, T. Polenova. *Inorg. Chem*. **42,** 1256, (2003).

[13] W. Huang, L. Todaro, G. P. Yap, R. Beer, L. C. Francesconi, T. Polenova. *J. Am. Chem. Soc*. **126**, 11564, (2004).

[14] R. K. Harris, E. D. Becker, S. M. Cabral de Menezes, R. Goodfellow, P. Granger. *Pure Appl. Chem.* **73**, 1795, (2001).

[15] P. Pyykkö. *Mol. Phys*. **106**, 1965, (2008).

[16] J. O. Nriagu. *Vanadium in the Environment. Part 1: Chemistry and Biochemistry*, John Wiley & Sons: New York, US, 1998.

[17] N. Pooransingh-Margolis, R. Renirie, Z. Hasan, R. Wever, A. J. Vega, T. Polevona. *J. Am. Chem. Soc*. **128**, 5190, (2006).

[18] D. Rehder. *Coord. Chem. Rev.* **182**, 297, (1999).

[19] M. Casny, D. Rehder, H. Schmidt, H. Vilter, V. Conte. *J. Inorg. Biochem.* **80**, 157, (2000).

[20] D. C. Crans, J. J. Smee, E. Gaidamauskas, L. Yang. *Chem. Rev*. **104**, 849, (2004).

[21] K. H. Thompson, C. Orvig. *Coord. Chem. Rev.* **219**, 1033, (2001).

[22] D. C. Crans, J. J. Smee, G. Teissedre. *J. Am. Chem. Soc*. **229**, 1002, (2005).

[23] H. Sakurai, S. Funakoshi, Y. Adachi. *Pure Appl. Chem*. **77**, 1629, (2005).

[24] A. Shaver, J. B. Ng, D. A. Hal, B. S. Lum , B. I. Posner. *Inorg. Chem.* **32**, 3109, (1993).

[25] B. I. Posner, R. Faure, J. W. Burgess, A. P. Bevan, D. Lachance, G. Zhang-Sun, I. G. Fantus, J. B. Ng, D. A. Hall, B. S. Lum, A. Shaver. *J. Biol. Chem*. **269**, 4596, (1994).

[26] F. Yraola, S. Garcı´a-Vicente, L. Marti, F. Albericio, A. Zorzano, M. Royo. *Chem. Biol. Drug*. **69**, 423, (2007).

[27] T. Hirao. *Chem. Rev.* **97**, 2707, (1997).

[28] V. Conte, F. Di Furia, S. Moro. *J. Phys. Org. Chem.* **9**, 329, (1996).

[29] V. S. Sergienko, *Crystallogr. Rep*. **49**, 907, (2004).

[30] W. D. Knight, V.W. Cohen. *Phys. Rev*. **76**, 1421, (1949).

[31] J. L. Ragle. *J. Chem. Phys*. **35 ,** 753, (1961).

[32] V. M. Mastikhin, O. B. Lapina, V. N. Krasilnikov, A. A. Ivankin. *React. Kinet. Catal. Lett*. **24** ,119, (1984).

[33] O. W. Howarth. *Prog. Nucl. Magn. Reson. Spectrosc*. **22**, 453, (1990).

[34] E. Oldfield, R. A. Kinsey, B. Montez, T. Ray, K. A. Smith. *J. Chem. Soc., Chem. Commun*. **4**, 254, (1982).

[35] M. D. Meadows, K. A. Smith, R. A. Kinsey, T. M. Rothgeb, R. P. Skarjune, E. Oldfield. *Proc. Natl. Acad. Sci. U. S. A*. **79,** 1351, (1992).

[36] O. B. Lapina, V. M. Mastikhin, A. A. Shubin, V. N. Krasilnikov, K. I. Zamaraev. *Prog. Nucl. Magn. Reson. Spectrosc*. **24**, 457, (1992).

[37] W. Koch, M. C. Holthausen. *A Chemist's Guide to Density Functional Theory*, Wiley-VCH: Weinheim, 2000.

[38] C. J. Cramer, D. G. Truhlar. *Phys. Chem. Chem. Phys*. **11**, 10757, (2009).

[39] J. Autschbach. *Struct. Bonding* (Berlin). **112**, 1, (2004).

[40] I. del Rosal, L. Maron, R. Poteau, F. Jolibois. *Dalton Trans.* **10**, 3959, (2008).

[41] A. Y. H. Lo, J. V. Hanna, R. W. Schurko. *Appl. Magn. Reson.* **32**, 691, (2007).

[42] B. A. Gee. *Solid. State. Nucl. Magn. Reson.* **30**, 171, (2006).

[43] H. Huber. *J. Chem. Phys*. **83**, 4591, (1985).

[44] P. C. Paul, S. J. Angus-Dunne, R. J. Batchelor, F. W. B. Einstein, A. S. Tracey. *Can. J. Chem*. **75**, 429, (1997).

[45] R. E. Drew, F. W. B. Einstein. *Inorg. Chem*. **12**, 829, (1973).

[46] N. Vuletic, C. Djordjevic. *J. Chem. Soc. Dalton Trans*. 1137, (1973).

[47] R. E. Drew, F. W. B. Einstein, S. E. Gransden. *Can. J. Chem*. **52**, 2184, (1974).

[48] A. E. Bennet, C. M. Rienstra, M. Auger, K. V. Lakshmi, R. G. Griffin. *J. Chem. Phys*. **103**, 6951, (1995).

[49] J. Skibsted, N. C. Nielsen, H. Bildsøe, H. J. Jakobsen. *J. Am. Chem. Soc*, **115**, 7351, (1993).

[50] G. M. Volkoff, H. E. Petch, D. W. L. Smellie. *Can. J. Phys*. **30**, 270, (1952).

[51] G. M. Volkoff. *Can. J. Phys*. **31**, 820, (1953).

[52] H. E. Petch, N. G. Cranna, G. M. Volkoff. *Can. J. Phys*. **31**, 837, (1953).

[53] K. Eichele, J. C. C. Chan, R. E. Wasylishen, J. F. Britten. *J. Phys. Chem*. **A 101**, 5423, (1997).

[54] L. B. Alemany. *Appl. Magn. Reson*. **4**, 179, (1993).

[55] F. Chen, G. Ma, G. M. Bernard, R. E. Wasylishen, R. G. Cavell, R. McDonald, M. J. Ferguson. *Chem. Eur. J*. **19**, 2826, (2013).

[56] J. F. Baugher, P. C. Taylor, T. Oja, P. J. Bray. *J. Chem, Phys*. **50**, 4914, (1969).

[57] P. C. Taylor, J. F. Baugher, H. M. Kriz. *Chem. Rev*. **75**, 203, (1975).

[58] W. P. Power, R. E. Wasylishen, S. Mooibroek, B. A. Pettitt, W. Danchura. *J. Phys. Chem*. **94**, 591, (1990)

[59] P. J. Chu, B. C. Gerstein. *J. Chem. Phys*, **91**, 2081, (1989).

[60] K. Eichele, R. E. Wasylishen. WSOLIDS *NMR Simulation Package,* (2001).

[61] M. Bak, J. T. Rasmussen, N. C. Nielsen. *J. Magn. Reson*. **147**, 296, (2000).

[62] J. Skibsted, N. C. Nielsen, H. Bildsøe, H. J. Jakobsen. *Chem. Phys. Lett*. **188**, 405, (1992).

[63] ADF 2006.01, Theoretical Chemistry, Vrije Universiteit, Amsterdam, http://www. Scm.com.

[64] S. H. Vosko, L. Wilk, M. Nusair. *Can. J. Phys*. **58**, 1200, (1980).

[65] A. D. Becke. *Phys. Rev.* **A 38**, 3098, (1988).

[66] J. P. Perdew. *Phys. Rev*. **B 33**, 8822, (1986).

[67] Gaussian 03, Revision C.02, M. J. Frisch, G. W. Trucks, H. B. Schlegel, G. E. Scuseria, M. A. Robb, J. R. Cheeseman, J. A. Montgomery, Jr., T. Vreven, K. N. Kudin, J. C. Burant, J. M. Millam, S. S. Iyengar, J. Tomasi, V. Barone, B. Mennucci, M. Cossi, G. Scalmani, N. Rega, G. A. Petersson, H. Nakatsuji, M. Hada, M. Ehara, K. Toyota, R. Fukuda, J. Hasegawa, M. Ishida, T. Nakajima, Y. Honda, O. Kitao, H. Nakai, M. Klene, X. Li, J. E. Knox, H. P. Hratchian, J. B. Cross, V. Bakken, C. Adamo, J. Jaramillo, R. Gomperts, R. E. Stratmann, O. Yazyev, A. J. Austin, R. Cammi, C. Pomelli, J. W. Ochterski, P. Y. Ayala, K. Morokuma, G. A. Voth, P. Salvador, J. J. Dannenberg, V. G. Zakrzewski, S. Dapprich, A. D. Daniels, M. C. Strain, O. Farkas, D. K. Malick, A. D. Rabuck, K. Raghavachari, J. B. Foresman, J. V. Ortiz, Q. Cui, A. G. Baboul, S. Clifford, J. Cioslowski, B. B. Stefanov, G. Liu, A. Liashenko, P. Piskorz, I. Komaromi, R. L. Martin, D. J. Fox, T. Keith, M. A. Al-Laham, C. Y. Peng, A. Nanayakkara, M. Challacombe, P. M. W. Gill, B. Johnson, W. Chen, M. W. Wong, C. Gonzalez, and J. A. Pople, Gaussian, Inc., Wallingford CT, 2004.

[68] A. D. Becke. *J. Chem. Phys*. **98,** 5648, (1993).

[69] C. T. Lee, W. T. Yang, R. G. Parr. *Phys. Rev*. **B 37** (2), 785, (1988).

[70] A. Schafer, H. Horn, R. Ahlrichs. *J. Chem. Phys*. **97** (4), 2571, (1992).

[71] A. Schafer, C. Huber, R. Ahlrichs. *J. Chem. Phys*. **100** (8), 5829, (1994).

[72] W. J. Hehre, R. Ditchfield, J. A. Pople. *J. Chem. Phys*. **56** (5), 2257, (1972).

[73] P. C. Harihara, J. A. Pople. *Theor. Chim. Acta*, **28** (3), 213, (1973).

[74] T. Clark, J. Chandrasekhar, G. W. Spitznagel, P. V. Rague Schleyer. *J. Comput. Chem*. **4** (3), 294, (1983).

[75] K. Wolinski, J. F. Hinton, P. Pulay. *J. Am. Chem. Soc*. **112** (23), 8251, (1990).

[76] S. J. Clark, M. D. Segall, C. J. Pickard, P. J. Hasnip, M. I. J. Probert, K. Refson, M. C. Payne, *Z. Kristallogr*. **220**, 567, (2005).

[77] M. Profeta, F. Mauri, C. J. Pickard. *J. Am. Chem. Soc.* **125**, 541, (2003).

[78] J. P. Perdew, K. Burke, M. Ernzerhof. *Phys. Re*v. *Lett.* **77**, 3865, (1996).

[79] J. P. Perdew, K. Burke, M. Ernzerhof. *Phys. Re*v. *Lett*. **80**, 891, (1998).

[80] C. J. Pickard, F. Mauri. *Phys. Re*v. **63 B**, 245101, (2001).

[81] J. R. Yates, C. J. Pickard, F. Mauri. *Phys. Re*v. **76 B**, 024401, (2007).

[82] J. Galy, R. Enjalbert, G. Jugie, J. Strahle. *J. Solid State Chem*. **47**, 143, (1983).

[83] S. I. Troyanov. *Russ. J. Inorg. Chem*. **50**, 1727, (2005).

[84] R. Bjornsson, H. Fruchtl, M. Buhl. *Phys. Chem. Chem. Phys.* **13,** 619, (2011).

[85] L. Truflandier, M. Paris, F. Boucher. *Phys. Rev.* **B 76**, 035102, (2007).

[86] T. Gutmann, A. Schweitzer, M. Wächtler, H. Breitzke, A. Buchholz, W. Plass. G. Buntkowsky. *Z. Phys. Chem*. **222**, 1389, (2008).

[87] W. Basler, H. Lechert, K. Paulsen, D. Rehder. *J. Magn. Reson*. **45**, 170, (1981).

[88] E. O. Fischer, W. Hafner. *Z. Naturforsch*. **9 B**, 503, (1954).

[89] J. B. Wilford, A. Whitla, H. M. Powell. *J. Organomet. Chem*. **8**, 495, (1967).

[90] M. J. Almond, E. M.Page, D. A. Rice, K. Hagen. *Organomet. Chem*. **511**, 303, (1996).

[91] R. T. McKay, J. L. Hubbard, S. G. Kukolich. *J. Mol. Spectrosc*. **172**, 378, (1995).

[92] R. Stomberg, S. Olson, I. B. Svensson. *Acta. Chem. Scand. Ser*. **A 38**, 653, (1984).

[93] R. E. Drew, F. W. B. Einstein. *Inorg. Chem*. **12**. 829, (1973).

[94] R. E. Drew, F. W. B. Einstein. *Inorg. Chem*. **11**, 1079, (1972).

[95] T. T. Nakashima, R. Teymoori, R. E. Wasylishen. *Magn. Reson. Chem*. **47**, 465, (2009).

[96] R. Siegel, T. T. Nakashima, R. E. Wasylishen. *Chem. Phys. Lett.* **388**, 441, (2004).

[97] R. Siegel, T. T. Nakashima, R. E. Wasylishen. *Concepts Magn. Reson*, **A 26**, 47, (2005).

[98] R. Siegel, T. T. Nakashima, R. E. Wasylishen. *Chem. Phys. Lett.* **403**, 353, (2005).

[99] R. Siegel, T. T. Nakashima, R. E. Wasylishen. *Chem. Phys. Lett.* **421**, 529, (2006).

[100] R. Siegel, T. T. Nakashima, R. E. Wasylishen. *J. Magn. Reson*. **184**, 85, (2007).

[101] R. E. Drew, F. W. B. Einstein. *J. Inorg. Chem.* **11**, 1079, (1972).

[102] J. Chrappova, P. Schwendt, D. Dudasove, J. Tatiersky, J. Marek. *J. Polyhedron*. **27**, 641, (2008).

[103] A. Samoson. *Chem. Phys. Lett*. **119**, 29, (1985).

[104] D. Begin, F. W**.** B. Einstein, J. Field. *Inorg. Chem*. **14**, 1785, (1975)

[105] B. R. Zeng, J. Zhang, R. Fu, S. H. Cai, Z. Chen. *Inorg. Chem. Commun*. **12**, 1259, (2009).

[106] S. Adiga, D. Aebi, D. Bryce. *Can. J. Chem.* **85**, 496, (2007).

[107] N. F. Ramsey. *Phys. Rev*. **78**, 699, (1950).

[108] G. te Velda, F. M. Bickelhaupt, E. J. Baerends , C. Fonseca Guerra, S. J. A. Van Gisbergen, J. G. Snijders. *J. Comput. Chem*. **2**. 931, (2001).

[109] W. Kohn, L. J. Sham. *Phys. Rev*. **140**, 1133, (1965).

[110] G. Schreckenbach, T. Ziegler. *Int. J. Quantum. Chem*. **60**, 753, (1996).

[111] S. K. Wolff, T. Ziegler. E. van Lenthe, E. J. Baerends. *J. Chem. Phys*. **110**, 7689, (1999).

[112] C. M. Widdifield, R. W. Schurko. *Concepts Magn. Reson*. **34 A**, 91, (2009).

[113] F. A. Cotton. *Chemical Applications of Group Theory*; John Wiley & Sons: New York, US, 1990.

[114] R. G. Kidd. *Annu. Rep. NMR Spectrosc*. **10 A**, 1, (1978).

[115] D. Rehder. *Magn. Reson. Rev*. **9**, 125, (1984).

[116] C. J. Jameson. *Multinuclear NMR*; Press: New York, 1987.

[117] J. S. Griffith, L. E. Orgel. *Trans. Faraday Soc*. **53**, 601, (1957).

[118] L. L. G. Justino, M . L. Ramos, M. Kaupp, H. D. Burrows, C. Fiolhais, V. M. S. Gil. *Dalton Trans*, 9735, (2009).

Chapter 5. A Solid-State ^{17}O NMR Study of an Indium Coordination Complex

5.1. Introduction

Carbon, hydrogen, oxygen, nitrogen, and phosphorus are the most important elements found in organic and biological molecules. All these elements except oxygen have at least one stable spin-1/2 isotope which makes these elements more accessible to NMR studies. The three stable isotopes of oxygen have natural abundances of ^{16}O (99.76%), ^{17}O (0.037%), and ^{18}O (0.204%), but only ^{17}O (S = 5/2) is NMR active. Recall here that nuclei with spin quantum number $I > 1/2$ have a non-spherical electrical charge distribution which gives rise to an electric quadrupole moment. An interaction of this with the EFG at the nucleus often leads to significantly broadened lines for solid samples. This quadrupole effect along with the need to enrich oxygen samples for NMR studies because of the very low natural abundance of oxygen-17 has limited its application in the solid-state. Nevertheless, despite these difficulties, with the recent development of higher magnetic fields, faster magic angle spinning (MAS) and techniques for improving resolution, there has been a significant increase in ^{17}O NMR studies from inorganic materials such as gels, glasses, zeolites and mineral compounds.[1-7]

In 1983 and 1984, the first high-resolution solid-state ^{17}O NMR studies using magic-angle spinning and variable-angle spinning (VAS) on inorganic solids was reported by Oldfield and co-workers.[8,9] In 1985, Haeberlen and co-workers[10] demonstrated the magnitude and orientation of the ^{17}O quadrupole interaction and chemical shift tensors with a single-crystal NMR study of benzophenone. In the late 1980s, two major breakthroughs occurred in the field of NMR for quadrupolar nuclei, the development of dynamic-angle spinning (DAS)[11] and double rotation (DOR)[12] techniques. These techniques made it possible to obtain high-resolution oxygen-17 NMR spectra by averaging the

second-order quadrupolar interaction. DAS and DOR were quickly used in the study of ^{17}O NMR for inorganic solids.[13-15]

Wu and coworkers[16-19] published a series of papers on solid-state ^{17}O NMR for organic molecules in 2000. Since then, many ^{17}O solid-state NMR studies have been done for organic and inorganic molecules.[20-27] These studies suggest that solid-state NMR spectroscopy is an ideal technique to provide insight about oxygen-containing compounds.

Potentially, ^{17}O solid-state NMR studies can provide information about the CS, and EFG tensors for oxygen. In addition, if ^{17}O nuclei are coupled to spin-1/2 nuclei such as phosphorus, indirect spin-spin coupling constants can be observed through the acquisition of spectra of the latter (*e. g.*, ^{31}P NMR).

In this study, we explore the possibility of using solid-state ^{17}O NMR for studying the influence of metal coordination on ^{17}O shielding and EFG tensors, in particular for the $InI_3[^{17}OP(p\text{-Anis})_3]_2$ compound. For this purpose a ^{17}O-enriched ligand and a $InI_3[^{17}OP(p\text{-Anis})_3]_2$ complex have been studied by solid-state NMR spectroscopy. The adducts of indium trihalide with substituted triarylphosphine ligands, first prepared by Carty and Tuck[28] over four decades ago, possess tetrahedral $X_3In(PR_3)$ (X = Cl, Br, I; PR_3 = substituded triarylphosphine) structures about the indium. The adducts of these indium compounds are classical Lewis acid-base complexes which are used as a precursors for preparing a wide range of indium semiconductors.[29] Previously solid-state ^{115}In NMR studies of some of the indium coordination complexes have been reported.[30,31] One of these indium samples, five-coordinate indium (III) triiodide bis(tris(4-methoxyphenyl) phosphine oxide), $InI_3[^{17}OP(p\text{-Anis})_3]_2$ is a matter of interest for this research.

With recent advances in computational chemistry and rapidly increasing computing capacity, it has now become routine practice to perform high-level quantum chemistry calculations for NMR parameters. Computational results often provide useful information in data analysis and interpretation of experimental

results. There are several reports of EFG and magnetic shielding calculations of ^{17}O for organic and inorganic compounds using DFT with extensive basis sets.[17,18,32]

In this study, we report the ^{17}O quadrupole coupling constant, EFG and CS tensors for $InI_3[^{17}OP(p\text{-Anis})_3]_2$. We also show that DFT calculations can reproduce reasonably well the experimental ^{17}O C_Q and CS tensors for this challenging molecule. By combining quantum chemical calculations with experimental solid-state ^{17}O NMR results, we are able to determine the ^{17}O EFG and CS tensor orientations in the molecular frame.

5.2. General Overview of Solid-State ^{17}O NMR Studies

The intrinsic nuclear properties for ^{17}O result in low sensitivity and complex spectra. Its resonance frequency is about 1/7 that for ^{1}H. For this non-integer quadrupolar nucleus usually only the central transition is observed and the quadrupolar effects have to be considered to second order.[33] This also reduces the sensitivity compared to spin-1/2 nuclei. Second-order quadrupolar broadening usually determines the line widths in MAS experiments. Like other quadrupolar nuclei, ^{17}O is sensitive to both the EFG and CSA. These anisotropic NMR interactions can be used as probes for characterizing the local environment of the nucleus. Indeed, both these parameters have been shown to be very sensitive to local structure and bonding. Non-symmetric bonding of oxygen atoms in many solids often produces strong electric field gradients at the oxygen nuclei and C_Qs of several MHz.

Recent study shows that the average for the ^{17}O C_Q is around 5.0 MHz ± 2.0 MHz in inorganic materials.,[34] This shows that the dominant interaction for ^{17}O is usually the quadrupolar interaction; however the CSA and dipolar interaction in some cases is not negligible. The range of oxygen isotropic chemical shifts in solution is on order of 2500 ppm, and the compounds containing phosphine oxides generally are in the range of 20-100 ppm.[35,36]

The standard technique for removing anisotropic broadening in powdered solids is MAS,[37] which is still the most common technique in solid-state NMR studies for quadrupolar nuclei. However, MAS is not able to remove second-order quadrupolar broadening; only partial narrowing occurs under MAS and anisotropic broadening remains in the spectrum. Therefore, for quadrupolar nuclei, it is necessary to rotate the sample at a frequency much greater than the size of the second-order quadrupolar interaction in order to maximize the signal to noise ratio and allow extraction of reliable NMR parameters from MAS spectra.

The position, width and shape of the lines are determined by the NMR parameters, the isotropic chemical shift, δ_{iso} , and the quadrupolar parameters C_Q and η_Q. Figure 5.1 shows typical oxygen-17 static and MAS spectra, assuming sample spinning is much greater than the total width of the CT for the static spectra. It is shown that MAS can only narrow the static second-order quadrupole interaction by a factor of approximately 3.

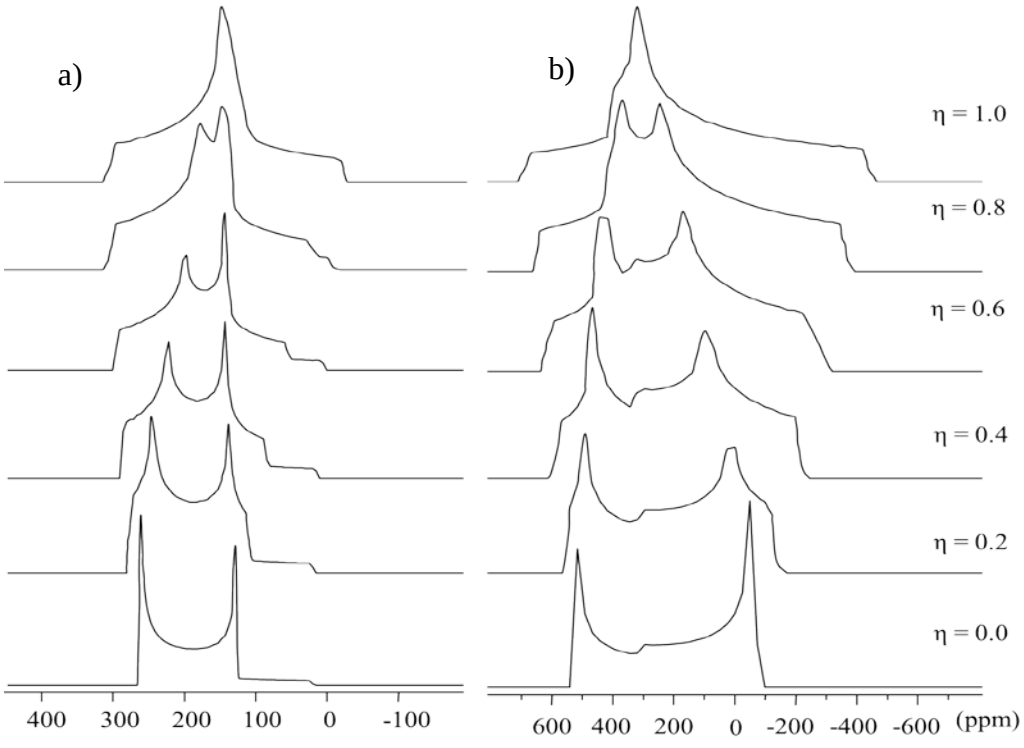

Figure 5.1. Simulated ^{17}O a) MAS and b) static NMR spectra at $\mathbf{B}_0$ = 11.75 T, C_Q = 8.50 MHz.

5.3. Experimental and Computational Details

5.3.1. Sample Preparation

Oxygen-17 solid-state NMR spectroscopy requires selective isotopic enrichment of the sample. For non-crystalline inorganic phases, enrichments of about 37% are preferable. The main precursors for ^{17}O enrichment are ^{17}O water, ^{17}O-dioxygen or ^{17}O-carbon monoxide. The synthesis of a ^{17}O-enriched sample can be difficult and expensive. In this study ^{17}O-water (37.5% ^{17}O) was used for enrichment of the ligand and complex sample of $InI_3[^{17}OP(p\text{-Anis})_3]_2$.

a) $^{17}OP(p\text{-Anis})_3$

For ligand preparation, 1.0 g (2.84 mmol) of P(*p*-Anis)$_3$ was dissolved in approximately 20.0 mL of dichloromethane (CH_2Cl_2).[38] The solution was cooled in an ice bath for two hours. A stoichiometric amount of bromine, Br_2, 0.46 g, was dissolved in 20.0 mL of dichloromethane, and the solution was added to the P(*p*-Anis)$_3$ solution under cooling conditions. The solution was allowed to warm to room temperature. At this stage 0.1 ml of labelled $H_2{}^{17}O$ was added directly to the solution and stirred for 120.0 minutes. In the last step the solution was washed with a solution of Na_2CO_3 (0.3 g) in distilled water and dried over $MgSO_4$. Finally the product was crystallized, yield; 0.8 g (80%), (See Figure 5.2).

b) $InI_3[^{17}OP(p\text{-Anis})_3]_2$

Initially, 0.13 g of InI_3 was dissolved in 5.0 ml ethyl acetate. In the next step 0.23 g of $^{17}OP(p\text{-Anis})_3$ (37.5% ^{17}O), was added to the solution. After filtration of the solution, yellow crystals formed as the solvent evaporated; this was collected and washed several times with a small amount of ethyl acetate and dried under vacuum. Yield; 0.274 g (90%).

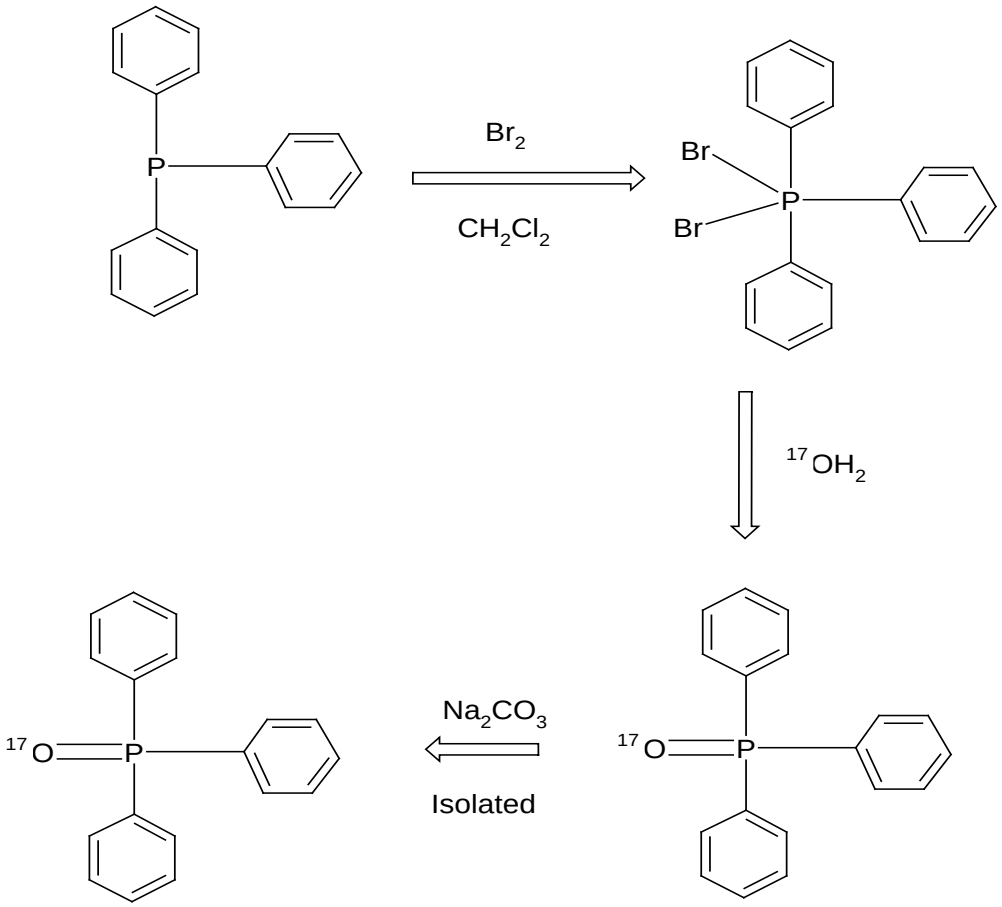

Figure 5.2. Synthetic procedure for $^{17}OP(p\text{-Anis})_3$.

5.3.2. Experimental Details

Solid-state ^{17}O NMR spectra of powdered samples of $^{17}OP(p\text{-anis})_3$ and $InI_3[^{17}OP(p\text{-Anis})_3]_2$ were obtained on Bruker Avance 11.75 and 7.05 T NMR spectrometers operating at 67.76 and 40.66 MHz, respectively. Samples were packed into 4 mm zirconia (ZrO_2) rotors and placed within a probe suitable for magic angle spinning NMR experiments. NMR spectra were acquired with a standard Hahn-echo[39] pulse sequence; recycle delays were 5 s. Proton decoupling was accomplished with the two-pulse phase modulation decoupling (TPPM) model of Griffin and coworkers.[40] MAS rates of 9.0, 10.0 and 12.0 kHz were used to acquire 55,000-100,000 scans of powder samples. Oxygen-17 NMR spectra

were referenced with respect to ^{17}O of a liquid water sample at natural abundance, (δ = 0 ppm).

5.3.3. Simulation of the NMR Spectra

All ^{17}O MAS and static NMR spectra were analyzed using WSOLIDS,[41] an NMR simulation package developed in our laboratory which incorporates the powder algorithm of Alderman *et al.*[42] The combined effect of the quadrupolar interaction and CSA was taken into account in the simulations.

5.3.4. Quantum Chemical Calculations

Calculations of the EFG and nuclear magnetic resonance tensors for ^{17}O were performed using DFT methods as implemented in the Amsterdam Density Functional (ADF)[43]and Gaussian03 programs.[44] For the former, the zeroth-order regular approximation density functional theory (ZORA DFT) method was used in the calculations, which utilized the Vosko-Wilk-Nusair (VWN)[45] local density approximation with the Becke[46]-Perdew[47] generalized gradient approximation (GGA) for the exchange-correlation functional; standard Slater-type-orbital (STO) basis sets, ZORA QZ4P and TZ2P were used. For the Gaussian03 calculations, the hybrid B3LYP exchange functional[48,49] was used with standard basis sets such as 3-21G or 6-311G with various diffuse functions.

In both ADF and Gaussian03, calculations of nuclear magnetic shielding tensors were performed using the GIAO (gauge-independent atomic orbitals) approach.[50] P, O, and C atom positions were obtained from single-crystal X-ray diffraction data.[30,51] Carbon-hydrogen bond lengths were set to 1.08 Å.

Calculations yield absolute shielding values, σ. One must establish the absolute shielding scale for a particular nucleus in order to make direct comparison between calculated magnetic shielding results and experimental chemical shift data. Calculated ^{17}O isotropic magnetic shielding (σ_{iso}) values were converted to the corresponding chemical shift (δ_{iso}) values by using the

oxygen in carbon monoxide (CO) as a secondary reference (relative to liquid H_2O) according to $\delta_{iso}^{(cal)} = 287.5 - \sigma_{iso}$ (all in ppm), where 287.5 ppm is the absolute shielding value of liquid H_2O (δ_{iso} = 0 ppm), based on the sum of experimental chemical shift of CO (350.2 ppm) and the absolute shielding (with respect to bare nucleus) value of CO (-62.7 ppm).[52,53] The NMR tensor parameters were extracted from the ADF and Gaussian output using the EFGShield program.[54]

Relativistic DFT calculations of $J(^{31}P,^{17}O)$ and $J(^{115}In,^{17}O)$ using the ZORA method with the QZ4P basis set were also performed on the complex. The theories of **J** which were formalized by Ramsey[55,56] are not employed by the computational programs, but rather an alternative approach of Autschbach and Ziegler[57] implemented in the NMR spin-spin coupling module of the ADF program has been used. Both ZORA scalar and spin-orbit calculations were carried out. All calculations included the relativistic analogues of the Fermi-contact (FC), spin-dipolar (SD), diamagnetic spin-orbital (DSO), and paramagnetic spin-orbital (PSO) coupling mechanisms. For relativistic calculations, the QZ4P basis set, optimized for ZORA calculations, was used for the O, In, P, and I atoms, while the TZP basis set was used for the H and C atoms.

5.4. Results and Discussion

5.4.1. Oxygen-17 Solid-State NMR Spectroscopy

a) ^{17}OP(*p*-Anis)$_3$

OP(*p*-Anis)$_3$ crystallizes as discrete molecular units with two molecules in the asymmetric unit cell. The crystal structure contains a three-fold symmetry axis passing through the P-O bond axis, as shown in Figure 5.3. The geometry about the phosphorus atom in this molecule is that of a distorted tetrahedron.[51] The X-ray data indicates that two ^{17}O NMR sites are expected for this sample.

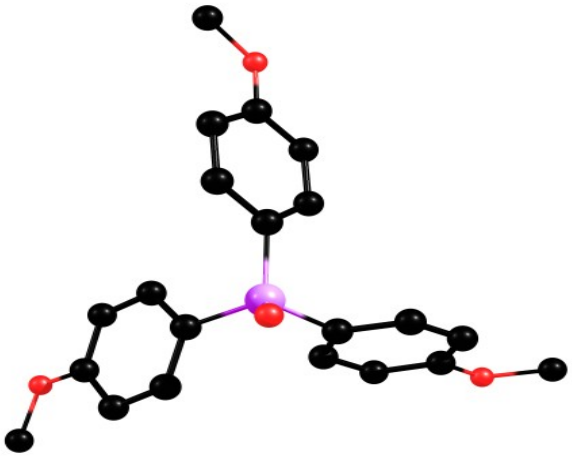

Figure 5.3. Molecular structure of ^{17}OP(*p*-Anis)$_3$.

Figures 5.4-5.5 show the ^{17}O MAS NMR spectra of ^{17}OP(*p*-Anis)$_3$ at 11.75 and 7.05 T along with simulated spectra, obtained using the parameters given in Table 5.1. These spectra provide δ_{iso}, the magnitude of C_Q and η_Q.

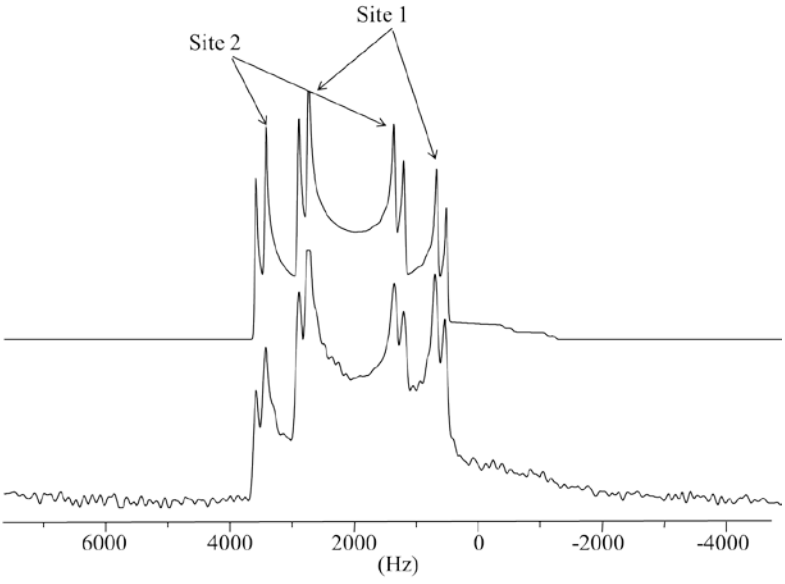

Figure 5.4. Experimental (lower trace) and simulated (upper trace) ^{17}O MAS NMR spectra of ^{17}OP(*p*-Anis)$_3$ at 11.75 T, ν_{rot} = 9 kHz. Note, within experimental error the two sites have identical C_Q values but isotropic chemical shifts that differ by 10.2 ± 2 ppm.

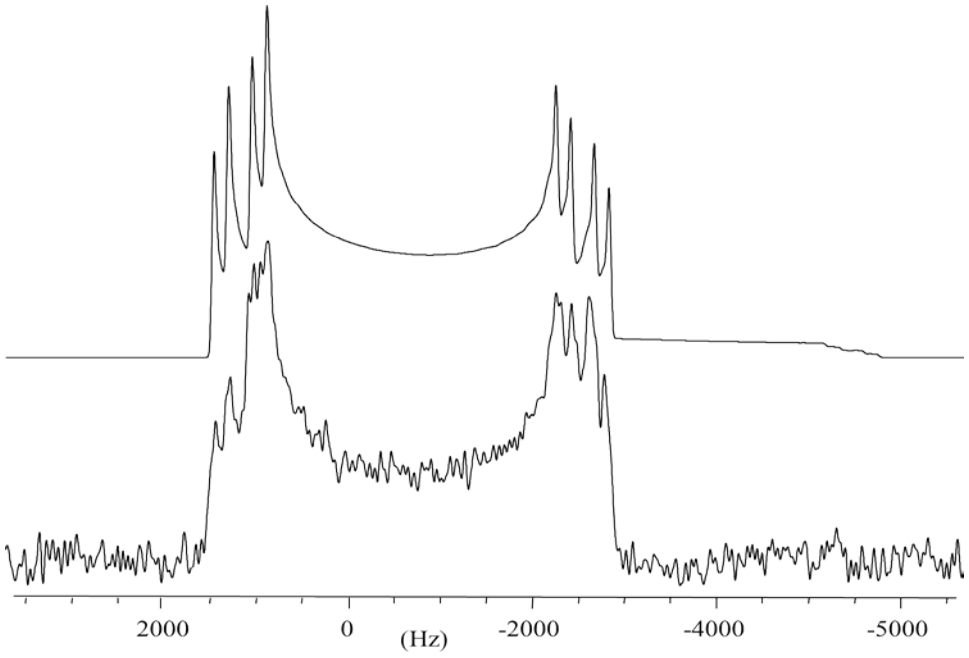

Figure 5.5. Experimental (lower trace) and simulated (upper trace) ^{17}O MAS NMR spectra of ^{17}OP(*p*-Anis)$_3$ at 7.05 T, ν_{rot} = 9 kHz.

NMR experimental results confirm the presence of two sites in the phosphine oxide ligand. It can be seen from NMR experimental results that the second-order quadrupolar interaction dominates the observed central transition lineshape. Results from the fits are summarized in Table 5.1.

After obtaining the values of δ_{iso}, C_Q, and η from an analysis of the MAS spectra, we now can analyze static ^{17}O NMR spectra to determine the CS tensor components. Figure 5.6 shows the static ^{17}O NMR spectrum of OP(*p*-Anis)$_3$ the frequency range of the static NMR spectrum is much larger than that of the MAS spectrum, indicating the presence of CSA. Analysis of the static NMR spectrum of OP(*p*-Anis)$_3$ is rather difficult since there are two ^{17}O NMR sites. Careful analysis of these spectra with the aid of calculated results, used as a starting point, yields the principal components of the ^{17}O CS tensor for OP(*p*-Anis)$_3$: site **1**: δ_{11} = 115 ± 2, δ_{22} = 22 ± 2, δ_{33} = 22 ± 2 ppm, site **2** : δ_{11} = 123 ± 3, δ_{22} =7 ± 1, δ_{33} = 7 ± 2 ppm.

Table 5.1. Experimental Oxygen-17 Chemical Shift Tensors and Quadrupolar Parameters for $^{17}OP(p\text{-Anis})_3$.

	Site 1	Site 2
C_Q (MHz)	4.7 ± 0.1	4.7 ± 0.1
η	0	0
δ_{iso} (ppm)	51.5 ± 2	61.7 ± 2
Ω (ppm)	93 ± 2	116 ± 3
κ	-1	-1

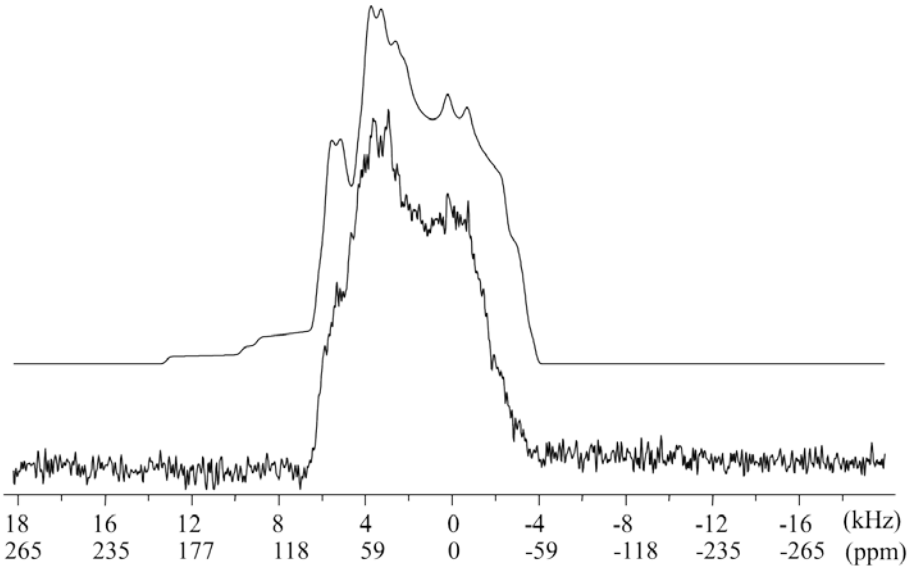

Figure 5.6. Experimental (lower trace) and simulated (upper trace) ^{17}O MAS NMR spectra of a stationary sample of $^{17}OP(p\text{-Anis})_3$ at 11.75 T.

b) $InI_3[^{17}OP(p\text{-Anis})_3]_2$

Five-coordinate indium(III) triiodide *tris* (4-methoxyphenyl) phosphine oxide, $I_3In[^{17}OP(p\text{-Anis})_3]_2$ is described as trigonal bipyramidal about the In centre. Single-crystal X-ray diffraction data for $InI_3[^{17}OP(p\text{-Anis})_3]_2$ indicate that there is one unique In site with D_3 molecular symmetry with the linear P-O-In-O-P fragment coincident with the C_3 axis. The structure of this compound is shown in Figure 5.7. The $C_Q(^{115}In)$ value for this complex reported by Chen *et al.*, 200.0

± 4.0 MHz, is the largest value found for the four compounds, {$In(acac)_3$, $In(trop)_3$, $InI_3[OP(p\text{-}Anis)_3]_2$, and $InCl_3(TMP)$ in their study. Also, the indium of this complex is the most shielded and has the largest shielding anisotropy, 550 ± 80 ppm, of these four complexes.

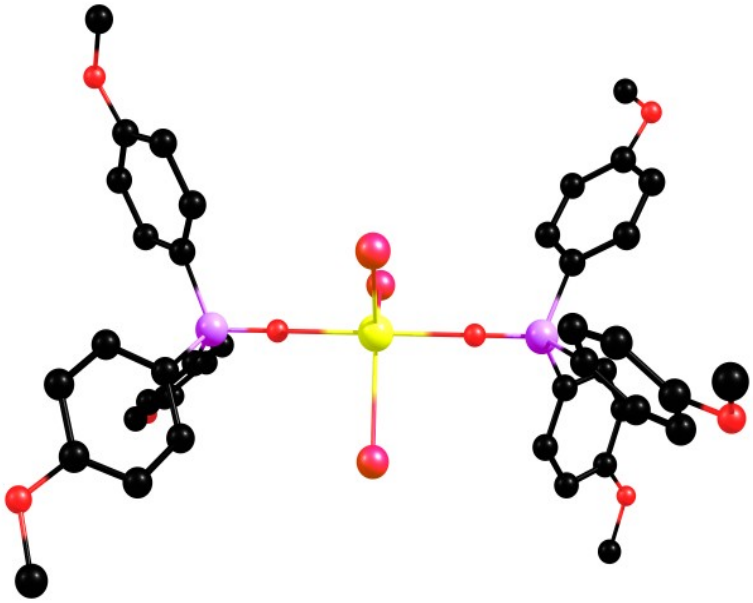

Figure 5.7. Molecular structure of $InI_3[^{17}OP(p\text{-}Anis)_3]_2$

Figures 5.8 and 5.9 show the experimental and simulated ^{17}O MAS NMR spectra for $InI_3[^{17}OP(p\text{-}Anis)_3]_2$ at 11.75 and 7.05 T, respectively. From the MAS lineshape, three ^{17}O NMR spectral parameters, C_Q, η, and δ_{iso} can be obtained in a straightforward fashion. Table 5.2 lists the results from such an analysis. The observed δ_{iso} value is different from that for the ligand compound, reflecting the different bonding about the oxygen. The asymmetry parameter, η = 0, is also consistent with the crystallographic structure which has a C_3 axis along the P-O-In bond. The larger value of $C_Q(^{17}O)$ for the complex compared to that for the ligand shows that the EFG is quite sensitive to changes in structure.

After obtaining the values of δ_{iso}, C_Q, η from an analysis of MAS spectra, we now can analyze static ^{17}O NMR spectra (Figure 5.10 and 5.11) to determine the remaining ^{17}O CS tensor data.

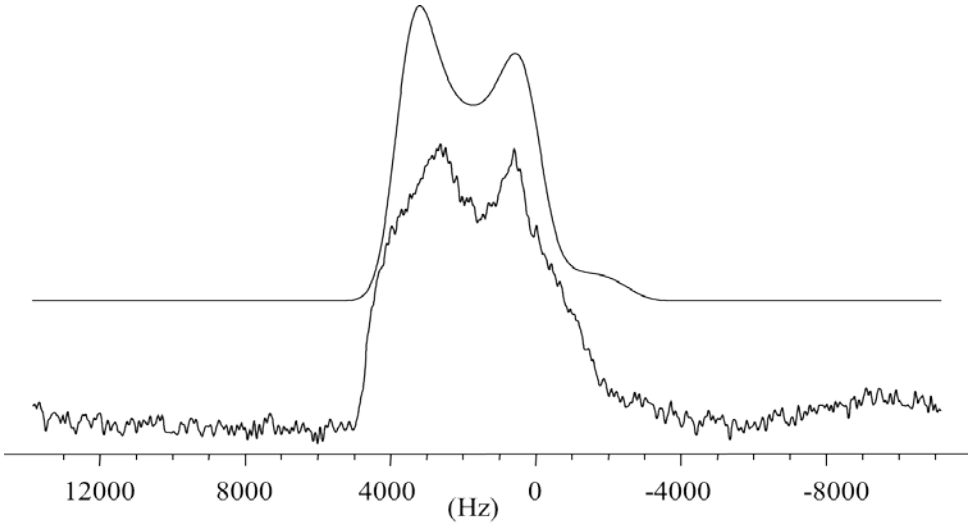

Figure 5.8. Experimental (lower trace) and simulated (upper trace) ^{17}O MAS NMR spectra of $InI_3[^{17}OP(p\text{-Anis})_3]_2$ at 11.75 T and ν_{rot} = 12 kHz.

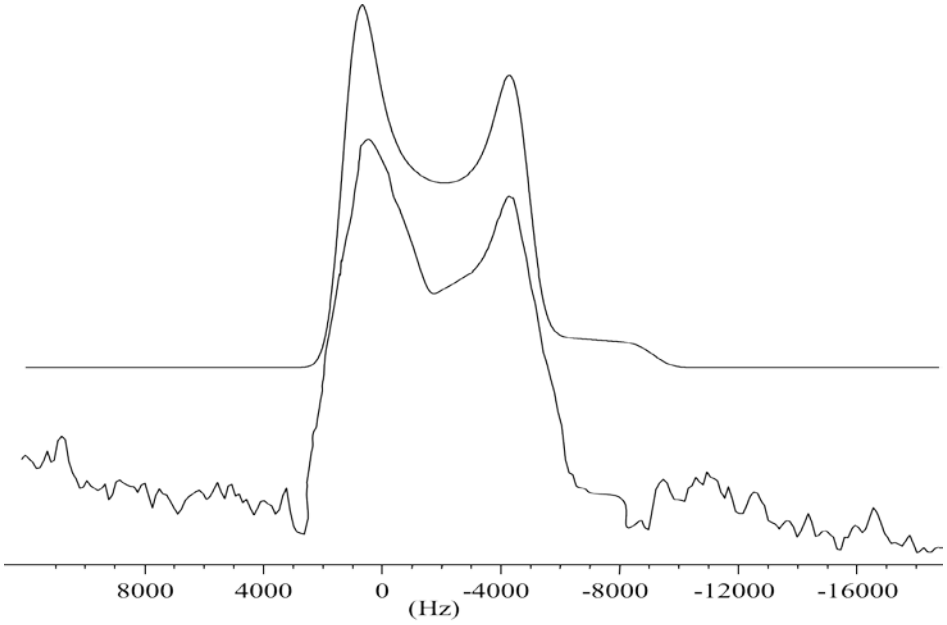

Figure 5.9. Experimental (lower trace) and simulated (upper trace) ^{17}O MAS NMR spectra of $InI_3[^{17}OP(p\text{-Anis})_3]_2$ at 7.05 T and ν_{rot} = 11 kHz.

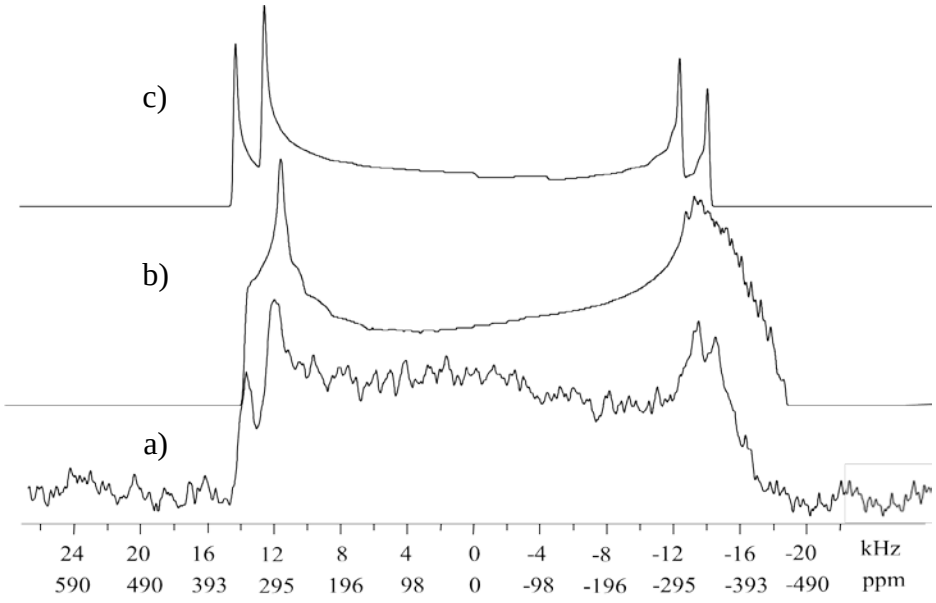

Figure 5.10. a) Experimental oxygen-17 NMR spectrum of a stationary powdered sample of $InI_3[^{17}OP(p\text{-Anis})_3]_2$ at 7.05 T, b) the simulated spectrum including the effect of the EFG and CS interactions and $^1J(^{115}In, ^{17}O)$, c) as for b) but with $^1J(^{31}P, ^{17}O)$ instead of $^1J(^{115}In, ^{17}O)$.

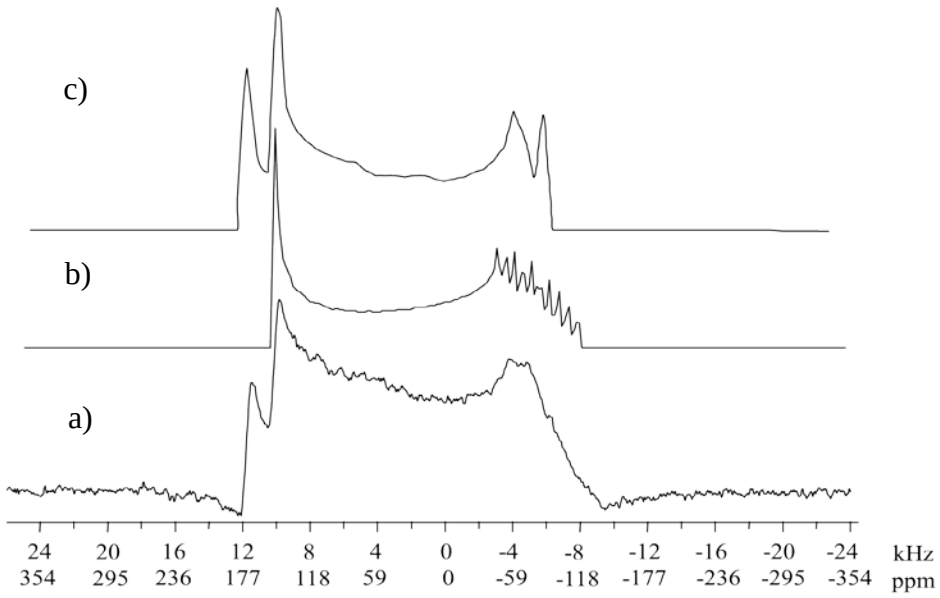

Figure 5.11. a) Experimental oxygen-17 NMR spectrum of a stationary powdered sample of $InI_3[^{17}OP(p\text{-Anis})_3]_2$ at 11.75 T, b) simulated spectrum including the effect of the EFG and CS interactions and $^1J(^{115}In, ^{17}O)$, c) as for b) but with $^1J(^{31}P, ^{17}O)$ instead of $^1J(^{115}In, ^{17}O)$.

Shown in Figures 5.10 and 5.11 are experimental and simulated spectra of a stationary powdered sample of $InI_3[^{17}OP(p\text{-Anis})_3]_2$ obtained with an external applied magnetic field of 7.05 and 11.75 T, respectively. Simulated spectra were calculated using the parameters summarized in Table 5.2.

Analysis of ^{17}O NMR spectra of stationary powdered sample at 7.05 T and 11.75 T allowed for the determination of the principal components of the oxygen chemical shift tensor, $\delta_{22} = \delta_{33} = 52$ ppm, $\delta_{11} = 102$ ppm. The span of the oxygen CS tensor is 50 ppm.

A difficulty in simulating the ^{17}O static spectra is the low signal to noise ratio which is due to low enrichment levels of these oxygen-17 labelled samples. Another major issue for simulating the static spectra of $InI_3[^{17}OP(p\text{-Anis})_3]_2$ is the lack of some simulation features in current simulation software. The ^{17}O NMR measurements of the phosphine-oxide indium dimer, $InI_3[^{17}OP(p\text{-Anis})_3]_2$ indicate that one must consider the second-order quadrupolar interaction, anisotropic magnetic shielding, and spin-spin interactions to both ^{31}P and ^{115}In. However the current simulation software only allows us to simulate the effect of ^{115}In and ^{31}P on ^{17}O spectra one at a time.

Table 5.2. Experimental Oxygen-17 Chemical Shift and Quadrupolar Parameters for $InI_3[^{17}OP(p\text{-Anis})_3]_2$.

C_Q (MHz)	5.8 ± 0.2	$^1J(^{17}O, ^{31}P)$ (Hz)	150 ± 30
η	0.0	$^1J(^{17}O, ^{115}In)$ (Hz)	250 ± 30
δ_{iso}(ppm)	69 ± 2	$R_{dd}(^{17}O, ^{31}P)$ (Hz)	1990 ± 20
Ω (ppm)	50 ± 2	$R_{dd}(^{17}O, ^{115}In)$(Hz)	300 ± 20
κ	-1.0		

The direct dipolar coupling constants, $R_{dd}(^{17}O,^{31}P)$ and $R_{dd}(^{17}O,^{115}In)$ are obtained from bond lengths determined in X-ray crystallography. For the magnitude of the indirect dipolar coupling, $J(^{17}O, ^{31}P)$ and $J(^{17}O, ^{115}In)$, the calculated value (obtained from ADF) are set as primary values and then the best

fit data are generated for simulation of stationary spectra at both fields. The value for $J(^{17}O, ^{31}P)$ is typical of known results for similar compounds provided in the literature. Parameters obtained from the best-fit simulated spectrum for $InI_3[^{17}OP(p\text{-Anis})_3]_2$ indicate that the CS tensor is axially symmetric, and the skew of the CS tensor is -1.0, which is consistent with crystallographic structure which has a C_3 axis along the In-O-P bond; this means that δ_{11} is the unique component of the CS tensor, coincident with V_{zz}. The span of the oxygen CS tensor for the complex is much smaller than those for the ligand, which indicates different chemical environment at oxygen site for the complex compound.

Figures 5.10-5.11 show the breadth and lineshape of ^{17}O NMR spectra of a stationary sample of $InI_3[^{17}OP(p\text{-Anis})_3]_2$. The broadening is mainly dominated by the quadrupolar interaction and then by CS and coupling to ^{31}P and ^{115}In. Some of the details in the experimental spectra are obscured because of the low signal to noise ratio.

To demonstrate how the individual NMR interactions contribute to the observed static ^{17}O NMR spectrum, the spectra that would arise for indirect and direct coupling, CS and quadrupole interaction, as well as the sum of all these contribution is shown in Figure 5.12. This shows that the total line shape has no resemblance to any of the individual contributions, which means that the spectrum is not dominated by any single interaction.

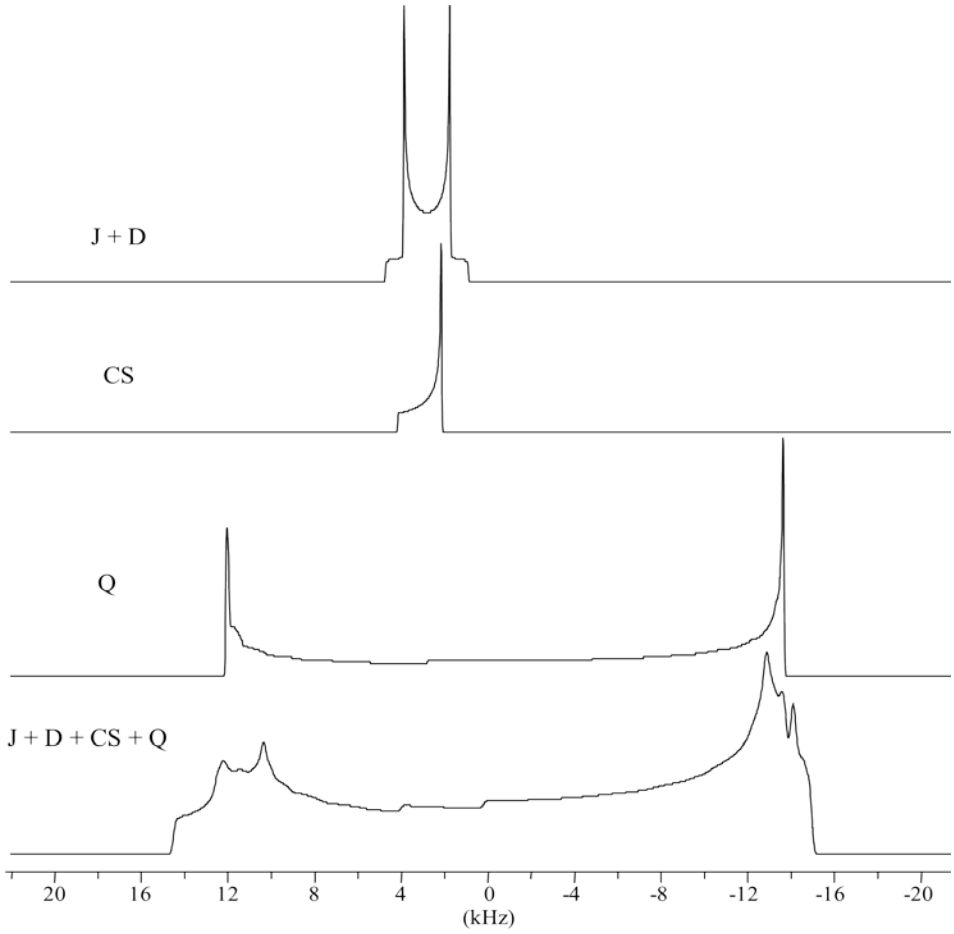

Figure 5.12. Simulated ^{17}O NMR spectra of $InI_3[^{17}OP(p\text{-Anis})_3]_2$ at 7.05 T, showing the individual contributions of indirect and dipolar coupling (J + D), chemical shift anisotropy (CS), and quadrupolar coupling (Q) to the static NMR line shape.

5.4.2. Theoretical Calculations

Another objective of the present work is to evaluate the quality of quantum chemical calculations for ^{17}O EFG and CS tensors for the ligand and complex compounds under study. For this purpose, in this section, extensive DFT computations of ^{17}O EFG and CS tensors for $^{17}OP(p\text{-Anis})_3$ and $InI_3[^{17}OP(p\text{-Anis})_3]_2$ using the geometries obtained from X-ray diffraction are presented. To supplement the experimental data two types of DFT calculations are performed. One is to use ZORA as incorporated in the ADF package and the other to employ the B3LYP functional as implemented in the Gaussian03 package.

The $^{1}J(^{17}O,^{115}In)$ and $^{1}J(^{17}O,^{31}P)$ for the complex were also calculated using the ADF package. The FC, SD, PSO and DSO mechanisms were included in the latter calculations.

5.4.2.1. DFT Calculations for $^{17}OP(p\text{-Anis})_3$

The results of B3LYP and ZORA calculations of ^{17}O CS and EFG tensors are summarized in Table 5.3 for $^{17}OP(p\text{-Anis})_3$. Experimental results are also shown for comparison.

One striking aspect of the calculations is the lack of quantitative agreement between the experimental and theoretical values of the ^{17}O quadrupolar coupling constant. While the experimental value is approximately -4.7 MHz, all of the calculated values except the one calculated by ZORA are significantly larger in magnitude than the experimental value. For DFT Gaussian methods, the value of C_Q generally decreases as the size of basis set is increased. For Gaussian calculations with the large basis set, the calculated value of C_Q is in better agreement with the experimental value compare to those calculated using small basis sets.

One of the methods suggested in the literature for obtaining accurate calculated oxygen-17 nuclear quadrupolar coupling constants is to use a calibrated ^{17}O nuclear quardupole moment, instead of the accepted experimental value of Q = -2.558 fm^2.[58] Calculated EFG tensor components (V_{XX}, V_{YY}, V_{ZZ}) are related to the nuclear quadrupole coupling parameters in the following fashion:

$$C_Q \text{ (MHz)} = -2.3496 \times Q(^{17}O)(\text{fm}^2) \times V_{ZZ} \text{ (a.u.)}$$

Slightly better agreement can be obtained between the calculated and observed C_Q values if a calibrated $Q(^{17}O)$ = - 2.40 fm^2 is used [58] to convert the computed electric field gradients to C_Q. The sign of C_Q, which cannot be determined from analysis of our spectra, is calculated as negative and it is consistent in all the basis set calculation results. Figure 5.13 shows a comparison between experimental and computed C_Qs for $^{17}OP(p\text{-Anis})_3$.

Table 5.3. DFT Calculations of the Oxygen-17 EFG and CS Tensors Parameters for ^{17}OP(*p*-Anis)$_3$.

Basis set	C_Q[a] /MHz	C_Q[b] /MHz	η_Q	δ_{iso} /ppm	σ_{iso} /ppm	Ω /ppm	κ	$\alpha°$	$\beta°$	$\gamma°$
6-31G	-9.8	-9.4	0	30	257	192	-1	2	88	0
6-31G(d)	-5.8	-5.6	0	35	252	106	-1	2	89	0
6-31G(d,p)	-5.8	-5.6	0	37	250	106	-1	2	89	0
6-31++G(d,p)	-5.8	-5.6	0	38	249	87	-1	2	89	0
6-311G	-10	-9.6	0	32	255	206	-1	1	89	0
6-311G(d)	-6.3	-6.0	0	37	250	105	-1	1	89	0
6-311+G	-10.4	-10.0	0	36	251	200	-1	1	89	0
6-311+G(d)	-6.3	-6.0	0	37	250	107	-1	0	88	1
6-311++G(d,p)	-5.1	-4.9	0	48	239	103	-1	0	90	0
6-31+G(3df,3pd)	-5.0	-4.7	0	49	238	87	-1	0	90	0
cc-pVTZ	-6.4	-6.2	0	40	247	115	-1	0	89	0
ZORA/QZ4P	-4.9	-4.7	0	67	220	102	-1	0	90	0
expt	-4.7	-4.7	0	51	236	93	-1	0	90	0

[a] Calculated using the standard value of $Q(^{17}O)$, -2.558 fm^2. [b] Calculated using the calibrated value of $Q(^{17}O)$, -2.40 fm^2.[58]

The experimental and calculated isotropic chemical shifts are shown in Table 5.3; overall the magnetic shielding values are generally overestimated. The skew of the oxygen CS tensor, about -1.0 is reproduced with great accuracy by all of the basis sets and method. A comparison between experimental and computed Ω and δ_{iso} for ^{17}OP(*p*-Anis)$_3$ is shown in Figure 5.14. The calculated Euler angles which define the rotations required to bring the PAS of the EFG tensor into coincidence with that of the CS tensor are as follow, $\alpha = 0°$, $\beta = 90°$, $\gamma = 0°$ which means that δ_{11} and V_{zz} are coincident.

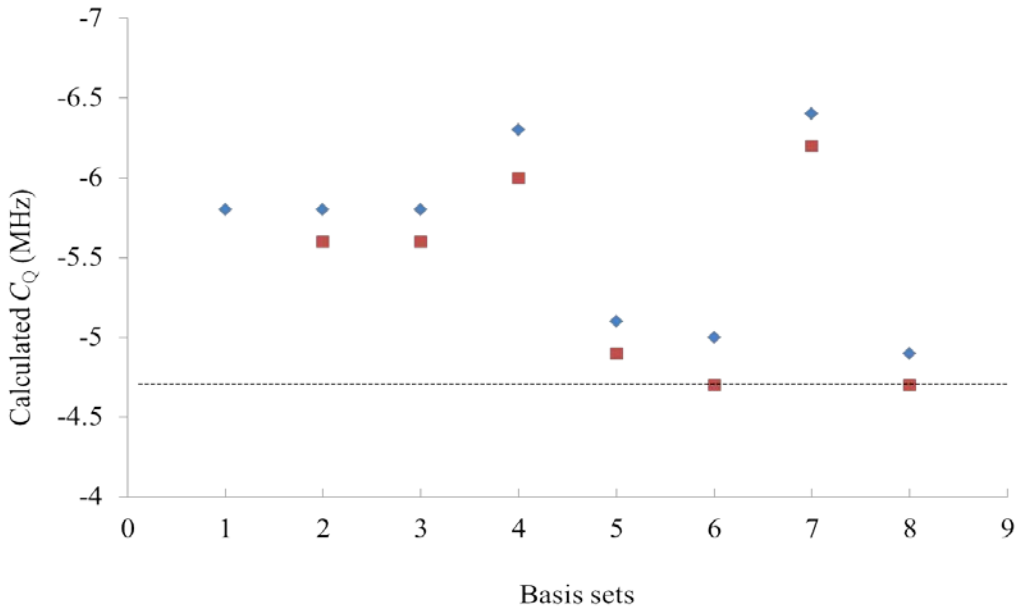

Figure 5.13. Calculated quadrupolar coupling constant C_Q (MHz). ♦ using the standard value of Q, ■ using the calibrated value of Q with different basis sets (1 = 6-31G(d), 2 = 6-31G(d,p), 3 = 6-31++G (d,p), 4 = 6-311G(d), 5 = 6-311+G(d), 6 = 6-311++G(d,p), 7 = 6-31+G(3df,3pd), 8 = ZORA/QZ4P. The horizontal line indicates the experimental values, assumed to be negative.

Overall the ZORA/QZ4P and Gaussian calculations at the 6-311++G(d,p) and 6-31+G(3df,3pd) levels show good agreement for both ^{17}O EFG and CS tensors. The absolute orientation of the ^{17}O CS and EFG tensors in the molecular framework, determined from the DFT/6-311++G(d,p) level, is shown in Figure 5.15. Since the asymmetry of the EFG tensor is zero, the V_{XX} and V_{YY} components are equal and are in a plane prependicular to P-O bond. The value of the skew = -1 obtained from calculations indicates that the δ_{11} is the unique component of the CS tensor, coincident with the V_{ZZ} component of EFG tensor.

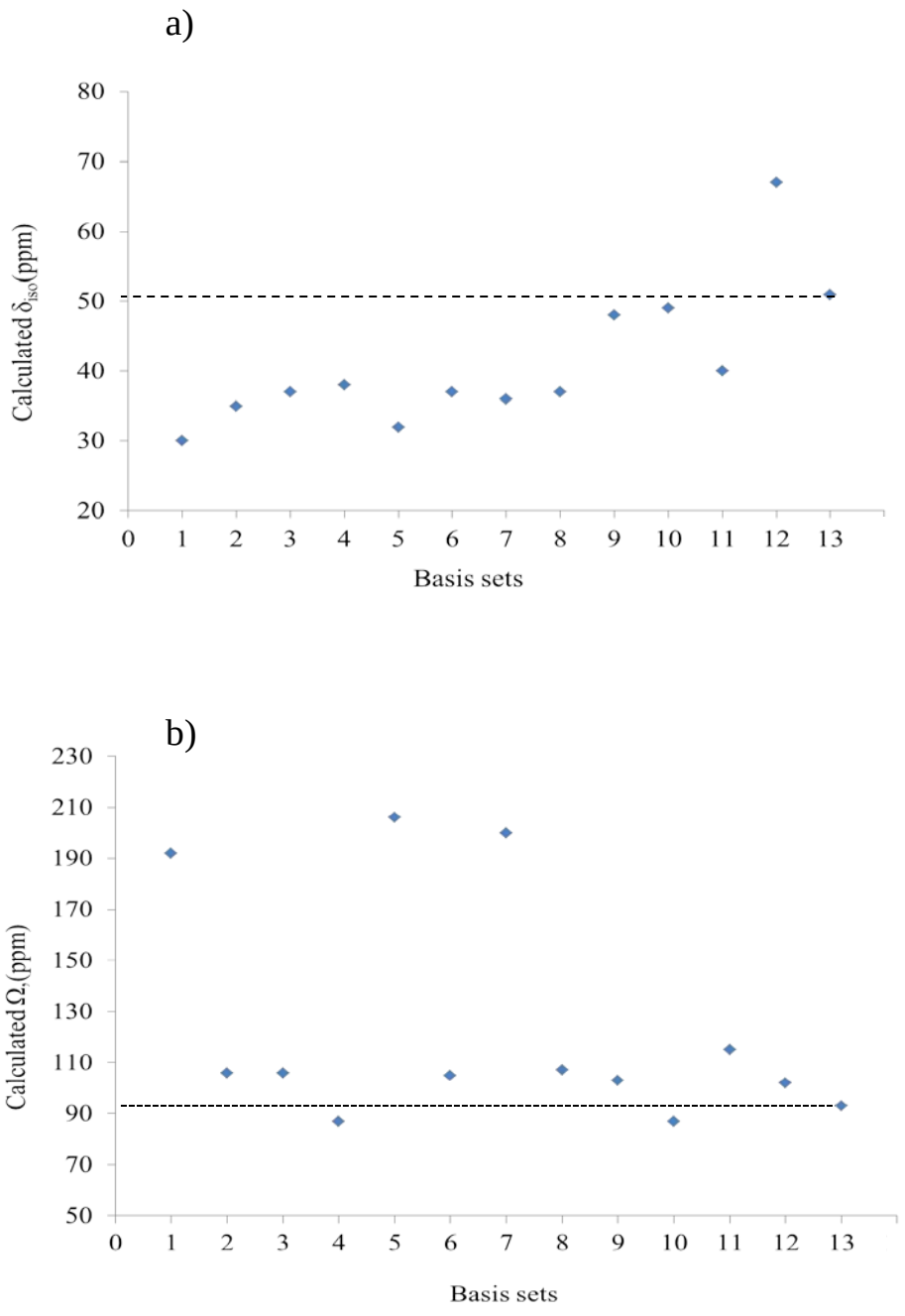

Figure 5.14. Calculated a) isotropic chemical shift and b) span with different basis sets, 1= 6-31G, 2 = 6-31G(d), 3 = 6-31G(d,p), 4 = 6-31++G (d,p), 5 = 6-311G, 6 = 6-311G(d), 7 = 6-311+G, 8 = 6-311+G(d), 9 = 6-311++G(d,p), 10 = 6-31+G(df,2pd), 11 = cc-pVDZ, 12 = ZORA/QZ4P, 13 = experimental value. The horizontal line indicates the experimental values.

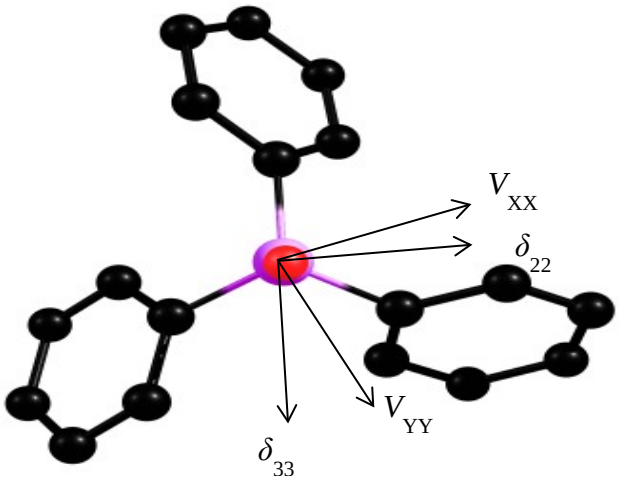

Figure 5.15. Calculated DFT/ 6-311++G(d,p) orientations of the ^{17}O chemical shift and EFG tensors for ^{17}OP(*p*-Anis)$_3$. The δ_{11} and V_{ZZ} components are along the P-O bond which is shown perpendicular to the plane in above picture.

The oxygen CS tensor span, 93 ppm, is small compared to the span values (135, and 155 ppm) reported by Bryce *et al*., for triphenylphosphine oxide. They are much smaller than those for carbonyl oxygen nuclei in organic compounds (for example $\Omega(^{17}O)$ = 1062 ppm for benzophenone-^{17}O).[10] An ^{17}O NMR study on amides by Wu and co-workers[17,18] showed that the span of the oxygen CS tensor generally ranges from 500 to 630 ppm. The span seems to be decreased to 270 ppm for thymine,due to intermolecular hydrogen bonding. However, in ^{17}OP(*p*-Anis)$_3$ the value of Ω for the terminal PO oxygen nuclei seems to be lower than those terminal C=O oxygen nuclei even in the absence of the hydrogen bonding to oxygen. This conclusion is confirmed by *ab initio* calculations performed by Power[59] which indicate the small span for the phosphine oxides is due to the lack of multiple bonding character for the phosphorus and oxygen atoms. The isotropic chemical shift, 51 ppm, obtained in this study may be contrasted with those of carbonyl compounds (350 to 600 ppm) reported in the literature.[60]The differences between the terminal oxygen CS tensors for phosphine oxides and carbonyl

groups can be understood by the nuclear magnetic shielding theory of Ramsey[61] (see section 2.1.4).[62] For example, in formaldehyde the span of the oxygen shielding tensor is 1530 ppm, as determined from spin-rotation tensor measurements.[63]The oxygen chemical shift tensor in carbonyl compounds is mainly dominated by a paramagnetic contribution of magnetic dipole-allowed mixing of $n \rightarrow \pi^*$ MO, which results in large deshielding along the C-O bond.[62] In contrast, all three components of the oxygen shielding tensor in $^{17}OP(p\text{-Anis})_3$ are close to the free atom value for oxygen (395.1 ppm).[64]This indicates a lack of a significant paramagnetic contribution due to the lack of availability of low-lying virtual orbitals of appropriate symmetry. This in turn may be attributed to the polarized single σ-bond, $R_3P^+ - O,^-$ as suggested by Rai and Symons,[65] and Dobado *et al*.,[66] who propose that a singly polarized σ-bond perhaps is the most appropriate representation.

5.4.2.2. DFT Calculations for $InI_3[^{17}OP(p\text{-Anis})_3]_2$

DFT calculations of ^{17}O EFG and CS tensors were performed using the geometries of the $InI_3[^{17}OP(p\text{-Anis})_3]_2$ obtained from X-ray diffraction.[30] Results are summarized in Table 5. 4.

All calculations predict the $\alpha \approx 0°$, $\beta = 90°$, $\gamma \approx 0°$ between the ^{17}O EFG and CS tensors, in excellent agreement with the experimental results. The B3LYP calculations for most of the basis sets overestimate the isotropic magnetic shielding value compared to the experimental value. The calculated span of the oxygen chemical shift tensor is overestimated for the majority of basis sets; however the value of skew is in excellent agreement with the experimental result, as expected from molecular symmetry. The $\kappa = -1$, indicates that δ_{11} is the unique component of the axially-symmetric CS tensor, thus, V_{ZZ} is coincident with δ_{11}. Comparison between experimental and computed δ_{iso} for $InI_3[^{17}OP(p\text{-Anis})_3]_2$ is shown in Figure 5.16 a.

Table 5.4. DFT Calculations of the Oxygen-17 EFG and CS Tensor Parameters for $InI_3[^{17}OP(p\text{-Anis})_3]_2$

Basis set[c]	C_Q[a] /MHz	C_Q[b] / MHz	η_Q	δ_{iso} /ppm	σ_{iso} /ppm	Ω /ppm	κ	$\alpha°$	$\beta°$	$\gamma°$
6-31G(d)	-6.9	-6.4	0	26	261	80	-1	14	90	0.3
6-31G(d,p)	-6.9	-6.4	0	26	261	80	-1	14	90	0.3
6-31++G(d,p)	-6.9	-6.4	0	40	247	78	-1	13	90	0.1
6-31+G(df,2pd)	-6.8	-6.4	0	58	229	78	-1	13	90	0
6-311G	-10.3	-9.6	0	38	251	80	-1	8	90	0.1
6-311+G	-10.3	-9.6	0	37	250	80	-1	8	90	0.1
6-311G(d)	-7.3	-6.8	0	38	249	69	-1	7	90	0.1
6-311+G(d)	-7.3	-6.8	0	38	249	69	-1	7	90	0.1
6-311G(d,p)	-7.4	-6.9	0	51	236	60	-1	7	90	0.1
6-311+G (d,p)	-7.3	-6.8	0	68	239	68	-1	7	90	0.1
6-311++G(d,p)	-6.9	-6.5	0	68	239	64	-1	3	90	0
6-311+G(3df,3pd)	-6.6	-6.2	0	63	224	63	-1	3	90	0
cc-pVTZ	-6.9	-6.5	0	67	220	47	-1	0	90	0
cc-pVQZ	-6.8	-6.4	0	65	222	45	-1	0	90	0
ZORA/QZ4P	-6.4	-6.0	0	77	210	42	-1	0	90	0
expt	-5.8	-5.8	0	69	218	50	-1	0	90	0

[a] Calculated using the standard value of $Q(^{17}O)$, -2.558 fm^2. [b]Calculated using the calibrated value of $Q(^{17}O)$, -2.40 fm^2. [c] Basis set used for ^{17}O and P. For the remaining atoms,3-21G was used for In and I and 6-311G used for C, H, and O on the Anis.

For the ^{17}O EFG tensor, as shown in Table 5.4, the calculated C_Q obtained using the standard Q are much larger than the experimental value even for the largest basis sets. Using the calibrated Q = -2.4 fm^2 improves the values of C_Q to much better agreement with the experimental value. The comparison between calculated C_Q and the experimental value is shown in Figure 5.16 b. For the asymmetry parameter of the EFG tensor, all calculation methods and basis sets reproduce the experimental value of $\eta = 0$.

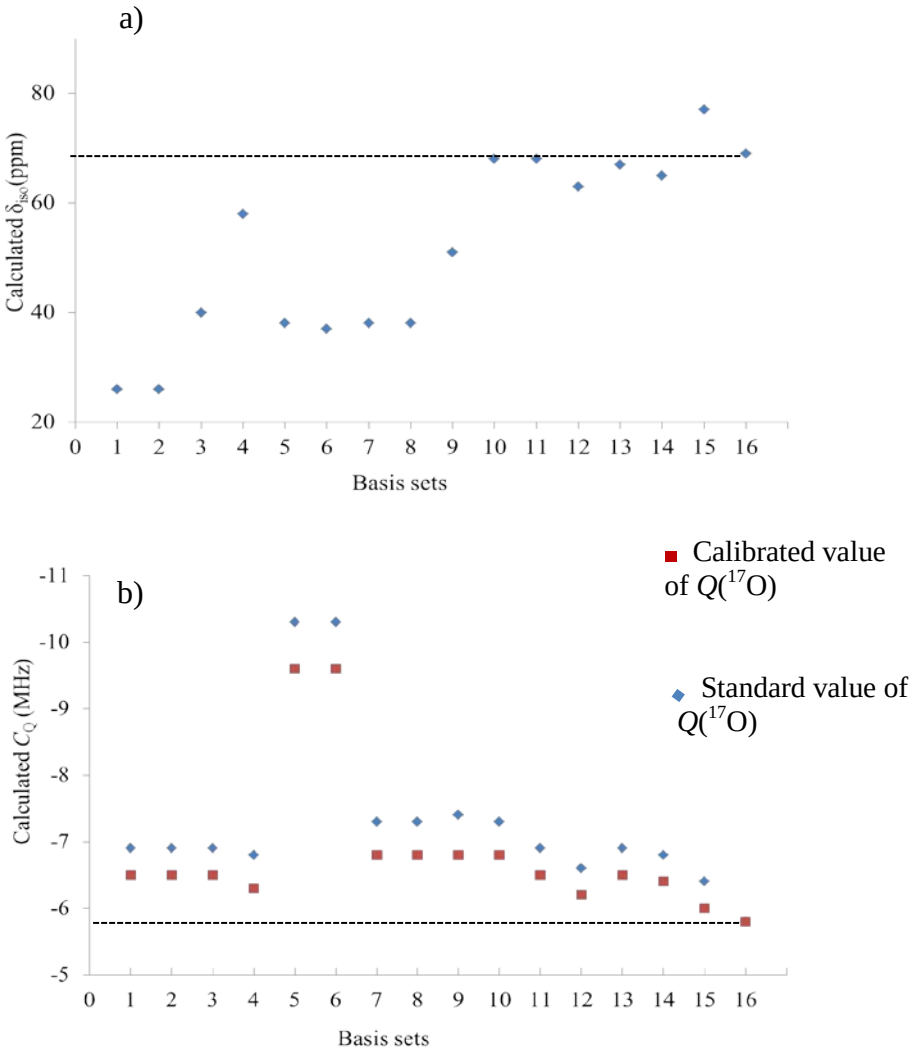

Figure 5.16. Calculated a) isotropic chemical shift and b) quadrupolar coupling constant C_Q (MHz) with different basis sets, 1= 6-31G(d), 2 = 6-31G(d,p), 3 = 6-31++G(d,p), 4 = 6-31+G(df,2pd), 5 = 6-311G, 6 = 6-311+G, 7 = 6-311G(d), 8 = 6-311+G(d), 9 = 6-311G(d,p), 10 = 6-31++G(d,p), 11= 6- 311++G(d,p), 12 = 6-311+G(3df,3pd) 13 = cc-pVTZ , 14 = cc-pVDZ, 15 = ZORA/QZ4P, 16 = experimental value. The horizontal line indicates the experimental value.

As seen from Table 5.4, the calculated ^{17}O NMR tensors are generally in good agreement with the experimental values. However, the best theoretical results are obtained using the ADF and B3YLP method at 6-311++G(d,p) and 6-311+G(3df,3pd) levels. The LANL2DZ effective core potential (ECP)[67] basis set was also used for all atoms to calculate ^{17}O NMR tensor parameters. However, the calculated results (data not shown) are drastically different from those reported in Table 5.4, suggesting that the LANL2DZ ECP may not be a good alternative basis set in the calculation of the ^{17}O NMR tensors. In addition, the effect of using different available Gaussian basis sets on a heavy atom such as In and I is negligible on ^{17}O NMR tensor calculations, (not shown here).

Phosphorus-oxygen and indium-oxygen indirect nuclear spin-spin coupling, $J_{iso}(^{31}P,^{17}O)$ = 180 Hz, $J_{iso}(^{115}In,^{17}O)$ = 270 Hz, were calculated by ZORA/ QZ4P. The value of $J_{iso}(^{31}P, ^{17}O)$ = 180 Hz lie within the known range of values for $J_{iso}(^{31}P,^{17}O)$ in phosphine oxides and related systems containing the P-O moiety, 81-220 Hz.[68] These values obtained from the calculation were used in the simulation of the stationary spectra of $InI_3[^{17}OP(p\text{-Anis})_3]_2$ discussed in the experimental section of this study.

5.5. Conclusions

In this study, an experimental determination of the ^{17}O CS and EFG tensors of ligand and of $InI_3[^{17}OP\text{-}(p\text{-}Anis)_3]_2$ has been presented. The results represent the first set of ^{17}O NMR tensor data for this class of compounds. The CS results show the bonding of oxygen to indium has a significant effect on the ^{17}O isotropic chemical shift of the complex. A similar result was obtained for the ^{17}O nuclear quadrupolar coupling constants, which increased in value by approximately 0.7 MHz in the complex. Theoretical calculations qualitatively reproduce the available experimental ^{17}O EFG and CS tensors, including their relative orientations. In general, the DFT calculations of ^{17}O EFG and nuclear magnetic shielding tensors reproduce the experimental values with good agreement if moderately large basis sets are used.

5.6. References

[1] B. L. Silver, Z. Luz. *Quart. Rev*. **21**, 458, (1967).

[2] W. G. Klemperer. *Angew*. *Chem. Int. Ed. Engl*. **17**, 246, (1978).

[3] J. P. Kintzinger, P. Diehl, E. Fluck, R. Kosfeld. *NMR Basic Principles and Progress*; Springer-Verlag: Berlin, 1981.

[4] S. E. Ashbrook, A. J. Berry, S. Wimperis. *Am. Mineral*, **84**, 1191, (1999).

[5] N. Godbout, K. L. Sanders, R. Salzmann, R. H. Havlin, M. Wojdelski, E. Oldfield. *J. Am. Chem. Soc.* **121**, 3829, (1999).

[6] R. Hussein, R. Dupree, D. Holland. *J . Non-Cryst. Solids*, 246, 159, (1999).

[7] D. M. Pickup, G. Mountjoy, G. W. Wallidge, R. Anderson, J. M. Cole, R. J. Newport, M. E. Smith. *J. Mat. Chem*, **9**, 1299, (1999).

[8] S. Schramm, E. Oldfield. *J. Am. Chem. Soc*. **106**, 2502, (1984).

[9] S. Schramm, R. J. Kirkpatrick, E. Oldfield. *J. Am. Chem. Soc.* **105**, 2483,(1983).

[10] W. Scheubel, H. Zimmermann, U. Haeberlen. *J. Magn. Reson*. **63**, 544, (1985).

[11] K. T. Mueller, Y. Wu, B. F. Chmelka, J. Stebbins, A. Pines. *J. Am. Chem. Soc*. **113**, 32, (1991).

[12] A. Samoson, E. Lippmaa, A. Pines. *Mol. Phys*. **65**, 1013, (1988).

[13] B. F. Chmelka, K. T. Mueller, A. Pines, J. Stebbins, Y. Wu, J. W. Zwanziger, *Nature* (London), **339**, 42, (1989).

[14] Y. Wu, B. Q. Sun, A. Pines, A. Samoson, E. Lippmaa. *J. Magn. Reson*. **89**, 297, (1990).

[15] P. J. Grandinetti, J. H. Baltisberger, I. Farnan, J. F. Stebbins, U. Werner, A. Pines. *J. Phys. Chem*. **99**, 12341, (1995).

[16] S. Dong, K. Yamada, G. Wu. *Z. Naturforsch*. **A 55**, 21, (2000).

[17] G. Wu, K. Yamada, S. Dong, H. Grondey. *J. Am. Chem. Soc*. **122**, 4215, (2000).

[18] K. Yamada, S. Dong, G. Wu. *J. Am. Chem. Soc*. **122**, 11602, (2000).

[19] S. Dong, R. Ida, G. Wu. *J. Phys. Chem*. **A 104**, 11194, (2000).

[20] M. Torrent, D. Mansour. E. P. Day, K. Morokuma. *J. Phys. Chem*. **A 105**, 4546, (2001).

[21] G. Wu, S. Dong, R. Ida. *Chem. Commun*. 891, (2001).

[22] G. Wu, S. Dong, R. Ida, N. Reen. *J. Am. Chem. Soc*. **124**, 1768, (2002).

[23] A. P. Howes, R. Jenkins. M. E. Smith, D. H. G. Crout, R. Dupree. *Chem. Commun*, 1448, (2001).

[24] V. Lemaitre, K. J. Pike, A. Watts, T. Anupold. A. Samoson, M. E. Smith, R. Dupree. *Chem. Phys. Lett*, **371**, 91, (2003).

[25] E. Y. Chekmenev. K. W. Waddell, J. Hu, Z. Gan, R. J. Wittebort, T. A. Cross. *J. Am. Chem. Soc*. **128**, 9849, (2006).

[26] K. W. Waddell, E. Y. Chekmenev, R. J. Witterbort. *J. Phys. Chem*. **B 110**, 22935, (2006).

[27] A. Brinkmann, A. P. M. Kentgens. *J. Phys. Chem*. **B 110**, 16089, (2006).

[28] A. J. Carty, D. G. Tuck. *J. Chem. Soc*. **A**, 1081, (1966).

[29] R. L. Wells, S. R. Aubuchon, S. S. Kher, M. S. Lube. *Chem. Mater*. **7**, 793, (1995).

[30] F. Chen, G. Ma, R. G. Cavell, V. V. Terskikh, R. E. Wasylishen. *Chem. Commun*. 5933, (2008).

[31] F. Chen, G. Ma, G. M. Bernard, R. G. Cavell, R. McDonald, M. J. Ferguson, R. E. Wasylishen. *J. Am. Chem. Soc.* **132**, 5479, (2010).

[32] G. Wu, J. Zhu, X. Mo, R. Wang, V. Terskikh. *J. Am. Chem. Soc*. **132**, 5143, (2010).

[33] K. J. D. MacKenzie, M. E. Smith. *Multinuclear Solid State NMR of Inorganic Materials*; Pergamon Press: Oxford, (2002).

[34] D. Freude. *Quadrupole Nuclei in Solid-State NMR*; Encyclopedia of Analytical Chemistry, R Meyers, John Wiley& Sons: Chichester, 2000.

[35] I. P. Gerothanassis, M. Momenteau. *J. Am. Chem. Soc*, **109**, 6944, (1987).

[36] I. P. Gerothanassis, M. Momenteau, B. Loock. *J. Am. Chem. Soc*, **111**, 7006, (1989).

[37] E. R. Andrew, A. Bradbury, R. G. Eades. *Nature*, **182**, 1659, (1958).

[38] D. L. Bryce, K. Eichele, R. E. Wasylishen. *J. Inorg. Chem*, **42**, 5085, (2003).

[39] E. L. Hahn. *Phys. Rev*. **77**, 297, (1950).

[40] A. E. Bennett, C. M. Rienstra, M. Auger, K. V. Lakshmi, R. G. Griffin. *J. Chem. Phys*. **103**, 6951, (1995).

[41] K. Eichele, R. E. Wasylishen. WSOLIDS *NMR Simulation Package*, 2001.

[42] D. W. Alderman, M. S. Solum, D. M. Grant. *J. Chem. Phys*. **84**, 3717, (1986).

[43] ADF 2006.01, Theoretical Chemistry, Vrije Universiteit, Amsterdam, http://www. Scm.com.

[44] Gaussian 03, Revision C.02, M. J. Frisch, G. W. Trucks, H. B. Schlegel, G. E. Scuseria, M. A. Robb, J. R. Cheeseman, J. A. Montgomery, Jr., T. Vreven, K. N. Kudin, J. C. Burant, J. M. Millam, S. S. Iyengar, J. Tomasi, V. Barone, B. Mennucci, M. Cossi, G. Scalmani, N. Rega, G. A. Petersson, H. Nakatsuji, M. Hada, M. Ehara, K. Toyota, R. Fukuda, J. Hasegawa, M. Ishida, T. Nakajima, Y. Honda, O. Kitao, H. Nakai, M. Klene, X. Li, J. E. Knox, H. P. Hratchian, J. B. Cross, V. Bakken, C. Adamo, J. Jaramillo, R. Gomperts, R. E. Stratmann, O. Yazyev, A. J. Austin, R. Cammi, C. Pomelli, J. W. Ochterski, P. Y. Ayala, K. Morokuma, G. A. Voth, P. Salvador, J. J. Dannenberg, V. G. Zakrzewski, S. Dapprich, A. D. Daniels, M. C. Strain, O. Farkas, D. K. Malick, A. D. Rabuck, K. Raghavachari, J. B. Foresman, J. V. Ortiz, Q. Cui, A. G. Baboul, S. Clifford, J. Cioslowski, B. B. Stefanov, G. Liu, A. Liashenko, P. Piskorz, I. Komaromi, R. L. Martin, D. J. Fox, T. Keith, M. A. Al-Laham, C. Y. Peng, A. Nanayakkara, M. Challacombe, P. M. W. Gill, B. Johnson, W. Chen, M. W. Wong, C. Gonzalez, and J. A. Pople, Gaussian, Inc., Wallingford CT, 2004.

[45] S. H. Vosko, L. Wilk, M. Nusair. *Can. J. Phys*, **58**, 1200, (1980).

[46] A. D. Becke. *Phys. Rev.* **A 38**, 3098, (1988).

[47] J. P. Perdew. *Phys. Rev.* **B 33**, 8822, (1986).

[48] A. D. Becke, *J. Chem. Phys*. **98**, 5648, (1993).

[49] C. T. Lee, W. T. Yang, R. G. Parr. *Phys. Rev.* **B 37**, 785, (1988).

[50] R. Ditchfield. *Mol. Phys*. **27**, 789, (1974).

[51] R.F. See, A. D. Dutoi, J. C. Fettinger, P. J. Nicastro, J. W. Ziller. *J. Chem. Crystallogr*. **28**, 893, (1998).

[52] R. E. Wasylishen, S. Mooibroek, J. B. Macdonald. *J. Chem. Phys.* **81**, 1057, (1984).

[53] R. E. Wasylishen, D. L. Bryce. *J. Chem. Phys*. **117**, 10061, (2002).

[54] S. Adiga, D. Aebi, D. L. Bryce. *Can. J. Chem*. **85**, 496, (2007).

[55] N. F. Ramsey. *Phys. Rev*. **91**, 303, (1953).

[56] N. F. Ramsey, E. M. Purcell. *Phys. Rev*. **85**, 143, (1952).

[57] J. Autschbach, T. Ziegler. *J. Chem. Phys*. **113**, 936, (2000).

[58] G. Wu. *Prog. Nucl. Magn. Reson. Spectrosc*. **52**, 118, (2008).

[59] W. P. Power. *J. Am. Chem. Soc*. **117**, 1800, (1995).

[60] J. P. Kintzinger. *NMR of Newly Accessible Nuclei*; P. Laszlo, Academic Press: New York, 1983.

[61] N. F. Ramsey. *Phys. Rev*. **78**, 699, (1950).

[62] M. Schindler, W. Kutzelnigg. *J. Chem. Phys*. **76**, 1919, (1982).

[63] R. Cornet, B. M. Landsberg, G. Winnewisser. *J. Mol. Spectrosc*. **82**, 253, (1980).

[64] G. Malli, C. Froese. *Int. J. Quantum Chem*. **1**, 95, (1967).

[65] U. S. Rai, M. C. R. Symons. *J. Chem. Soc. Faraday Trans*. **90**, 2649, (1994).

[66] J. A. Dobado, H. Martinez-Garcia, J. M. Molina, M. R. Sundberg. *J. Am. Chem. Soc*. **120**, 8461, (1998).

[67] P. J. Hay, W. R. Wadt. *J. Chem. Phys*. **82**, 270, (1985).

[68] H. C. E. McFarlane, W. McFarlane. *J. Chem. Soc. Chem. Commun*. 531, (1978).

Chapter 6. Nitrogen-15, Oxygen-17 and Sodium-23 NMR Studies of Sodium Nitroprusside Dihydrate

6.1. Introduction

Since the initial characterization[1,2] of the nitroprusside ion,$[Fe(CN)_5NO]^{2-}$, it has attracted interest because of its chemical properties.[3,4] The $[Fe(CN)_5NO]^{2-}$ ion has been studied extensively and is used as a vasodilator and hypotensive agent.[5] The nitrosyl, NO, moiety which dominates the chemical and spectral properties of $[Fe(CN)_5NO]^{2-}$ attracts most attention due to its electronic and structural characterization. The reactivity of the nitrosyl moiety, either free or bound to transition metal centres, plays significant roles in chemistry,[6] and particulary in modern biochemistry studies.

Sodium nitroprusside dihydrate, $Na_2[Fe(CN)_5NO]\cdot 2H_2O$ which is often abbreviated as SNP, has become a promising basis for holographic information storage devices with extreme high capacity.[7,8] In 1978, Mössbauer spectroscopy measurments showed that SNP may also be found in long-lived metastable states.[9] In the following years extensive spectroscopic studies have given further insight about SNP.[10,11] The Mössbauer spectrum of 'normal' (ground state) SNP consists of a signal split by the quadrupolar interaction. If a crystal of SNP is irradiated with intense laser light at a temperature $T < 150$ K under appropriate polarization a new state slowly develops which reveals itself in the Mössbauer spectrum by the appearance of an extra pair of lines. This new state persists even after the laser irradiation is stopped, provided the temperature of the sample is kept low enough. If the transition of SNP to the new state involves not only reorienation of the NO group but also a change of its electronic state this would result in a change of the ^{14}N quadrupole coupling constant of the respective nitrogen.

In 1999, an optical spectroscopy investigation of excited electronic states of SNP was undertaken by Imlau *et al.*[12] In this research two metastable electronic states, MS1 and MS2, were obtained in single crystals containing the nitrosyl

anion by exposure in the blue-green spectral range. Irradiation with a laser in the 400 - 540 nm region at 77 K generates a mestastable state in which some of the $[Fe(CN)_5NO]^{2-}$ molecules are transformed into one of its long-lived excited states. The X-ray diffraction studies by Coppens and coworkers[13] reveal that in the MS1 state the NO group is inverted and takes the isonitrosyl structure N-C-Fe-O-N, and that in the MS2 state the NO group takes a side-on molecular confirmation, Figure 6.1.

Gross and coworkers found that the ^{14}N EFG tensors for the NO and CN groups of SNP are nearly axially symmetric and that the values for the unique components (V_{zz} = 3.358 and 5.340 MHz for NO and CN respectively) of these tensors are sensitive to reorienation of these groups.[14]

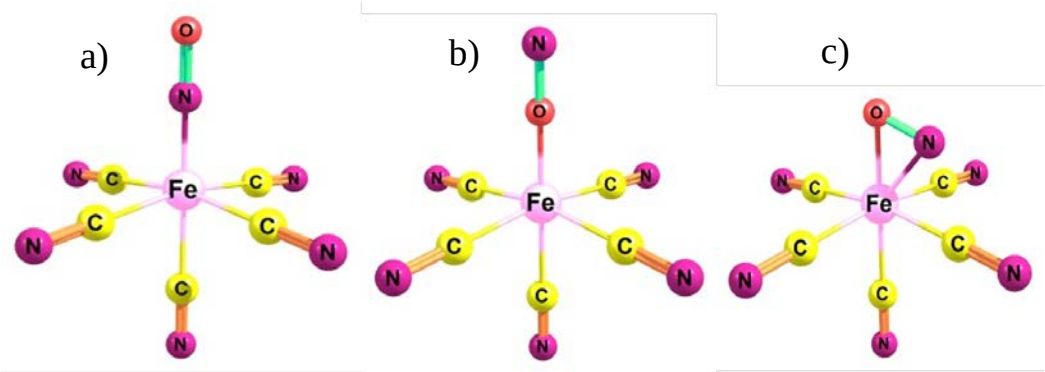

Figure 6.1. Geometry of (a) the ground state, (b) the isonitrosyl (MS1) and c) the side-on bonding (MS2) structure of the NP anion.

To our knowledge, the majority of the structural studies of SNP have been performed on single crystals, and the complex behaviour of a bulk powder of SNP is not fully understood. The objective of the present research is to provide more detailed information about the electronic environment of SNP in the ground state. For this reason, in the first part of this research, a solid-state NMR study of ^{15}N has been undertaken on MAS and stationary powder samples of SNP. Such a study is useful since this nucleus is not quadrupolar, which makes the analysis and

simulations of related spectra much easier. In the next part of this study, ^{17}O and ^{23}Na NMR spectra of MAS and stationary SNP samples were acquired, allowing the determination of the ^{17}O (S = 5/2) and ^{23}Na (S = 3/2) EFG and CS tensors as well as their relative orientations.

Another objective of the present study is to address the question about whether the available computation programs and techniques may reproduce the CS and EFG tensor parameters for the above nuclei in SNP. For this purpose Gaussian[15] DFT and ADF/ZORA[16] calculations were performed on the isolated molecule of $[(Fe(CN)_5(NO)]^{2-}$ for ^{15}N and ^{17}O. Results are compared with those obtained from fully periodic calculations using the GIPAW NMR methods as implemented in the CASTEP[17] program.

In the final part of this study, a method developed for the calculation of NMR parameters in periodic systems within the program BAND[18] for ^{23}Na in SNP has been examined. The results obtained from the two periodic calculation programs are compared and discussed.

6.2. Experimental and Computational Details

6.2.1. Sample Preparation

Sodium nitroprusside dihydrate at natural abundance was purchased from Sigma-Aldrich and used without further purifications.

Preparation of $Na_2[(Fe(CN)_5(^{15}NO)]\cdot 2H_2O$

The preparation was similar to the one discussed by Chacon Villalba *et al.*,[19] 1.6 g of a commercial sample of $Na_4[Fe(CN)_6]$ (5.0 mmol) and 0.35 g of $Na^{15}NO_2$ (5.0 mmol) were dissolved in a solution of 2.2 g $BaCl_2$ in 50 ml distilled water and refluxed for 6 hours under a slow stream of CO_2. After filtration under vacuum to remove $BaCO_3$, the solvent was evaporated and the remaining solid was air dried at 60 ^oC for 2 hours. The residue was extracted with absolute

methanol and finally $Na_2[Fe(CN)_5(^{15}NO)]\cdot 2H_2O$ was crystallized (yield: 0.99 g, 66%).

Preparation of $Na_2[(Fe(CN)_5(N^{17}O)]\cdot 2H_2O$

$$Na_2[Fe(CN)_5NO] + 2NaOH \leftrightarrow Na_4[Fe(CN)_5NO_2] + H_2O$$

This compound was synthesized in two steps.[20] $Na_4[Fe(CN)_5(NO_2)]$ was prepared by dissolving 10 g of anhydrous sodium pentacyanonitrosylferrate(II), $Na_2[Fe(CN)_5(NO)]$, in a mixture of 30 ml of distilled water and 70 ml of methanol. The mixture was cooled to 2 °C and 30 ml of 45 % sodium hydroxide was added to the solution. The yellow product was recrystallized twice from methanol, washed three times with anhydrous ether and dried in a vacuum desiccator over magnesium perchlorate at room temperature.

$$[Fe(CN)_5NO_2]^{-4} + H_2{}^{17}O \leftrightarrow [Fe(CN)_5N^{17}O]^{-2} + 2\,OH^{-1}$$

$Na_2[Fe(CN)_5N^{17}O]$ was prepared by an exchange reaction. In principle 0.3 ml of enriched $H_2{}^{17}O$ is enough for the exchange reaction, however, in practice, it is very difficult to dissolve 1.5 g $Na_4[Fe(CN)_5NO_2]$ in less than 5-10 ml water. To resolve this issue the literature procedure was modified; the reaction solvent was changed to absolute methanol. The exchange reaction was maintained for about week, and a very small amount of concentrated HCl aqueous solution (12 M) was occasionally added to the solution to reduce the pH of the reaction solution. The colour changed from yellow to red after a few days (about one week). The sample was isolated by evaporating methanol and then dried. The residue was extracted and filtered; finally a powder (0.9) of the light red sample was obtained.

6.2.2. Experimental Details

Nitrogen-15 NMR experiments of a powdered sample of SNP were performed at an applied magnetic field strength of 11.75 T on a Bruker Avance 500 spectrometer operating at 50.7 MHz for ^{15}N. Samples were packed into 4 mm zirconium oxide (ZrO_2) rotors and placed within a probe suitable for MAS NMR

experiments. NMR spectra were acquired with the cross polarization (CP) pulse sequence.[21,22] Proton decoupling was accomplished with the two-pulse phase modulation decoupling (TPPM) method of Griffin and coworkers;[23] the recycle delay was 30 s. MAS rates of 4.5 and 5.5 kHz were used to acquire 1500-1700 scans of the powder sample. For ^{15}N NMR spectra of stationary samples 7000 scans were acquired. Nitrogen-15 NMR spectra were referenced with respect to neat liquid ammonia, $^{15}NH_3$, ($\delta = 0$) by setting the isotropic ^{15}N NMR peak of the nitrate signal for solid ammonium nitrate, $^{15}NH_4{}^{15}NO_3$ to 4.4 ppm.[24]

Oxygen-17 NMR spectra of powdered samples of SNP were recorded using a standard single-pulse sequence on Bruker Avance 11.75 and 21.14 T spectrometers, operating at frequencies of 67.80 and 122.6 MHz, respectively. Oxygen-17 NMR spectra were referenced with respect to the ^{17}O signal of water, ($\delta = 0$ ppm). MAS rates of 10 and 12 kHz were used to acquire 5500 - 8500 scans of powder samples. Samples were packed into 4 mm Si_3N_4 and ZrO_2 rotors and recycle delays were 20 or 10 s.

Sodium-23 NMR spectra of powdered samples of SNP were obtained on 7.05, 11.75, and 21.14 T NMR spectrometers, operating at 79.3, 132. 2, and 238.0 MHz, respectively. Samples were packed into 4 mm zirconia rotors and placed within a probe suitable for MAS NMR experiments. NMR spectra were acquired with a standard single-pulse sequence; recycle delays were 3 s. MAS rates ranging from 5 - 15 kHz were used to acquire 1200 - 5000 scans of powder samples. Proton decoupling was accomplished with TPPM for ^{23}Na NMR spectra of stationary samples. All spectra were referenced with respect to 1.0 M NaCl at 0 ppm.[25] The magic angle was first set with a potassium bromide (KBr) sample at a ^{79}Br resonance of 125.302 MHz and second with $NaBrO_3$ powder sample at a ^{23}Na resonance of 132.94 MHz; in both cases the angle was set such that the intensities of the spinning sidebands were at their maximum.

Parameters describing the EFG and CS tensors were determined from simulations of the MAS and stationary sample spectra using the program WSOLIDS[26] and the SIMPSON[27] simulation software.

6.2.3. Computational Details

DFT calculations of the nitrogen and oxygen nuclear magnetic shielding and EFG tensors were performed on an isolated molecule of $[(Fe(CN)_5(NO)]^{2-}$ using both Gaussian and ADF/ZORA.[16] For the Gaussian calculations the B3LYP functional which provides good agreement with experimental nitrogen δ_{ii} values,[28,29,30] was used. ZORA DFT calculations were undertaken using the VWN[31] local density approximation with the generalized gradient approximation (GGA) for the exchange–correlation functional.

Sodium-23 nuclear magnetic shielding and EFG tensor calculations were carried out using the CASTEP code.,[32] CASTEP is a DFT-based code using the projector augmented waves (PAW)[33] and gauge-including projector-augmented waves (GIPAW)[34] algorithm for the EFGs and NMR chemical shifts, respectively. The generalized gradient approximation (GGA) with a revised Perdew, Burke and Ernzerhof (PBE)[35] functional were used for the exchange-correlation energy.

Additional calculations were carried out using BAND code, the Bloch basis set is constructed from Slater-type orbitals or numeric atomic orbitals (NAOs) or both. Atomic centred basis functions further allow for the use of GIAOs to ensure gauge invariant results. The BAND code is discussed in more detail in *Chapter 7*.

6.3. Results and Discussion

6.3.1. Crystal Structure of SNP

The structure of $Na_2[Fe(CN)_5NO]\cdot 2H_2O$ (Figure6.2) was first determined in 1963 by Manoharan and Hamilton[36] by the X-ray diffraction method and later refined by Bottomley and White in 1979.[37]The crystals of SNP are orthorhombic, space group *P*nnm, and the unit cell holds two pairs of SNP complexes. The two complexes in each pair are related by an inversion centre. The highest symmetry possible for the $[Fe(CN)_5NO]^{2-}$ ion should be bipyramidal, point group C_{4V}, with NO and CN axial collinear groups and four equatorial CN groups slightly bent towards the axial CN group. However, the $Na_2[Fe(CN)_5NO]\cdot 2H_2O$ crystal belongs to the D_{2h}^{12}(*P*nnm) space group, the anion site symmetry is *C*s (a mirror plane contains the axial CN and NO groups, bisecting the angle between opposite equatorial $Fe(CN)_2$ groups).[36,37]

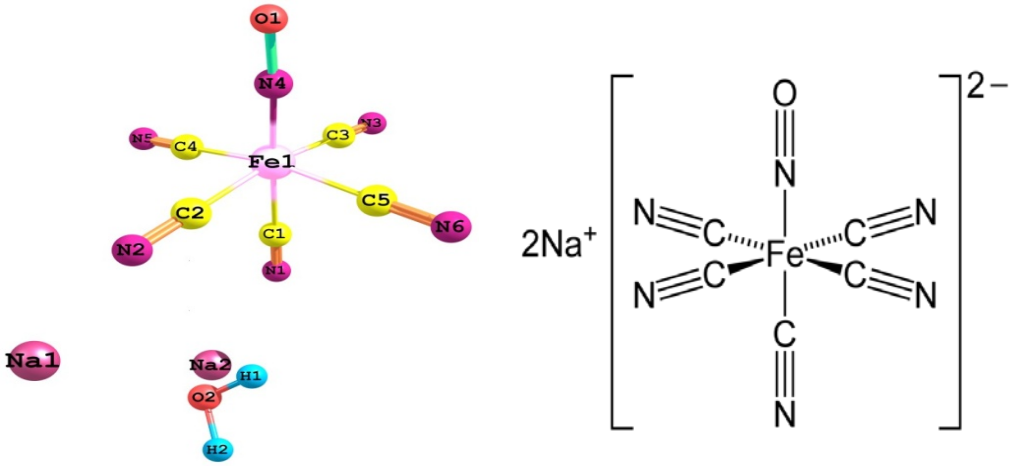

Figure 6.2. Molecular structure of $Na_2[Fe(CN)_5NO]\cdot 2H_2O$

SNP has a very short Fe-N bond length, which is a distinguishing structural characteristic of complexes of NO with transition metal ions. The metal to nitrosyl bond contains one σ-bond involving the nitrogen lone pair and available metal *d*-orbital, and two π-bonds involving filled metal ion *d*-orbitals and the unoccupied π^*-orbital of NO. With this assignment one would predict a

Fe-N-O bond angle of approximate 180 degrees which is experimentally observed. The short Fe-NO distance found in several nitrosyl complexes shows that the NO^+ group is strongly bonded to the metal ion. MO calculations show that the Fe-NO bonding dominates the overall electronic structure of the $[Fe(CN)_5NO]^{2-}$ ion.[38,39] Although there are a large number of papers in the literature containing interpretation and results on the electronic structure of the $[Fe(CN)_5NO]^{2-}$ compound, there appears to have been considerable disagreement on an interpretation of the ordering of the energy levels and of the π^* NO orbitals of the ion.[40-44]

6.3.2. Solid-State ^{15}N NMR Spectroscopy

Nitrogen-15 NMR spectra of MAS and stationary SNP powder samples acquired at B_0 = 11.75 T are shown in Figures 6.3 and 6.4. By comparing two spectra of the MAS sample with different spinning rates, the ^{15}N isotropic peak for SNP was identified δ_{iso} = -2 ± 2 ppm (Figs. 6.3b-c).

The static ^{15}N NMR spectrum acquired at 11.75 T (Figure 6.4) yields further information about the nitrogen CS tensor components. From the simulation of this spectrum the following parameters were obtained: Ω = 685 ± 10 ppm, κ = 1, δ_{iso} = -2 ± 2 ppm.

The value of δ_{iso} is in good agreement with the study by Moore and coworkers[45] reported in 2002. In their study, it was shown the σ_{iso} for ^{15}N of linear Fe−N =O ranges from -130 to -200 ppm, corresponding to δ_{iso}= -2 to 65 ppm.

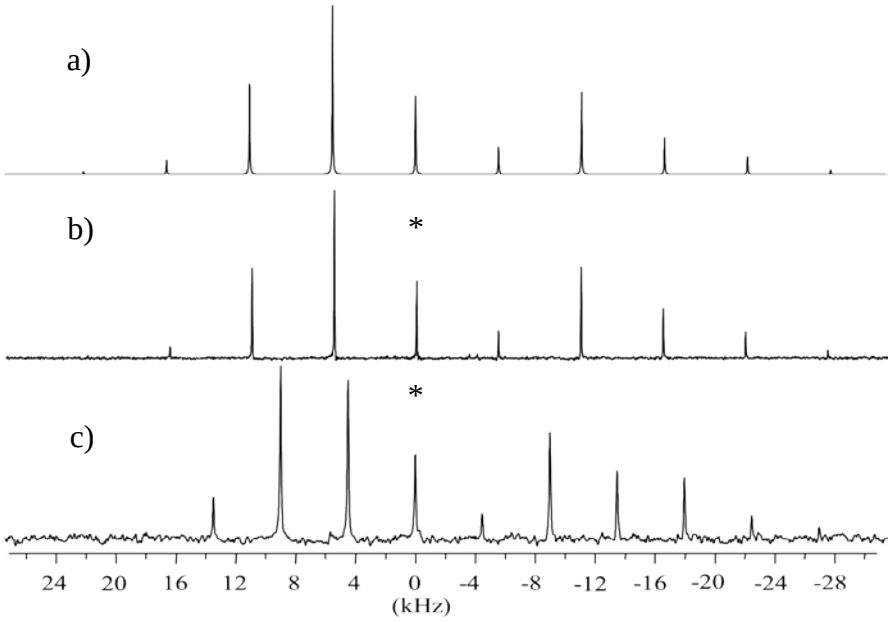

Figure 6.3. a) Simulated, b) and c) experimental ^{15}N MAS NMR spectra of $Na_2[(Fe(CN)_5(^{15}NO)]\cdot 2H_2O$ acquired at B_0 = 11.75 T with different MAS frequencies: (b) 5.5 kHz, and (c) 4.5 kHz. The asterisk indicates the isotropic peak.

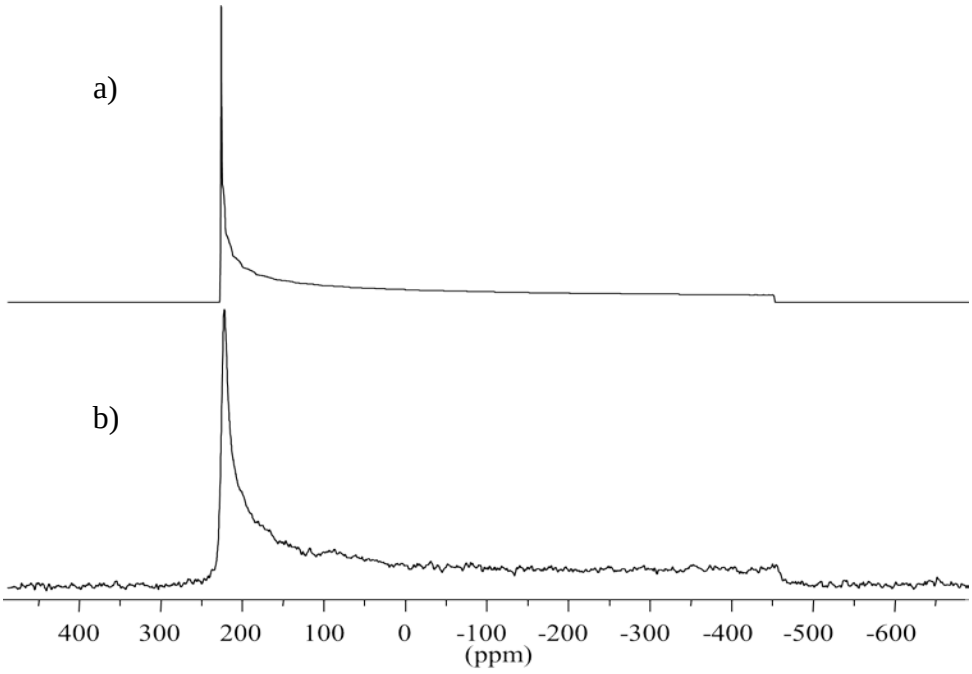

Figure 6.4. a) Simulated and b) experimental ^{15}N stationary CP NMR spectra of $Na_2[(Fe(CN)_5(^{15}NO)]\cdot 2H_2O$ acquired at 11.75 T.

6.3.2.1. Theoretical Calculations for Nitrogen-15

Table 6.1 lists the $\delta_{iso,}$ Ω, and κ values for nitroprusside anion, $[(Fe(CN)_5(^{15}NO)]^{2-}$ calculated with both ADF and Gaussian and with various basis sets. The results of CASTEP calculations are also listed in the Table 6.1.

Direct comparison of the results of these calculations with observed chemical shift values requires that the absolute magnetic shielding tensor components, σ_{ii}, be converted to the chemical shift scale. Since an absolute shielding scale for ^{15}N has been established, such a conversion can be accomplished;[46] $\delta_{ii} = -135.8 - \sigma_{ii}$, where δ is the chemical shift with respect to pure liquid nitromethane and σ is the absolute shielding relative to the "bare" nucleus. The calculated span for the ^{15}N CS tensor of $[(Fe(CN)_5(NO)]^{2-}$ for all basis sets are in reasonable agreement with experiment. In particular, the relativistic ZORA/QZ4P and B3LYP/cc-pVDZ calculations reproduce the value of the span with good agreement compared to the experimental results. Likewise, the CASTEP result is in excellent agreement with the experimental value of Ω = 680 ppm; the good agreement was expected, since the calculation included the effect of the periodic structure of $Na_2[Fe(CN)_5NO]\cdot 2H_2O$, including Na atoms and water molecules. The calculated δ_{iso} values are overestimated by most methods; however, the ZORA/QZ4P and B3LYP/cc-pVDZ calculations again show good agreement with the experimental results.

Table 6.1. Calculated Nitrogen NMR Chemical Shift and Electric Field Gradient Tensor Parameters for SNP.

Basis set	δ_{iso}/ppm	Ω/ppm	κ
ZORA/QZ4P	4	652	1
B3LYP/6-311G(d,p)	34	739	1
B3LYP/6-311++G(d,p)	37	739	1
B3LYP/cc-pVDZ	3	693	1
B3LYP/cc-pVTZ	34	733	1
B3LYP/cc-pVQZ	47	752	1
CASTEP[a]	15	698	1
Expt[b]	-2 ± 2	680 ± 10	1

[a] computation results on the periodic system of $Na_2[Fe(CN)_5NO]\cdot 2H_2O$ [b] Experimental results observed in this study for nitrogen-15.

Recall here that primary isotope effects on nitrogen shifts are negligible, and thus ^{14}N and ^{15}N chemical shifts are interchangable. Since the ^{15}N (I = 1/2) nucleus has no quadrupole moment, the calculation results for C_Q and η are those predicted for the ^{14}N isotope. Usually, coupling to nitrogen is relatively small because of the small gyromagnetic ratio γ for ^{15}N. Some spin-spin coupling measurements in nitrosyl have been reported in the literature such as ^1J (^{14}N, ^{17}O) = 37 Hz.[47] For the EFG results, a literature search revealed that quadrupole coupling constants measured by NQR (*i.e.*, in the absence of an applied magnetic field) and by NMR often differ from each other by a few kHz (the effect of the shielding anisotropy has been neglected). Using NMR spectroscopy with $\mathbf{B_0}$ = 8.35 T, Gross *et al.*[14] measured the four distinct ^{14}N quadrupole coupling constants in SNP at room temperature. The C_Qs derived from these data are listed in Table 6.2. Murgich and Ambrosetti,[48] measured by NQR the temperature dependence of the ^{14}N C_Q in SNP. Their room-temperature results are also listed Table 6.2. For comparison, the calculation results for all four different nitrogen nuclei are also shown in Table 6.2, and all basis sets reproduce the value of C_Q

with good agreement with the experimental value. However the best result belongs to the B3LYP/cc-pVDZ.

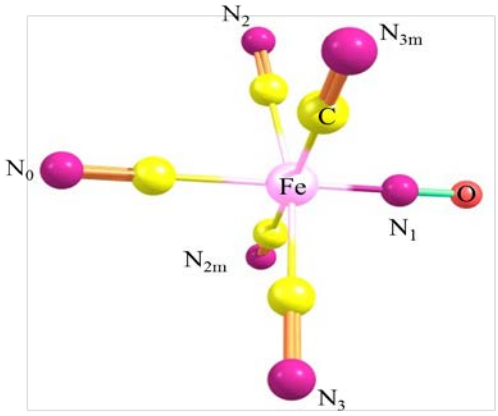

Figure 6.5. The $Fe(CN)_5NO$ complex of SNP. The Fe atom and N, O, and C atoms of the N_0 and N_1 groups all lie in the mirror plane.

Table 6.2. Calculated and Literature Values of Quadrupole Coupling Constants of the Four Distinct Nitrogen atoms in SNP at Room Temperature.[a]

Basis set	C_Q/MHz N_1	C_Q/MHz N_0	C_Q/MHz N_2	C_Q/MHz N_3
ZORA/QZ4P	-2.11	-3.81	-3.95	-3.99
B3LYP/6-311G(d,p)	-2.51	-3.91	-4.05	-4.08
B3LYP/6-311++G(d,p)	-2.50	-3.89	-3.95	-3.98
B3LYP/cc-pVDZ	-2.00	-3.30	-3.51	-3.55
B3LYP/cc-pVTZ	-2.79	-4.00	-4.20	-4.25
B3LYP/cc-pVQZ	-2.89	-4.10	-4.23	-4.34
CASTEP[b]	-2.31	-3.72	-4.01	-4.13
Expt from NMR	±2.24	3.58	3.49	3.63
Expt from NQR	±2.24	3.61	3.55	3.62

[a] The labelling of the sites is shown in Figure 6.5. The NMR data are from measurements at a field of 8.35 T. [b]Computation results on the periodic system of $Na_2[Fe(CN)_5NO]\cdot 2H_2O$.

6.3.3. Solid-State ^{17}O NMR Spectroscopy

Solid–state ^{17}O MAS NMR spectrum of powdered sample of $Na_2[(Fe(CN)_5(N^{17}O)]\cdot 2H_2O$ packed in a zirconia rotor was obtained at 11.75 T and is shown in Figure 6.6a. The first problem in acquiring ^{17}O NMR spectra arose because zirconia rotors were used. The intense peak in range of 350- 400 ppm is due to zirconia rotor (Figure 6.6b), which is also the expected chemical shift range for ^{17}O of a linear nitrosyl group.

To avoid this problem, a 4 mm Si_3N_4 rotor was used to acquire the ^{17}O NMR spectra of oxygen-labelled SNP powder samples. However, a remaining problem is the large ^{17}O background signal of the probe at 11.75 T (Figure. 6.7).

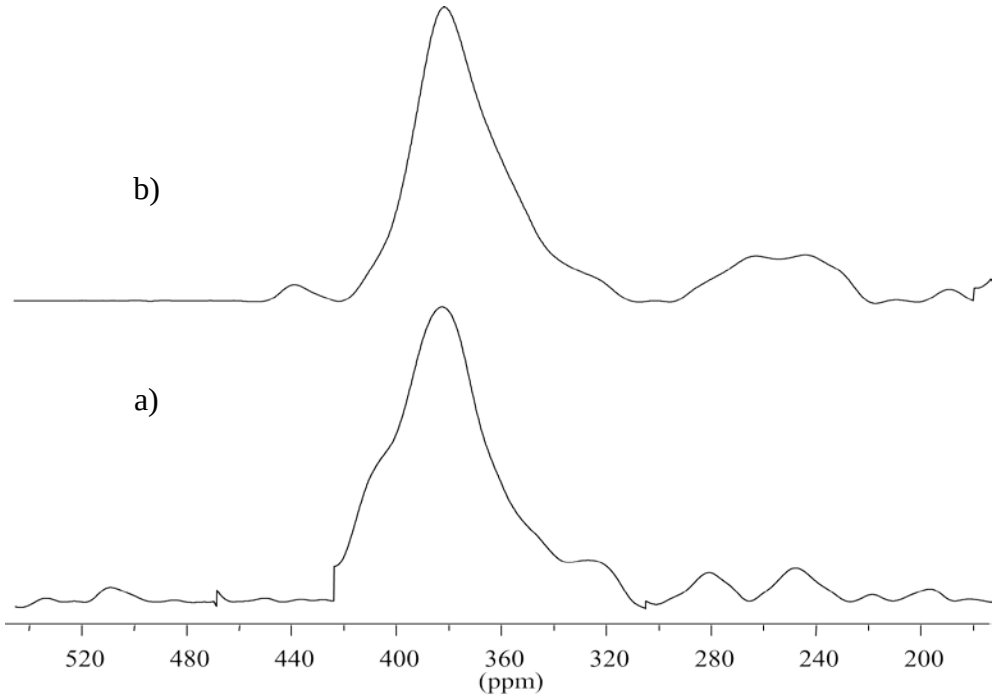

Figure 6.6. Experimental ^{17}O MAS NMR spectra of $Na_2[(Fe(CN)_5(N^{17}O)]\cdot 2H_2O$ acquired at B_0 = 11.75 T and ν_{rot} = 10 kHz. a) Sample packed in zirconia rotor, b) empty zirconia rotor.

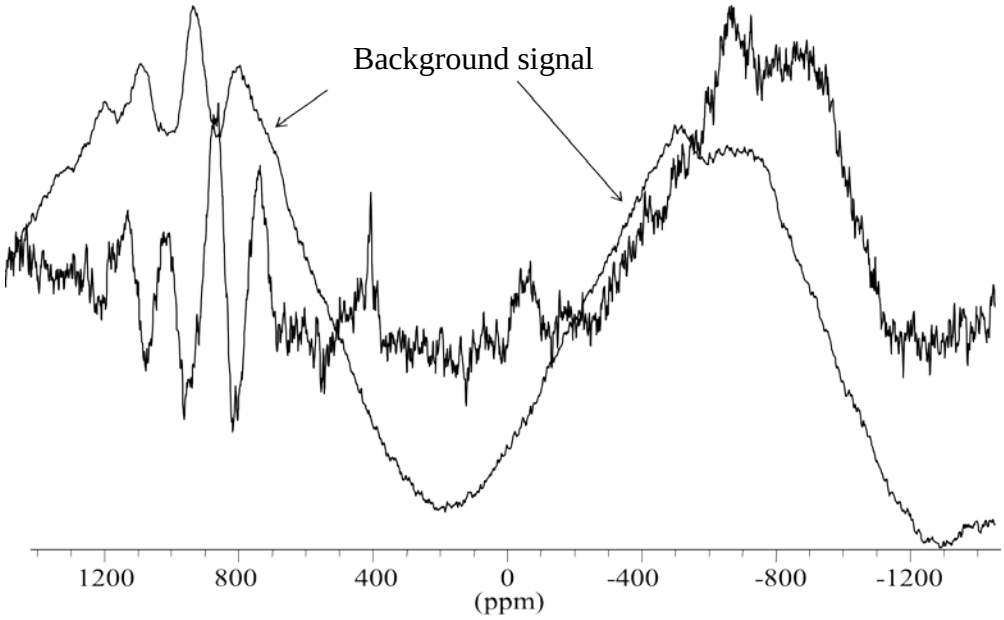

Figure 6.7. Experimental ^{17}O MAS NMR spectra of $Na_2[(Fe(CN)_5(N^{17}O)]\cdot 2H_2O$ acquired at B_0 = 11.75 T and ν_{rot} = 10 kHz; sample packed in Si_3N_4 rotor.

Figure 6.8 shows experimental and simulated ^{17}O MAS NMR spectra for $Na_2[(Fe(CN)_5(N^{17}O)]\cdot 2H_2O$ at 21.14 T. From the symmetry of this molecule we expect that the CS and EFG tensors are axially symmetric. From an analysis of these spectra, three ^{17}O NMR spectral parameters, δ_{iso} = 416 ppm (marked by *), Ω = 800 ± 15 ppm and κ = 1 were obtained.

The peak at zero ppm is assigned to water, as confirmed by the CASTEP calculated result (this work) of σ_{iso} = 288 ppm, since ($\delta_{iso} = 287.5 - \sigma_{iso}$),[49] δ_{calc} = -0.5 ppm. However, the value of C_Q = 9.3 MHz predicted by CASTEP is substantially bigger than the experimental value of 7.9 ± 0.3 MHz,[50] however it is in good agreement with the *ab initio* value of 9.2 MHz which was obtained by Gaussian90 at SCF level.[51]

Figure 6.8 clearly illustrates the benefits of employing higher magnetic fields but even at this high field, the signal to noise ratio is very low, which is typical for ^{17}O NMR spectra. Not surprisingly, solid-state ^{17}O NMR

studies of the $Na_2[(Fe(CN)_5(N^{17}O)]\cdot 2H_2O$ have never been reported in the literature.

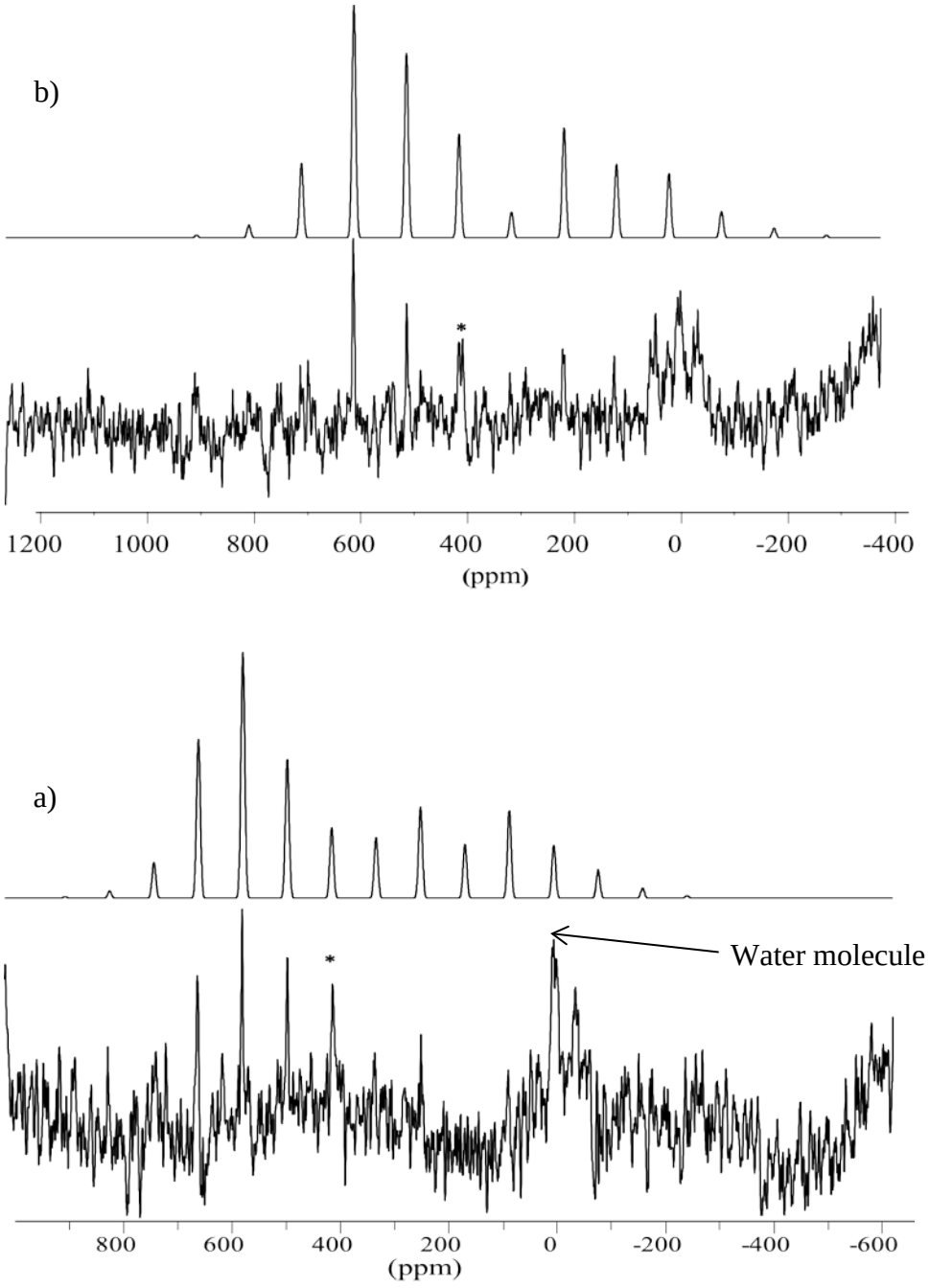

Figure 6.8. Experimental and simulated solid-state ^{17}O MAS NMR spectra of $Na_2[(Fe(CN)_5(N^{17}O)]\cdot 2H_2O$ acquired at B_0 = 21.14 T, a) ν_{rot} = 10 kHz and b) ν_{rot} = 12 kHz, with a sample packed in a Si_3N_4 rotor. The peak at zero ppm is assigned to the water molecule.

6.3.3.1. Theoretical Calculations for Oxygen-17

Table 6.3 summarizes the NMR and EFG parameters for the oxygen nucleus of the $Na_2[(Fe(CN)_5(N^{17}O)]\cdot 2H_2O$ calculated with DFT.

Accurate calculations of CS tensors for nuclei that are highly sensitive to the local environment is particularly challenging. DFT results for δ_{iso}, performed using the CASTEP code, predict a value in good agreement with experiment. However, calculation results on an isolated SNP molecule using Gaussian with a large basis set also shows good agreement with experimental values. This suggests that intermolecular interactions between sodium nuclei and water may not have a significant effect on ^{17}O chemical shifts for SNP.

Table 6.3. Calculated and Experimental Oxygen-17 NMR Chemical Shift and Electric Field Gradient Tensor Parameters for SNP

Basis set	δ_{iso}/ppm	Ω/ppm	κ	C_Q/MHz	η
ZORA/QZ4P	386	601	1	-3.71	0
B3LYP/6-311G(d,p)	375	760	1	-4.12	0
B3LYP/6-311++G(d,p)	356	736	1	-4.05	0
B3LYP/cc-pVDZ	356	707	1	-4.48	0
B3LYP/cc-pVTZ	377	735	1	-3.70	0
B3LYP/cc-pVQZ	384	740	1	-3.60	0
CASTEP[a]	442	749	1	-3.20	0
Expt	416 ± 5	800 ± 15	1	± 3.10 ± 0.05	0

[a,] Computation results on the periodic system of $Na_2[Fe(CN)_5NO]\cdot 2H_2O$.

Calculated ^{17}O isotropic magnetic shielding (σ_{iso}) values were converted to the corresponding chemical shift (δ_{iso}) values by $\delta_{iso} = 287.5 - \sigma_{iso}$

DFT calculations of the span show reasonable results for all basis sets and methods. In the Gaussian calculations, which were performed on$[(Fe(CN)_5(NO)]^{2-}$ the B3LYP/6-311G(d,p) basis set yielded the best agreement with experiment. CASTEP results are in good agreement with the experimental

value, within 50 ppm. Similarly, the calculated C_Q with CASTEP reproduces the value in excellent agreement with experiment.

All calculations reported here accurately predict that the CS and EFG tensors are axially symmetric (which is expected from the molecular structure of this compound). Calculations also predict the experimental Euler angles, which indicates that δ_{33} is in the direction of V_{ZZ}.

6.3.4. Solid-State ^{23}Na NMR Spectroscopy

Sodium-23 (S = 3/2, $N.A$ =100%) is a quadrupolar nucleus with a relatively high receptivity compared to ^{1}H and an average quadrupole nuclear moment (Q = 10.4 × fm^2). To extract the ^{23}Na quadrupolar coupling constant, asymmetry parameters, CS tensor, and relative orientations of the EFG and CS tensors, our routine technique is to first acquire MAS NMR spectra at several fields. As mentioned in previous chapters, analysis of MAS NMR spectra provides the C_Q, η, and δ_{iso}. Second, by fixing these parameters, simulation of stationary spectra of powdered sample depends only on the CS tensor parameters and relative orientation of the EFG and CS tensors. However, in the absence of symmetry for the molecule these orientations are difficult to extract. Therefore, by quantum mechanical calculations, one may obtain information about the relative orientations of the two tensors. In last step, these orientations are used as initial parameters in the simulation of the spectra.

Figure 6.9 shows ^{23}Na NMR spectra of MAS samples of SNP acquired at 7.05, 11.75, and 21.14 T, respectively. The isotropic region indicates the presence of two sodium sites, **1** and **2**, as expected from the crystallography data. The spinning sidebands observed for this compound span a range of approximately 1.4 MHz. Detailed information is shown in Figure 6.9c. The peaks at 18 and 14 ppm are spinning sidebands of the central transition of sites **1**, and **2**, respectively. These peaks are due to a combination of CSA and the second-order quadrupolar interaction. This was verified by Simpson simulations of the spectra with and without CSA and EFG parameters (listed in Table 6.4). The other two peaks at 19

and 17 ppm are assigned to the satellite transitions (ST) of sites **1** and **2**. The position of these peaks can be predicted from the following equation proposed by Samoson:[52]

$$\delta(\mathrm{ST}) - \delta(\text{centre of gravity}) = \frac{1}{40}\left(\frac{{C_Q}^2}{{\nu_l}^2}\right)\left(1 + \frac{{\eta_Q}^2}{3}\right) \qquad (6.1)$$

The value of δ(ST) − δ(centre of gravity) can be obtained by using the above equation and C_Q and η_Q, listed in Table 6.4. The value of δ (centre of gravity) may be found from the following equation;

$$\delta_{iso} - \delta\ (\text{centre of gravity}) = \frac{3}{40}\left(\frac{{C_Q}^2}{{\nu_l}^2}\right)\left(1 + \frac{{\eta_Q}^2}{3}\right) \qquad (6.2)$$

These calculations predict the δ (ST2) = 17 ppm and δ (ST1) = 19 ppm, in agreement with the observed values.

Shown in Figure 6.10 are experimental ^{23}Na NMR spectra of MAS sample of SNP at four different spinning frequencies. From these spectra, the values of δ_{iso} = -2 ± 1 ppm for site 1, and δ_{iso} = -5 ± 3 ppm for site 2 were obtained and are listed in Table 6.4.

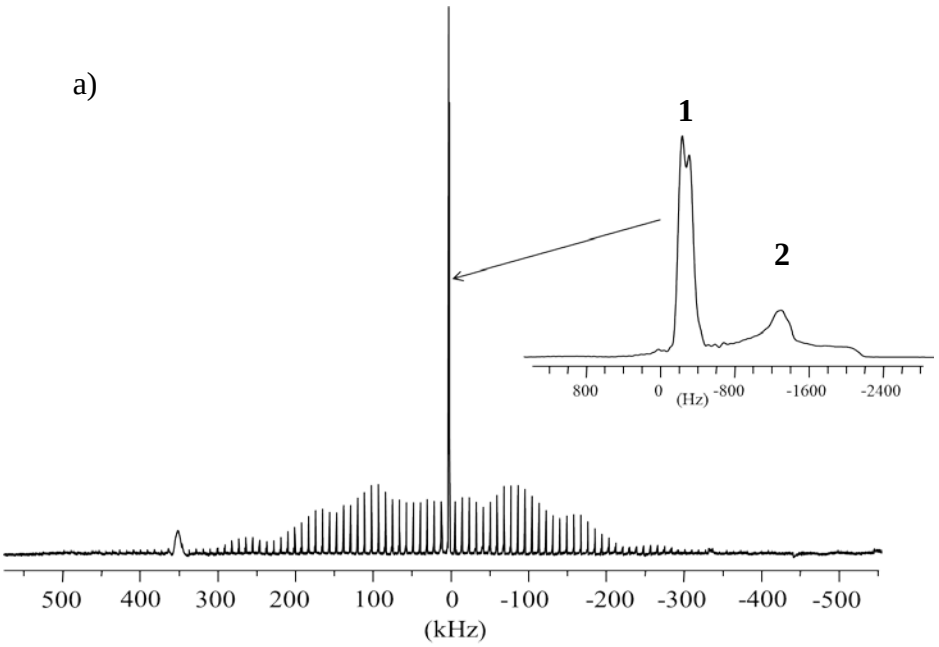

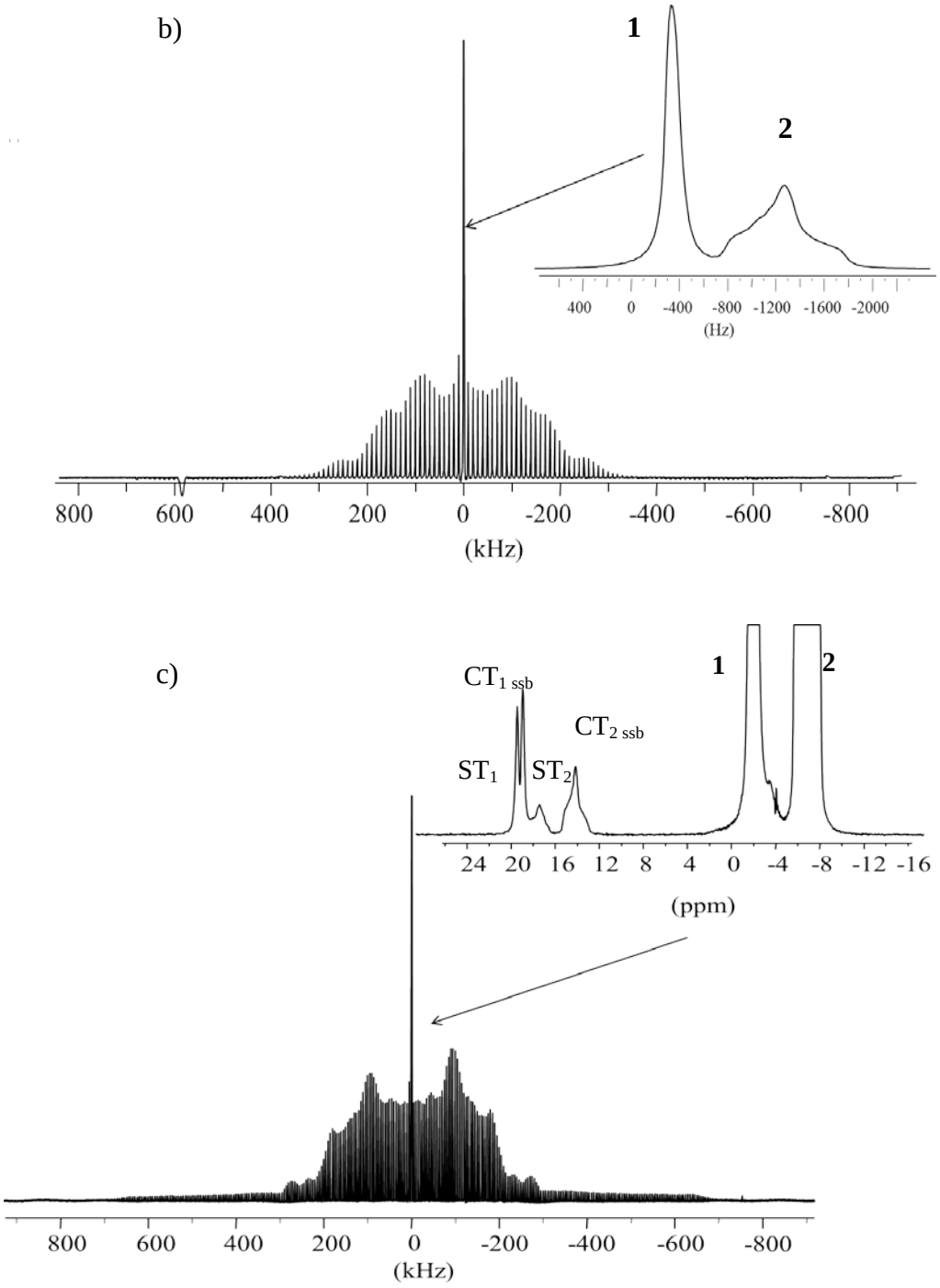

Figure 6.9. ^{23}Na NMR spectra of SNP acquired at a) 7.05 T and b) 11.75, both with an MAS rate of 10.0 kHz and c) at 21.1 T with an MAS rate of 5.0 kHz. Each spectrum is the sum of 3000 scans.

Table 6.4. Calculated and Experimental Sodium-23 NMR Chemical Shift and Electric Field Gradient Tensor Parameters for SNP.

	δ_{iso}/ppm	Ω/ppm	κ	C_Q/MHz	η
Site **1** (expt)	-2 ± 0.5	2.0 ± 0.5	-0.80 ± 0.05	0.70 ± 0.05	0.2 ± 0.2
Site **2 (** expt**)**	-5 ± 0.5	7.0 ± 1.0	0.20 ± 0.05	1.54 ± 0.05	0.9 ± 0.1
CASTEP site **1**	-1	2.5	-0.70	0.80	0.4
CASTEP site **2**	-5	7.5	0.18	1.63	0.9
BAND/ADF site **1**	2	7.0	-0.58	0.9	0.5
BAND/ADF site **2**	-8	15.0	0.37	1.72	0.9

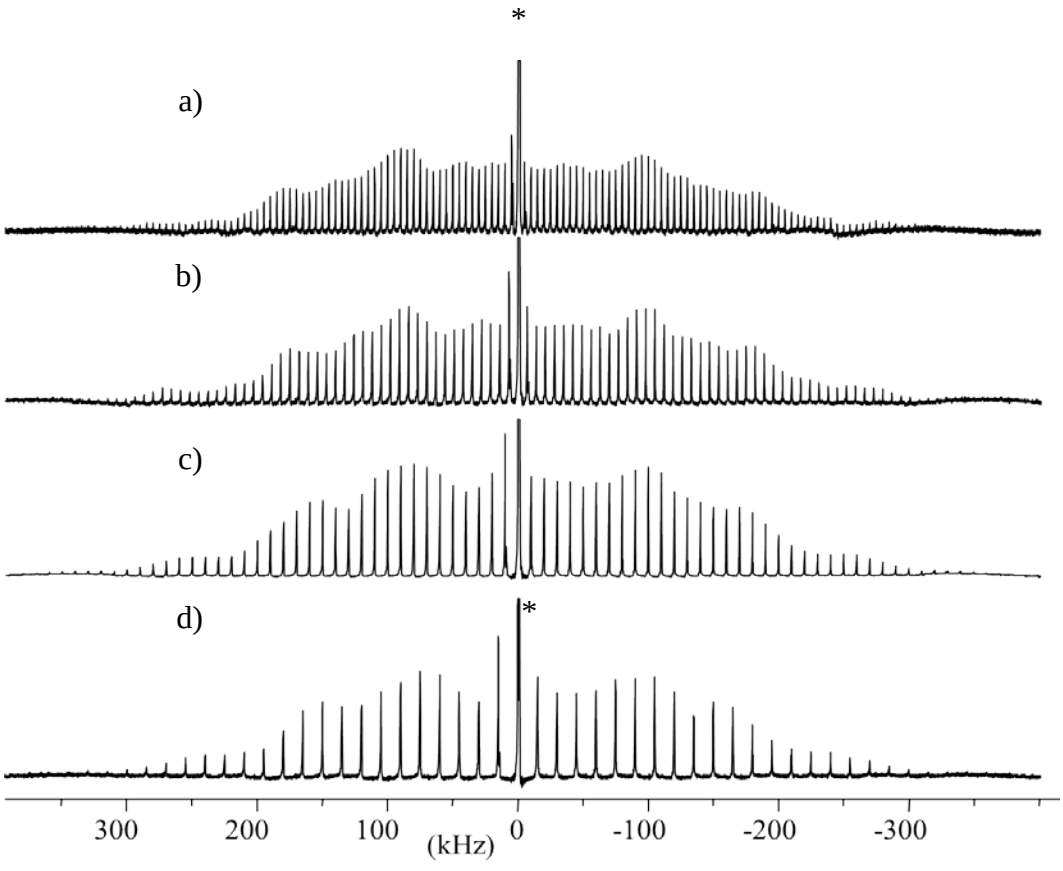

Figure 6.10. ^{23}Na NMR spectra of SNP acquired at 11.75 T with MAS rates of a) 5.0, b) 7.0, c) 10.0, and d) 15.0 kHz. The asterisk indicates the isotropic peak.

Figure 6.11 shows typical sodium-23 central transition region of MAS spectra calculated with various η_Q values. By comparing these lineshape with the experimental line shape observed as shown in Figure 6.12, asymmetry parameters of $\eta = 0.2 \pm 0.2$ for site **1**, and $\eta = 0.9 \pm 0.1$ for site **2** are obtained. From the total spinning sideband pattern in the ^{23}Na NMR spectra $C_Q = 0.70 \pm 0.05$ MHz for site **1** and $C_Q = 1.54 \pm 0.05$ MHz for site **2** can be obtained in a straightforward fashion.

To study the effect of water removal from the hydrated SNP powder sample, two samples labelled **a** and **b,** were prepared from the same commercial powder sample of SNP. Spectra for sample **a** were acquired without further treatment of the sample. Sample **b** was placed in an oven at approximately 110 °C for 5 hours to evaporate the water. By comparing spectra for **a** and **b** (Figure 6.13), one can see that water removal changes the structure of SNP as indicated by the broad central transition peak on the sample **b** spectrum. Rodriguez and coworkers[53] showed that the main structural changes related to dehydration were observed around the M sites for $M[Fe(CN)_5NO]$ (M = Mn, Cd, Zn).

The effect of proton decoupling has also been examined and, as shown in Figure 6.14, the effect of decoupling on lineshape is significant.

In a final step, spectra of stationary samples were recorded with the goal of extracting the sodium CS tensor and its orientation relative to the EFG tensor. Presented in Figures 6.15(a-c), are experimental and simulated ^{23}Na NMR spectra of a stationary sample of SNP. Spectral simulation provides the values of Ω and κ for sites **1** and **2,** listed in Table 6.4. Despite the fact that these spans are very small, it seems that the CS tensor has an effect on the experimental lineshape as shown in Figure 6.16.

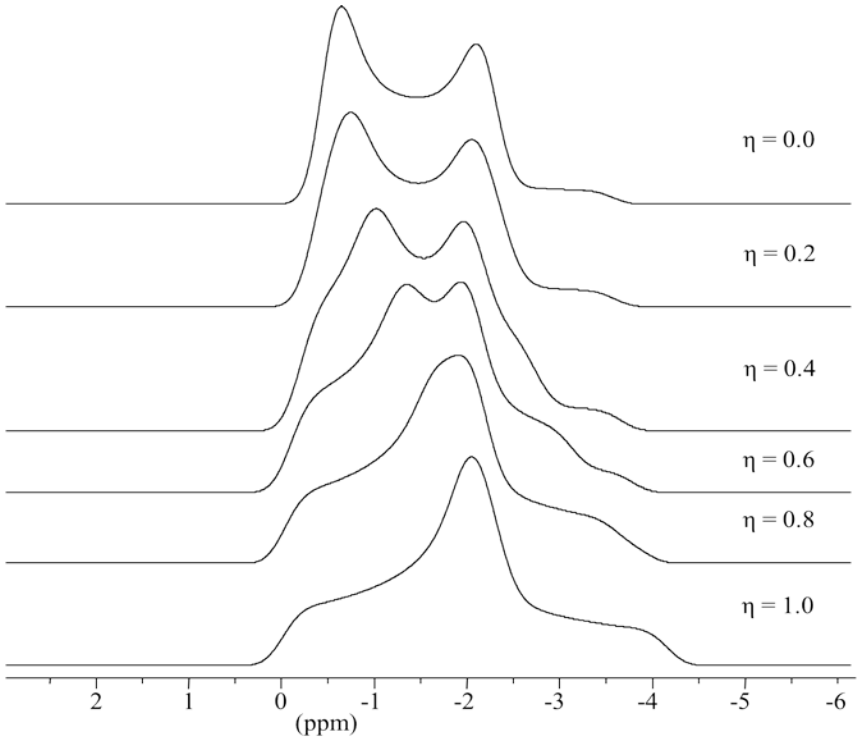

Figure 6.11. Simulated ^{23}Na MAS NMR spectra at 11.75 T, C_Q = 1.0 MHz.

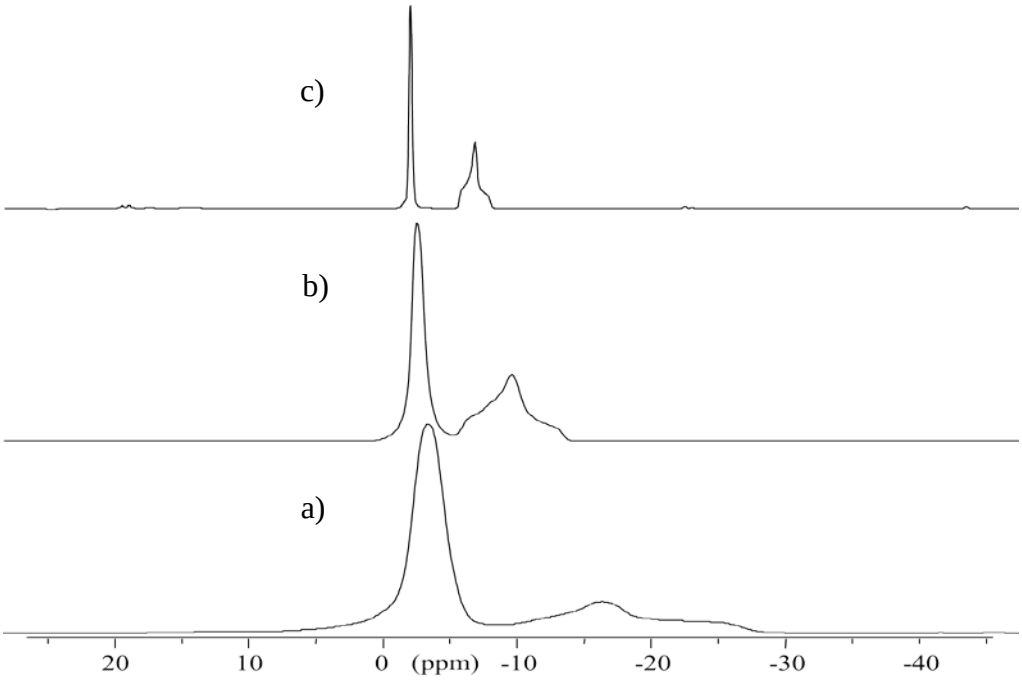

Figure 6.12. Solid-state ^{23}Na MAS NMR spectra of SNP recorded with proton decoupling at MAS rates 5.0 kHz acquired at a) 7.05, b) 11.75, and c) 21.14 T.

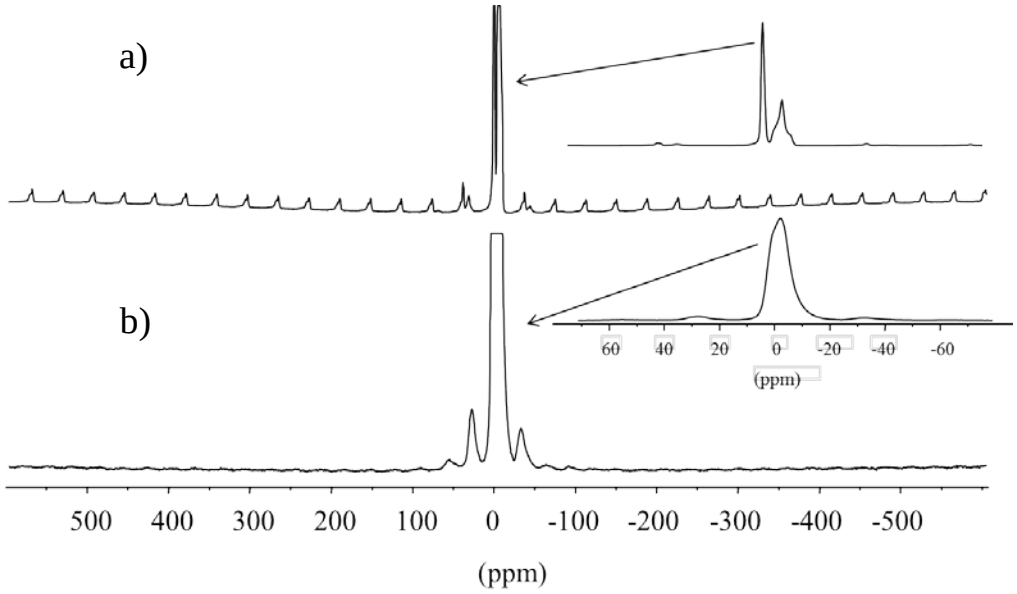

Figure 6.13. Solid-state ^{23}Na NMR spectra of a) hydrated and b) dehydrated sample of SNP at 11.75 T.

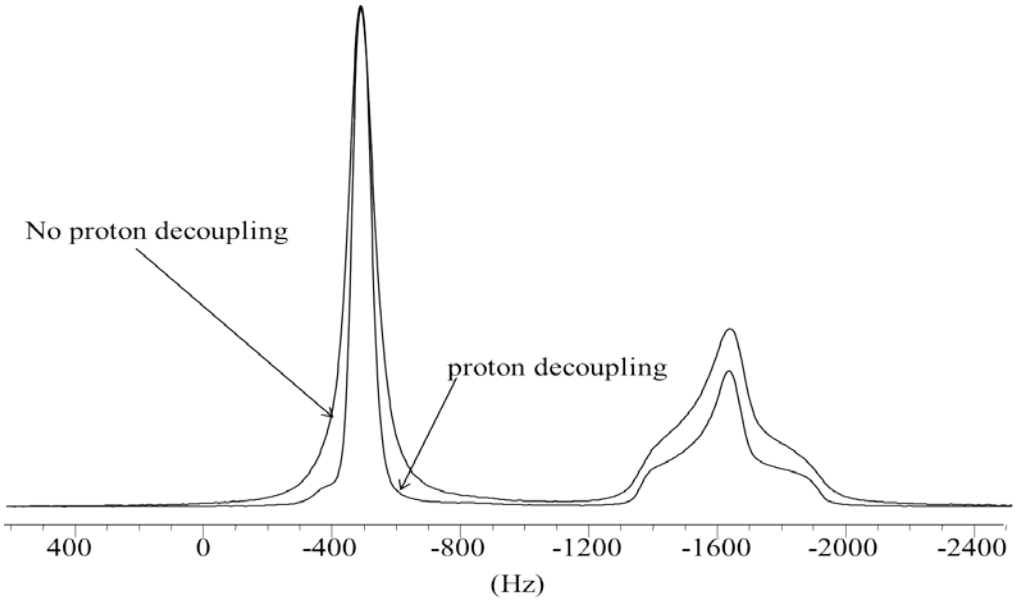

Figure 6.14. Solid-state ^{23}Na MAS NMR spectra of SNP at 21.1 T, at an MAS rate of 5.0 kHz.

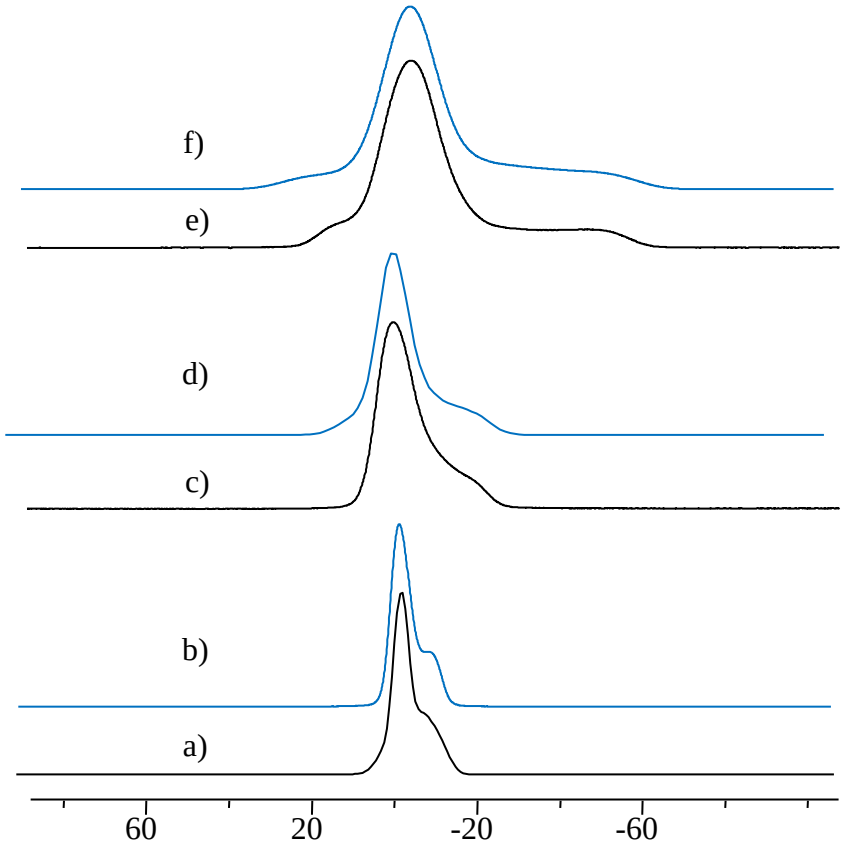

Figure 6.15. Solid-state ^{23}Na NMR spectra of a stationary sample of SNP a, c, e; experimental NMR spectra acquired at 21.1, 11.75, and 7.05T, respectively and (b, d, f) simulated spectra, including site **1** and site **2** using the EFG and CS tensor parameters listed in Table 6.4.

It is known from the literature that the span for sodium compounds is less than 30.0 ppm. For example, in a study on sodium metallocenes, Willans and Schurko[54] reported that Ω = 9.0 - 12.0 ppm. Studies[55] on a series of sodium salts using single-crystal NMR by Sagnowski *et al*. also found a small span, in the range of 0.0 to 17.0 ppm (see chapter 7 for more details). Spectral simulations confirm these parameters through simultaneous fitting of spectra of an MAS sample at three magnetic field strengths, shown in Figures 6-17 (a-c).

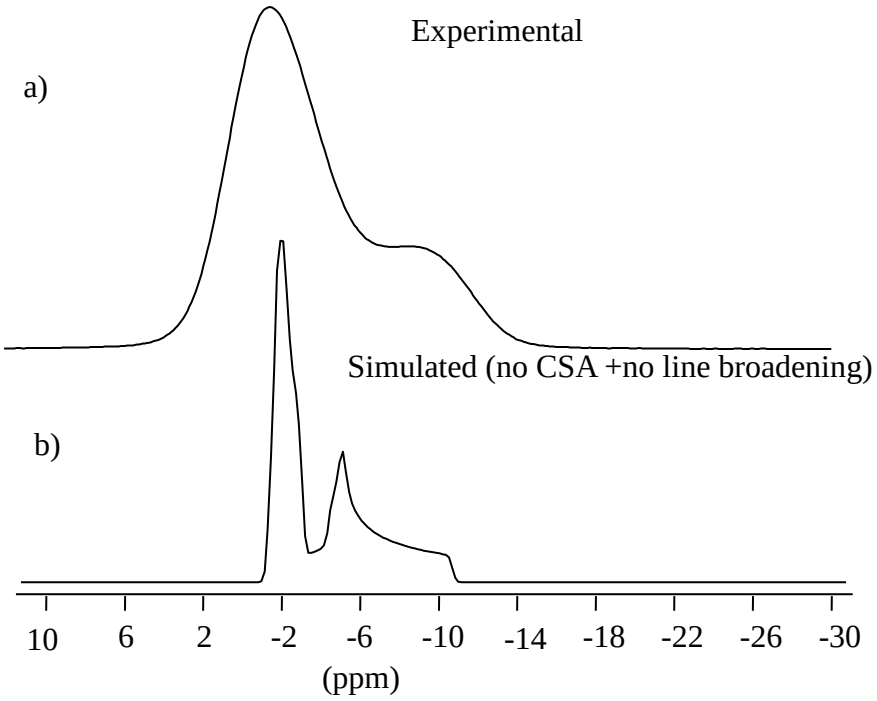

Figure 6.16. Solid-state ^{23}Na MAS NMR spectra of a stationary sample SNP, recorded at 21.1 T, a) experimental b) simulated with $\Omega = 0$

a)

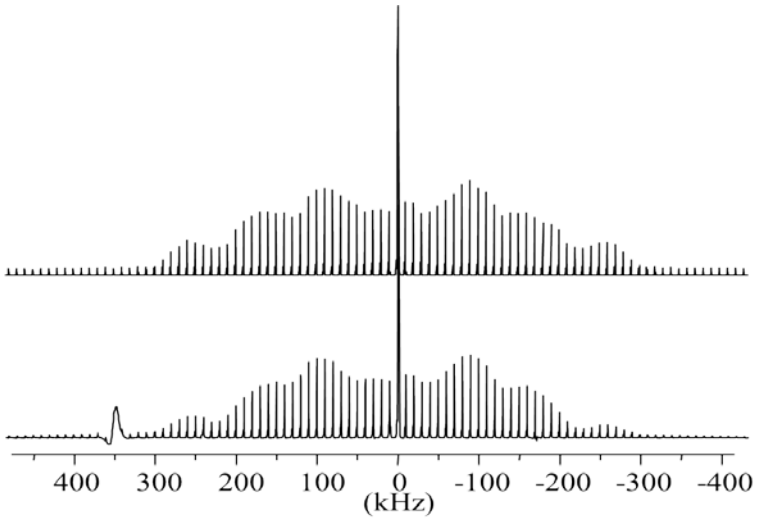

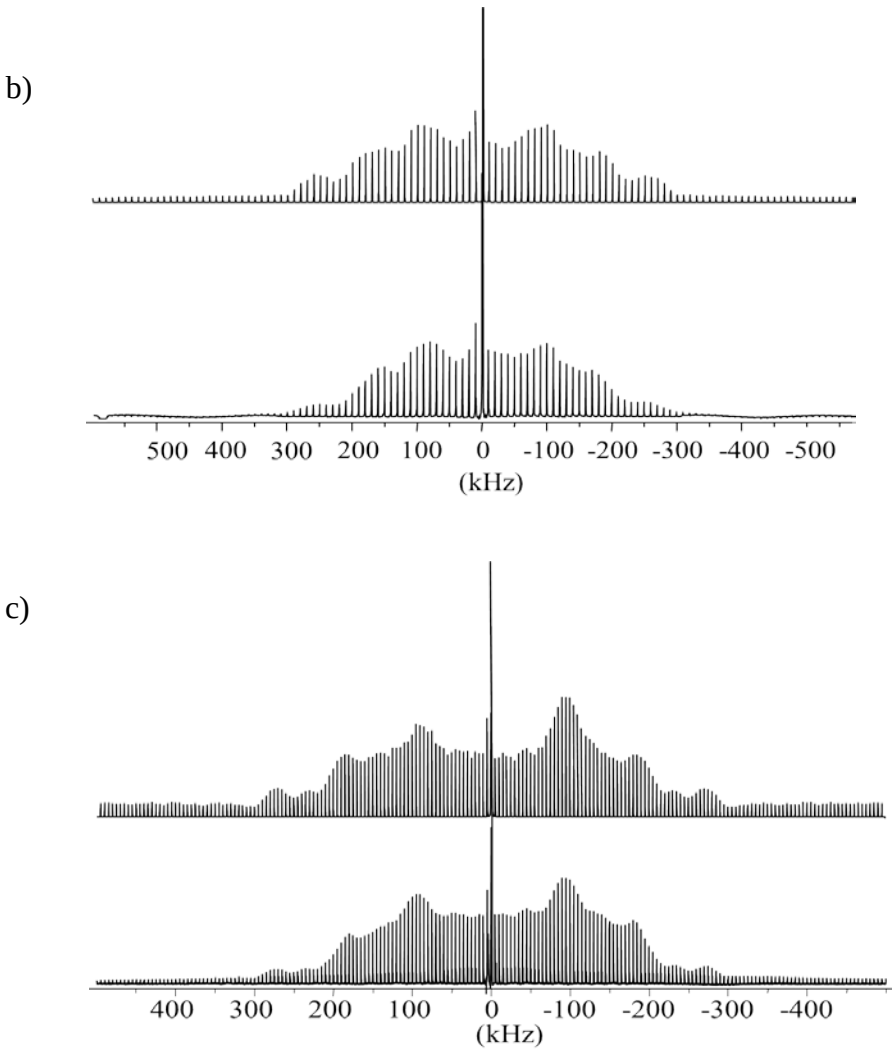

Figure 6.17. Experimental (lower traces) and simulated (upper traces) ^{23}Na NMR spectra of SNP acquired a) 7.05 T, b) 11.75 T, and c) 21.1 T. MAS rates 5.0 kHz. The NMR simulation parameters are listed in Table 6.4.

6.3.4.1. Theoretical Calculations for Sodium-23

To confirm the ^{23}Na experimental NMR parameters, DFT calculations of the magnetic shielding and electric field gradient tensors were undertaken using the NMR CASTEP and BAND code which exploit the inherent periodicity of solid structures. The latter were found through a search in the Inorganic Crystal Structure Database data.

The calculated C_Q and η are reported in Table 6.4. The experimental values of $C_Q(^{23}Na)$ for site **1** and **2** are best reproduced by the CASTEP code. For example, CASTEP calculated a C_Q value of 0.80 MHz for site **1**, whereas the experimental value for site **1** is 0.70 ± 0.05 MHz. The values obtained with BAND are overestimated for site **1** and **2** by 0.2 MHz. Similarly the calculated values of η by CASTEP and BAND for both sites are less than 0.2, in agreement with experiment.

The calculated δ_{iso} values are also reported in Table 6.4. Calculated values of σ_{iso} were converted to δ_{iso} by using the chemical shift value of solid NaCl, δ_{iso} = 7.1 ppm[56] and a CASTEP calculated magnetic shielding value for NaCl, σ_{iso} = 544.74 ppm.

The experimental δ_{iso} (Table 6.4) are fairly reproduced by the calculations by BAND code. On the other hand the value of span and skew calculated by CASTEP code is in better agreement with experimental values for both site **1** and **2**. However the BAND code also predicted these values in agreement with the CASTEP results.

The Euler angles of α = 90°, β = 90°, γ = 1° for site **1** and α = 90°, β = 86°, γ = 0° for site **2** are produced by the CASTEP code. It is evident that these angles may not be reliable because of the small CS tensor. Simulations with different alternate sets of Euler angles indicate that β must be more than 60°, this means the largest components of magnetic shielding and EFG tensors are not coincident. Furthermore, with the aid of computational results, the two sodium sites are assigned as it shown in Figure 6.18.

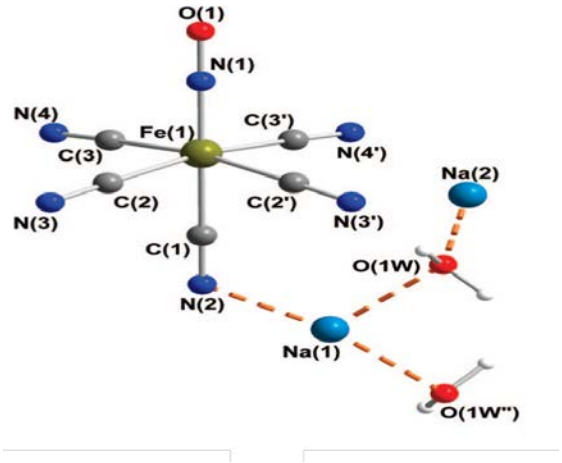

Figure 6.18. Molecular structure of SNP.

Overall the calculation of sodium nuclear magnetic shielding and EFG tensors by CASTEP and BAND reproduce the experimental values in fairly good agreement. Discrepancies between experimental and theoretical values obtained with the BAND code may originate from factors such as the accuracy number, and basis sets in the preparation of the input file. Since the computation time required for the BAND code is very long compared to the CASTEP method is impractical for the current project to use higher accuracy number and basis sets. This may continue to prevent the use of large accuracy numbers or basis sets which will reduce the accuracy of the results especially for the calculation of magnetic shielding tensor parameters.

6.4. Conclusions

In the first part of this study, a nitrogen-15 NMR spectroscopy and quantum chemical study of $Na_2[(Fe(CN)_5(^{15}NO)]\cdot 2H_2O$ was undertaken to investigate the nitrogen NMR parameters. DFT calculated magnetic shielding and EFG tensor parameters obtained by Gaussian and ADF/ZORA on $[(Fe(CN)_5(NO)]^{2-}$ and with the CASTEP code on the periodic system of SNP reproduced the experimental values with good agreement. This suggests that the surrounding lattice may not have a significant effect on the calculation of nitrogen NMR parameters in SNP. The experimental value of $\delta_{iso}(^{15}N)$ is in the range of

chemical shifts for linear NO bonds, confirming the linear structure of the NO ligand in $Na_2[(Fe(CN)_5(^{15}NO)]\cdot 2H_2O$.

In the second part of this study, solid-state ^{17}O NMR spectroscopy was undertaken to determine the ^{17}O EFG and CS tensors of $Na_2[(Fe(CN)_5(N^{17}O)]\cdot 2H_2O$. In addition to reporting the experimental ^{17}O NMR results, extensive DFT calculations by Gaussian and ZORA/ADF on $[(Fe(CN)_5(NO)]^{2-}$ and with the CASTEP code on a full molecule of SNP was also performed. The computed results for the ^{17}O CS tensors are in reasonable agreement with the observed value for all three methods used. Similar to the case for nitrogen this suggests that the lattice has a minimum effect on the ^{17}O NMR parameters.

In the final part of this study, NMR analysis of ^{23}Na spectra of SNP assisted by DFT calculations (using the CASTEP and BAND code) of the NMR parameters was successfully conducted to gain crucial information on the magnitudes and orientations of the sodium-23 CS and EFG tensors. Calculations suggest that the CASTEP code on periodic systems may be used to gain information about CS tensor parameters for some ionic compounds for which the extraction of CS tensor parameters experimentally is difficult. Although the computed results by the second available package on periodic system, the BAND code, show reasonable agreement with experimental values, the long computation time (with reduced accuracy number) makes it less practical compared to the CASTEP code.

6.5. References

[1] P. T. Manoharan, W. C. Hamilton. *Inorg. Chem*. **2**, 1043, (1963).

[2] U. Hauser, V. Oestreich, H. D. Rohrweck. *Z. Phys*. **A 280**, 17, (1977).

[3] A. R. Butler, C. Glidewell. *Chem. Soc. Rev.* **16**, 361, (1987).

[4] A. R. Butler, I. L. Megson. *Chem. Rev*. **102**, 1155, (2002).

[5] M. J. Clarke, J. B. Gaul. *Struct. Bond*. **81**, 147, (1993).

[6] J. H. Swinehart. *Coord. Chem. Rev*. **2**, 385, (1967).

[7] a) T. H. Woike, W. Krasser, P. S. Bechthold, S. Haussühl. *Phys. Rev. Lett*. **53**. 1767, (1984), b) T. H. Woike, W. Kirchner, G. Schetter, T. H. Barthel, H. Kim, S. Haussühl. *Opt. Commun*. **106**, 6, (1994).

[8] V. Dieckmann, S. Eicke, K. Springfeld, M. Imlau. *Materials*. **5**, 1155, (2012).

[9] U. Hauser, V. Oestreich, H. D. Rohrweck. *Z. Phys*. **A 284**, 9, (1978).

[10] H. Zöllner, W. Krasser, T. H. Woike, S. Haussühl. *Chem. Phys. Lett.* **161**, 497, (1989).

[11] K. Ookubo, Y. Morioka, H. Tomizawa, E. Miki. *J. Mol. Struct*. **379**, 241, (1996).

[12] M. Imlau, S. Haussühl, T. H. Woike, R. Schieder, V. Angelov, R. A. Rupp, K. Schwarz. *Appl. Phys.* **B 68**, 877, (1999).

[13] P. Coppens, I. Novozhilova, A. Kovalevsky. *J. Chem. Rev*. **102**, 861, (2002).

[14] D. Gross, N. Pislewski, U. Haeberlen, K. H. Hausser. *J. Magn. Reson*. **54**, 236, (1983).

[15] Gaussian 03, Revision C.02, M. J. Frisch, G. W. Trucks, H. B. Schlegel, G. E. Scuseria, M. A. Robb, J. R. Cheeseman, J. A. Montgomery, Jr., T. Vreven, K. N. Kudin, J. C. Burant, J. M. Millam, S. S. Iyengar, J. Tomasi, V. Barone, B. Mennucci, M. Cossi, G. Scalmani, N. Rega, G. A. Petersson, H. Nakatsuji, M. Hada, M. Ehara, K. Toyota, R. Fukuda, J. Hasegawa, M. Ishida, T. Nakajima, Y. Honda, O. Kitao, H. Nakai, M. Klene, X. Li, J. E. Knox, H. P. Hratchian, J. B. Cross, V. Bakken, C. Adamo, J. Jaramillo, R. Gomperts, R. E. Stratmann, O. Yazyev, A. J. Austin, R. Cammi, C. Pomelli, J. W. Ochterski, P. Y. Ayala, K. Morokuma, G. A. Voth, P. Salvador, J. J. Dannenberg, V. G. Zakrzewski, S. Dapprich, A. D. Daniels, M. C. Strain, O. Farkas, D. K. Malick, A. D. Rabuck, K. Raghavachari, J. B. Foresman, J. V. Ortiz, Q. Cui, A. G. Baboul, S. Clifford, J. Cioslowski, B. B. Stefanov, G. Liu, A. Liashenko, P. Piskorz, I. Komaromi, R. L. Martin, D. J. Fox, T. Keith, M. A. Al-Laham, C. Y. Peng, A. Nanayakkara, M. Challacombe, P. M. W. Gill, B. Johnson, W. Chen, M. W. Wong, C. Gonzalez, and J. A. Pople, Gaussian, Inc., Wallingford CT, 2004.

[16]ADF 2006.01, Theoretical Chemistry, Vrije Universiteit, Amsterdam, http://www. Scm.com.

[17] M. D. Segall, P. J. D. Lindan, M. J. Probert, C. J. Pickard, P. J. Hasnip, S. J. Clark, M. C. Payne. *J. Phys. Condens. Matter*. **14**, 2717, (2002).

[18] G. te Velde, E. J. Baerends. *Phys. Rev*. **B 44**, 7888, (1991).

[19] M. E. Chacon Villalba, E. L. Varetti, P. J. Aymonino. *Vib. Spectrosc*. **14**, 275, (1997).

[20] D. X. West. *J. Inorg. Nucl. Chem*. **29**, 1163, (1967).

[21] A. Abragam, W. G. Proctor. *Phys. Rev*. **106**, 160, (1957).

[22] A. Pines, J. S. Waugh. *J. Magn. Reson*. **8**, 354, (1972).

[23] A. E. Bennett, C. M. Rienstra, M. Auger, K. V. Lakshmi, R. G. Griffin. *J. Chem. Phys*. **103**, 6951, (1995).

[24] S. Hayashi, K. Hayamizu. *Bull. Chem. Soc. Jpn*. **64**, 688, (1991).

[25] S. F. Dec. G. E. Maciel . J. J. Fitzgerald. *J. Am. Chem. Soc.* **112**, 9069, (1990).

[26] K. Eichele, R. E. Wasylishen. WSOLIDS *NMR Simulation Package,* 2001.

[27] M. Bak, J. T. Rasmussen, N. C. Nielsen. *J. Magn. Reson*. **147**, 296, (2000).

[28] M. S. Solum, K. L. Altmann, M. Strohmeier, D. A. Berges, Y. Zhang, J. C. Facelli, R. J. Pugmire, D. M. Grant. *J. Am. Chem. Soc*. **119**, 9804, (1997).

[29] M. Strohmeier, A. M. Orendt, J. C. Facelli, M. S. Solum, R. J. Pugmire, R. W. Parry, D. M. Grant. *J. Am. Chem. Soc*. **119**, 7114, (1997).

[30] J. Z. Hu, J. C. Facelli, D. W. Aldermann, R. J. Pugmire, D. M. Grant. *J. Am. Chem. Soc*. **120**. 9863, (1998).

[31] S. H. Vosko, L. Wilk, M. Nusair. *Can. J. Phys*. **58**, 1200, (1980).

[32] J. R. Yates, C. J. Pickard, F. Mauri. *Phys. Rev.* **B 76**, 024401, (2007).

[33] M. Profeta, F. Mauri, C. J. Pickard. *J. Am. Chem. Soc*. **125**, 541, (2003).

[34] C. J. Pickard, F. Mauri. *Phys. Rev.* **B 63**, 245101, (2001).

[35] J. P. Perdew, K. Burke, M. Ernzerhof. *Phys. Rev. Letter*. **77**, 3865, (1996).

[36] P. T. Manoharan, W. C. Hamilton. *Inorg. Chem*. **2**, 1043, (1963).

[37] F. Bottomley, P. S. White. *J. Acta. Cryst.* **B 35**, 2193, (1979).

[38] P. T. Manoharan, H. B. Gray. *J. Am. Chem. Soc*. **87**, 3340, (1965).

[39] F. Bottomley, F. Grein. *J. Chem. Soc. Dalton. Trans*. 1359, (1980).

[40] H. B. Gray, C. J. Ballhausen. *J. Chem. Phys*. **36**, 1151, (1962).

[41] D. A. C. McNeil, J. B. Raynor, M. C. R. Symons. *J. Chem. Soc*, 410, (1965).

[42] H. A. Kuska, M. T. Rogers. *J. Chem. Phys*. **40**, 910, (1964).

[43] J. Danon. *J. Chem. Phys*. **41**, 3378, (1964).

[44] J. Danon, R. P. A. Muniz, H. Panepucci. *J. Chem. Phys.* **41**, 3651, (1964).

[45] J. Mason, L. F. Larkworthy, E. A. Moore. *Chem, Rev*. **102**, 913, (2002).

[46] C. J. Jameson, J. Mason. *Multinuclear NMR*; J. Mason, Plenum Press: New York, US, 1987.

[47] J. M. Robert, R. F. Evilia. *J. Am. Chem. Soc*. **37**, 107, (1985).

[48] J. Murgich, R. Ambrosetti. *J. Magn. Reson*. **74**, 344, (1987).

[49] R. E. Wasylishen, D. L. Bryce. *J. Chem. Phys*. **117**, 10061, (2002).

[50] R. P. W. J. Struis, J. De Bleijser, J. C. Leyte. *J. Phys. Chem*. **91**, 1639, (1987).

[51] R. Eggenberger, S. Gerber, H. Huber, D. Searles, M. Welker. *J. Chem. Phys.* **97**, 5898, (1992).

[52] A. Samoson. *Chem. Phys. Lett*. **29**, 119, (1985).

[53] J. Rodriguez-Hernandez, E. Reguera, M. Mir, Y. P. Mascarenhas, *J. Powder. Diff*. **22**, 40, (2007).

[54] M. J. Willans, R. W. Schurko, *J. Phys. Chem*. **B 107**, 5144, (2003).

[55] S. F. Sagnowski, Z. Sulek, M. Stachura, J. Ogar. *Z. Phys. B- Condensed Matter,* **46**, 123, (1982).

[56] R. K. Harris, G. J. Nesbitt. *J. Magn. Reson.* **78**, 245, (1988).

Chapter 7. First-Principles Calculations and Solid-State NMR Studies of Sodium Magnetic Shielding and Electric-Field Gradient Tensors on Sodium Salts

7.1. Introduction

Among the NMR-active alkali metal nuclei, sodium-23 is preferred to study because of its 100% natural abundance and relatively high gyromagnetic ratio (comparable to ^{13}C). However, the fact that ^{23}Na is also a quadrupolar nucleus (S = 3/2) with an intermediate nuclear quadrupole moment and small chemical shift range may create some difficulties in carrying out solid-state NMR experiments and in interpreting the solid-state NMR spectra of sodium complexes. In recent years, the acquisition of high-resolution NMR spectra for quadrupolar nuclei has become much more common with the development of experimental techniques and the application of strong magnetic fields. Under favourable conditions, experiments performed on magic angle spinning (MAS) and stationary powdered samples can yield information on the EFG and CS tensors, and their relative orientations. However, in some cases, such as the presence of several distinct crystallographic sites, or if the magnetic shielding information is not obtainable by simulation of the experimental spectra, an alternative strategy is the performance of quantum chemistry computations. Thus, the development of reliable computation methods for the calculation of NMR parameters from structural data is a very important task.

In recent years, significant advances have been made in the development and improvement of accurate computational methods, including those based on DFT. The latter offer many benefits, such as their flexibility and reliability. Another advantage is the possibility of carrying out calculations on large molecular systems containing heavy atoms, while producing accurate and reliable results at relatively low computational costs.

The common quantum chemical packages such as Gaussian[1] and ADF[2] have become perhaps the most widely used in recent years for calculations of EFG and (MS) tensors of isolated molecules. However, for periodic systems these packages, which do not model the lattice environment of the system, are not suitable for calculation of NMR parameters. In the past 10 years several approaches have been developed to tackle this problem. The best-known and perhaps most reliable program is the Cambridge Serial Total Energy Package, (CASTEP)[3,4] code which exploits the inherent periodicity of solids and calculates the NMR parameters of all nuclei in the system. CASTEP is a first-principles approach, using DFT. te Velda and Baerends [5] have developed the BAND code within the ADF program which also deals with periodic systems. Similarly, ABINIT by Zwanziger and coworkers,[6] WIEN97[7] and CRYSTAL[8] have been successful in predicting both the orientation and magnitude of the EFG tensor principal components in a range of materials.

Unfortunately, access to the CASTEP code is rather expensive compared to other packages that have become available. In this work we compared the ability of the CASTEP and BAND codes in reproducing experimental NMR parameters for some alkali metal salts.

In the solid-state, ^{23}Na nuclei commonly exhibit quadrupolar coupling constants ranging from 0.30 to 4.5 MHz, and rarely exceeding 5.0 MHz.[9,10,11] At the same time the magnetic shielding anisotropy is normally below 30 ppm, and is often found within a 5-15 ppm range, depending on the chemical environment.[9,10,11,12] However, quadrupolar coupling constants determined in the gas phase by microwave and molecular beam experiments for sodium halides, NaX (X = F, Cl, Br, I), range from -8.44 to -4.07 MHz.[13,14,15,16] The values of shielding anisotropy acquired via these techniques are currently the largest values reported for sodium compounds, with a range from 72.0 to 130.0 ppm for NaF and NaI respectively. [13,14,15,16] These values are tabulated in Appendix 7.1 and are compared to calculation results which are performed in the current research.

In the first part of this chapter, ^{23}Na NMR spectroscopy has been performed on a series of sodium salts at several applied magnetic field strengths. In most cases it is possible to extract the EFG parameters associated with the ^{23}Na nuclei in each salt. In the second part of this study, DFT calculations of the ^{23}Na EFG and magnetic shielding tensors and their relative orientations were carried out with the CASTEP and BAND programs. In the final part, calculated ^{23}Na NMR parameters are compared with the experimental results and some general conclusions are presented.

7.2. Computational Chemistry Theory

7.2.1. Introduction

In general, the solution of the non-relativistic time-independent Schrödinger equation contains all the information required to calculate the energies of a system, *e.g.*, properties such as the NMR parameters, and is defined by

$$\mathcal{H}\Psi(x_1, x_2, \dots x_N, R_1, R_2, \dots R_M) = E\Psi(x_1, x_2, \dots x_N, R_1, R_2, \dots R_M) \qquad (7.1)$$

$\mathcal{H}$ is the Hamiltonian for a system consisting of *M* nuclei and *N* electrons.

Since the nuclei are heavy and slow in movement compare to the electrons, the system can be assumed to contain fixed nuclei and moving electrons. By this assumption, referred to as the Born-Oppenheimer approximation,[17] the nuclear kinetic energy is neglected. The Schrödinger equation describing the electronic structure of the system can be written as a linear combination of one-electron atomic orbitals, Ψ_i as follows

$$H\Psi_i = \left(-\sum_i \frac{h^2}{2m_e}\nabla_i^2 + V_{ext} + V_{eff}\right)\Psi_i = E\Psi_i \qquad (7.2)$$

where the $\nabla^2 = \nabla \cdot \nabla = \nabla \cdot \left(\frac{\partial}{\partial x_1}, \dots, \frac{\partial}{\partial x_n}\right)$

The first term on the right in equation 7.2 corresponds to the kinetic energy of the electrons and nuclei, V_{ext} is the external potential of the nuclei and V_{eff} is the effective potential and describes the potential between an electron and all other electrons in the system (Hartree potential).[18]

Owing to the number of electrons in even medium-sized molecules, this simplified equation is still impossible to solve exactly. Therefore a different approach to the energy calculations was introduced by Hohenberg and Kohn,[19] with the methodology later developed by Kohn and Sham.[20] In this approach, the so called density functional theory, the complicated N-electron wavefunction has been replaced by an electron density term, ρ(r), that is defined for any position in an isolated molecule and the crystal (3-degrees of freedom):

$$E[\rho(r)] = \int dr V_{ext}(r)\rho(r) + F[\rho(r)] \tag{7.3}$$

Where $F[\rho(r)] = E_k[\rho(r)] + E_H[\rho(r)] + E_{XC}[\rho(r)]$ describes the electron kinetic energy $E_k[\rho(r)]$, the Hartree-Coulomb term $E_H[\rho(r)]$ and the exchange-correlation functional $E_{XC}[\rho(r)]$ reducing the $3N$ parameters Hartree-Fock problem to a three dimensional problem, which leads to a greatly reduced computational cost. The final term, E_{XC}, which is the exchange correlation energy, is not known and must be approximated.

In an ideal uniform electron gas situation, the exchange-correlation functional is known with a high degree of accuracy, and therefore Kohn and Sham proposed that E_{XC} can be described by the exchange correlation energy per particle of a uniform electron gas of similar density ε_{XC}, leading to the so called local density approximation (LDA)

$$E_{XC}^{LDA}[\rho] = \int \rho\,(r)\varepsilon_{XC}\big(\rho(r)\big)dr \tag{7.4}$$

However, the LDA approach is not always the best solution since it does not include any information about the non-homogeneity of the true electron density. To resolve this issue, the generalized gradient approximation (GGA)[21,22] approach

was introduced, which includes an additional term that incorporates some dependency on the gradient of the charge density:

$$E_{XC}^{GGA}[\rho] = \int \rho\,(r)\varepsilon_{XC}(\rho(r), \nabla\rho)dr \tag{7.5}$$

There are many proposed GGA methods; however the method by Perdew, Burke and Ernzerhof (PBE)[23] has been widely used in the literature.

For any calculations involving a crystal, (infinite repeat structure), some simplifications are required as it is impossible to include an infinite number of particles. This situation is addressed by creating a cluster of atoms of significant size, so the environment about the central atom replicates what is obtained in an infinitely repeating structure. To achieve an accurate representation of the crystal, a large number of atoms are required. In a crystal, the nuclei will be arranged in a periodic fashion, and therefore the potential acting on the electrons will also be periodic. Bloch's theorem indicates that if the potential is periodic, so is the density and magnitude of the wave function. This wave function can be described as

$$\Psi(r) = e^{ikr}u_k(r) \tag{7.6}$$

where e^{ikr} is an arbitrary phase factor, $u_k(r)$ is the periodic magnitude, and k is a point in the reciprocal space, referred to as a k-point. $u_k(r)$ then can be defined as a three-dimensional Fourier series

$$u_k(r) = \sum_G C_{GK}e^{iGR} \tag{7.7}$$

where the C_{GK} are complex Fourier coefficients, and e^{iGR} is a plane wave.[24]

In practice, there are an infinite number of reciprocal lattice vectors, G, and therefore an infinite number of coefficients and plane waves. However, the higher energy plane waves have a correspondingly small coefficient and therefore contribute negligibly to the formation of the wave function. Therefore it is

possible to limit the number of plane waves to reduce the computational cost with the so-called energy cut-off:

$$\frac{1}{2}|G|^2 < E_{cut} \tag{7.8}$$

In principle to construct the electron density it would be necessary to integrate over an infinite number of *k*-points. However, the wave functions change slowly while *k* is varied; therefore an infinite number is not always required, leading to an approximation over the summation of an appropriate number of *k*-points,

$$\rho(r) = \int |\Psi\_k(r)|^2 \, d^3k \approx \sum_k |\Psi\_k(r)|^2 \tag{7.9}$$

By replacing the *k*-points throughout reciprocal space using the Monkhorst-Pack *k*-point grid[25]a uniform distribution of the *k*-points is obtained. Thus when sampling the electron density, the *k*-point spacing controls the accuracy of the calculation. However controlling the cut-off energy and *k*-points is not the only key to create a computational approach. There are two more approximations which allow the simplification of the form of the wavefunction which ultimately reduces the computational cost and time.

As the core electrons lie near the nuclei, they have little effect upon bonding and therefore their effect on the chemical, mechanical and electronic properties of a solid is negligible. Thus their effect can be described by a fixed potential, with only the valence electrons being allowed to respond to the changes in the environment; this is referred to as the frozen core. However, the nature of the valence wave functions close to the nucleus demand a large number of plane waves to reproduce. This may be simplified by the way that the wave function is artificially smoothed close to the nucleus, within the core region which is called the pseudopotential. This simplification requires fewer plane waves for its construction, therefore it reduces the cost and time for calculating or minimizing the energy. Although the application of pseudopotentials leads to accurate calculation of the energies, other properties, such as those that are important in

NMR spectroscopy, are strongly dependent on the form of the wave function in the defined core region and therefore may not be accurately defined by a pseudowave function. To solve this issue, the projector augmented-wave (PAW)[26,27] approach was developed, which can derive the all-electron wave function from a linear transformation of the pseudowave function. However, the PAW approach was not developed for systems under the influence of a magnetic field. Thus, another computational method was developed, which directly derives the all-electron wave function in the presence of a magnetic field, named the gauge-including projector augmented-wave (GIPAW) approach.[28]

7.2.2. CASTEP and BAND Methodology

CASTEP is a computer code using DFT to calculate physical properties, such as NMR parameters, from the crystal structure. CASTEP employs the GIPAW method which uses pseudopotentials to describe the electrons in the core regions of the atoms and plane waves to describe the valence electrons. Of the three NMR tensors (EFG, magnetic shielding (**σ**), and indirect spin-spin coupling (**J**)) that may be calculated by computation, perhaps the calculation of EFG tensors is less demanding since it only depends on the ground-state charge density. This is directly available in the GIPAW code which has been widely used and shown to reliably predict EFG tensors at nuclei in solids. It should be noticed that in some studies the GIPAW code is combined with the Linear Augmented Planewave method (LAPW) code for EFG calculations, showing that both approaches are in very good agreement.[29,30] Recall here that theoretically, the shielding tensor is treated as the second-order derivative of the total electronic energy with respect to an external magnetic field and nuclear magnetic moment. In the GIPAW code the external magnetic field is considered as a first perturbation inducing a current density and the nuclear magnetic dipole is assumed to be a second perturbation which is the response to the induced current density. In the CASTEP code, which employs the GIPAW method, the external magnetic field is considered as oscillating in order to adopt the periodic symmetry of the solid. However for proper calculation of magnetic shielding using the

CASTEP code there are some more approximations implemented in the GIPAW method, the discussions of which are beyond the scope of this *thesis*.

The BAND program, which was originally written by te Velde,[31] and further developed by Wiesenekker[32] is a program that can perform electronic structure calculations on periodic systems. BAND is the periodic density functional theory extension of the ADF code. Linear combinations of atomic orbitals (LCAO) basis sets allow for proper modeling of periodic structures without artifacts. Furthermore, reliable relativistic methods (ZORA[33]and spin-orbit coupling) are available with all-electron basis sets for the whole periodic table, removing the need for a pseudopotential/effective core potential approximation. In BAND, the Bloch basis set is constructed from Slater-type orbitals, (STOs) or numeric atomic orbitals (NAOs) or both. An accurate electronic density matrix about the nuclei is critical for the calculation of magnetic shielding. Both STOs and NAOs provide a good description of the Kohn-Sham (KS) orbitals in the region of interest. It is also known that the use of gauge including atomic orbitals, (GIAOs)[34,35] also ensure gauge invariant results. In the BAND code, two methods for the calculation of magnetic shielding are proposed by Ziegler and coworkers[36,37] In the first method, called the supercell method, the KS equation is solved with the supercell as a periodic unit to obtain a zero-order basis for the perturbation treatment which determines the current density, **J**. This method can be costly since a supercell usually consists of five or more primitive cells. In the second method, which is called the single dipole moment method, both the induced current density, **J** due to the first perturbation from the nuclear magnetic moment as well as the interaction of the current density, **J** with the second perturbation in the form of an external magnetic field is evaluated. The new scheme represents an improvement over the previous method since calculations can be undertaken on primitive cells instead of supercells. This improvement obviously reduces the required computational time significantly. Zeigler and coworkers,[36,37] demonstrated the compatibility of these two methods by calculating the magnetic shielding for one-dimensional periodic systems, a diatomic chain, polyethylene, and two- or three-dimensional periodic systems.

The calculated results reported in their research were in good agreement with experiment for both methods discussed above.

7.3. Experimental and Computational Details

7.3.1. Sample Preparation

Powder samples of six sodium compounds, $NaBrO_3$, $NaNO_3$, $NaNO_2$, $NaClO_3$, Na_2HPO_4, and Na_2SeO_3 used in this work were obtained from commercial sources, and used without further purifications.

7.3.2. Experimental Details

Sodium-23 NMR spectra of powdered samples of six sodium salts were obtained on 7.05, 11.75, and 21.14 T NMR spectrometers, operating at 79.3, 132.2, and 238.0 MHz, respectively. Samples were packed into 4 mm zirconia rotors and were placed within a probe suitable for MAS NMR experiments. NMR MAS spectra of samples without ^1H were acquired with a standard single-pulse sequence, recycle delays were 1 to 3 s. Several MAS rates in the range of 5.0 to 15.0 kHz were used to acquire 2000-4000 scans of powder samples. For Na_2HPO_4 a standard single-pulse sequence was acquired; proton decoupling was accomplished with the two-pulse phase modulation decoupling (TPPM) model.[38] All spectra were referenced with respect to 0.1 M NaCl at 0 ppm.[39] The magic angle was checked first with a potassium bromide (KBr) sample at a ^{79}Br resonance of 125.302 MHz ($\mathbf{B}_0$ = 11.75 T) and second with $NaBrO_3$ powder sample at a ^{23}Na resonance of 132.94 MHz ($\mathbf{B}_0$ = 11.75 T); the angle was considered optimum when the sideband intensities were maximized. Simulations of ^{23}Na NMR spectra were carried out using the WSOLIDS[40] and SIMPSON[41] simulation packages.

7.3.3. Quantum Chemical Calculations

Both quadrupolar and chemical shift parameters were calculated using the NMR CASTEP and BAND codes. Our CASTEP calculations utilized the GGA (PBE) functional, ultrasoft pseudopotentials, the frozen core approximation and GIPAW. To determine the optimum *k*-point spacing and the cut-off energy, an initial set of "convergence studies" are required. Typically, the *k*-point spacing was fixed (at 0.05 Å) and the cut-off energy varied from 30 to 60 Ry (1 Ry is equivalent to 13.6 eV). Pseudopotentials were used, with 2s and 2p valence orbitals for O, 2s, 2p and 3s valence orbitals for Na and 3s, and 3p valence orbitals for P. The DFT calculations were performed on the Material Studio 4.3 environment on an HP xw 4400 workstation with a single intel Dual-core 2.67 processor and 8 GB DDR RAM (These calculations have been done by Dr. Victor Terskikh at Steacie Institute of Molecular Science, Ottawa, Canada).

Our BAND calculations are based on SCF calculations, employing the GGA approximation for the exchange correlation energy which follows the Becke-Perdew BP approach. For magnetic shielding calculations the method called "single dipole" was used.[37] The TZ2P basis set and medium size accuracy number were used in our EFG and magnetic shielding tensor calculations. The calculated values of σ_{iso} were converted to δ_{iso} by using the chemical shift value of solid NaCl, δ_{iso} = 7.1 ppm[42] and CASTEP calculated magnetic shielding value (this study) for NaCl, σ_{iso} = 544.74 ppm.

All crystal structures used for this study were obtained from the Inorganic Crystal Structure Database, which is obtained from (X-ray or Neutron) diffraction data.

7.4. Results and Discussion

7.4.1. Experimental Spectra and Simulations

7.4.1.1. Sodium Bromate $NaBrO_3$, Sodium Chlorate $NaClO_3$, and Sodium Nitrate $NaNO_3$.

The crystal structure of $NaXO_3$ (X = C1, Br) is shown in Figure 7.1. The unit cell is cubic with space group, $P2_13$, which contains four molecules.[43] The XO_3 ions form pyramids with the halogen atoms at the apex. Each of the sodium ions and associated XO_3^- pyramids lie along a direction parallel to a body diagonal. Therefore sodium ions have trigonal symmetry. This means that the EFG and CS tensors are axially symmetric, with their symmetry axes parallel to the corresponding threefold axes of the crystal. The four sodium ions in the unit cell are crystallographically equivalent; therefore, in the NMR experiment we expect one sodium site.

The room temperature ^{23}Na NMR spectra of an MAS sample of $NaBrO_3$ obtained at three fields of (7.05, 11.75 and 21.14 T) are shown in Figure 7.2. The C_Q, η, and δ_{iso} parameters listed in Table 7.1 were extracted from simulations of these spectra as explained in earlier chapters.

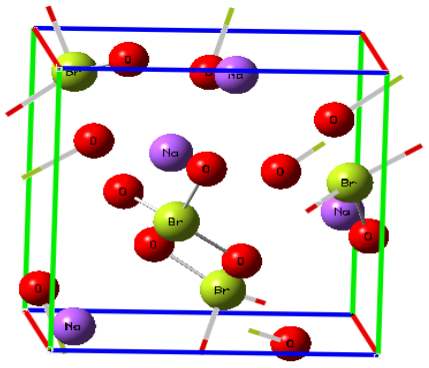

Figure 7.1. Crystallographic structure of $NaBrO_3$

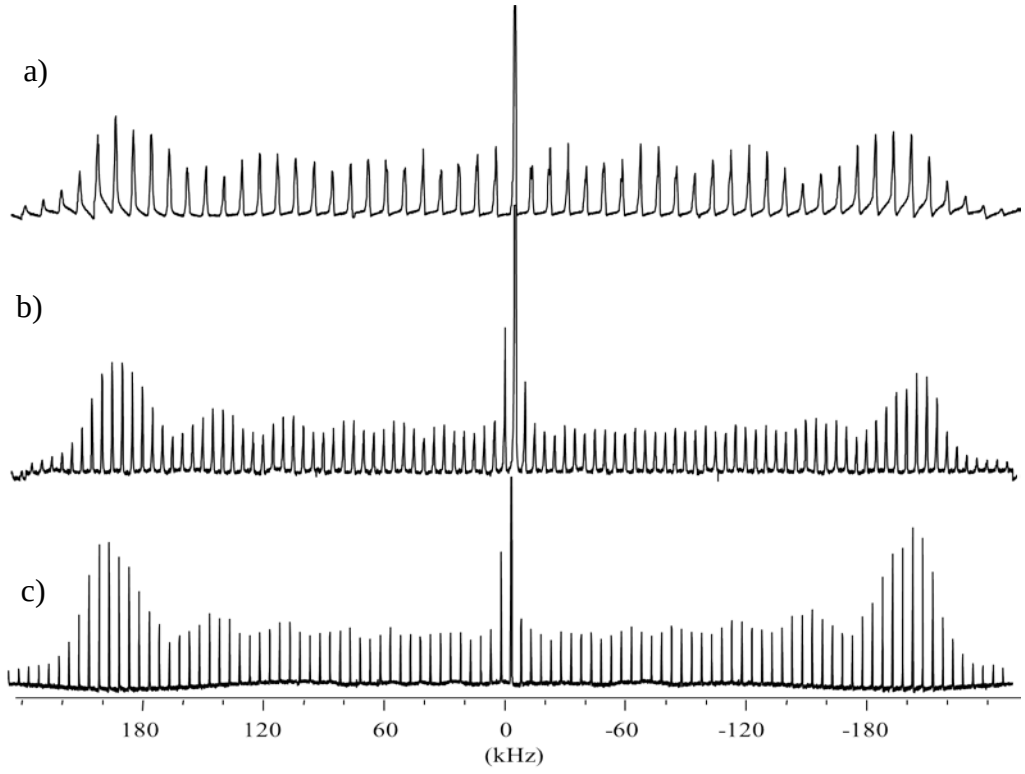

Figure 7.2. ^{23}Na NMR spectra of $NaBrO_3$ acquired at a) 7.05 T, MAS rate of 9 kHz, b) 11.75 T, MAS rate of 5 kHz, and c) 21.14 T, MAS rate of 5 kHz. Each spectrum is the sum of 2000 scans, (Up to 480.0 kHz is shown).

Table 7.1. Experimental Sodium-23 NMR Chemical Shift and Electric Field Gradient Tensor Parameters for $NaXO_3$ (X = C1, Br and N).

Compund name	δ_{iso}/ppm	Ω/ppm	κ	C_Q/MHz	η
$NaBrO_3$ [a]	-0.22 ± 2.00	12 ± 6	1	0.840 ± 0.002	0.0
$NaBrO_3$ [b]		19 ± 4	1	0.848 ± 0.008	0.0
$NaClO_3$ [a]	-3.43 ± 1.00	8 ± 4	1	0.780 ± 0.002	0.0
$NaClO_3$ [b]		12 ± 4	1	0.788 ± 0.008	0.0
$NaNO_3$ [a]	-7.6 ± 1.00	2 ± 2	1	0.340 ± 0.002	0.0
$NaNO_3$ [b]		1 ± 4	1	0.332 ± 0.008	0.0

[a] Experimental NMR parameters obtained in this study. [b]Experimental NMR parameters reported in literature.

Simulation of the stationary spectra, shown in Figure 7.3, yielded the remaining NMR parameters (Ω, κ) which are also provided in Table 7.1.

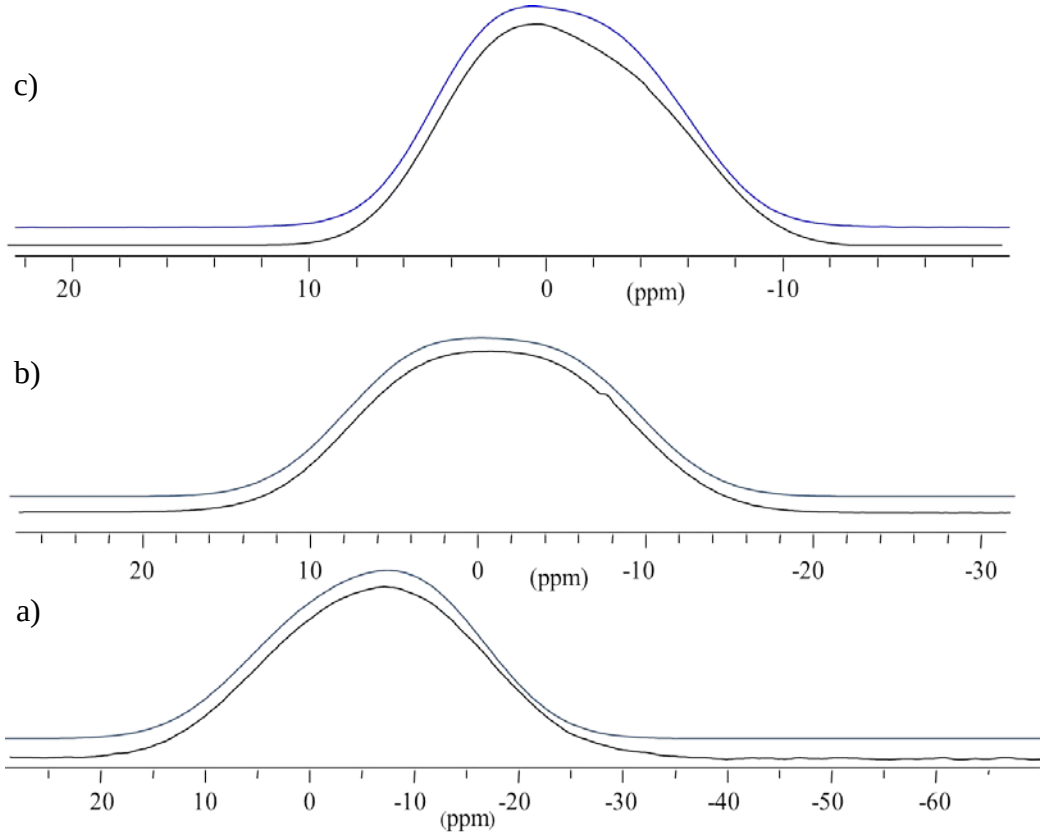

Figure 7.3. Simulated (upper traces) and experimental (lower traces) ^{23}Na stationary spectra of $NaBrO_3$ acquired at a) 7.05 T b) 11.75 T, and c) 21.14 T. Each spectrum is the sum of 3000 scans.

Similarly, experimental ^{23}Na NMR MAS and stationary NMR spectra for $NaClO_3$ were collected at 11.75 and 21.14 T, these are shown in Figures 7.4-7.5. Experimental EFG and chemical shift tensors parameters were obtained in a similar manner as for $NaBrO_3$, and are listed in Table 7.1. The value of $\eta = 0$ and $\kappa = 1$ for both compounds confirms that both the EFG and CS tensors are axially symmetric and that V_{zz} is coincident with δ_{33}. The values of the C_Q are 0.780 ± 0.002 and 0.840 ± 0.002 MHz for $NaClO_3$ and $NaBrO_3$, respectively. The

experimental values of the CS tensor parameters for powder samples obtained in this research are in good agreement with the related values obtained from single crystal studies reported by Sagnowski *et al.* [9] However for both compounds the value of the span within error is slightly smaller than that obtained from single-crystal studies.

SIMPSON calculations were also conducted using the NMR parameters listed in Table 7.1; the best-fit simulated and experimental spectra for both $NaBrO_3$ and $NaClO_3$ are in good agreement as shown in Figures 7.6 and 7.7, respectively.

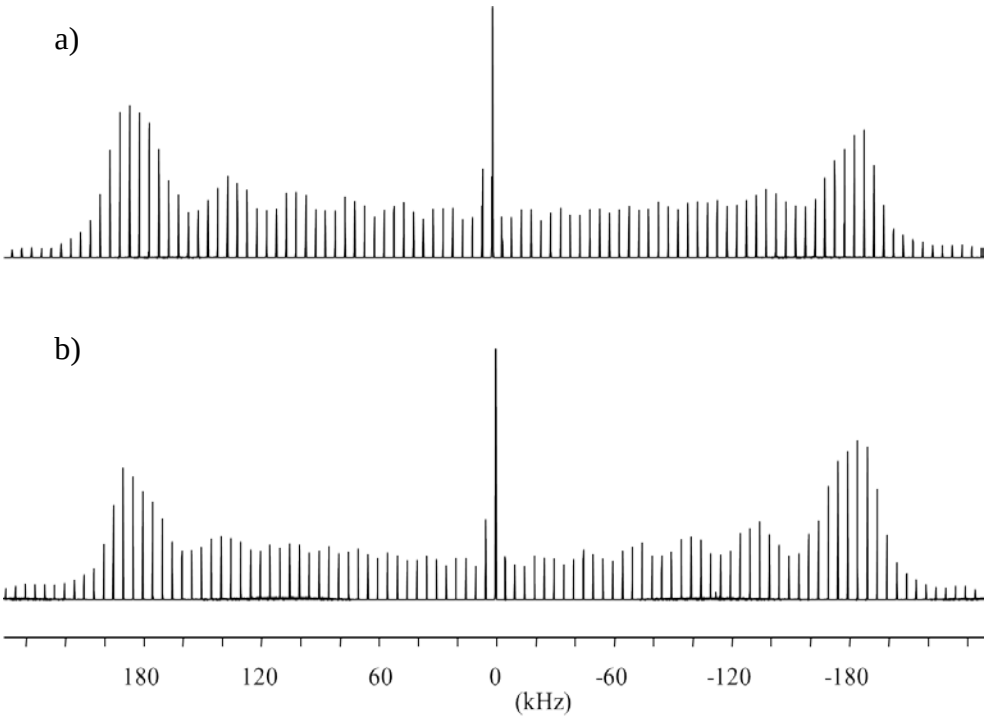

Figure 7.4. ^{23}Na NMR spectra of $NaClO_3$ acquired at a) 11.75 T and b) 21.14 T, with an MAS rate of 5 kHz; each spectrum is the sum of 3000 scans.

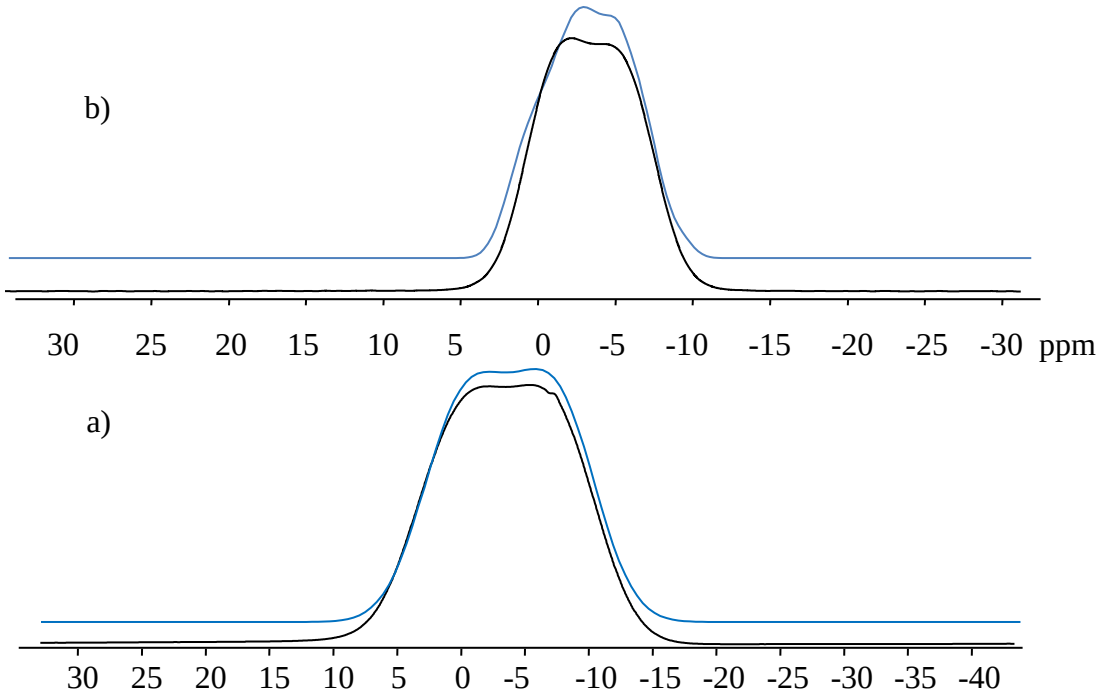

F**igure 7.5**. Simulated (upper traces) and experimental (lower traces) ^{23}Na stationary spectra of $NaClO_3$ acquired at a) 11. 75 T and b) 21.14 T.

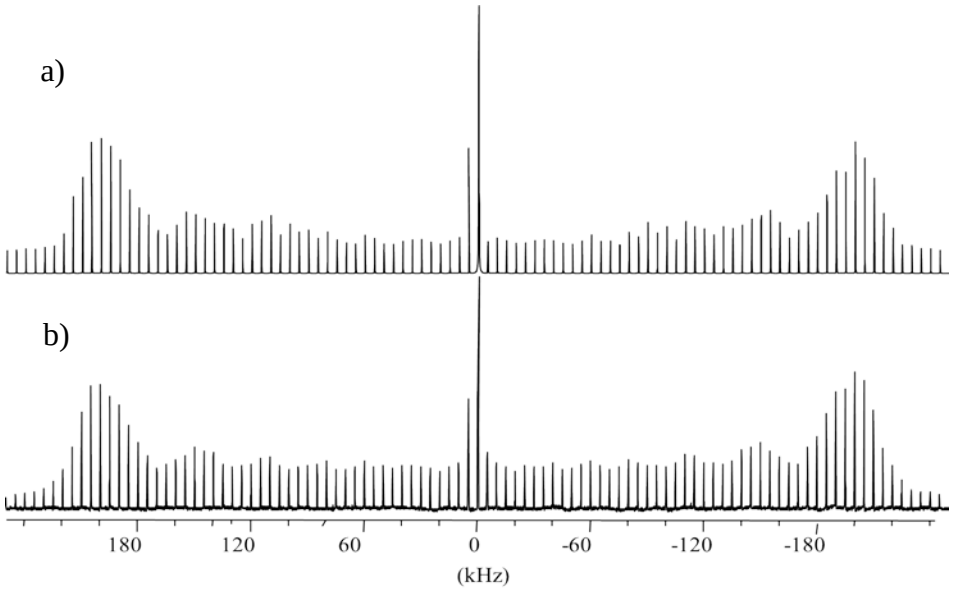

Figure 7.6. ^{23}Na NMR spectra of $NaBrO_3$, acquired at 21.14 T. a) Simulated and b) experimental with an MAS rate of 5 kHz. The NMR parameters obtained from the simulation are summarized in Table 7.1.

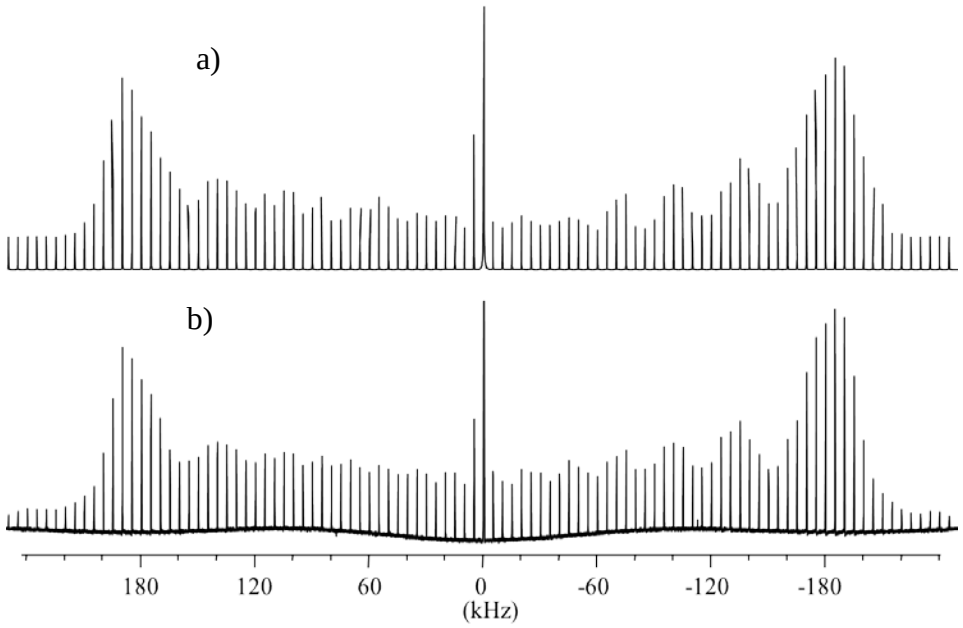

Figure 7.7. ^{23}Na NMR spectra of $NaClO_3$, acquired at 21.14 T. a) Simulated and b) experimental with an MAS rate of 5 kHz. The NMR parameters obtained from the simulation are summarized in Table 7.1.

Sodium nitrate belongs to the rhombohedral system with space group *R*3c, with two molecules in the unit cell. At each corner there are nitrogen atoms as well as at the centre of the cell, and the sodium ions lie half-way between the nitrogen atoms on a threefold axis, as shown in Figure 7.8. The sodium ions therefore have three-fold symmetry which means that the EFG and MS tensors are axially symmetric with their symmetry axes parallel to the threefold axis of the crystal.[44] The two sodium ions in the unit cell are crystallographically and magnetically equivalent; therefore, in the NMR spectra of $NaNO_3$ we expect only one sodium site.

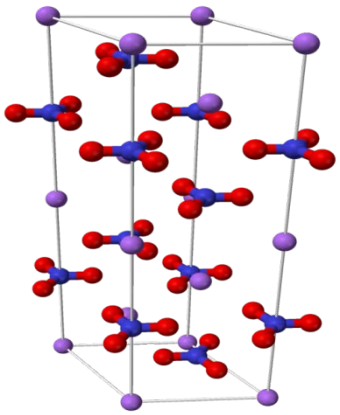

Figure 7.8. Crystallographic structure of $NaNO_3$

The MAS ^{23}Na NMR spectra of powdered $NaNO_3$ acquired at 11.75 and 21.14 T are shown in Figure 7.9. As discussed in an earlier chapter, the intensity distributions over the spinning sidebands are very sensitive to variation of η, while the change in C_Q scales the width of the spectrum. MAS spectra at both fields confirm that η = 0, as expected from the structure data. The value of C_Q, 0.340 ± 0.002 MHz, was obtained from the total width of the spectra. This value is in good agreement with the value reported in the literature.[45]

The static ^{23}Na NMR spectra, shown in Figure 7.10, display the typical line shape for a first-order quadrupolar interaction of a spin-3/2 nucleus in an axially symmetric environment. Comparing the linewidths of the static spectra at three fields, they are nearly identical when measured in Hz (not shown). This indicates that the CSA contributes only slightly to the powder lineshape. This compound has Ω = 2 ± 2 which is the smallest span compared to other sodium salts studied in this research. The static spectra were simulated using the CS and quadrupolar parameters determined from the MAS spectra as initial input; the simulated spectra are provided in Figures 7-10. As a final step, the MAS spectra of $NaNO_3$ were simulated by SIMPSON considering all NMR parameters, which reproduce the experimental spectrum (Figure 7.11).

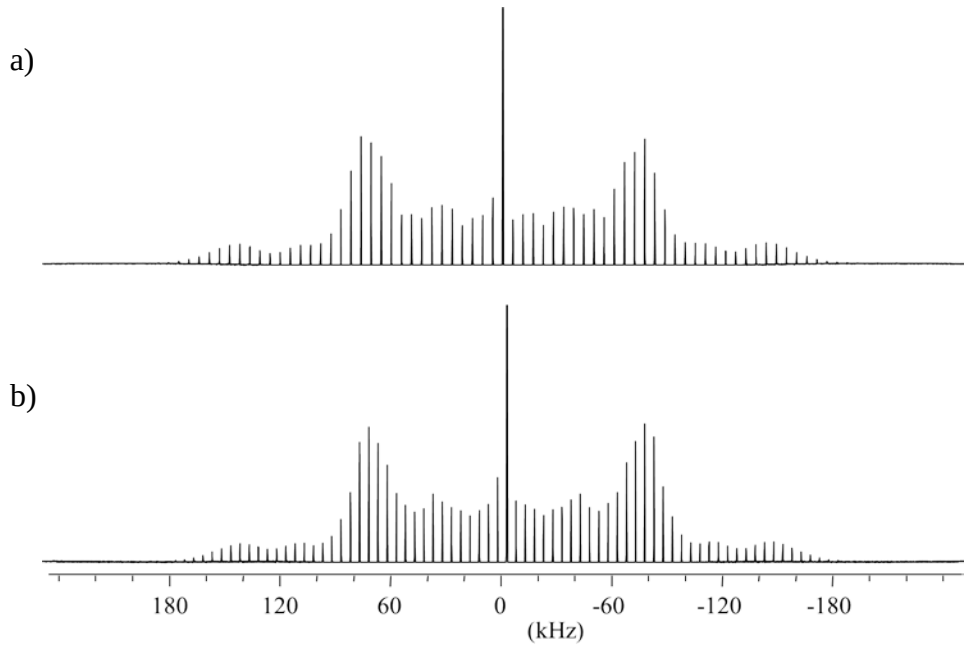

Figure 7.9. ^{23}Na NMR spectra of $NaNO_3$ acquired at a) 11.75 and b) 21.14 T with MAS rates of 5 kHz. Each spectrum is the sum of 3000 scans.

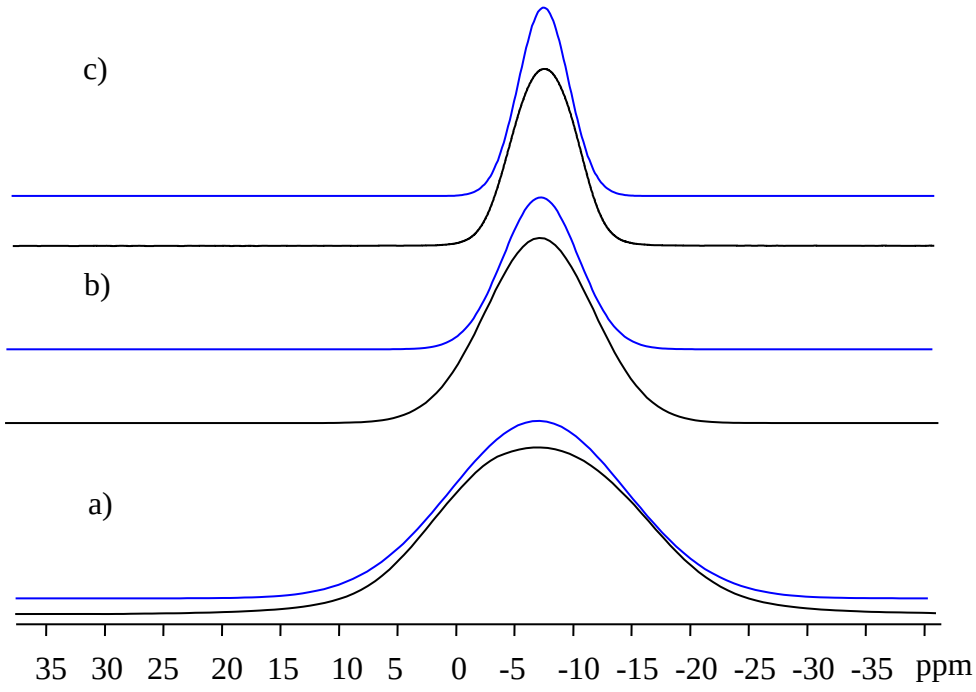

Figure 7.10. Simulated (upper traces) and experimental (lower traces) ^{23}Na stationary spectra of $NaNO_3$ acquired at a) 7.05 T b) 11.75 T, and c) 21.14 T. Each spectrum is the sum of 3000 scans.

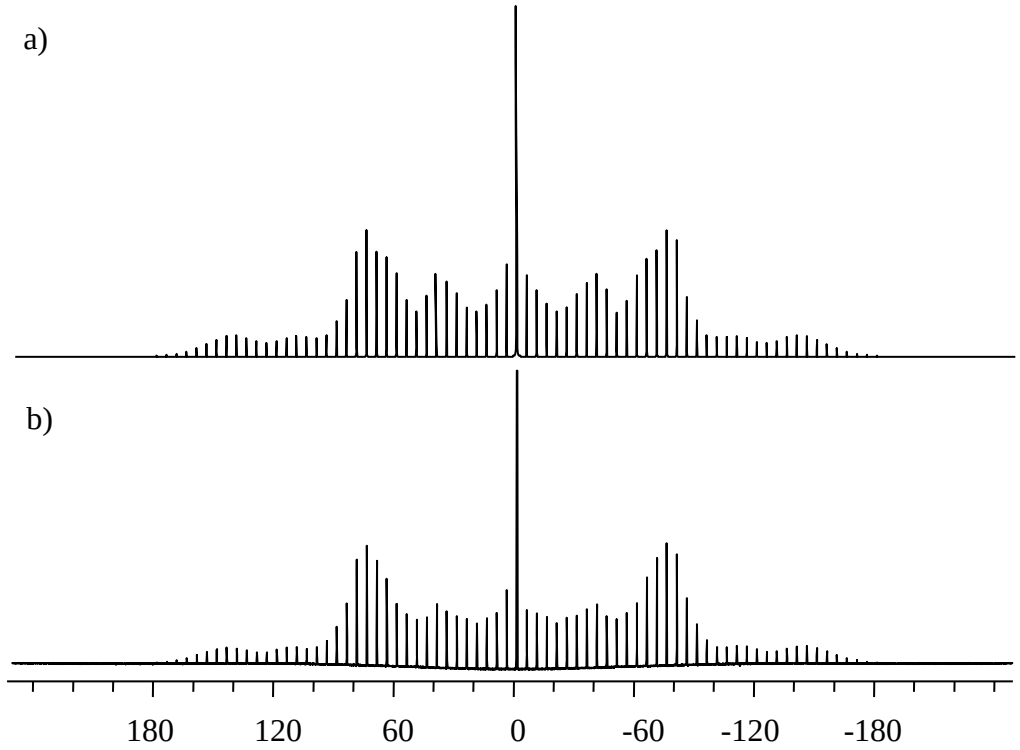

Figure 7.11. ^{23}Na NMR spectra of $NaNO_3$, acquired at 21.14 T, a) Simulated and b) experimental with MAS rates of 5 kHz. The NMR parameters obtained from the simulation are summarized in Table 7.1.

7.4.1.2. Sodium Nitrite, $NaNO_2$

The crystal structure of $NaNO_2$ which was first determined by Ziegler[46] and later refined by others,[47,48] belongs to the non-centro symmetric body-centred orthorhombic symmetry group, space group *Im2m* Figure 7.12. The unit cell has two molecules both with the same point symmetry. There is no higher-order symmetry for the sodium site; therefore no information about the relative orientations of the EFG and CS tensors are available beforehand.

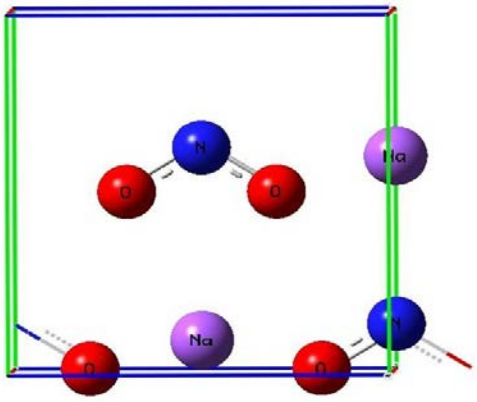

Figure 7.12. Crystallographic structure of $NaNO_2$

Figure 7.13 displays ^{23}Na MAS NMR spectra of $NaNO_2$ obtained at 7.05, 11.75, and 21.14 T. The effect of the second-order quadrupolar interaction on the lineshape is observed for the central transition, as shown in the inset of Figure 7.13(a); this indicates that the quadrupole interaction is significant. Values of C_Q, 1.10 ± 0.02 MHz, and η, 0.10 ± 0.05 (Table 7.2), were extracted from the width of the spectra and lineshape of the central transition, respectively. These values are in good agreement with the literature values reported for a single crystal,[49] and for a powder sample.[50]

Table 7.2. Experimental Sodium-23 NMR Chemical Shift and Electric Field Gradient Tensor Parameters for $NaNO_2$.

	δ_{iso}/ppm	Ω/ppm	κ	C_Q/MHz	η
$NaNO_2$ [a]	-8.0 ± 0.2	17 ± 3	-0.9 ± 0.1	1.10 ± 0.02	0.10 ± 0.05
$NaNO_2$ [b]	-8.0 ± 0.1			1.09 ± 0.03	0.11 ± 0.03

[a] Experimental NMR parameters obtained in this study. [b] Experimental NMR parameters reported in literature.[51]

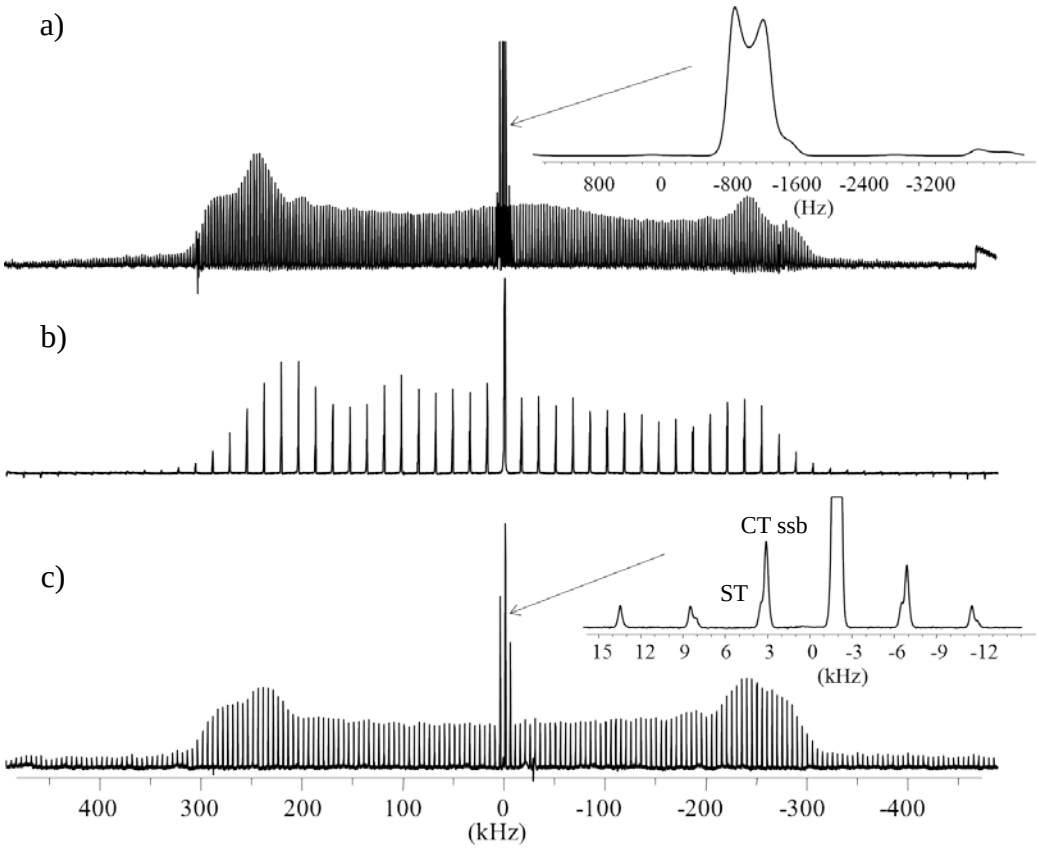

Figure 7.13. ^{23}Na NMR spectra of $NaNO_2$ acquired at a) 7.05 T, 3 kHz, b) 11.75 T, 17 kHz and c) 21.14 T, with an MAS rate of 5 kHz. Each spectrum is the sum of 2000 scans.

The inset of Figure 7.13(c) show that of the CT overlap with those sidebands of the satellite transition for the spectrum acquired at 21.14 T (a similar effect is seen on the lower frequency side); this is due to the MS interaction. To verify this conclusion SIMPSON simulations of the spectra, shown in Figure 7.14, were undertaken. Simulations were done with and without including the MS effect on the related simulated spectra (Figure 7.14 b-a), respectively). These spectra clearly confirm the presence of the MS which is expected to be small compared to the EFG interaction.

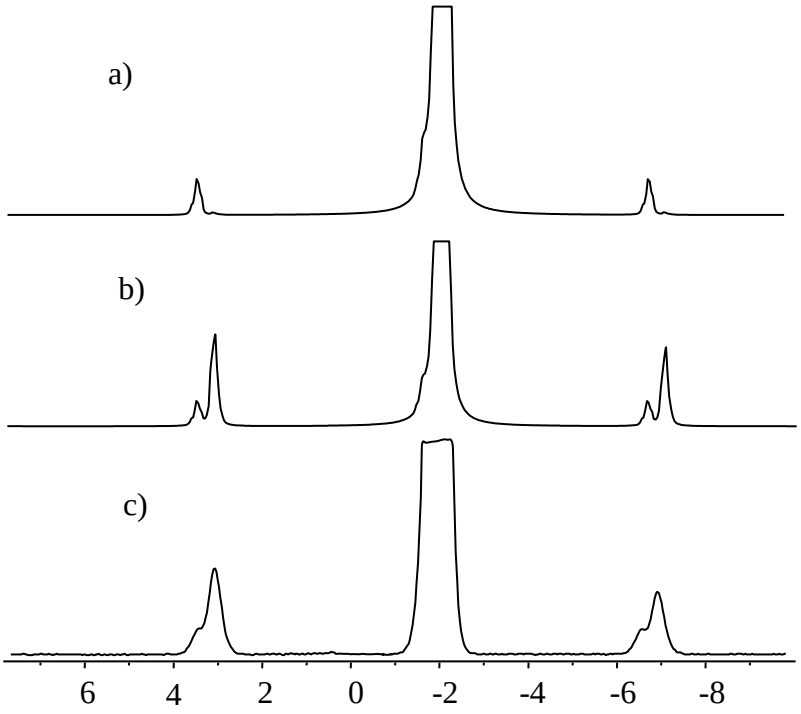

Figure 7.14. Simulated ^{23}Na NMR spectra of $NaNO_2$ a) without, b) with the CS interaction, and c) experimental acquired 21.14 T with an MAS rate of 5 kHz (only the CT and 1storder ssb are shown).

The static ^{23}Na NMR spectrum acquired at 21.14 T (Figure. 7.15) yields further information about the sodium CS tensor components. From the simulation of this spectrum the following parameters were obtained: Ω = 17 ± 3 ppm and κ = -0.9 ± 0.1 (Table 7.2). To our knowledge there is no experimental CS parameters for $NaNO_2$ reported in the literature. Spectral analysis indicates that the CS tensor is also approximately axially symmetric and that δ_{11}, the unique component, is nearly coincident with V_{zz}.

SIMPSON simulations were conducted using the NMR parameters listed in Table 7.2; the best-fit simulated and experimental spectra are in good agreement as shown in Figure 7.16.

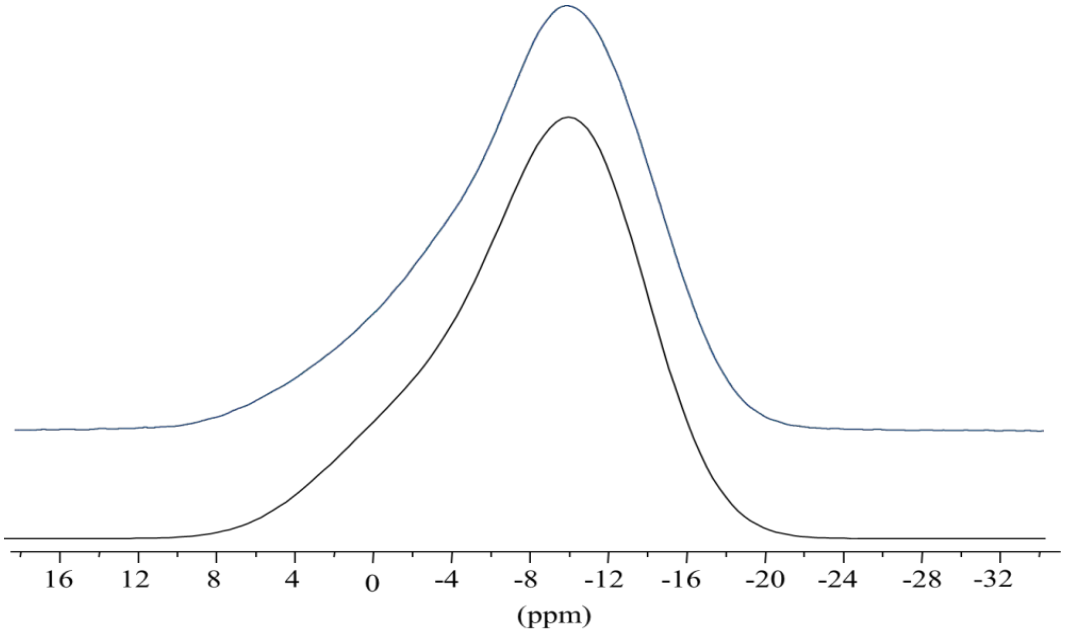

Figure 7.15. Simulated (upper trace) and experimental (lower trace) ^{23}Na stationary spectra of $NaNO_2$ acquired at 21.14 T.

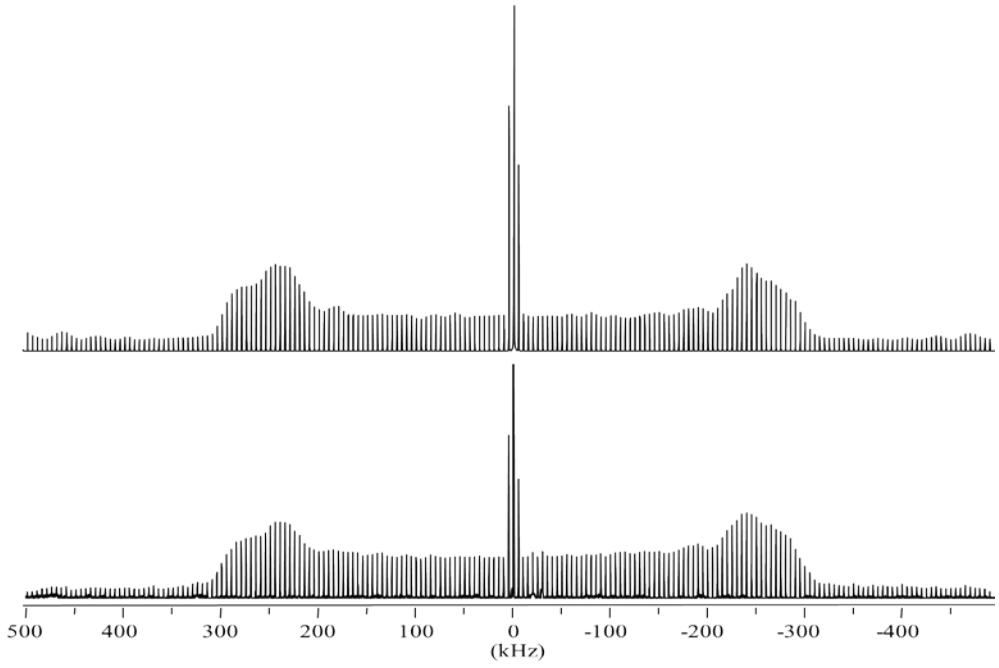

Figure 7.16. Simulated (upper trace) and experimental (lower trace) ^{23}Na MAS spectra of $NaNO_2$ acquired at 21.14 T with an MAS rate of 5.0 kHz.

7.4.1.3. Sodium Selenite, Na_2SeO_3.

The crystal structure of Na_2SeO_3 was first reported by Helmholdt *et al.*,[52] and refined by Wickleder.[53] The unit cell is monoclinic and contains two crystallographically distinct Na^+ ions, Na_1, and Na_2. Na_1 is coordinated by four monodentate and one chelating selenite ion, while two monodentate and two chelating selenite ions are attached to Na_2 (Figure 7.17).

The ^{23}Na NMR experimental spectrum (Figure 7.18) confirms the presence of two distinct sodium sites in Na_2SeO_3. In the ^{23}Na MAS NMR spectrum of Na_2SeO_3, second-order quadrupolar lineshapes for the CT for both sodium sites are observed. Also ssb's are observed over a spectral range of 2.7 MHz, (only 2 MHz are shown in Figure 7.18).

The quadrupolar parameters, C_Q = 2.65 ± 0.05 MHz, η = 0.50 ± 0.05 for site **1** and C_Q = 1.75 ± 0.05 MHz, η = 0.40 ± 0.10 for site **2**, were determined from the linewidth and lineshape of the MAS spectra, respectively (Table 7.3). Figure 7.19 shows the simulated and experimental MAS spectra of the central transition for two sodium sites in Na_2SeO_3. A spinning sideband of the CT, due to the presence of the CSA, is also observed, shown in Figure 7.18 inset (left). This has been examined using the same procedure as discussed in the previous section.

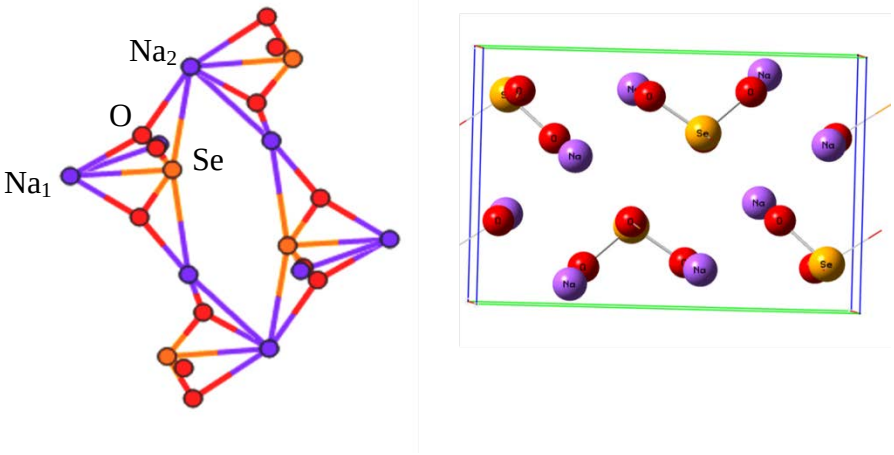

Figure 7.17. Perspective view (left) and along [100] (right) of the crystal structure of Na_2SeO_3.

Table 7.3. Experimental Sodium-23 NMR Chemical Shift and Electric Field Gradient Tensor Parameters for Na_2SeO_3.

Na_2SeO3	δ_{iso}/ppm	Ω/ppm	κ	C_Q/MHz	η
Site **1**	10.0 ± 1.0	25 ± 5	-0.1 ± 0.0	2.65 ± 0.05	0.50 ± 0.05
Site **2**	20.2 ± 0.5	20 ± 5	-0.5 ± 0.1	1.75 ± 0.05	0.40 ± 0.10

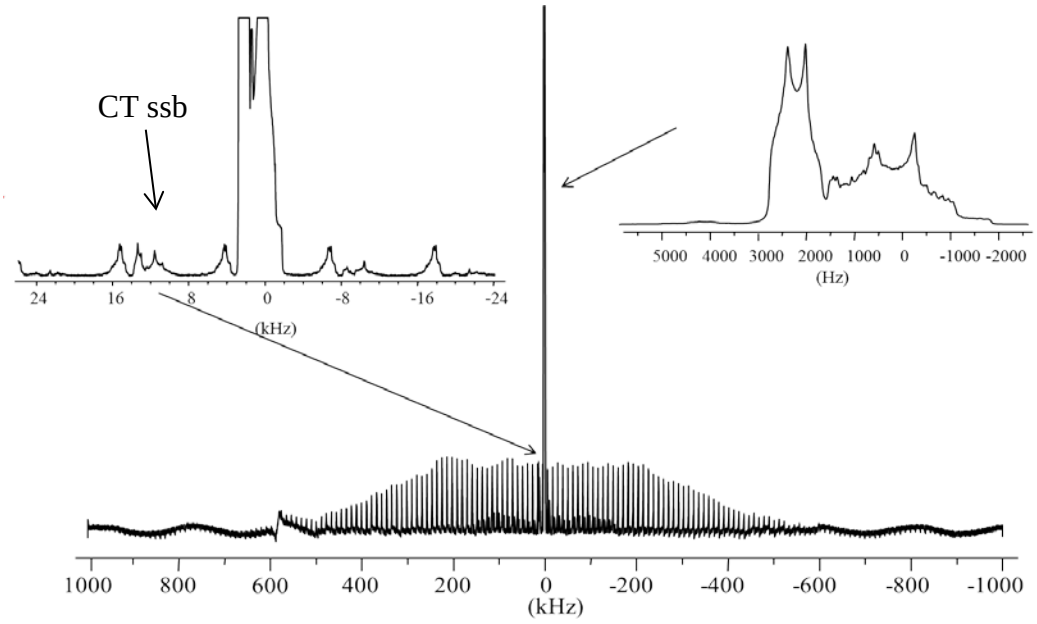

Figure 7.18. ^{23}Na NMR spectra of Na_2SeO_3 acquired at 11.75 T, with an MAS rate of 11 kHz. Inset (right) shows the CT which indicates the presence of two sodium sites. Inset (left) shows the spinning sidebands of the CT.

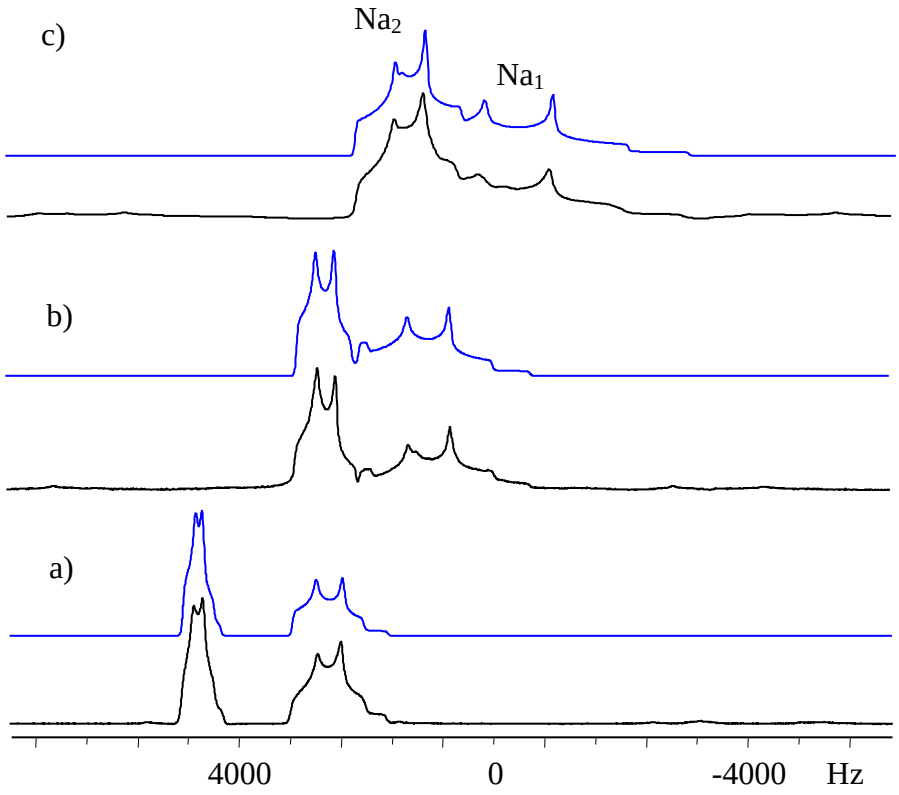

Figure 7.19. Simulated (upper traces) and experimental (lower traces) central transition powder patterns of ^{23}Na MAS NMR spectra of Na_2SeO_3 acquired at a) 21.14 T, 10 kHz b) 11.75 T, 11 kHz, and c) 7.05 T, 7 kHz.

Sodium-23 NMR spectra of static samples of Na_2SeO_3 obtained at three fields (7.05 and 11.75, and 21.14 T) are shown in Figure 7.20. Analysis of these spectra is rather difficult since two sites overlap. Careful analysis of these spectra with the aid of calculated results as a starting point yields the CS parameters which are provided in Table 7.3.

Numerical simulations of the experimental ^{23}Na solid-state NMR spectra of MAS samples were performed using SIMPSON (Figure 7.21). The combined effect of the quadrupolar interaction and CSA was taken into account in the simulations. As seen in the inset of the Figure 7.21 (right), the simulated CT lineshape for both sodium sites are reproduced in good agreement with

experiment. The effect of the CSA was tested as discussed and shown in inset of Figure 7.21 (left).

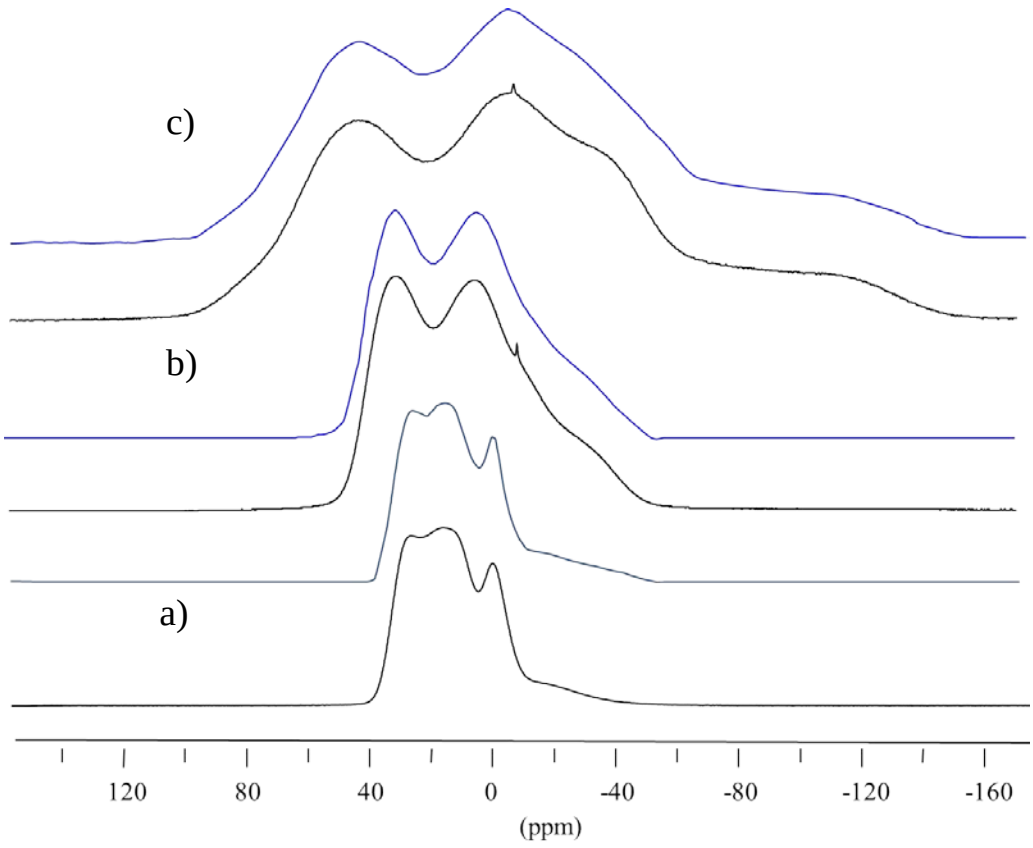

Figure 7.20. Simulated (upper traces) and experimental (lower traces) solid-state ^{23}Na spectra of stationary sample of Na_2SeO_3 acquired at a) 21.14 T, b) 11.75 T and c) 7.05 T.

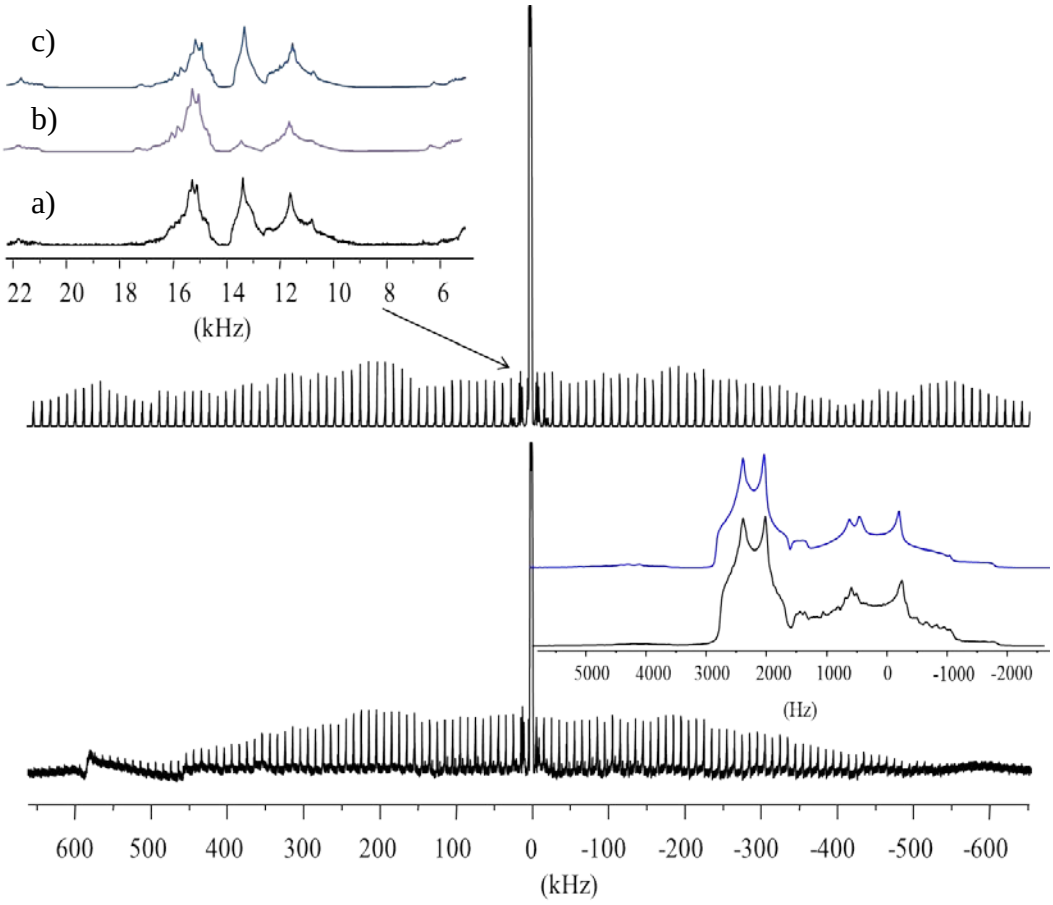

Figure 7.21. Simulated (upper trace) and experimental (lower trace) solid-state ^{23}Na NMR spectra of Na_2SeO_3 acquired at 11.75 T, with an MAS rate of 10 kHz. Inset (right) shows the simulated and experimental CT for the two sodium sites. Inset (left) shows the a) Experimental CT ssb, b) simulated with EFG and no CSA and c) simulated with CS and EFG.

7.4.1.4. Anhydrous Disodium Hydrogen Phosphate, Na_2HPO_4.

Anhydrous Na_2HPO_4 belongs to space group $P2_1/c$, and may be described by hydrogen-bonded zigzag chains of phosphate anions.[54] There are three non-equivalent sodium sites in this structure, Figure 7.22. Atoms Na_1 and Na_2 are distinct but both have a slightly distorted octahedral coordination by six oxygen atoms. In contrast, Na_3 has a strongly distorted tetrahedral arrangement of oxygen atoms and has the shortest distances to the hydrogen atoms. The number of sodium atoms per unit cell for Na_1, Na_2 and Na_3 are 2, 2, and 4, respectively.

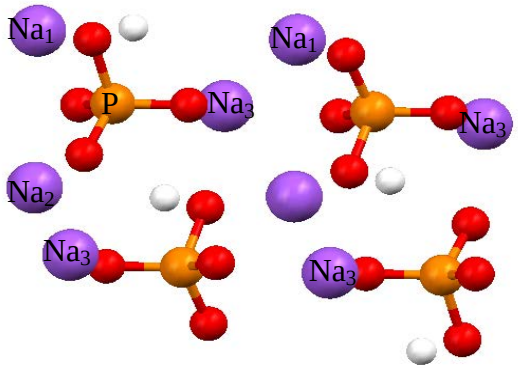

Figure 7.22. The crystallographic structure of Na_2HPO_4.

Presented in Figure 7.23 is the ^{23}Na MAS NMR spectrum of Na_2HPO_4, which confirms the presence of three distinct sodium sites. The experimental spectrum was simulated and the parameters extracted from the simulation are listed in Table 7.4. Because there are twice as many Na_3 atoms as Na_1 or Na_2, this NMR site is easily identified; however distinguishing between Na_1 and Na_2 is not straightforward. The EFG tensor parameters obtained experimentally in this study are in excellent agreement with the value reported by Baldus *et al*., thus Na_1 and Na_2 have been assigned as in their work. In this report the quadrupolar coupling constant for the three sodium sites have also been calculated by using the model I (point charge model) introduced by Koller *et al*.,[55] which are consistent with the results reported in our study.

Figure 7.24 shows the CT region simulated with WSOLIDS and experimental ^{23}Na MAS NMR spectra for Na_2HPO_4 at 7.05, 11.75 and 21.14 T, respectively. Each spectrum exhibits a typical line shape arising from the second-order quadrupole interaction. The simulation of spectra acquired at three magnetic field strengths using EFG parameters listed in Table 7.4 reproduces the experimental spectra.

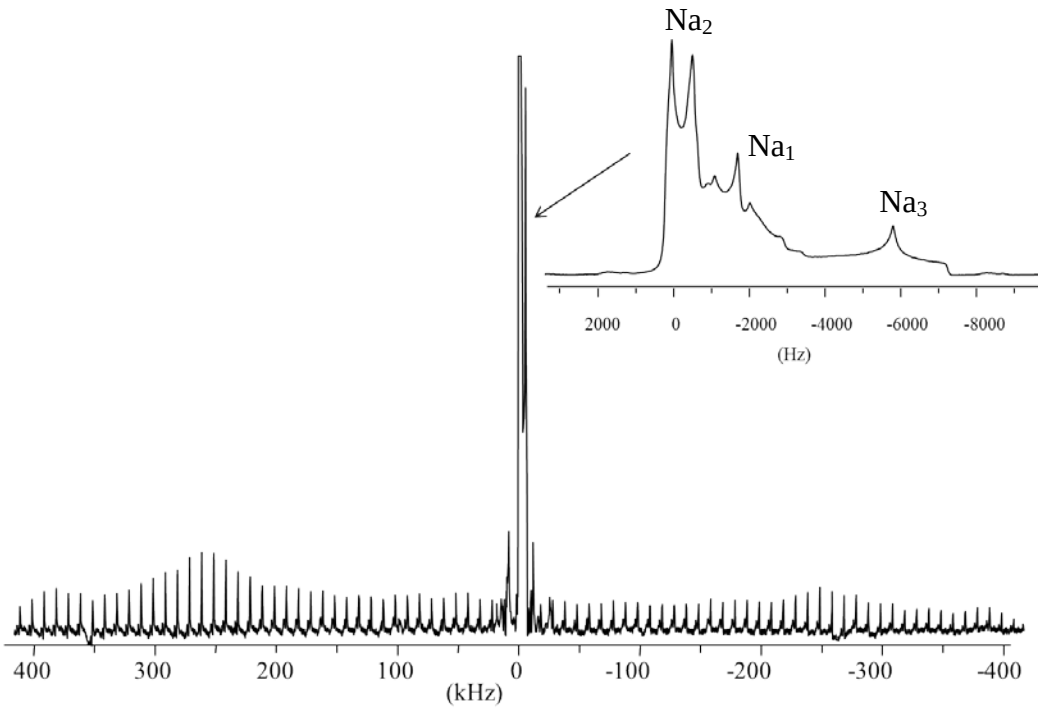

Figure 7.23. ^{23}Na NMR spectra of Na_2HPO_4 acquired at 7.05 T, with an MAS rate of 10 kHz. The inset shows the CT which indicates the presence of three sodium sites. Also ssb's are observed over a spectral range of 3.7 MHz, (up to 0.8 MHz is shown here).

Figure 7.25 shows the simulated and experimental spectra of a stationary sample of Na_2HPO_4 at three magnetic field strengths. Extracting the CSA parameters is very difficult since the three sodium sites are simultaneously present. However with the aid of the computational results and values obtained from MAS spectra as a starting point, magnetic shielding tensor parameters were extracted for the three sodium site and are listed in the Table 7.4.

Finally, the EFG and CS tensor parameters provided in Table 7.4 were confirmed through fitting of spectra of an MAS sample, shown in Figure 7.26.

Table 7.4. Experimental Sodium-23 NMR Chemical Shift and Electric Field Gradient Tensor Parameters for Na_2HPO_4

Compund	δ_{iso}/ppm	Ω/ppm	κ	C_Q/MHz	η
Na_2HPO_4					
Site **1**	5.00 ± 0.5	10 ± 5	0.2 ± 0.2	2.100 ± 0.050	0.65 ± 0.05
ref	5.52 ± 0.2			2.130 ± 0. 012	0.69 ± 0.05
Site **2**	6.00 ± 0.40	8 ± 5	0.0 ± 0.1	1.350 ± 0.050	0.15 ± 0.05
ref[54]	6.20 ± 0.15			1.370 ± 0.007	0.21 ± 0.03
Site **3**	7.00 ± 0.50	15 ± 5	0.5 ± 0.1	3.650 ± 0.060	0.30 ± 0.05
ref[54]	7.24 ± 0.12			3.702 ± 0.008	0.27 ± 0.12

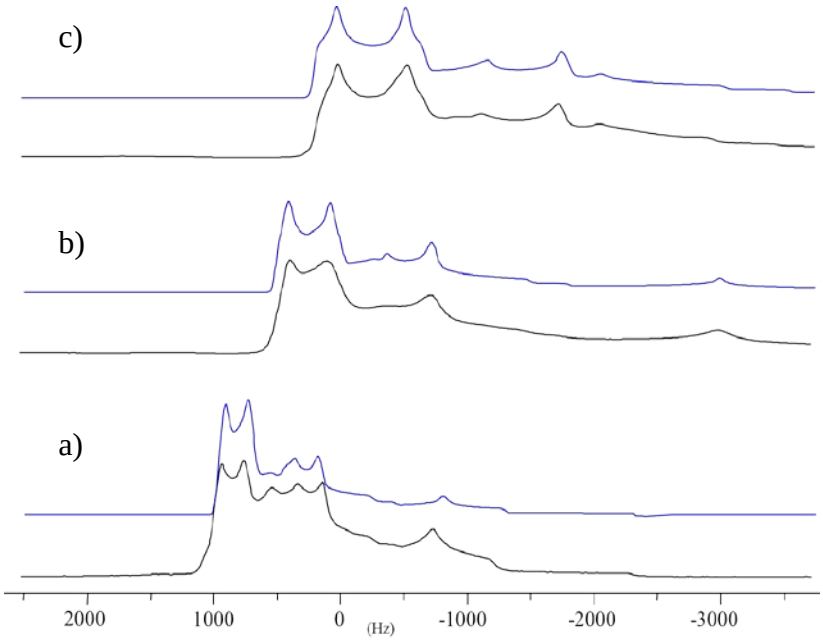

Figure 7.24. Simulated (upper traces) and experimental (lower traces) central transition powder patterns of ^{23}Na MAS NMR spectra of Na_2HPO_4 acquired at a) 21.14 T, 10 kHz b) 11.75 T, 7 kHz and c) 7.05 T, 10 kHz.

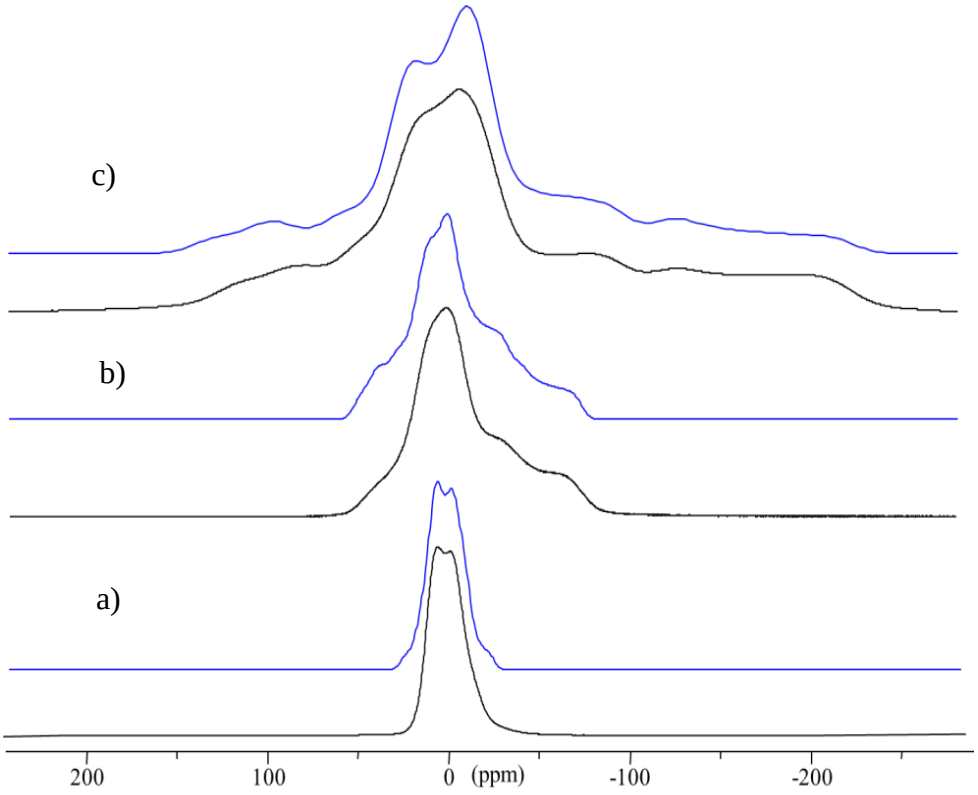

Figure 7.25. Simulated (upper traces) and experimental (lower traces) solid-state ^{23}Na NMR spectra of a stationary sample of Na_2HPO_4 acquired at a) 21.14 T b) 11.75 T and c) 7.05 T.

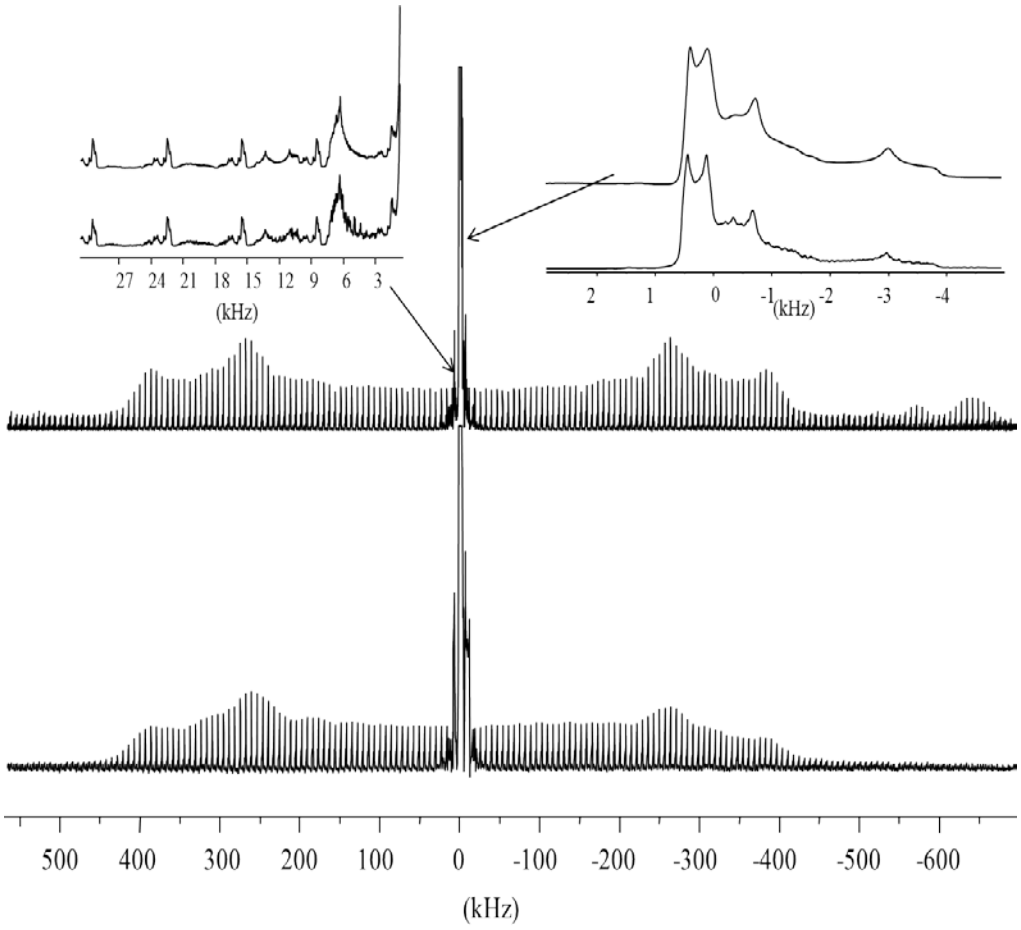

Figure 7.26. Simulated (upper trace) and experimental (lower trace) solid-state ^{23}Na spectra of a sample of Na_2HPO_4 acquired at 11.75 T, with AN MAS rate of 7 kHz. Inset (right) shows the simulated and experimental CT of three sodium sites. Inset (left) shows the ST and spinning sidebands of the CT.

7.4.2. Computational Results

Quantum chemical calculations of the sodium-23 magnetic shielding and EFG tensors were carried out with the CASTEP and BAND codes on a series of sodium salts to provide additional insight into the experimental results. These results are summarized in Table 7.5 along with experimental results from this study. To our knowledge, there are no previous reports of calculated sodium magnetic shielding tensors on this series of sodium salts. A 2005 report on sodium EFG tensors of some salts did not include $NaBrO_3$ and Na_2SeO_3.[56]

$NaBrO_3$, $NaClO_3$, $NaNO_3$. Both computational codes overestimated the value of C_Q for these sodium salts. The greatest discrepancy is the value for $NaNO_3$ CASTEP and BAND overestimated the value by 1.2 and 0.6 MHz, respectively. Both computational codes predicted a negative sign for C_Q for these three sodium salts, in agreement with previously reported computational results for $NaClO_3$ and $NaNO_3$. For $NaNO_3$, the experimental sign of C_Q is reported to be negative by Hughes,[57] as predicted by the calculations. Recall here that the sign of the C_Q normally cannot be obtained from single crystal or powder NMR experiments. Generally, specialized experiments are required which involve using very low temperature and high magnetic fields for a powder sample.[58] for example, Kuhns and Waugh have obtained the sign of the ^{7}Li nuclear quadrupolar coupling constant in $LiNO_3$ by working at mK temperatures. At room temperature however, it may be possible to determine the sign by investigating the trend in the asymmetry of the satellites of quadrupole-split NMR spectra for single crystals.[57] The calculated values of the asymmetry parameters for these three sodium salts obtained by both computational codes are consistent with the experimental value.

The values of the span for the CS tensor calculated by CASTEP for these three salts are underestimated except for the case of $NaNO_3$. In contrast, BAND overestimated these parameters in range of 8-10 ppm. This may be due to the use of medium-sized basis sets for these calculations. The skew predicted by both computational codes are consistent with the experimental values. Calculations predict that V_{zz} is in the direction of δ_{33}.

Table 7.5. Calculated and Experimental Sodium-23 NMR Chemical Shift and Electric Field Gradient Tensor Parameters for a Variety of Single and Multiple-Site Sodium Compounds.

Compound /method	C_Q/ MHz	η_Q	δ_{iso}/ppm	Ω/ppm	κ
$NaBrO_3$					
CASTEP					
ref[59]	-0.99	0.0	-17	7.0	1
ref(geometry optimized)	-1.11	0.0	-14	7.5	1
ref[60]	-0.99	0.0	-17	6.5	1
ref(geometry optimized)	-1.09	0.0	-14	7	1
BAND	-1.01	0.0	-4	30	1
Exp[a]	0.840 ± 0.002	0.0	-0.22 ± 0.20	12 ± 6	1
Ref/exp[9]	0.848 ± 0.008	0.0		19 ± 4	1
$NaClO_3$					
CASTEP	-0.93	0.0	12	4.4	1
BAND	-0.86	0.0	-8	25	1
Exp[a]	0.780 ± 0.002	0.0	-3.43 ± 1.00	8 ± 4	1
Ref/exp[9]	0.788 ± 0.008	0.0		12 ± 4	1
Ref/Cal	-0.51[b]	0.0			
	-1.27[c]	0.0			
$NaNO_3$					
CASTEP	-1.58	0.0	9	2.8	1
BAND	-0.95	0.0	-1	6	1
Exp [a]	0.340 ± 0.000	0.0	-7.6 ± 1.00	2 ± 2	1
Ref/exp	0.332 ± 0.006	0.0		1 ± 4	1
Ref/Cal	-0.42[b]	0.0			
	-0.31[c]	0.0			
$NaNO_2$					
CASTEP	-1.99	0.5	7	21.2	-0.9
BAND	-1.76	0.3	-2	20.0	-0.9
Exp[a]	1.10 ± 0.02	0.10 ± 0.05	-8.0 ± 0.2	17 ± 3	-0.9 ± 0.1
Ref/exp	1.09 ± 0.03	0.11 ± 0.03	-8.1 ± 0.1		
Ref/Cal	-1.46[b]	0.6			
	-1.24[c]	0.17			
Na_2SeO_3					
CASTEP/site 2	-2.05	0.4	22	26	-0.5
Exp site 2[a]	1.75 ± 0.05	0.40 ± 0.10	20.2 ± 0.5	20 ± 5	-0.5 ± 0.1
CASTEP/site 1	-3.03	0.3	12	29	-0.1
Exp site 1[a]	2.65 ± 0.05	0.50 ± 0.05	10.0 ± 1.0	25 ± 5	-0.1 ± 0.0
Na_2HPO_4					
CASTEP/site 1	2.36	0.90	10	18	0.311
Exp/site 1[a]	2.100 ± 0.050	0.65 ± 0.05	5.00 ± 0.50	10 ± 5	0.2 ± 0.2
Ref/Exp site 1	2.130 ± 0.012	0.69 ± 0.05	5.52 ± 0.2		
Ref/Cal site 1	2.11[b]	0.84			
	3.20[c]	0.95			
CASTEP/site 2	-1.12	0.87	11	13	-0.05
Exp/site 2[a]	1.350 ± 0.050	0.15 ± 0.05	6.00 ± 0.40	8 ± 5	0.0 ± 0.1
Ref/Exp site 2[54]	1.370 ± 0.007	0.21 ± 0.03	6.20 ± 0.15		
Ref/Cal site 2	0.98[b]	0.81			
	1.50[c]	0.99			
CASTEP/site 3	4.07	0.27	13	26	0.40
Exp/site 3[a]	3.650 ± 0.060	0.30 ± 0.05	7.00 ± 0.50	15 ± 5	0.50 ± 0.1
Ref/Exp site 3	3.702 ± 0.008	0.27 ± 0.12	7.24 ± 0.12		
Ref/Cal site 3	3.99[b]	0.24			
	6.00[c]	0.28			

[a] Experimental values from this work. [b] HF calculations using a modified 3-21G basis set. [c] HF calculations using a modified 6-21G basis set.

$NaNO_2$. The calculated values of C_Q are overestimated by range of 0.5 to 0.8 MHz by both computation codes, which is similar to the computational value reported in literature. Mortimer and coworkers,[61] have suggested that this discrepancy may be due to the high sensitivity of this compound to the basis sets employed in the calculation. The negative sign of C_Q predicted by the calculations are in agreement with that obtained experimentally.[49,62,63] On the other hand both computational codes predicted accurately the value of span and skew. To our knowledge, there is no previous computation and experimental report on sodium CS tensor parameters for $NaNO_2$. The CS tensor is close to axially symmetric with V_{zz} almost coincident with δ_{33}.

Na_2SeO_3. The C_Q values calculated by CASTEP for both sites are overestimated by approximately 0.4 MHz. The sign for C_Q are predicted to be negative for both sodium sites. The calculated asymmetry parameters for both sites are in agreement with the experimental values obtained in this study. The values of the span and skew predicted by CASTEP were used as an initial setting for the simulation of experimental stationary spectra of Na_2SeO_3 to obtain CS parameters discussed earlier. The calculated CS parameters are in good agreement with the experimental value. This is a good example showing that quantum chemical calculations may complement solid-state NMR experiments to extract the NMR parameters.

Na_2HPO_4. The C_Q values obtained by CASTEP calculations for the three sodium sites of Na_2HPO_4 are overestimated by 0.2 to 0.4 MHz compared to the experimental values, however qualitatively CASTEP results are in good agreement with the experimental for C_Q: $Na_3 > Na_2 > Na_1$. The signs for C_Q are predicted to be positive except for Na_2; this is contrary to the computational results reported in literature. This change of sign however corresponds to a change of the order of the principal components of the EFG tensor. There is a large discrepancy in the calculated asymmetry parameters for Na_2, approximately 0.7 greater than the experimental value. Based on the crystal structure, there are two hydrogen atoms that are equivalent to the Na_2 site with a linear arrangement.

Therefore, the calculation of the EFG parameters for this site may be very sensitive to the position of these hydrogen atoms. A possible explanation is that the position of the hydrogen atoms in the hydrogen-bonded structure of this compound as described in the X-ray report is not accurate.

The CS tensor parameters (span and skew) for the three sodium sites are in agreement with the experimental values obtained in this study. As for Na_2SeO_3, the calculated CS parameters have been used as an initial setting for simulation of the experimental spectra.

Figure 7.27 shows a plot of the experimental versus calculated $|C_Q|$ values obtained by CASTEP. The straight line in the plot corresponds to a best fit line. The slope value, 0.9 shows that overall the calculated C_Q values are in fairly good agreement with the observed values.

A plot of the experimental Ω versus the calculated values obtained by CASTEP is shown in Figure 7.28; however these results do not include $NaBrO_3$. Based on these results the calculated values for $NaClO_3$ and $NaNO_3$ are underestimated. The calculated results for $NaNO_2$, Na_2SeO_3 and Na_2HPO_4 on the other hand are overestimated but show better agreement with experimental values. But they are within better agreement with the experimental values obtained in this study. This probably is due to the better resolved crystal structures available for these compounds.

Overall from experimental and computational results, we conclude that the spans of the sodium CS tensors are less than 28.0 ppm for the six sodium salts studied in this research. Although these are very small spans, it is apparent that the anisotropy of the CS tensor has an effect on the observed line shape of the NMR spectra obtained at high field. The CS tensor spans are comparable to those obtained for sodium metallocenes (Ω = 9.0 - 12.5 ppm) as well as those obtained for $NaBPh_4$ (Ω = 14 ± 2 ppm)[64] and Na(12-crown-4)$_2ClO_4$ (Ω = 14 ppm). The sodium CS tensor spans are also small in a series of inorganic salts studied using

single-crystal NMR spectroscopy by Sagnowski *et al.*,: Ω ($NaNO_3$) = 0 ± 2 ppm; Ω ($NaClO_3$) = 12 ± 2 ppm; Ω ($NaBrO_3$) = 17 ± 2 ppm.

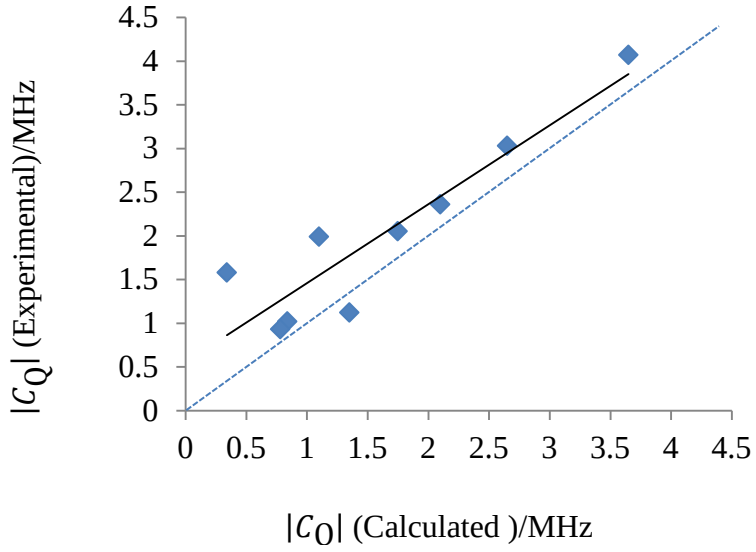

Figure 7.27. Plot of experimental versus the calculated C_Q values obtained with CASTEP ($|C_Q|_{exp}$ = 0.9039 $|C_Q|_{calc}$ + 0.5544, R^2 = 0.8355).

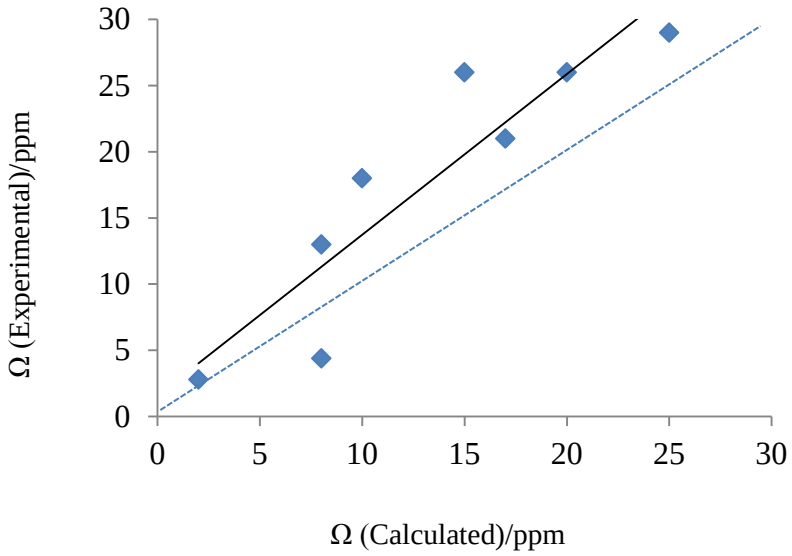

Figure 7.28. Plot of experimental span versus the calculated values by CASTEP, (Ω_{exp} = 1.2133 Ω_{calc} + 1.6004, R^2 = 0.8295).

7.5. Conclusions

Six sodium salts have been characterized by solid-state ^{23}Na NMR spectroscopy and quantum chemistry. In addition to providing ^{23}Na quadrupolar coupling constants for these sodium salts, useful information on the sodium chemical shift tensors has been obtained. The use of a 21.14 T NMR spectrometer offered some advantages in the present study. First, the increased chemical shift resolution at this high field enabled accurate spectral simulations, in particular the definitive resolution of two crystallographically nonequivalent sodium sites. Second, the measurement of ^{23}Na CS tensor spans on the order of 3.0 to 10.0 ppm would not have been possible at lower fields since the powder pattern from the different sites overlap.

Another objective of this work has been to demonstrate that periodic DFT calculations, using the CASTEP or BAND codes, can be used in a routine and reliable manner to calculate ^{23}Na EFG and CS tensor parameters for sodium compounds. However, to obtain good agreement between experiment and calculations, it is essential to have an accurate crystal structure. In general, both the CASTEP and BAND code calculation results overestimated the C_Q values, but, the BAND program was better at predicting the trend of the span values for $NaBrO_3$, $NaClO_3$, and $NaNO_3$. However the calculated values of the spans for $NaBrO_3$ and $NaClO_3$ have the largest discrepancy with experiment compared to calculated span values for other sodium salts in this study. However, the computation time required for NMR parameters determined from BAND calculations is long compared to the similar calculation done with the CASTEP code. For this reason medium-sized basis sets were used for all NMR parameter calculations done with the BAND code. Perhaps using larger basis sets and increasing the cluster memory size will improve the BAND calculation accuracy.

Apart from applications to assignment problems, the CASTEP calculation offers the possibility of detecting inconsistencies in published crystal structures, such as for Na_2HPO_4. Furthermore for the Na_2SeO_3 and Na_2HPO_4, which have

two and three distinct sodium sites, respectively, CASTEP calculations aid in the assignment of the sodium sites for the NMR experimental results.

7.6. References

[1] Gaussian 03, Revision C.02, M. J. Frisch, G. W. Trucks, H. B. Schlegel, G. E. Scuseria, M. A. Robb, J. R. Cheeseman, J. A. Montgomery, Jr., T. Vreven, K. N. Kudin, J. C. Burant, J. M. Millam, S. S. Iyengar, J. Tomasi, V. Barone, B. Mennucci, M. Cossi, G. Scalmani, N. Rega, G. A. Petersson, H. Nakatsuji, M. Hada, M. Ehara, K. Toyota, R. Fukuda, J. Hasegawa, M. Ishida, T. Nakajima, Y. Honda, O. Kitao, H. Nakai, M. Klene, X. Li, J. E. Knox, H. P. Hratchian, J. B. Cross, V. Bakken, C. Adamo, J. Jaramillo, R. Gomperts, R. E. Stratmann, O. Yazyev, A. J. Austin, R. Cammi, C. Pomelli, J. W. Ochterski, P. Y. Ayala, K. Morokuma, G. A. Voth, P. Salvador, J. J. Dannenberg, V. G. Zakrzewski, S. Dapprich, A. D. Daniels, M. C. Strain, O. Farkas, D. K. Malick, A. D. Rabuck, K. Raghavachari, J. B. Foresman, J. V. Ortiz, Q. Cui, A. G. Baboul, S. Clifford, J. Cioslowski, B. B. Stefanov, G. Liu, A. Liashenko, P. Piskorz, I. Komaromi, R. L. Martin, D. J. Fox, T. Keith, M. A. Al-Laham, C. Y. Peng, A. Nanayakkara, M. Challacombe, P. M. W. Gill, B. Johnson, W. Chen, M. W. Wong, C. Gonzalez, and J. A. Pople, Gaussian, Inc., Wallingford CT, 2004.

[2] ADF 2006.01, Theoretical Chemistry, Vrije Universiteit, Amsterdam, http://www. Scm.com.

[3] M. D. Segall, P. J. D. Lindan, M. J. Probert, C. J. Pickard, P. J. Hasnip, S. J. Clark , M. C. J. Payne. *J. Phys. Condens. Matter*. **14**, 2717, (2002).

[4] S. J. Clark, M. D. Segall, C. J. Pickard, P. J. Hasnip, M. J. Probert, K. Refson, M. C. Payne. *Z. Kristall*. **220**, 567, (2005).

[5] G. te Velde , E. J. Baerends. *Phys. Rev*. **B 44**, 7888, (1991).

[6] X. Gonze, B. Amadon, P. M. Anglade, J. M. Beuken, F. Bottin, P. Boulanger, F. Bruneval, D. Caliste, R. Caracas, M. Cote, T. Deutsch, L. Genovese, Ph. Ghosez, M. Giantomassi, S. Goedecker, D. R. Hamann, P. Hermet, F. Jollet, G. Jomard, S. Leroux, M. Mancini, S. Mazevet, M. J. T. Oliveira, G. Onida, Y. Pouillon, T.

Rangel, G. M. Rignanese, D. Sangalli, R. Shaltaf, M. Torrent, M. J. Verstraete, G. Zerah, J. W. Zwanziger. *Computer Phys. Commun*. **180**, 2582, (2009).

[7] P. Blaha, K. Schwarz, J. Luitz, WIEN97, Vienna University of Technology, Austria, 1999.

[8] V. R. Saunders, R. Dovesi, C. Roetti, M. Causa, N. M. Harrison, R. Orlando, C. M. Zicovich-Wilson, CRYSTAL98, University of Torino, Torini, 1998.

[9] S. F. Sagnowski, Z. Sulek, M. Stachura, J. Ogar. *Z. Phys. B-Condensed Matter*, **46**, 123, (1982).

[10] D. L. Bryce, S. Adiga, E. K. Elliott, G. W. Gokel. *J. Phys. Chem.* **A 110**, 13568, (2006).

[11] A. Wong, G. Wu. *J. Phys. Chem.* **A 104**, 11844, (2000).

[12] M. J. Willans, R. W. Schurko. *J. Phys. Chem.* **B 107**, 5144, (2003).

[13] J. Cederberg, L. Kang, C. Conklin, E. Berger. *J. Mol. Spectrosc*. **263**, 142, (2010).

[14] F. H. De Leeuw, R. Van Wachem, A. Dymanus. *J. Chem. Phys*. **53**, 981, (1970).

[15] J. Cederberg, D. Nitz, A. Kolan, T. Rasmusson, K. Hoffmann, S. Tufte. *J. Mol. Spectrosc*. **122**, 171, (1987).

[16] C. E. Miller, J. C. Zorn. *J. Chem. Phys*. **50**, 3748, (1969).

[17] M. Born, J. R. Oppenheimer. *Ann. Physik*. **84**, 457, (1927).

[18] P. H. M. Uylings. *J. Phys.* **B 26**, 2743, (1993).

[19] P. Hohenberg, W. Kohn. *Phys. Rev*. **B 136**, 864, (1964).

[20] W. Kohn, L. Sham, *Phys. Rev*. **A 140**, 1133, (1965).

[21] A. D. Becke. *Phys. Rev*. **A 38**, 3098, (1988).

[22] J. P. Perdew, J. A. Chevary, S. H. Vosko, K. A. Jackson, M. R. Pederson, D. J. Singh, C. Fiolhais. *Phys. Rev.* **B 46**, 6671, (1992).

[23] J. P. Perdew, K. Burke. M. Ernzerhof. *Phys. Rev. Lett*. **77**, 3865, (1996).

[24] R. Carr, M. Parrinello. *Phys. Rev. Lett*. **55**, 2471, (1985).

[25] H. J. Monkhorst, J. D. Pack. *Phys. Rev.* **B 13**, 5188, (1976).

[26] P. E. Blöchl. *Phys. Rev*. **B 50**, 17953, (1994).

[27] C. G. Van de Walle, P. E. Blöchl. *Phys. Rev*. **B 47**, 4244, (1993).

[28] C. J. Pickard. F. Mauri. *Phys. Rev*. **B 63**, 245101, (2001).

[29] S. E. Ashbrook, L. Le Polles, R. Gautier, C. J. Pickard, R. I. Walton. *Phys. Chem. Chem. Phys*. **8**, 3423, (2006).

[30] J. V. Hanna, K. J. Pike, T. Charpentier, T. F. Kemp, M. E. Smith, B. E. G. Lucier, R. W. Schurko, L. S. Cahill. *Chem.-Eur.* J **16**, 3222, (2010).

[31] G. te Velde. *Numerical integration and other methodological aspects of Bandstructure Calculations*. PhD thesis, Vrije Universiteit, Amsterdam, The Netherlands, 1990.

[32] G. Wiesenekker, E. J. Baerends. *J. Phys. Condens. Matter*. **3,** 6721, (1991).

[33] E. van Lenthe, E. J. Baerends, J. G. Snijders. *J. Chem. Phys*. **101**, 9783 (1994).

[34] F. London. *J. Phys. Radium*. **8**, 397 (1937).

[35] R. Ditchfield. *Mol. Phys*. **27**, 789 (1974).

[36] D. Skachkov, M. Krykunov, E. Kadantsev, T. Ziegler. *J. Chem. Theory Comput*. **6**, 1650, (2010).

[37] D. Skachkov, M. Krykunov, T. Ziegler. *Can. J. Chem.* **89**, 1150, (2011).

[38] A. E. Bennett, C. M. Rienstra, M. Auger, K. V. Lakshmi, R. G. Griffin. *J. Chem. Phys*. **103**, 6951, (1995).

[39] S. F. Dec, G. E. Maciel , J. J. Fitzgerald. *J. Am. Chem. Soc.* **112**, 9069, (1990).

[40] K. Eichele, R. E. Wasylishen. WSOLIDS *NMR Simulation Package*, 2001.

[41] M. Bak, J, T. Rasmussen, N. C. Nielsen. *J. Magn. Reson*. **147**, 296, (2000).

[42] R. K. Harris, G. J. Nesbitt. *J. Magn. Reson.* **78**, 245, (1988).

[43] R. W. G. Wyckoff. *Crystal Structures*;Vol. I, Chap.VII. New York: Inter science Publishers, 1948

[44] A. D. Buckingham, S. M. Malm. *Mol. Phys*. **22**, 1127 (1971).

[45] H. J. Jakobsen, J. Skibsted, H. Bildsøe, N. C. Nielsen. *J. Magn. Reson*. **85**, 173, (1989).

[46] G. E. Ziegler. *Phys. Rev*. **38**, 1040, (1931).

[47] M. R. Truter. *Acta Cryst*. **7**, 73, (1954).

[48] M. I. Kay, B. C. Frazer. *Acta Cryst*. **14**, 56, (1961).

[49] A. Weiss. *Z. Naturforsch*. **A 15**, 536, (1960).

[50] A. Samoson, E. Kundla, E. Lippmaa. *J. Magn. Reson*. **49**, 350, (1982).

[51] J. Skibsted, N. C. Nielsen, H. Bildsøe, H. J. Jakobsen. *J. Magn. Reson*. **95**, 88, (1991).

[52] R. B. Helmholdt, E. J. Sonneveld, H. Schenk. *Z. Kristallogr*. **214**, 151, (1999).

[53] M. S. Wickleder. *Acta Cryst*. **E 58**, 103, (2002).

[54] M. Baldus, B. H. Meier, R. R. Ernst, A. P. M. Kentgens, H. Meyer zu Altenschildesche, R. Nesper. *J. Am. Chem. Soc*. **117**, 5141, (1995).

[55] H. Koller, G. Engelhardt, A. P. M. Kentgens, J. Sauer. *J. Phys. Chem*. **98**, 1544, (1994).

[56] C. Johnson, E. A. Moore, M. Mortimer. *Solid State Nucl. Magn. Reson*. **27**, 155, (2005).

[57] D. G. Hughes. *J. Chem. Phys*. **74**, 3236, (1981).

[58] P. L. Kuhns, J. S. Waugh. *J. Chem. Phys*. **97**, 2166, (1992).

[59] S. C. Abrahams, J. L. Bernstein. *Acta Cryst*. **B 33**, 3601, (1977).

[60] D. H. Templeton, L. K. Templeton. *Acta Cryst*. **A 41**, 133, (1985).

[61] E. A. Moore, C. Johnson, M. Mortimer, C. Wigglesworth. *Phys. Chem. Chem. Phys*. **2**, 1325, (2000).

[62] T. Kanashiro, T. Ohno, M. Satoh. *J. Phys. Soc. Jpn*. **54**, 2720, (1985).

[63] K. T. Han, H. W. Shin, I. W. Park, S. H. Chon. *J. Korean Phys. Soc*. **25**, 67, (1992).

[64] A. Wong, R. D. Whitehead, Z. Gan, G. Wu. *J. Phys. Chem.* **A 108**, 10551, (2004).

Chapter 8. Concluding Remarks and Suggestions for Future Work

8.1. Conclusions

This *thesis* has focused on solid-state NMR investigations of important half-integer spin quadrupolar nuclei (I (^{51}V) = 7/2, I (^{17}O) = 5/2, and I (^{23}Na) =3/2) with moderate quadrupole moments of 5.2, -2.5, and 10.4 fm^2, respectively. However, the spin-1/2 nucleus, ^{15}N was also investigated in the case of SNP.

In this study, first, the feasibility of solid-state ^{51}V solid-state NMR study of oxo, peroxo vanadium complexes was demonstrated despite the fact that these complexes have large magnetic shielding anisotropy. The EFG and MS tensors were determined for all these complexes, the vanadium-51 C_Q values range from 4.2 to 7.0 MHz and the vanadium CSA is as great as 1450 ± 30 ppm. The contributions from the anisotropy of vanadium magnetic shielding for all these compounds are significant for ^{51}V NMR spectra acquired at high magnetic field strength. Furthermore, the experimental and theoretically (DFT) predicted NMR parameters are in good agreement. The use of three fields (7.05, 11.75 and 21.14 T) in combination with the appropriate pulse sequence, has ultimately led to the success of the NMR investigation presented herein.

Second, the ^{17}O solid-state NMR studies of ^{17}O-labelled samples of the ligand and complex of indium (III) triiodide bis (tris(4-methoxyphenyl) phosphine oxide) have been illustrated. This study provides more insights regarding the influence of metal bonding to oxygen in this class of compounds. These experimental results were corroborated by DFT calculations of oxygen EFG and MS tensors.

And finally, the sodium-23 EFG and CS tensors for sodium salts were determined using solid-state ^{23}Na NMR spectroscopy. The presence of two and three distinct sodium sites for three of these sodium salts leads to more challenges

in both interpreting and determining CSA parameters for these sodium spectra. The CASTEP code which exploits the inherent periodicity of solids was employed to calculate the NMR parameters. The calculated EFG and MS parameters for the different sodium sites in most cases are consistent with the experimentally measured parameters. This both confirms the assignment, and verifies that the calculated NMR parameters from CASTEP in most cases can be used as an aid for spectral assignment. This study provides the first experimental demonstration of sodium CS tensors from solid-state NMR spectroscopy of powder samples for this class of sodium salts.

Overall, the aims of this *Thesis* were reached with assistance of the computational methods, which provide much useful information complementary to the experimental results.

8.2. Future Work

First, it is thought that no additional work is required on the ^{51}V solid-state NMR studies on oxo- peroxo compound as an unambiguous assignment and analysis of the ^{51}V NMR spectra has been carried out, concluding the NMR parameters. However, in order to determine the orientation of the NMR tensors (EFG and MS) with respect to the molecular frame from ^{51}V solid-state NMR spectra, the results of a study of the ^{51}V in a single crystal of vanadium compounds are needed. This analysis which may complement the results presented in this study has not yet been completed.

Second, it was hoped that the ^{17}O solid-state NMR studies on the ligand and complex of $InI_3[^{17}OP(p\text{-Anis})_3]_2$ can provide insight into the influence of metal coordination on ^{17}O shielding and EFG tensors. However, to complete this research, the ^{17}O NMR studies of the trend of this class of compounds, $InX_3(^{17}OP(p\text{-Anis})_3)_2$ and $GaX_3(^{17}OP(p\text{-Anis})_3)_3$, (X = Cl, Br, I) is recommended.

Third, since $Na_2[Fe(CN)_5(NO)]\cdot 2H_2O$, SNP has two metastable states (MS1, MS2) which has a linkage to inversion of the NO group, and side NO molecular conformation, respectively, one objective may be studying relative orientation of ^{15}N magnetic shielding tensor by MAS and stationary NMR for the different states of SNP. A solid-state NMR ^{15}N (I = 1/2) study of SNP can be useful since ^{15}N is not quadrupolar nuclei, which it makes the analysis and simulations of related spectra much easier. However, a major difficulty in observing SNP in the metastable via solid-state NMR is that one must work with thin disks of sample crystals (thickness, L <0.5 mm), and thus obtaining spectra with low signal-to-noise (S/N) ratio. This is required since the light needed to populate the new state simply does not penetrate into the bulk of a long rod.

Finally, solid-state ^{23}Na NMR spectroscopy has not previously been used to determine the sodium CS parameters for the powder samples of sodium salts, because of the multi sodium sites and small CSA range for sodium salts; however this study demonstrated that this is possible by spectral simulation of NMR spectra aided by computational results. In general, the use of DFT calculations employed by CASTEP was relatively straightforward and proved an invaluable technique to this study. However, its application to determine ^{23}Na MS tensor components in some sodium salts proved challenging. This could, perhaps, lead to the use of larger computational clusters which allow the use of large supercells, which could better represent the possible environments present in these materials.

Appendix 4.1. Calculated NMR Parameters for $VOCl_3$ with Different Basis Sets.

Program/Method	Basis sets	X-ray structure (Solid exp)[1]	X-ray structure (Solid exp)[2]
Gaussian/B3LYP	6-31G	-2018	-2010
Gaussian/B3LYP	6-31G(d)	-1944	-1923
Gaussian/B3LYP	6-31G(d,p)	-1944	-1923
Gaussian/B3LYP	6-31++G(d,p)	-1952	-1930
Gaussian/B3LYP	6-311G	-2340	-2230
Gaussian/B3LYP	6-311G(d)	-2240	-2180
Gaussian/B3LYP	6-311+G	-2288	-2190
Gaussian/B3LYP	6-311+G(d)	-2203	-2145
Gaussian/B3LYP	6-311++G(d,p)	-2203	-2145
Gaussian/B3LYP	6-31+G(df,2pd)	-1968	-1948
Gaussian/B3LYP	TZV	-2498	-2320
Gaussian/B3LYP	TZVP	-2223	-2100
ADF/ZORA DFT	QZ4P	-1990	-1906
CASTEP	GIPAW	-2019	-2052

[1] S. I. Troyanov. *Russ. J. Inorg. Chem.* **50**, 1727, (2005).

[2] J. Galy, R. Enjalbert, G. Jugie, J. Strahle. *J. Solid State Chem.* **47**, 143, (1983).

Appendix 4.2. Carbon and Phosphorus Shielding

Table A1. Contributions to Carbon Magnetic Shielding for C_2H_4.

Contribution	σ_{11}(ppm)	σ_{22} (ppm)	σ_{33} (ppm)	σ_{iso}(ppm)
σ^d(total)	247	249	218	238
σ^p(total)	-313	-187	-48	-183
σ (total)	-65	61	169	55

Table A2. Significant Diamagnetic Contributions to σ for C_2H_4.

φ	MO	σ_{11}	σ_{22}	σ_{33}	σ_{iso}	*s* char(%)	*P* char(%)
1	a_{1g}	100	100	100	100	100	0
2	$1b_{3u}$	100	100	100	100	100	0
3	$2a_{1g}$	15	18	15	16	86	12
4	$1b_{1u}$	22	19	9.6	17	0	99

Table A3. Occ-vir: Significant Contributions to Paramagnetic Shielding for C_2H_4.

φ	MO Occ	φ	MO Vir	σ_{11}	σ_{22}	σ_{33}	σ_{iso}
5	$1b_{2u}$	15	$2b_{1u}^*$	0	-34	0	-11
5		24	$6b_{3u}^*$	0	0	-34	-11
6	$3a_{1g}$	9	$1b_{2g}^*$	-218	0	0	-72
6		19	$2b_{2g}^*$	-44	0	0	-14
6		23	$3b_{1g}^*$	0	0	-27	-9
7	$1b_{1g}$	9	$1b_{2g}^*$	0	-130	0	-43
7		10	$4a_{1g}^*$	0	0	-29	-9
7		18	$6a_{1g}^*$	0	0	0	-11
7		19	$2b_{2g}^*$	0	-43	0	-14

a) b)

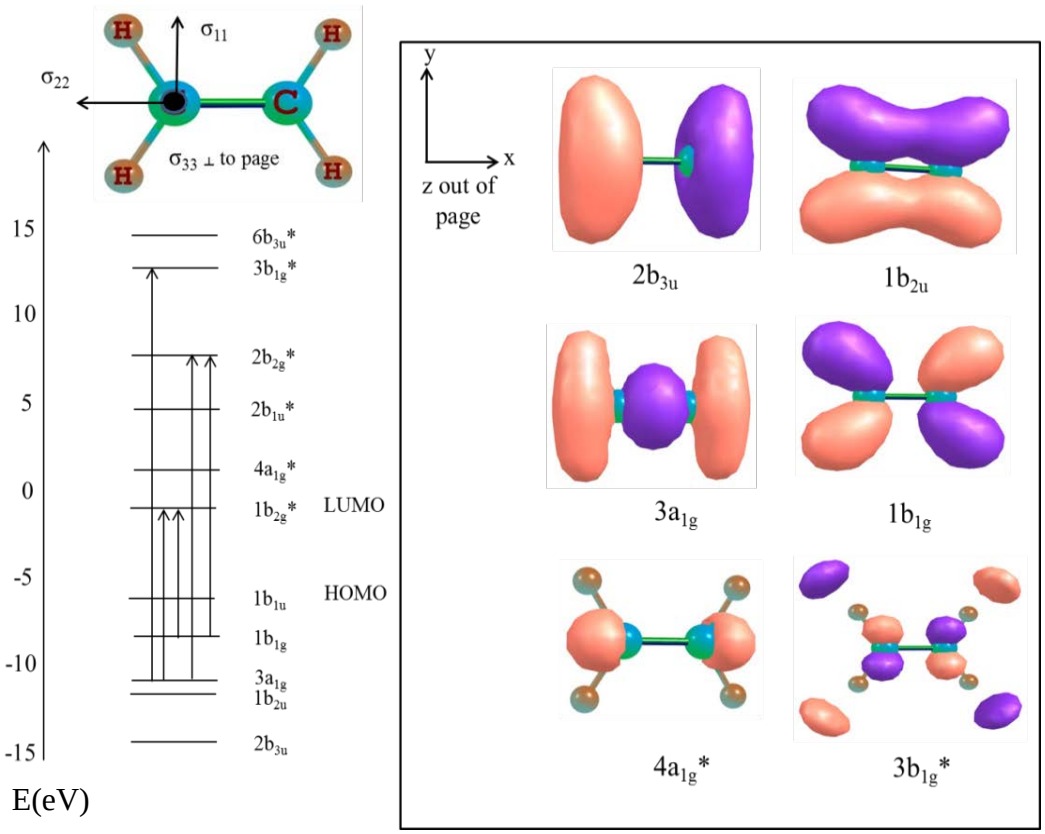

Figure A. a) MO energy-level diagram for C_2H_4. b) Visual representations of MOs which contribute significantly to the paramagnetic shielding tensor.

The results produced here are in good agreement for the results reported in the literature.[1] Generally speaking, important occ-vir contributions in a system with a small energy difference between HOMO and LUMO, such as a conjugated carbon system commonly involve MOs in Table A3 or other MOS which are energetically similar.

Table B1. Contributions to the Phosphorus Magnetic Shielding for PF_3.

Contribution	σ_{11}(ppm)	σ_{22} (ppm)	σ_{33} (ppm)	σ_{iso}(ppm)
σ^d(total)	958	958	956	956
σ^p(total)	-906	-906	-657	-823
σ (total)	51	51	294	132

Table B2. Significant Diamagnetic Contributions to σ for PF_3.

φ	MO	σ_{11}	σ_{22}	σ_{33}	σ_{iso}	*s* char(%)	*P* char(%)
1	$1a_1$	517	517	517	517	100	0
5	$3a_1$	99	99	99	99	100	0
6	2e(1)	114	57	115	95	0	100
7	2e(2)	53	118	115	97	0	100
8	$4a_1$	114	114	57	95	0	98

Table B3. Occ-vir: Significant Paramagnetic Shielding Contributions to σ for PF_3.

φ	MO Occ	φ	MO Vir	σ_{11}	σ_{22}	σ_{33}	σ_{iso}
13	4e(1)	23	$7e(2)^*$	0	0	-162	-54
13		28	$11a_1^*$	-153	0	0	-51
14	4e(2)	22	$7e(1)^*$	0	0	-162	-54
14		28	$11a_1^*$	0	-153	0	-51
21	$8a_1$	22	$7e(1)^*$	-411	0	0	-137
21		23	$7e(2)^*$	0	-411	0	-137

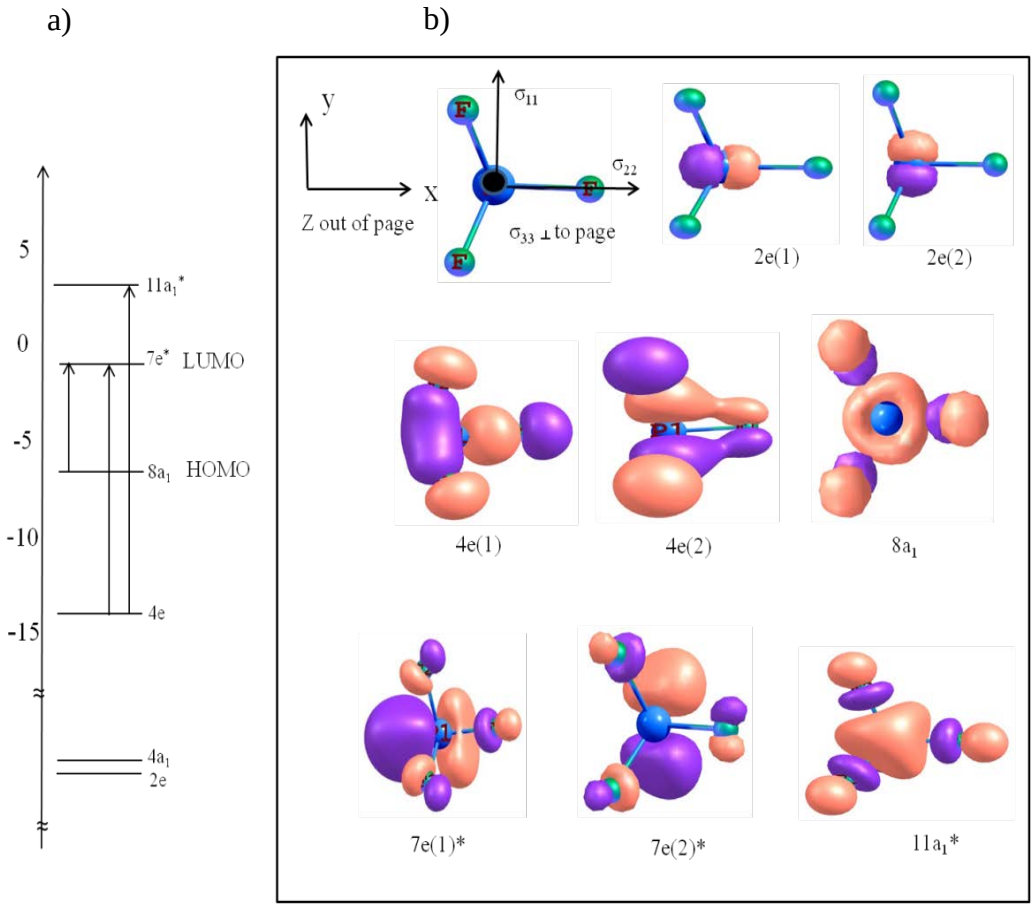

Figure B. a) MO energy level diagram for PF_3. b) Visual representations of the important MOs.

The produced results presented here are in agreement with the literature results for PF_3 reported by Widdifield and Schurko.[1] For example within this set, it is clear that $8a_1$ (HOMO) ↔ 7e* (LUMO) mixing contributes very significantly along the σ_{11} and σ_{22} directions.

In the next step, the carbon MS values and the paramagnetic shielding MO contributions for formaldehyde are calculated using the same method described in the literature. Formaldehyde has C_{2V} symmetry which fixes the axes of the shielding tensor, as shown in Figure C. The calculation results (Table C1) indicate that σ_{33} is perpendicular to the plane, σ_{22} is along the C = O bond and σ_{11} is perpendicular to C = O bond in the plane (Figure C).

Table C1. Calculated Contributions to the Carbon Magnetic Shielding for Formaldehyde.[a]

Contribution	σ_{11}(ppm)	σ_{22} (ppm)	σ_{33} (ppm)	σ_{iso}(ppm)
σ^{d}(total)	260	286	269	272
σ^{p}(total)	-373	-345	-181	-300
σ (total)	-113	-59	88	-27
σ $(total)_{exp}$ [2]	-88	-26	101	-4
σ $(total)^{b}_{calc}$ [3]	-113	-45	96	-20

[a] QZ4P basis sets on all atoms.[b] Gaussina-94 DFT levels of theory using gauge including atomic orbitals GIAOs methods have been used in this study.

Diamagnetic shielding at the carbon nucleus is largely the result of core MOs that possess high carbon character (Table C2).

Table C2. Significant Diamagnetic Contributions to the Carbon Magnetic Shielding for Formaldehyde.

MO[a]	σ_{11}(ppm)	σ_{22} (ppm)	σ_{33} (ppm)	σ_{iso}(ppm)
$3a_1$	200	200	200	200
$4a_1$	17	15	16	20
$1b_1$	7	19	14	15

[a] MOs are illustrated in Figure C.

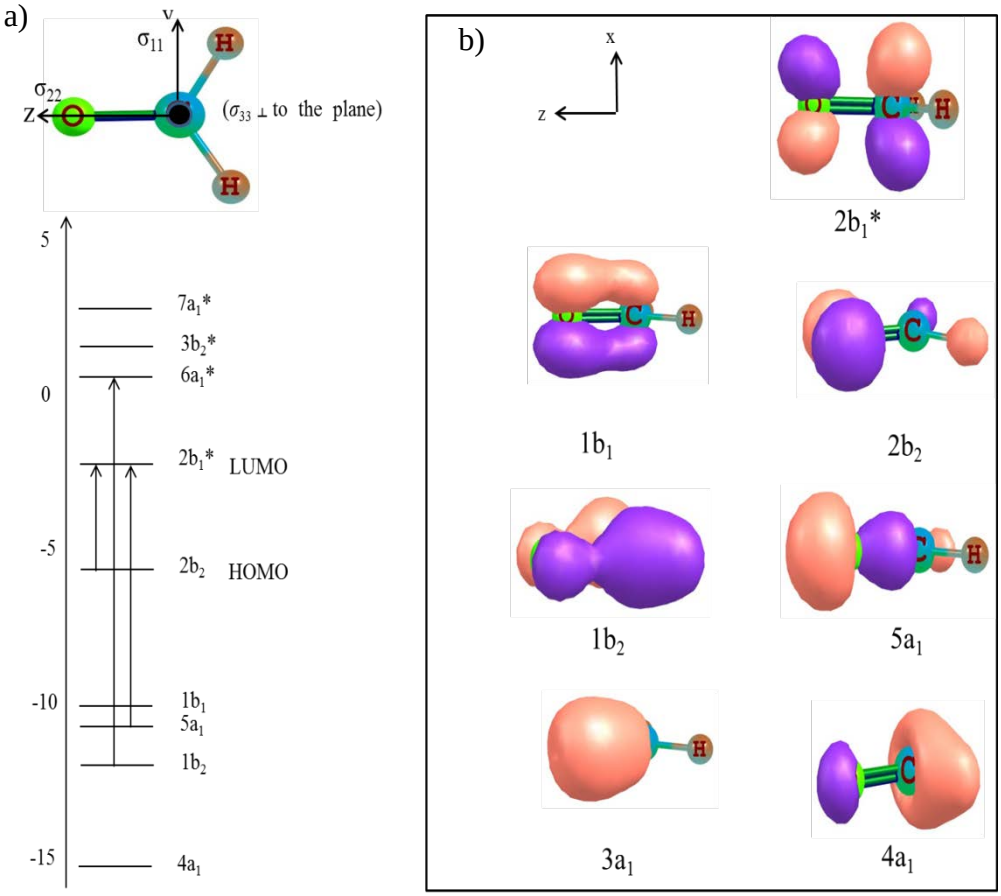

Figure C. a) MO energy-level diagram and carbon magnetic shielding tensor orientation for Formaldehyde and b) visual representation of the MOs which contribute substantially to the paramagnetic shielding tensor.

However, the contributions to σ^p are largely due to mixing of occupied and virtual MO with the $2b_2 \leftrightarrow 2b_1^*$, $5a_1 \leftrightarrow 2b_1^*$ and $1b_2 \leftrightarrow 6a_1^*$ MO pairs making the most significant contributions (Table C3).

Table C3. Significant Contributions to σ^{p} for the Carbon Magnetic Shielding of Formaldehyde.

MO Occupied	MO Virtual	σ_{11}(p pm)	σ_{22} (ppm)	σ_{33} (ppm)	σ_{iso} (ppm)	$\langle\phi_b\|R_n\|\phi_a\rangle$
$1b_2$	$6a_1$*	0	0	-132	-44	$\langle 1b_2\|R_x\|6a_1^*\rangle$
$5a_1$	$2b_1$*	-207	0	0	-69	$\langle 5a_1\|R_y\|2b_1^*\rangle$
$2b_2$	$2b_1$*	0	-183	0	-61	$\langle 2b_2\|R_z\|2b_1^*\rangle$

According to the calculation results, mixing of the $5a_1$ and $2b_1$* MOs leads to paramagnetic deshielding along the y-axis parallel to $\sigma_{11.}$ Three nondegenerate rotational operators are available in the C_{2V} point group (Tables C4, C5) where $R_x = B_2$, $R_y = B_1$, and $R_z = A_2$.

$$\phi_b \times R_n \times \phi_a = B_1 \times \begin{bmatrix} R_x \\ R_y \\ R_z \end{bmatrix} \times A_1 = B_1 \times \begin{bmatrix} B_2 \\ B_1 \\ A_2 \end{bmatrix} \times A_1 = B_1 \times \begin{bmatrix} B_2 \\ B_1 \\ A_2 \end{bmatrix}$$

$$= \begin{bmatrix} A_2 \\ A_1 \\ B_2 \end{bmatrix}$$

From the above formula it is clear that only L_y possesses the symmetry that is required to generate nonzero overlap between the MOs. This is because only this matrix element equals or contains the totally symmetric representation of the C_{2V} point group which is A_1. By observing the orientation of the CS tensor in the frame of the molecule, Figure C, it is seen that the y axis and σ_{11} are collinear.

Table C4. Character Table for the C_{2v} Point Group.[4]

	E	C2(Z)	σv(xz)	σv(yz)	Linear rotation	quadratic
A_1	1	1	1	1	z	x^2, y^2, z^2
A_2	1	1	-1	-1	R_z	xy
B_1	1	-1	1	-1	x, R_y	xz
B_2	1	-1	-1	1	y, R_x	yz

Table C5. Product Table for the C_{2v} Point Group[4]

	A_1	**A_2**	**B_1**	**B_2**
A_1	A_1	A_2	B_1	B_2
A_2	A_2	A_1	B_2	B_1
B_1	B_1	B_2	A_1	A_2
B_2	B_2	B_1	A_2	A_1

To determine the magnitude of the shielding that is produced by a given MO pair, two factors must be considered: the degree of the overlap between the two MOs and their separation in energy, ΔE. From Figure C, it can be seen that by performing a rotational transformation on the $5a_1$ MO along the y-axis (the y axis passing through the carbon), a high degree of overlap with the $2b_1$* MO results (the MO overlap is destructive if the pink and purple lobes overlap which corresponds to a negative contribution to shielding), therefore mixing of the $5a_1$ and $2b_1$* MOs is symmetry allowed and must produce deshielding along σ_{11}, in agreement with the ADF calculated results. It can be seen from Figure C(a) that these two MOs are relatively close in energy (ΔE = 9.45 eV). If the same procedure is applied to predict the direction of the deshielding produced by the $2b_2 \leftrightarrow 2b_1$* MO pair, it is clear that the symmetry of the angular momentum operator must be along the z-axis of the molecule (Figure C) coincident with σ_{22}, which is consistent with the calculation results in Table C3. Despite the smaller

energy difference, the contributions to the paramagnetic shielding are less than what is observed in y-direction (presumably due to less favourable mixing of MO pairs).

---

[1] C. M. Widdifield, R. W. Schurko. *Concepts Magn. Reson*. **34A**, 91-123, (2009).

[2] G. Wu, M. D. Lumsden, G. C. Ossenkamp, K. Eichele. R. E. Wasylishen. *J. Phys. Chem*. **99**, 15806, (1995).

[3] N. Gonzales, J. Simons. *Int. J. Quantum Chem*. **63**, 875, (1997)

[4] F. A. Cotton. *Chemical Applications of Group Theory*; John Wiley & Sons: New York, US, 1990.

Appendix 7.1 . NMR Parameters for Sodium Halides

Experimental ^{23}Na quadrupole coupling constant and magnetic shielding anisotropy for sodium halides obtained by microwave spectroscopy.

Molecule	C_Q (^{23}Na)/ kHz	C_I (^{23}Na) /kHz	Δσ/ppm	σ_{iso}/ppm
NaF[1]	-8428.94 ± 0.05	1.5078 ± 0.0030	72	580
NaCl[2]	-5669.80 ± 0.06	1.00 ± 0.41	94	565
Na^{79}Br[3]	-4932.50 ± 0.10	0.686 ± 0.006	93	566
NaI[4]	-4073.00 ± 0.10	0.74 ± 0.08	130	541

The following equations are used to derive quadrupolar coupling constant and magnetic shielding anisotropy from experimental results.[5] Using the Flygare approximation [6] for the diamagnetic shielding then leads to

$$\sigma_{\perp} = -\frac{m_p C_I}{2 m_e g_N B} + \sigma^d(\text{free atom})$$

The diamagnetic shielding of the free atoms are well known from the tabulations of Malli and Froese,[7] and for a linear molecule:

$$\sigma_{iso} = \sigma^d \approx \sigma^d(\text{free atom})$$

since $\sigma_{\|}^p$ is identically zero for a linear molecule. Thus, one may obtain the absolute shielding directly from the measured anisotropy in a linear molecule. A theoretically calculated diamagnetic term provides the rest of the required information.

$$\Delta\sigma = \sigma_{iso} - \sigma_{\perp} = -\left(-\frac{m_p C_I}{2 m_e g_N B}\right) = -\acute{\sigma}_{\perp}$$

$$\sigma_{iso} = \frac{2}{3}\acute{\sigma}_{\perp} + \sigma^{d}(\text{free atom})$$

$$\gamma\ (^{23}\text{Na}) = 7.08013 \times 10^{7}\ \text{rad s}^{-1}\text{T}^{-1}$$

Note error in $C_{\perp}$ for NaCl is very large; also the error for NaF is significant.

Calculated ^{23}Na quadrupolar coupling constant and magnetic shielding anisotropy for sodium halides.

Molecule	C_Q (^{23}Na)/ kHz[a]	Δσ/ppm[a]	σ_{iso}/ppm[a]
NaF	-7749.49	96	579
NaCl	-5236.30	99	565
Na^{79}Br	-4468.69	106	562
NaI	-3708.31	116	557

[a]Values are computed by Zora DFT in ADF using (VWN)[8] local density approximation with the Becke,[9] Perdew[10] generalized gradient approximation (GGA) for the exchange correlation functional. The QZ4P basis set was employed on all atoms.

The *ab initio* calculations seem to support the idea that σ_{iso} decreases as one descends the group *VII* halides. The anisotropy also appears to increase.

References

[1] J. Cederberg, L. Kang, C. Conklin, E. Berger. *J. Mol. Spectrosc*. **263**, 142, (2010).

[2] F. H. De Leeuw, R. Van Wachem, A. Dymanus. *J. Chem. Phys*. **53**, 981, (1970).

[3] J. Cederberg, D. Nitz, A. Kolan, T. Rasmusson, K. Hoffman, S. Tufte. *J. Mol. Spectrosc*. **122**, 171, (1987).

[4] C. E. Miller, J. C. Zorn. *J. Chem. Phys*. 50, 3748, (1969).

[5] C. J. Jameson. *Encyclopedia of Nuclear Magnetic Resonance*; Vol. 2, D. M. Grant and R. K. Harris, John Wiley &Sons: London, (1996).

[6] W. H. Flygare. J. *Chem. Phys*. **41**, 793, (1964).

[7] G. Malli and C. Froese. *Int. J. Quantum Chem*. 1 S, 95, (1967).

[8] S. H. Vosko, L. Wilk, M. Nusair. *Can. J. Phys*. **58**, 1200, (1980).

[9] A. D. Becke. *Phys. Rev.* **A 38**, 3098, (1988).

[10] J. P. Perdew. *Phys. Rev.* **B 33**, 8822, (1986).